Graphene, layered materials and hybrid structures for advanced photodetectors

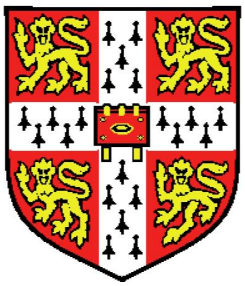

Domenico De Fazio

Department of Engineering
University of Cambridge

This dissertation is submitted for the degree of
Doctor of Philosophy

St. Edmund's College January 2018

Abstract

Photodetectors are essential in optoelectronics as they allow the conversion of optical signals into electrical outputs. Silicon, germanium and III-V semiconductors currently dominate the photodetector market.

In this dissertation I exploit the potential of layered materials to demonstrate a class of photodetectors able to challenge existing technological issues. I first demonstrate a fabrication method for high-mobility, chemical-vapour-deposited graphene devices which could help to increase the responsivity in graphene-based photodetectors.

I then show three examples of graphene-based Schottky photodetectors working at the telecommunication wavelength λ=1550nm, two for free-space illumination and one for on-chip applications. These are able to achieve responsivities up to 1A/W with relatively-low operation voltage (-3V), similar to those achieved with germanium.

I then target the mid-infrared range ($\lambda \sim 10\mu$m), where emission from objects at room temperature has a peak. I show graphene-based pyroelectric bolometers with temperature coefficient of resistance up to 900%/K, two orders of magnitude higher compared to current solutions based on thin oxide membranes.

I present flexible photodetectors working in the visible range (λ=642nm) with gate-tunable graphene/MoS_2 heterostructures and show responsivity up to 45A/W, 82% transparency, and low voltage operation (-1V). The responsivity is two orders of magnitude higher compared to semiconducting flexible membranes. Graphene/MoS_2 photodetectors can be bent without loss in performance down to a bending radius of 1.4cm.

I finally report on the investigation of superconducting properties of layered materials with the target of realizing ultra-sensitive superconducting photodetectors. Unconventional superconductivity is induced in graphene by proximity with a cuprate superconductor. I used gating to turn semiconducting, few-layer MoS_2 into a superconductor, which allowed us to unveil the presence of a multi-valley transport in the superconducting state. Electrical properties of the layered superconductor $NbSe_2$ are then studied. I then used $NbSe_2$ ultrathin flakes to realize superconducting photodetectors at λ=1550nm, reaching a sensitivity down to few thousand photons.

Declaration

I hereby declare that except where specific reference is made to the work of others, the contents of this dissertation are original and have not been submitted in whole or in part for consideration for any other degree or qualification in this, or any other university. This dissertation is my own work and contains nothing which is the outcome of work done in collaboration with others, except as specified in the text and Acknowledgements. This dissertation contains fewer than 65000 words including appendices, bibliography, footnotes, tables and equations and has fewer than 150 figures.

Acknowledgements

I would like to express my gratitude to my supervisor, Prof. Andrea Ferrari, for giving me the opportunity of joining the Nanomaterials and Spectroscopy Group (NMS), and the Cambridge Graphene Centre (CGC) as a doctoral student at the Engineering Department of the University of Cambridge.

I would also would like to thank Dr Ilya Goykhman for his constant guidance throughout my Ph.D. studentship both as a teacher and as a friend. His deep and thorough knowledge in the field of optoelectronics and silicon photonics have offered me crucial scientific support for all the projects presented here. I am thankful to him about the time taken for every-day discussions and constant motivation. In particular I want to thank him for the time dedicated to simulate the structures and fabricate optical waveguides (in The Hebrew University of Jerusalem, Israel) for integrated photodetectors in Section 6.4. I also thank him for the preparation of the measurement setup needed for the results in Section 6.4 as well as the effort devoted in the preparation of optoelectronic measurement setups here at the CGC, utilized for most of the applications in this dissertation.

I also thank Prof. Paul Midgley and Duncan Johnstone (Material Science, University of Cambridge, UK) for having performed the TEM measurements shown in Fig.5.8. A sincere acknowledgement goes to Prof. Stephan Hofmann and Philipp Braeuninger-Weimer (CGC, University of Cambridge, UK) for the growth of graphene single crystals used in Section 5.5 as well as for providing the TEM data shown in Fig.5.9. A big thanks also goes Dr Maurizio Casalino (CNR-IMM, Italy) for his pivotal role in the preparation of the setup needed to achieve the results in Section 6.2. Moreover, I want to thank Prof. Frank Koppens, as well as Romain Parret and Sebastien Nanot (ICFO, Spain) for their help while realizing the optoelectronic characterization of devices discussed in Chapter 7. I also acknowledge the work of Dr Alan Colli (Emberion, UK), who has performed thermo-electrical characterization of devices in Chapter 7. I am also thankful to Prof. Andras Kis, Dr Dumitru Dumcenco and Kolyo Marinov (EPFL, Switzerland) for the preparation of MoS_2 films necessary for the devices shown in Chapter

8. I also acknowledge the work of Dr Angelo Di Bernardo and Dr Jason Robinson (Material Science, University of Cambridge, UK), as well as that of Prof. Oded Millo (The Hebrew University of Jerusalem, Israel): the former two grew PCCO films on STO, while the latter performed STM/STS measurements to study superconducting properties in graphene. I am thankful to Prof. Renato Gonnelli, Dr Erik Piatti and Prof. Dario Daghero (Polytechnic University of Turin, Italy) as they introduced me to the field of low temperature transport, providing essential support toward learning of gating techniques shown in Section 9.4. Furthermore, I thank Prof. Robert Hadfield for having offered me the possibility to work in his labs at Univerisity of Glasgow (UK), alongside with Gavin Orchin, in order to characterize the optoelectronic properties of superconducting devices shown in Chapter 10.

I hereby want to thank my colleagues here at the CGC. In particular I am thankful to Dr Ugo Sassi for having taught the fundamentals of chemical vapour deposition of graphene and transfer techniques. He has also helped performing fabrication of devices in Section 6.2 and Chapter 7 and their optoelectronic characterization. I am thankful to David Purdie for having shared with me his knowledge about transport measurements in graphene and offered help for the fabrication of encapsulated graphene devices. I thank Dr Anna Eiden for the great help in the realization of devices in Sections 6.3 and Chapter 8. I also would like to thank Dr Duhee Yoon, Dr Anna Ott, Dr Silvia Milana, for sharing their knowledge regarding material and device characterization by means of Raman and photoluminescence spectroscopy. A big thanks goes also to Dr Giancarlo Soavi for the great dedication to build the pump-probe spectroscopy setup for the characterization shown at the end of Chapter 8. I also thank Dr Matteo Bruna for the realization of the polymer electrolyte utilized in Chapter 8 and for the great personal help offered in the first years of my Ph.D.

Another deep and sincere thanks goes to my dearest friends here at CGC: Lucia Lombardi, Flavia Tomarchio, Dr Matteo Barbone, Dr Matteo Bruna, Dr Ugo Sassi and Dr Giancarlo Soavi whose help has come not only from a scientific but also from a moral point of view.

I want to thank my partner Antonella for her constant love and support in these years, as she represents for me a constant source of motivation.

Last but not least I am always thankful to my parents Nino and Daniela, as well as my syster Flavia, whose sacrifices in these years have allowed me to embark in this great adventure. I am also thankful to my family and dearest friends, who I have now known for a lifetime. Even though they are far, far away, their love lies close to my heart.

Table of contents

Publications and conference presentations

Peer reviewed journals and manuscripts

1. G. Soavi, G. Wang, H. Rostami, D. Purdie, **D. De Fazio**, T. Ma, B. Luo, J. Wang, A. K. Ott, D. Yoon, S. Bourelle, J. E. Muench, I. Goykhman, S. Dal Conte, M. Celebrano, A. Tomadin, M. Polini, G. Cerullo, and A. C. Ferrari, *Broadband, electrically tuneable, third harmonic generation in graphene*, arXiv:1710.03694 (2017).

2. C. Ferrante, A. Virga, L. Benfatto, M. Martinati, **D. De Fazio**, U. Sassi, C. Fasolato, A.K. Ott, P. Postorino, D. Yoon, G. Cerullo, F. Mauri, and A.C. Ferrari, T. Scopigno, *Raman spectroscopy of graphene under ultrafast laser excitation*, arXiv:1704.00186 (2017).

3. M. Casalino, U. Sassi, I. Goykhman, A. Eiden, E. Lidorikis, S. Milana, **D. De Fazio**, F. Tomarchio, M. Iodice, G. Coppola, and A. C. Ferrari, *Vertically-illuminated, resonant-cavity-enhanced, graphene-silicon Schottky photodetectors*, ACS Nano **11**, 10955 (2017).

4. U. Sassi, R. Parret, S. Nanot, M. Bruna, S. Borini, **D. De Fazio**, Z. Zhao, E. Lidorikis, F. H. L. Koppens, A. C. Ferrari and A. Colli, *Graphene-based mid-infrared room-temperature pyroelectric bolometers with ultrahigh temperature coefficient of resistance*, Nature Communications **8**, 14311 (2017).

5. A. Di Bernardo, O. Millo, M. Barbone, H. Alpern, Y. Kalcheim, U. Sassi, A. K. Ott, **D. De Fazio**, D. Yoon, M. Amado, A. C. Ferrari, J. Linder and J. W. A. Robinson, *p-Wave triggered superconductivity in single-layer graphene on an electron-doped oxide superconductor*, Nature Communications **8**, 14024 (2017).

6. **D. De Fazio**, I. Goykhman, D. Yoon, M. Bruna, A. Eiden, S. Milana, U. Sassi, M. Barbone, D. Dumcenco, K. Marinov, A. Kis and A. C. Ferrari, *High responsivity, large-area graphene/MoS_2 flexible photodetectors*, ACS Nano **10**, 8252 (2016).

7. E. A. A. Pogna, M. Marsili, **D. De Fazio**, S. Dal Conte, C. Manzoni, D. Sangalli, D. Yoon, A. Lombardo, A. C. Ferrari, A. Marini, G. Cerullo and D. Prezzi, *Photo-induced bandgap renormalization governs the ultrafast response of single-layer MoS_2*, ACS Nano **10**, 1182 (2016).

8. I. Goykhman, U. Sassi, B. Desiatov, N. Mazurski, S. Milana, **D. De Fazio**, A. Eiden, J. Khurgin, J. Shappir, U. Levy and A. C. Ferrari, *On-chip integrated, silicon-graphene plasmonic Schottky photodetector with high responsivity and avalanche photogain*, Nano Letters **16**, 3005 (2016).

9. S. Dal Conte, F. Bottegoni, E. A. A. Pogna, **D. De Fazio**, S. Ambrogio, I. Bargigia, C. D'Andrea, A. Lombardo, M. Bruna, F. Ciccacci, A. C. Ferrari, G. Cerullo and M. Finazzi, *Ultrafast valley relaxation dynamics in monolayer MoS_2 probed by non-equilibrium optical techniques*, Physical Review B **92**, 235425 (2015).

10. M. Trushin, A. Grupp, G. Soavi, A. Budweg, **D. De Fazio**, U. Sassi, A. Lombardo, A. C. Ferrari, W. Belzig, A. Leitenstorfer and D. Brida, *Ultrafast pseudospin dynamics in graphene*, Physical Review B **92**, 165429 (2015).

11. Y. Ivry, C. S. Kim, A. E. Dane, **D. De Fazio**, A. N. McCaughan, K. A. Sunter, Q. Zhao and K. K. Berggren, *Universal scaling of the critical temperature for thin films near the superconducting-to-insulating transition*, Physical Review B **90**, 214515 (2014).

12. Q. Zhao, A. N. McCaughan, A. E. Dane, F. Najafi, F. Bellei, **D. De Fazio**, K. A. Sunter, Y. Ivry and K. K. Berggren, *Eight-fold signal amplification of a superconducting nanowire single-photon detector using a multiple-avalanche architecture*, Optics Express **22**, 24574 (2014).

13. Q. Y. Zhao, A. McCaughan, F. Bellei, F. Najafi, **D. De Fazio**, A. Dane, Y. Ivry and K. K. Berggren, *Superconducting- nanowire single-photon-detector linear array*, Applied Physics Letters **103**, 142602 (2013).

Conference proceedings

1. W. Wei, **D. De Fazio**, U. Sassi, A. C. Ferrari, E. Pallecchi, and H. Happy, *Graphene field effect transistors with optimized contact resistance for current gain*, IEEE Device Research Conference (2017).

2. I. Goykhman, A. Eiden, **D. De Fazio**, U. Sassi, M. Barbone and A. C. Ferrari, *High responsivity silicon-graphene schottky avalanche photodetectors for visible and telecom wavelengths*, CLEO: Science and Innovation (2015).

3. A. Grupp, M. Trushin, G. Soavi, A. Budweg, **D. De Fazio**, A. Lombardo, A. C. Ferrari, W. Belzig, A. Leitenstorfer and D. Brida, *Ultrafast pseudospin dynamics in graphene*, CLEO: QELS Fundamental Science (2015).

Conference presentations

- **D. De Fazio**, A.C. Ferrari, *Growth, transfer and characterization of layered materials and their heterostructures*, Advances on the Synthesis of Graphene Workshop, Fuerteventura, Spain (2016)

- **D. De Fazio**, I. Goykhman, M. Bruna, A. Eiden, U. Sassi, M. Barbone, D. Dumcenco, K. Marinov, A. Kis and A.C. Ferrari, *Large-area graphene/MoS_2 flexible photodetector*, MRS Spring 2015 Conference, San Francisco, U.S.A. (2015)

- **D. De Fazio**, I. Goykhman, M. Bruna, A. Eiden, U. Sassi, M. Barbone, D. Dumcenco, K. Marinov, A. Kis and A.C. Ferrari, *High responsivity graphene/MoS_2 flexible photodetector*, EMRS Spring 2015 Conference, Lille, France (2015)

- **D. De Fazio**, I. Goykhman, M. Bruna, A. Eiden, U. Sassi, M. Barbone, D. Dumcenco, K. Marinov, A. Kis and A.C. Ferrari, *Graphene/MoS_2 flexible photodetector*, Graphene 2015 Conference, Bilbao, Spain (2015)

Posters

- **D. De Fazio**, I. Goykhman, D. Yoon, M. Bruna, A. Eiden, S. Milana, U. Sassi, M. Barbone, D. Dumcenco, K. Marinov, A. Kis, A. C. Ferrari, *High responsivity graphene/MoS_2 flexible photodetectors*, Graphene EU-US Workshop on 2D Materials, Heterostructures and Devices, Manchester, U.K. (2016)

Contributed talks and posters

- A. Di Bernardo, O. Millo, M. Barbone, H. Alpern, Y. Kalcheim, U. Sassi, A. K. Ott, D. De Fazio, D. Yoon, M. Amado, A. C. Ferrari, J. Linder, J. W. A. Robinson, *p-Wave superconductivity in single layer graphene on an electron-doped oxide superconductor*, APS March Meeting 2017, New Orleans, U.S.A. (2017)

- G. Soavi, D. De Fazio, S. R. Tamalampudi, D. Yoon, E. Mostaani, A. R. Botello, S. Dal Conte, G. Cerullo, I. Goykhman, A. C. Ferrari, *Gate tuneable ultrafast charge transfer in graphene/MoS_2 heterostructures*, Graphene 2017 Conference, Barcelona, Spain (2017)

- H. P. A. G. Astier, J. M. Fruhman, L. Eyre, B. Ehrler, M. Böhm, P. R. Kidambi, U. Sassi, **D. De Fazio**, J. Griffiths, B. Robinson, S. Hofmann, A. C. Ferrari, C. J. B. Ford, *Electrically contacting self-assembled PbS nanocrystals using graphene*, Graphene 2017 Conference, Barcelona, Spain (2017)

- D. N. Johnstone, R. K. Leary, A. S. Eggeman, S. Hodge, U. Sassi, **D. De Fazio**, A. C. Ferrari, *Structure and topology of chemical vapour deposited graphene by scanning electron diffraction*, European Microscopy Congress, Lyon, France (2016)

- U. Sassi, M. Casalino, I. Goykman, A. Eiden, G. Coppola, S. Milana, E. Lidorikis, **D. De Fazio**, F. Tomarchio, M. Iodice, L. Sirleto, and A. C. Ferrari, *Cavity integrated silicon-graphene Schottky photodetectors*, Graphene 2016 Conference, Bilbao, Spain (2016)

- A. K. Ott, N. Dwivedi, R. J. Yeo, C. Dou, U. Sassi, **D. De Fazio**, C. S. Bhatia, A. C. Ferrari, *Graphene as protective coating for ultra-high storage density hard disks*, Graphene 2016 Conference, Bilbao, Spain (2016)

- S. Dal Conte, F. Bottegoni, E. A. A. Pogna, **D. De Fazio**, S. Ambrogio, I. Bargigia, C. D'Andrea, A. Lombardo, M. Bruna, F. Ciccacci, A. C. Ferrari, G. Cerullo, M. Finazzi, *Intervalley scattering in monolayer MoS_2 probed by non-equilibrium optical techniques*, SPIE Optics + Photonics 2015, San Diego, U.S.A. (2015)

- A. Grupp, M. Trushin, G. Soavi, A. Budweg, **D. De Fazio**, U. Sassi, A. Lombardo, A.C. Ferrari, W. Belzig, A. Leitenstorfer, D. Brida, *Pseudospin carrier coupling in graphene on the femtosecond timescale*, EDISON Conference 2015, Salamanca, Spain (2015)

- I. Goykhman, **D. De Fazio**, M. Bruna, A. Eiden, U. Sassi, M. Barbone, D. Dumcenco, K. Marinov, A. Kis and A.C. Ferrari, *High responsivity graphene/MoS_2 flexible photodetector*, Graphene Week 2015, Manchester, U.K. (2015)

- M. Marsili, D. Prezzi, D. Sangalli, E. A. A. Pogna, S. Dal Conte, C. Manzoni, **D. De Fazio**, M. Bruna, I.Goykhman, A. C. Ferrari, A. Marini, and G. Cerullo, *Bandgap renormalization governs the ultrafast response of MoS_2*, Graphene Week 2015, Manchester, U.K. (2015)

- A. Eiden, I. Goykhman, **D. De Fazio**, U. Sassi, M. Barbone, S. Milana, D. Yoon, A. C. Ferrari, *High responsivity graphene-silicon avalanche photodetectors for visible and telecom wavelengths*, Graphene Week 2015, Manchester, U.K. (2015)

- S. Dal Conte, F. Bottegoni, E. A. A. Pogna, S. Ambrogio, **D. De Fazio**, A. Lombardo, M. Bruna, A.C. Ferrari, F. Ciccacci, G. Cerullo, M. Finazzi, *Disentangling intra and intervalley dynamics in monolayer MoS_2 by ultrafast optical techniques*, Graphene Week 2015, Manchester, U.K. (2015)

- F. Roux, F. Emieux, V. Muffato, **D. De Fazio**, U. Sassi, A.C. Ferrari and E. Quesnel, *Integration of CVD graphene as transparent front electrode into conventional a-Si:H thin film solar cells*, Graphene Week 2015, Manchester, U.K. (2015)

- S. Dal Conte, F. Bottegoni, E. A. A. Pogna, S. Ambrogio, **D. De Fazio**, A. Lombardo, M. Bruna, I. Bargigia, C. D'Andrea, A.C. Ferrari, F. Ciccacci, G. Cerullo, and M. Finazzi, *Disentangling intra and intervalley dynamics in monolayer MoS_2 by ultrafast optical techniques*, CLEO Europe - EQEC 2015, Munich, Germany (2015)

- A. Grupp, M. Trushin, G. Soavi, A. Budweg, **D. De Fazio**, U. Sassi, A. Lombardo, A.C. Ferrari, W. Belzig, A. Leitenstorfer, D. Brida, *Ultrafast pseudospin dynamics of carriers in graphene*, CLEO Europe - EQEC 2015, Munich, Germany (2015)

- E. A. A. Pogna, S. Dal Conte, M. Marsili, D. Prezzi, D. Sangalli, C. Manzoni, A. Marini, **D. De Fazio**, M. Bruna, I. Goykhman, A. C. Ferrari, and G. Cerullo, *Bandgap renormalization governs the ultrafast response of single-layer MoS_2*, CLEO Europe - EQEC 2015, Munich, Germany (2015)

- I. Goykhman, A. Eiden, **D. De Fazio**, U. Sassi, M. Barbone, S. Milana, D. Yoon, A. C. Ferrari, *Plasmonic silicon-graphene Schottky photodetector for on-chip applications in the telecom spectral band*, SPP7, Jerusalem, Israel (2015)

- A. Eiden, I. Goykhman, **D. De Fazio**, U. Sassi, M. Barbone, A.C. Ferrari, *High responsivity silicon-graphene Schottky avalanche photodetectors for visible and telecom wavelengths*, EMRS Spring 2015 Conference, Lille, France (2015)

- A. Grupp, M. Trushin, G. Soavi, A. Budweg, **D. De Fazio**, U. Sassi, A. Lombardo, A.C. Ferrari, W. Belzig, A. Leitenstorfer, D. Brida, *Ultrafast pseudospin dynamics in graphene*, CLEO 2015, San Jose, U.S.A. (2015)

- I. Goykhman, A. Eiden, **D. De Fazio**, U. Sassi, M. Barbone, S. Milana, D. Yoon, A. C. Ferrari, *High responsivity graphene-silicon avalanche photodetectors for visible and telecom wavelengths*, CLEO 2015, San Jose, U.S.A. (2015)

- I. Goykhman, A. Eiden, **D. De Fazio**, U. Sassi, M. Barbone, S. Milana, D. Yoon, A. C. Ferrari, *High responsivity graphene-silicon avalanche photodetectors for visible and telecom wavelengths*, MRS Spring 2015 Conference, San Francisco, U.S.A. (2015)

- S. Dal Conte, F. Bottegoni, E. A. A. Pogna, S. Ambrogio, **D. De Fazio**, A. Lombardo, M. Bruna, A. C. Ferrari, F. Ciccacci, G. Cerullo, M. Finazzi, *Disentangling spin and valley dynamics in monolayer MoS_2 by non-equilibrium optical techniques*, Graphene 2015 Conference, Bilbao, Spain (2015)

- E.A.A. Pogna, S. Dal Conte, M. Marsili, D. Prezzi, D. Sangalli, C.Manzoni, A. Marini, **D. De Fazio**, M. Bruna, I. Goykhman, A. C. Ferrari, G. Cerullo, *Ultrafast broadband study of photocarrier dynamics in MoS_2 single layer*, Graphene 2015 Conference, Bilbao, Spain (2015)

- A. Eiden, I. Goykhman, **D. De Fazio**, U. Sassi, M. Barbone and A. C. Ferrari, *High responsivity silicon-graphene Schottky avalanche photodetectors for visible and telecom wavelengths*, Graphene 2015 Conference, Bilbao, Spain (2015)

- W. Belzig, A. Leitenstorfer, D. Brida, M. Trushin, A. Grupp, G. Soavi, A. Budweg, **D. De Fazio**, A. Lombardo, U. Sassi and A. C. Ferrari, *Momentum resolved optical pump-probe spectroscopy in monolayer graphene: An analytical model and measurements*, APS March Meeting 2015, San Antonio, U.S.A. (2015)

- I. Goykhman, U. Sassi, B. Desiatov, **D. De Fazio**, N. Mazurski, U. Levy and A. C. Ferrari, *Plasmonic silicon-graphene Schottky photodetector for on-chip applications in the telecom spectral band*, Graphene Week 2014, Gothenburg, Sweden (2014)

List of Acronyms and Symbols

Acronyms:

2d	Two dimensional
3d	Three dimensional
ALD	Atomic layer deposition
AFM	Atomic force microscopy
APS	Ammonium persulfate
BOE	Buffer oxide etch
CDW	Charge density wave
CMOS	Complementary metal-oxide-semiconductor
CNP	Charge neutrality point
CP	Cooper pairs
CVD	Chemical vapour deposition
DE	Detection efficiency
DI	Deionized
EBL	Electron beam lithography
EDL	Electrical double layer
EQE	External quantum efficiency
F-P	Fabry-Perot
FBZ	First Brillouin zone
FET	Field effect transistor
FL	Few layer
FSR	Free spectral range
FWHM	Full width at half maximum
GFET	Graphene field effect transistor
GRM	Graphene related materials
h-BN	Hexagonal boron nitride
IQE	Internal quantum efficiency
IPA	Isopropyl alcohol

IPE	Internal photoemission
IR	Infrared
LM	Layered materials
IoT	Internet of things
LDOS	Local density of states
LED	Light emitting diode
LN	Lithium niobate
LOCOS	Local oxidation of silicon
LPE	Liquid phase exfoliation
MBE	Molecular beam epitaxy
MGM	Metal-graphene-metal
MIR	Mid infrared
MOCVD	Metal-organic chemical vapour deposition
NEP	Noise equivalent power
NEST	Noise equivalent substrate temperature
NIR	Near infrared
NW	Nanowire
PC	Polycarbonate
PCCO	Praseodymium cerium copper oxide
PE	Polymer electrolyte
PECVD	Plasma-enhanced chemical vapour deposition
PET	Poly-ethylene oxide
PET	Poly-ethylene terephthalate
PL	Photoluminescence
PD	Photodetector
PDMS	Polydimethylsiloxane
PMMA	Polymethyl metacrylate
PPC	Polypropylene carbonate
PTE	Photo-thermoelectric effect
PVA	Polyvinyl alcohol
LL	Landau level
QHE	Quantum Hall effect
RCE	Resonant cavity enhanced
RIE	Reactive ion etching
RT	Room temperature
SC	Superconductivity

SBH	Schottky barrier height
SEM	Scanning electron microscopy
SLG	Single layer graphene
SOI	Silicon on insulator
SPP	Surface plasmon polaritons
SSPD	Superconducting single photon detector
STM	Scanning tunneling microscopy
STO	Strontium titanate
STS	Scanning tunneling spectroscopy
TCR	Temperature coefficient of resistance
TEM	Transmission electron microscopy
TES	Transition edge sensor
TMD	Transition metal dichalcogenide
UV	Ultraviolet
WI	Waveguide integrated
ZBCP	Zero-bias conductance peaks

Symbols:

Many symbols have been omitted as they are simply variations of symbols listed here. Their significance is specified in the subscript and/or in the text.

A	Optical absorbance
A	Area
A^*	Richardson constant
α	Fine structure constant
$\alpha_{\parallel}$	Spring constant (parallel)
$\alpha_{\perp}$	Spring constant (perpendicular)
B	Magnetic field
C	Shear modes
C	Capacitance
C_T	Heat capacity
c	Speed of light in vacuum
$\Delta(0)$	Half-superconducting gap at T$\rightarrow$0K
δ	Optical contrast
E	Energy
E_F	Fermi level

E_p	Photon energy
ϵ_0	Permittivity of vacuum
ϵ_r	Relative permittivity
F	Finesse
$\vec{F}$	Force
Φ_B	Schottky barrier potential
ϕ	Phase shift
G_0	Optical conductance
G_{ph}	Optical gain
G_T	Thermal conductance
$\hat{H}$	Hamiltonian operator
h	Planck constant
$\hbar$	Reduced Planck constant
η	Fraction of absorbed photons
η_D	Diode ideality factor
I	Optical intensity
I	Electrical current
I_{ph}	Photocurrent
J	Current density
J_C	Superconducting critical current density
j	Imaginary unit
$\mathbf{k}$	Momentum, wavenumber
k_B	Boltzmann constant
κ	Extinction coefficient
LBM	Layer breathing modes
λ	Wavelength
M	Avalanche multiplication gain factor
m	Electron mass
m^*	Electron effective mass
μ	Mobility
μ_m	Single layer mass per unit area
N	Number of atomic layers
N_{ph}	Number of photons
n	Charge carrier concentration (electron or hole)
n	Real part of the refractive index
$\tilde{n}$	Complex refractive index

n_g	Group index
ν	Frequency
P_{att}	Attenuated oprtical power
P_{abs}	Absorbed oprtical power
P_o	Optical power
$\mathbf{P}$	Polarization
p	Hole concentration
p_c	Pyroelectric constant
π	Pi constant
Q	Charge
q	Elementary charge
R	Optical reflectance
R	Electrical resistance
R_{ext}	External responsivity
R_{int}	Internal responsivity
r_B	Bending radius
ρ	Electrical resistivity
S	Seebeck coefficient
S_I	Spectral density of current fluctuations
σ	Electrical conductivity
T	Optical transmittance
T	Temperature
T_C	Superconducting critical temperature
T_g	Glass transition temperature
t	Time
τ	Carrier lifetime
τ_d	Dead time
V	Electrical voltage
V_{ph}	Photo-voltage
$\vec{v}$	Velocity
v_d	Carrier drift velocity
v_F	Fermi velocity
ω	Angular frequency

Chapter 1

Introduction

1.1 Motivation

The density of information being exchanged user-to-user and the number of interconnected devices has grown exponentially in the last few decades. Smart devices are revolutionizing our lives and 30 billion units are expected to be connected to a unique network by 2020, forming the so-called "Internet of Things" (IoT). So far, the need to continuously increase data rates has been achieved by scaling electronic components (transistors) in integrated circuits. Shorter length-scales indeed allow to perform more computations (bits) per seconds, increasing the operation frequency. The downscaling of transistor dimensions has been constantly ruled by the Moore's law, which predicted that the number of transistors per unit area would have doubled every 18 months. This trend has continued unperturbed but is also expected to slow down due to fundamental limits while approaching the nanometre scale. The close packing of numerous transistors on a chip also increases the number of wires and interconnections leading to parasitic effects such as increased parasitic capacitances, cross talk, latency. These generate delays in signal propagation. Furthermore the use of copper wires for off-chip communication (chip-to-chip, board-to-board, rack-to-rack, etc.) is associated with losses when operating at GHz regime and high power consumption. These problems can be identified in what is referred to as the "interconnect bottleneck".

Exchanging information with optical signals could be a viable path around the interconnect bottleneck. In "optical interconnects" or "optical links" light sources such as lasers and light emitting diodes (LEDs) are needed to generate optical signals, while optical fibres carry those signals to modulators and photodetectors for manipulation and detection, respectively. In order to support the ever increasing data rate, integrated short-reach optical interconnects are expected to operate at hundreds GHz with fJ/bit

energy consumption (the target for 2020 is 1 fJ/bit). Last but not least, the costs per component need to be minimized.

The photodetector is a key component of the optical link enabling the conversion of light in electrical signals. Silicon, germanium and III-V semiconductors have been the pillars of modern optoelectronic devices. Silicon is the material of choice for the complementary metal-oxide-semiconductor (CMOS)-based integrated circuit technology. It has an indirect bandgap of ∼1.1eV which hinders the absorption at the telecommunication wavelength λ=1550nm (∼0.8eV), where losses in optical fibres are lowest[1, 2]. Conversely, III-V semiconductors have direct bandgaps which can also be sized by growing ternary compounds, but they are costly and not compatible with standard CMOS process. Germanium, with a indirect bandgap of ∼0.67eV is currently the primary choice for photodetectors at 1550nm, also owing to the possibility to be integrated in the silicon fabrication line. However the large lattice mismatch (∼4%) between germanium and silicon generates defect states at the interface, causing increased leakage currents even in the light-off state (dark currents)[3]. Furthermore the detection of thermal radiation at longer wavelengths (λ ∼8-12μm) is impractical with all of the so far listed semiconductors, unless defects are induced in their bandgaps.

The density of information exchanged among peers grows side-by-side with the necessity to guarantee secure communication. Quantum cryptography or quantum key distribution is emerging as the primary candidate for secure data communication by offering encryption of signals in quantum states of photons, such as spin or polarization. This requires single photon sources and detectors. The latter need to possess extremely high performance in terms of photon detection efficiency, signal-to-noise ratio and speed. Current photon counting technologies mainly rely on technologies such as photomultipliers, avalanche photodiodes and superconducting photon detectors. The drive for perfected technologies is so intense that novel materials are constantly being investigated.

In parallel to the assembly of architectures on rigid platforms, the concept of integration is recently evolving. Modern technologies need to enable a completely different kind of integration, based on direct positioning of device architectures on irregularly-shaped objects or directly on the human body. Wearable technologies therefore require flexible devices which can conformally adapt to follow the shape of those objects or the human skin and most-importantly to resist and remain unperturbed by stretching or bending caused by movements. Flexible smart sensors to measure changes in humidity, temperature, pressure, heart-beat are now in the list of most desired tools in modern wearable devices. Moving from rigid to flexible platform is extremely complicated and sometimes requires re-thinking of the entire fabrication line. The first steps for the development of

flexible photodetectors have been made in the visible range: λ ∼400-800nm. The high stiffness of bulk semiconductors complicates their utilization in flexible detectors and other flexible technologies. Flexible photodetectors are indeed now realized mainly by exploiting semiconducting nanowires and nano-membranes. Despite reasonable performances have been achieved with these in terms of response to light, the early stage of the field leaves considerable room for improvement.

Graphene and layered materials (LM) offer an opportunity to complement the properties of their bulk counterpart and tackle the described issues in optoelectronic devices, including photodetectors. With its zero band-gap, graphene is a broadband absorber and it can potentially be integrated at the back end of line in CMOS process. It can absorb 2.3% of the incoming light in the visible and infrared range, from ∼400nm to ∼1300nm. Despite being a remarkable number for an atomically thin material, this absorption is not sufficient for efficient photodectors. Nonetheless, confinement of light into waveguides or cavities can lead to enhanced light-graphene interaction. Besides, the high mobility of graphene can enable fast conversion of light in electrical signals, leading to fast photodetectors. The successful fabrication of efficient graphene-based photodetectors at the telecom wavelength could therefore promote graphene as the best candidate to open alternatives to germanium-based photodetectors. The broadband absorption could also be proved effective for detection to longer (thermal) wavelenghts inaccessible by most bulk semiconductors. The world of layered materials is also not only limited to graphene. The number of materials in the family is in expansion along with the properties that they can offer. In this context the family of transition metal dichalcogenides has been one of the first to capture the attention of researchers, comprehending semiconductors, semimetals and superconductors. The performance of transition metal dichalcogenides in photodetectors needs to be addressed in order to allow benchmarking with existing technologies. Furthermore graphene and other layered materials have flexible properties and could open an entire new chapter in the field of flexible and wearable technologies.

1.2 Structure of the thesis

This dissertation is organized as follows. Chapter 2 introduces the field of graphene and layered materials. I discuss about the synthesis techniques with focus on those I utilized. I then give an overview of the most common characterization techniques. In Chapter 3 I introduce concepts on the assembly of heterostructures. In particular I discuss about wet and dry transfer methods.

Chapter 4 is an overview of optoelectronic applications with focus on different type of photodetectors. The chapter ends with a discussion on the key material requirements for optimal photodetector performance.

In Chapter 5 I discuss on the synthesis techniques I used for the fabrication of all devices in the dissertation and the standard characterization I performed for each material. I also present a novel method for the wet encapsulation of CVD graphene.

The next Chapters are dedicated to results. I start with presenting graphene-based Schottky photodetectors working in the near-infrared both for vertical illumination and for on-chip integration in Chapter 6. I then continue with showing a graphene-based pyroelectric bolometer working in the mid-infrared in Chapter 7. This is followed by results in Chapter 8 on a gate-tunable flexible photodetector realized from a graphene/molybdenum disulphide heterostructure working in the visible range. I then investigate superconducting properties of layered materials in Chapter 9 as a preamble to studies on ultra-sensitive superconducting photodetectors shown in Chapter 10.

Chapter 11 is dedicated to conclusions and future works.

Chapter 2

Graphene and Layered Materials

2.1 Introduction

Graphite is an allotropic form of carbon characterized by a layered crystal structure, where atoms in each plane are bonded covalently, whilst atomic planes are held together by weak Van der Waals forces. Graphene can be visualized as the isolation of a single plane in the structure of graphite. It is indeed a one atomic layer thick material formed by carbon atoms and organized in a honeycomb lattice.

Studies on graphene started in 1947, when its band structure was theoretically predicted by P. R. Wallace, along with that of graphite[4]. Thousands of crystals other than graphite have layered structures and their library is yet to be completed[5]. The first experimental works on layered crystals, mechanically cleaved to reduce their thickness and study their two-dimensional counterpart, have been pioneered by R.F. Frindt since 1963[6–8]. He focused his research on layered materials such as molybdenum disulfide and niobium diselenide, which are still of great interest nowadays, belonging to the class of transition metal dichalcogenides (TMDs). Other early theoretical studies on atomically thin crystals pointed that thermal fluctuations at finite temperatures in such materials would lead to displacements of atoms of the order of interatomic distances, making them thermodynamically unstable and preventing their existence in a free-standing state[9–12]. This scenario deeply changed in 2004 when graphene was isolated and proved to exist in a free-standing state by Nobel prize winners A. K. Geim and K. S. Novoselov[12, 13]. Since then, the attention toward graphene and layered materials has grown exponentially. Indeed, unveiling the exceptional properties of graphene has lead scientists to reconsider layered materials which were already studied in the past in their 3-dimensional counterpart, but not down to the 2d limit. These include the layered

insulator hexagonal boron nitride (h-BN) and the family of TMDs, whose properties will be discussed in details, and many others.

2.2 Properties

2.2.1 Graphene

The atomic structure of graphene can be seen as the interpenetration of two triangular sub-lattices, where the unit cell is formed by two carbon atoms. Each atom has one valence s orbital and three valence p orbitals, in a configuration that is referred to as sp^2 hybridization[4, 14]. The s orbital and the p_x, p_y orbitals form in-plane covalent σ-bonds with the neighbour atoms; the σ band is responsible for the robustness of the lattice[15]. The third p-orbital, p_z, that is perpendicular to the plane of the lattice can bind with the neighbour atoms, with a covalent π bond, forming a π band which is half-filled and and thus plays a key role in the electrical and thermal conduction in graphene. The thickness of a single layer is $\sim$3.4Å[15, 16].

The electronic properties of graphene can be understood by using a tight binding model, which means assuming that electrons are tightly bounded to the atom to which they belong and they can hop with a certain probability to neighbour atomic sites[15]. Since the basis of the lattice is represented by two carbon atoms, the two lattice vectors in real space are (Fig.2.1):

$$\mathbf{a_1} = \frac{a}{2}(3, \sqrt{3}), \mathbf{a_2} = \frac{a}{2}(3, -\sqrt{3}) \tag{2.1}$$

where "a" is the distance between two neighbour carbon atoms and is estimated to be equal to 1.42Å. Therefore the reciprocal lattice vector are:

$$\mathbf{b_1} = \frac{2\pi}{3a}(1, \sqrt{3}), \mathbf{b_2} = \frac{2\pi}{3a}(1, -\sqrt{3}) \tag{2.2}$$

By restricting the hopping to nearest neighbours and next-nearest neighbours the Hamiltonian of the system can be written as:

$$H = -t \sum_{<i,j>,\sigma} (a^{\dagger}_{\sigma,i} b_{\sigma,j} + Hermitian\, conjugate) - t' \sum_{<i,j>,\sigma} (a^{\dagger}_{\sigma,i} a_{\sigma,j} + b^{\dagger}_{\sigma,i} b_{\sigma,j} + H.c.) \tag{2.3}$$

where $a^{\dagger}_{\sigma,i}$ is a creation operator of an electron in the triangular sublattice A, with spin σ and in position R_i. While $a_{\sigma,j}$ is an annihilation operator of an electron in the

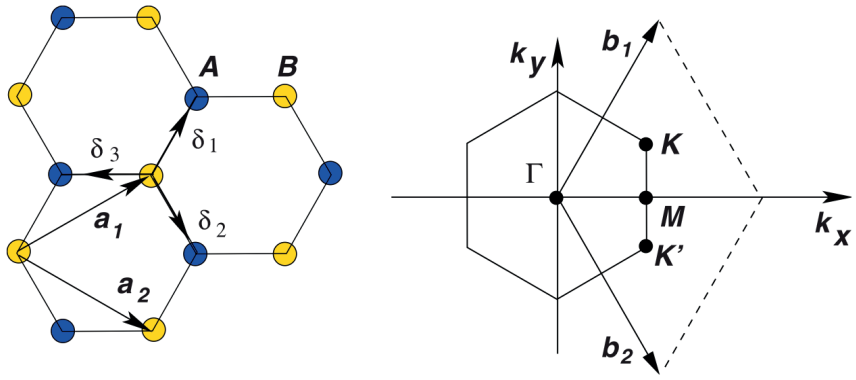

Figure 2.1: Lattice structure of graphene and its corresponding Brillouin zone in the reciprocal space. Taken from Ref.[15].

triangular sublattice A, with spin σ and in position R_j. The same applies for operator b which conversely refers to electrons in the sublattice B. Finally $t\,(\sim 2.8eV)$ and t' are the hopping energies required to hop to a nearest neighbour and next-nearest neighbour respectively[4].
The energy bands derived from the use of this Hamiltonian are:

$$E_{\pm}(\mathbf{k}) = \pm t\sqrt{3 + f(\mathbf{k})} - t' f(\mathbf{k}) \tag{2.4}$$

with $f(\mathbf{k})$ equal to:

$$f(\mathbf{k}) = 2\cos(\sqrt{3}k_y a) + 4\cos(\frac{\sqrt{3}}{2}k_y a)\cos(\frac{3}{2}k_x a) \tag{2.5}$$

where the "+" sign applies to the π^* band (conduction), while the "-" is valid for the π band (valence). A sketch is shown in Fig.2.2.

The conduction and valence bands intersect at zero energy in the K and K′ points of the Brillouin zone (Fig.2.1), making graphene a semimetal or zero band-gap semiconductor[12, 15]. The K and K′ points, named after their momentum, are referred to as Dirac points. They are located at the coordinates:

$$\mathbf{K} = (\frac{2\pi}{3a}, \frac{2\pi}{3\sqrt{3}a}), \mathbf{K}' = (\frac{2\pi}{3a}, -\frac{2\pi}{3\sqrt{3}a}) \tag{2.6}$$

By expanding the equation for energy bands near the Dirac point, that is near the K vector, the following dispersion equation can be obtained:

$$E_{\pm}(\mathbf{q}) \approx \pm v_F|\mathbf{q}| + O[(q/K)^2] \tag{2.7}$$

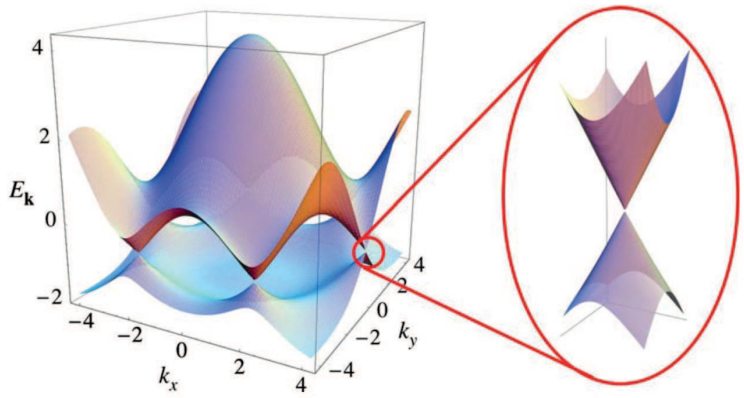

Figure 2.2: Electronic band structure of graphene calculated with tight binding method using t=2.7 eV and t′=-0.2t. On the right a zoom of one of the Dirac points. Taken from Ref.[15].

considering that **k**=**K**+**q**, where q is the momentum measured relatively to the Dirac points ($|\mathbf{q}| \ll |\mathbf{K}|$). Besides, v_F is the Fermi velocity and it is equal to $v_F = \frac{3}{2}ta \sim 10^6$m/s and independent from momentum[4, 15]. In pristine graphene the valence band is completely filled with electrons, whereas the conduction band is filled with holes; the presence of doping causes a shift of the Fermi level. The result that differentiates graphene from most of the known semiconductors is that close to the Dirac points the relation of energy dispersion is quasi-linear and not quadratic. In standard semiconductors, electrons are studied with a semiclassical approach. They follow the Schroedinger equation and the mass m is replaced by an "effective mass" m^*, which takes into account the interaction of electrons with the potential generated by the atom cores. The linear energy dispersion spectrum of graphene resembles the one of massless Dirac fermions, which are relativistic particles described by the Dirac equation. The Hamiltonian of carriers in "standard" semiconductors, obeying the Schroedinger equation is:

$$\hat{H} = \hat{p}^2/2m^\star \tag{2.8}$$

In the case of Dirac fermions the Hamiltonian takes the form:

$$\hat{H} = c\ \vec{\sigma} \cdot \hat{p} \tag{2.9}$$

where c is the speed of light and $\vec{\sigma}$ the Pauli matrix taking into account the presence of spin. Electrons and holes in graphene follow a 2-dimensional approximation of the equation for Dirac fermions but with the Fermi velocity v_F and a pseudospin matrix $\vec{\sigma}_{PS}$

replacing c and $\vec{\sigma}$ respectively[17]. The pseudospin matrix $\vec{\sigma}_{PS}$ changes value depending on which of the two sublattices the electron is located[17]. Therefore Eq.2.9 becomes[15, 17]:

$$\hat{H} = v_F \ \vec{\sigma}_{PS} \cdot \hat{p} \tag{2.10}$$

Another important aspect of the conduction in graphene is the ambipolar transport. One of the first experiments on graphene was showing that charge carrier concentrations n in the order of 10^{13}cm^{-2} could be achieved both for electron and holes through the application of an external electric field by means of a gate voltage (Fig.2.3(a))[13]. The electric field can shift the Fermi level of graphene and it allows continuous tuning of carriers from electrons (for positive V_g) to holes (for negative V_g). The resistivity has a peak, when the Fermi level is at the charge neutrality (Dirac) point and progressively diminishes on both sides when an electric field is applied, due to increasing of n. In contrast with other ambipolar semiconductors, here the consequence of the total absence of a bandgap is that current cannot be completely switched off[13]. The carrier mobility is defined as the ratio between the carrier drift velocity and the applied electric field. In transport measurements, the mobility is related to how rapidly the resisitivity changes upon application of the gate voltage. Even the first experiments performed on graphene, showed room temperature mobilities up to $10000\text{cm}^2\text{V}^{-1}\text{s}^{-1}$, already competitive with those reached in state-of-the-art semiconductor technologies[12, 13, 18].
Further transport measurements also showed that graphene has a minimum quantum conductivity of $4q^2/h$, even at the Dirac point. The factor "4" originates from the double valley and spin degeneracy. Measurements upon application of magnetic fields also allowed us to observe what is referred to as the Half-Integer Quantum Hall Effect. The Quantum Hall Effect (QHE) is the quantization of transverse (Hall) conductivity in a channel due to quantization of carrier trajectories upon application of magnetic fields; carriers can therefore occupy discrete energy levels, called Landau levels (LLs). This effect has been observed in other 2d electron systems but it assumes peculiar aspects in graphene. The transversal conductivity σ_{xy} in graphene has the shape of a ladder with steps of $4q^2/h$, persisting at the neutrality point[18][19]:

$$\sigma_{xy} = \pm 4\frac{q^2}{h}(N + 1/2) \tag{2.11}$$

where N is an integer index for LLs. With respect to the standard QHE here the ladder is shifted by a factor of 1/2, which justifies the name. This shift is understood in terms of quantization of the energy spectrum in the presence of magnetic field[19]. In 2d electron systems obeying the "standard" Integer QHE:

$$E_N = (N + 1/2)\hbar\frac{qB}{m} \tag{2.12}$$

In graphene the quantization assumes the form[19]:

$$E_N = \sqrt{2q\hbar BN} \tag{2.13}$$

This implies the presence of a LL (N=0) at zero energy, shared between electron and holes, half-filled at the neutrality point, which explains the difference with the Integer QHE case[18, 19]. The longitudinal resistivity ρ_{xx} drops to zero when a plateau appears in σ_{xy}, i.e. when the Fermi level is in between two LL, whereas it assumes finite values while carriers are filling a "new" Landau level.

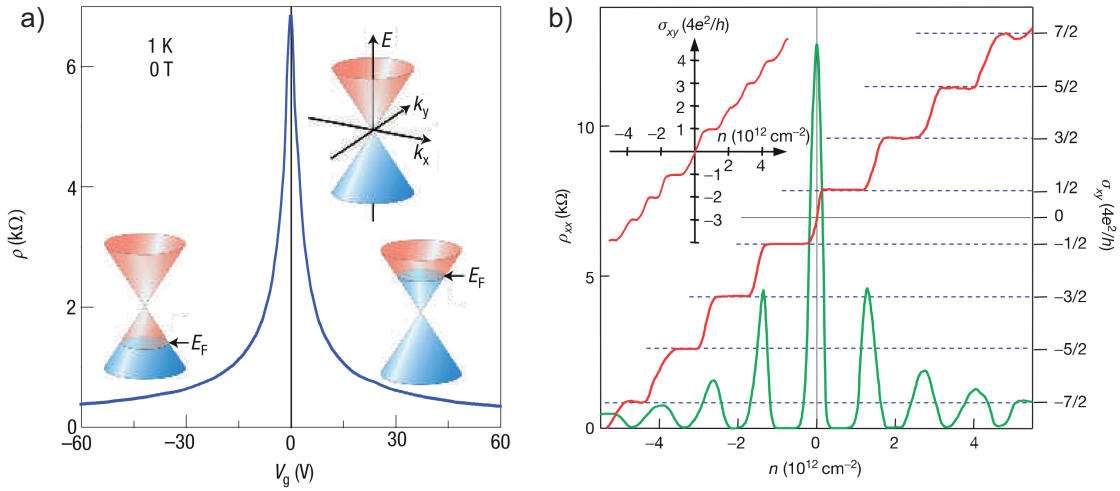

Figure 2.3: (a) Field effect (back-gate) dependence of the resistivity of a graphene channel (b) Longitudinal resistivity (ρ_{xx}) and transversal conductivity (σ_{xy}) as a function of charge carrier concentration, measured for a graphene Hall bar with application of a 14T magnetic field. The electron charge is e in these figures. Taken from Refs.[12, 18].

The optical properties of graphene are also of great interest. The isolation of graphene was enabled by inspection through optical microscope of graphitic flakes on a silicon (Si) wafer covered with a layer of silicon dioxide (SiO_2) of thickness ~300nm[13]. This oxide thickness allows an interference-like contrast, which enhances the graphene visibility in white light[12, 20, 21].

The optical conductance of graphene, due to valence-to-conduction band (interband) transitions, has been predicted to be different from the electrical conductance, seen for instance in the QHE. The optical conductance G_0 in graphene is frequency-independent and equal to[22, 23]:

$$G_0 = \frac{q^2}{4\hbar} \approx 6.08 \times 10^{-5}\,\Omega^{-1} \tag{2.14}$$

The optical absorbance and transmittance of graphene are defined solely by the fine structure constant α, which describes the interaction between light and Dirac fermions[22]:

$$\alpha = \frac{q^2}{\hbar c} = 1/137 \tag{2.15}$$

By applying the Fresnel equations with the hypothesis of thin film limit the transmittance can be determined:

$$T = \frac{1}{\left(1 + \frac{2\pi G_0}{c}\right)^2} = \frac{1}{\left(1 + \frac{\pi\alpha}{2}\right)^2} \approx 1 - \pi\alpha \approx 97.7\% \tag{2.16}$$

Graphene is thus able to absorb $\pi\alpha$ ≈2.3% of incident light in the visible (400nm to 700nm) range. This is a remarkable number considering its atomic thickness[23]. In fact, the absorption spectrum is quasi-flat from 300nm to 2500nm and it has a peak in the ultraviolet (UV) region (∼250nm)[24]. The optical absorption in graphene is also found to be quasi-linearly proportional to the number of layers (L) (Fig.2.4(b)). Each layer contributing a percentage of 2.3%[23, 25].

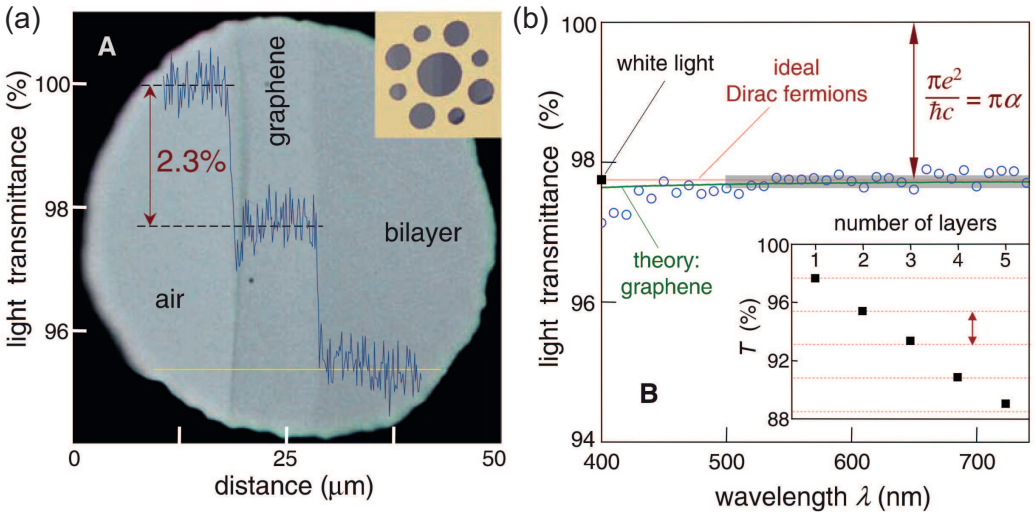

Figure 2.4: (a) Image of single layer and bilayer graphene suspended over a 50μm hole, showing the percentage of white light transmittance changing of 2.3% when passing through graphene. (b) Transmittance spectrum of single-layer graphene in the visible range with an inset showing the quasi-linear decrease of transmittance as the number of layers increases. Electron charge is e in (b). Taken from Ref.[23].

Due to the linear dispersion and zero band-gap two kind of optical transitions are present: inter- and intra-band, depending on whether photo-excited electrons cross the Dirac point (Fig.2.5). The existence of induced or spontaneous doping can block the absorption of photons at wavelengths whose energy is less than $2E_F$. This mechanism is referred to as Pauli blocking[25]

.

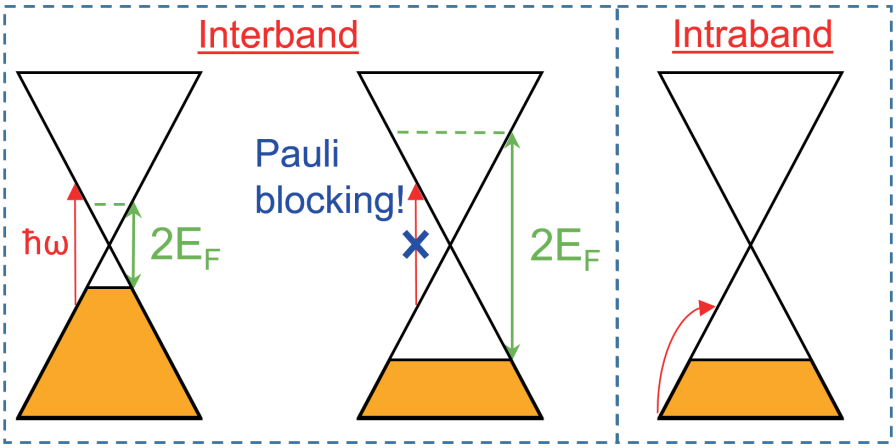

Figure 2.5: Examples of interband and intraband transitions in a hole(p)-doped graphene sample. Depending on the doping level and the energy $\hbar\omega$ or the respective λ, certain transitions can be blocked (Pauli blocking)

2.2.2 Hexagonal boron nitride

The isolation of graphene triggered the necessity to perform more profound studies of materials with layered structures down to the atomic thickness. Layered materials share with graphene the peculiarity of having strong covalent in-plane bonds and weak Van der Waals forces holding together two adjacent layers[26]. Boron nitride is a refractory, binary compound of boron and nitrogen which attracted the attention of researchers as a possible 2d insulator. Specifically, it exists in different crystalline forms: cubic (c-BN), wurtzite (w-BN) and hexagonal (h-BN). h-BN has a layered, graphitic-like structure with atoms of boron and nitrogen alternating in the lattice and one fundamental structural difference: atoms of boron on one layer face nitrogen atoms on the two adjacent layers, whereas in graphite hexagons are offset from one layer to another[27, 28].
The difference between the onsite energies of boron and nitrogen originates a large bandgap of ∼5.97eV[27, 29]. This property together with a dielectric constant $\epsilon_r \sim 3 \div 4$ and a voltage breakdown of ∼0.7 V/nm, make of h-BN a unique 2d dielectric[28]. Furthermore,

there are other attracting properties that hinted the possible utilization of h-BN as a substrate and/or capping layer in heterostructures with graphene and layered materials. The lattice mismatch between graphene and h-BN is less than ∼2%, which should minimize the amount of strain[30]. Furthermore, unlike the surface of SiO_2, the surface of cleaved crystals of h-BN is atomically flat and free of dangling bonds and surface charge traps[28].

2.2.3 Transition metal dichalcogenides

Transition metal dichalcogenides (TMDs) are a class of layered materials with a large number of compounds (Fig.2.6) and formula MX_2. M is a transition metal atom and X is a chalcogen atom (selenium, sulphur or tellurium). The family of TMDs comprehends metals, some of which show superconducting properties at low temperatures, semimetals and semiconductors. As for graphene, the properties of many of these materials depend on the number of layers.

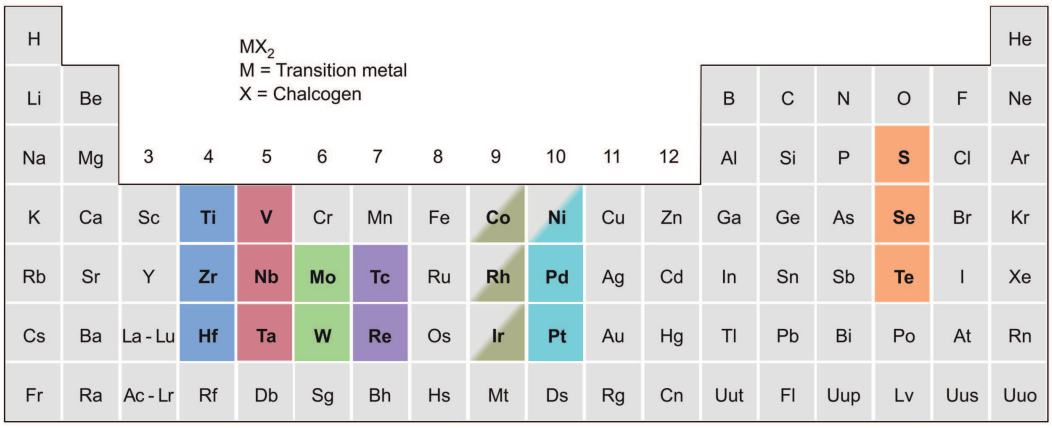

Figure 2.6: Table of elements with transition metals and chalcogens highlighted. Partially highlighted elements form layered structures only in some of the compounds. Adapted from Ref.[31]

Molybdenum disulfide (MoS_2), present in nature in the mineral form of "molybdenite" was the first of layered semiconducting materials cleaved and studied down to the 2d limit[7]. Metal atoms of molybdenum (Mo) are coordinated through covalent bonds with six neighbouring sulphur (S) respectively, in a trigonal prismatic arrangement (Fig.2.7(a-b)). Each layer of metal atoms is sandwiched between two layers of chalcogen atoms[32, 33]. Seen from above the atomic structure looks similar to that of graphene. However, being a monolayer (1L)-MoS_2 the composition of three atomic layers, the thickness of a 1L becomes larger than that of graphene and equal to ∼6.5Å. In the most

common hexagonal (2H) phase, layers stack so that chalcogen atoms sit on top of metal atoms and vice-versa (Fig.2.7(c)).

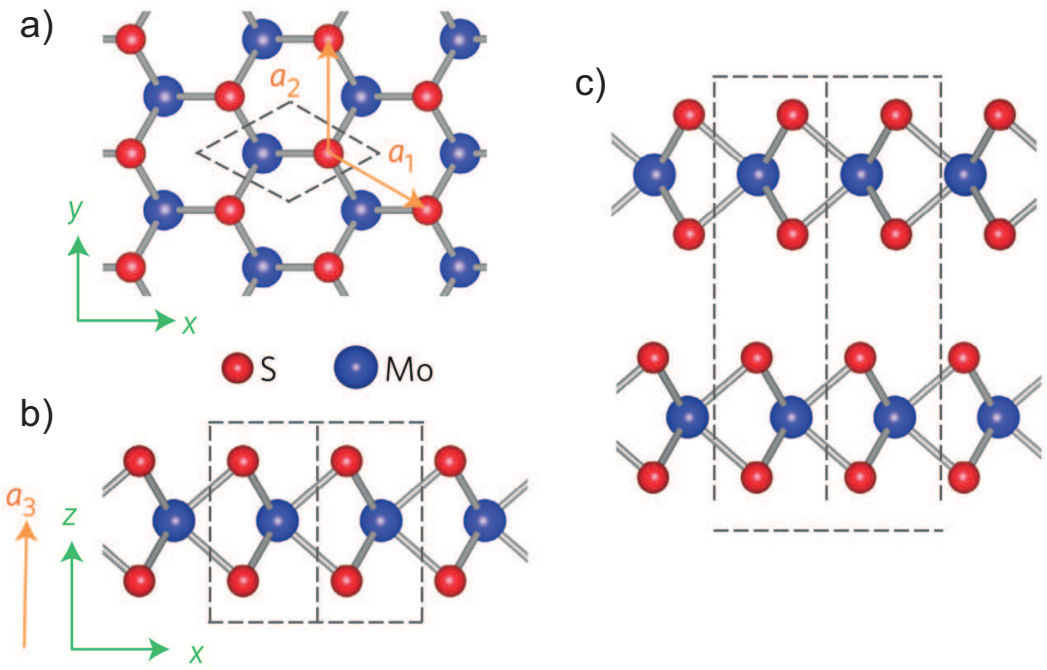

Figure 2.7: Top- (a) and side- (b) view of monolayer 1L-MoS_2. Black dashed lines indicate unit cells. Green and orange arrows indicate orthogonal axis in the real space and lattice vectors, respectively. (c) Side view of 2L-MoS_2. Taken from Ref.[33]

The electronic band structure deeply changes from bulk to monolayer as the material experiences a indirect-to-direct bandgap transition [32, 34]. An MoS_2 monolayer has a direct bandgap of ∼1.9eV, whilst in the bulk the indirect bandgap is ∼1.2eV[34]. This behaviour has a huge impact on optical properties as absorption and emission processes at wavelengths corresponding to the bandgap do not need to be activated by phonons.

The inversion symmetry of the crystal is preserved in bulk and even layers of MoS_2 2.7(c), but it is broken in odd layers, in particular, in 1L-MoS_2 2.7(b). The reciprocal lattice in 1L-MoS_2 is also hexagonal and the bandgap lies at the K point of the Brillouin zone[32, 34]. A consequence of the breaking of inversion symmetry is that K valleys in different directions of the reciprocal space are no longer equivalent, therefore K and -K valleys need to be differentiated[35]. The interaction between the magnetic spin and the magnetic field generated by electron trajectories around the nucleus is called spin-orbit coupling. The *d*-orbitals in the heavy atoms of MoS_2 have large spin-orbit coupling. The consequence of this is the splitting of valence band maxima and conduction

band minima between spin-up and spin-down states. If the splitting of the conduction band is only a few meV in 1L-MoS_2, the splitting of the valence band is of the order of ∼150meV[35, 36]. Time-reversal symmetry is preserved in 1L-MoS_2 and this requires $E_{\uparrow}(\mathbf{K})=E_{\downarrow}(-\mathbf{K})$. This means that spin-splitting must have opposite sign at K and -K points. Circularly-polarized light can thus address specific valleys: electrons in the K and -K valleys are sensitive to right- and left-circular polarized photons, respectively[35, 36].

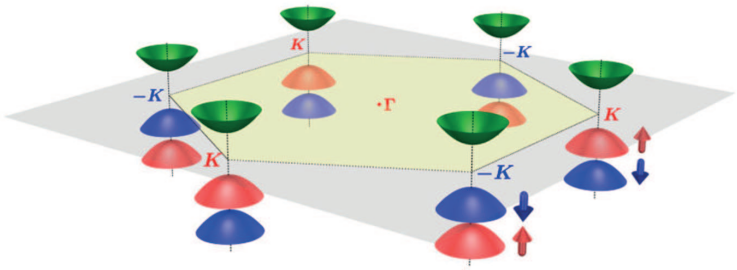

Figure 2.8: Schematic of the first Brillouin zone, showing the opposite sign splitting at the K and -K points in 1L-MoS_2[36]

The mobility of monolayer TMDs is lower with respect to the one obtained in graphene, with values ∼20$cm^2V^{-1}s^{-1}$ in a top-gated MoS_2 transistor[37]. The advantage of the presence of a bandgap arises when the ON/OFF ratio is considered: this is the ratio between the current flowing in the channel in the ON and that in the OFF state. In contrast to the case of graphene transistors, which suffer the absence of a significant ON/OFF ratio (around ∼10[13]) due to lack of an energy band-gap, transistors made with semiconductors such as MoS_2 have shown ON/OFF ratios as high as 10^8, similar to those in current silicon technologies [37].

TMDs such as molybdenum diselenide ($MoSe_2$), tungsten disulfide (WS_2) and tungsten diselenide (WSe_2) are all semiconductors showing similar crystal structure and properties to those of MoS_2[38, 39]. They also experience indirect-to-direct bandgap transitions when reduced to 1L. Being tungsten heavier than molybdenum, WS_2 and WSe_2 compounds have larger spin-orbit coupling (>400meV) compared to MoS_2[38, 39].

Niobium diselenide ($NbSe_2$) is a metal of the family of TMDs with crystal structure similar to that of MoS_2. The persistence of superconductivity in thin layers was already investigated by R.F. Frindt in 1972[8]. More recent studies have confirmed superconducting transport down to the 1L, although it has also been shown that thinner crystals are sensitive to air and require encapsulation or capping for stable operation[40, 41]. One of the unusual properties of $NbSe_2$ is the co-existence of superconductivity and charge-density wave (CDW), which have lead this material under the spotlight to understand the interplay between the two phenomena. The CDW is a periodic modulation of the

electronic density of states and a distortion of the lattice structure appearing for certain crystals in specific range of temperatures[41, 42].

2.3 Fabrication

The production of graphene and layered materials has increased exponentially in the last decade and several techniques have been developed to make these available both for fundamental studies and for up-scalable applications (Fig.2.9)[26]. Here we will focus our attention on micro-mechanical cleavage and growth by chemical vapour deposition, while only having a glimpse of the other techniques.

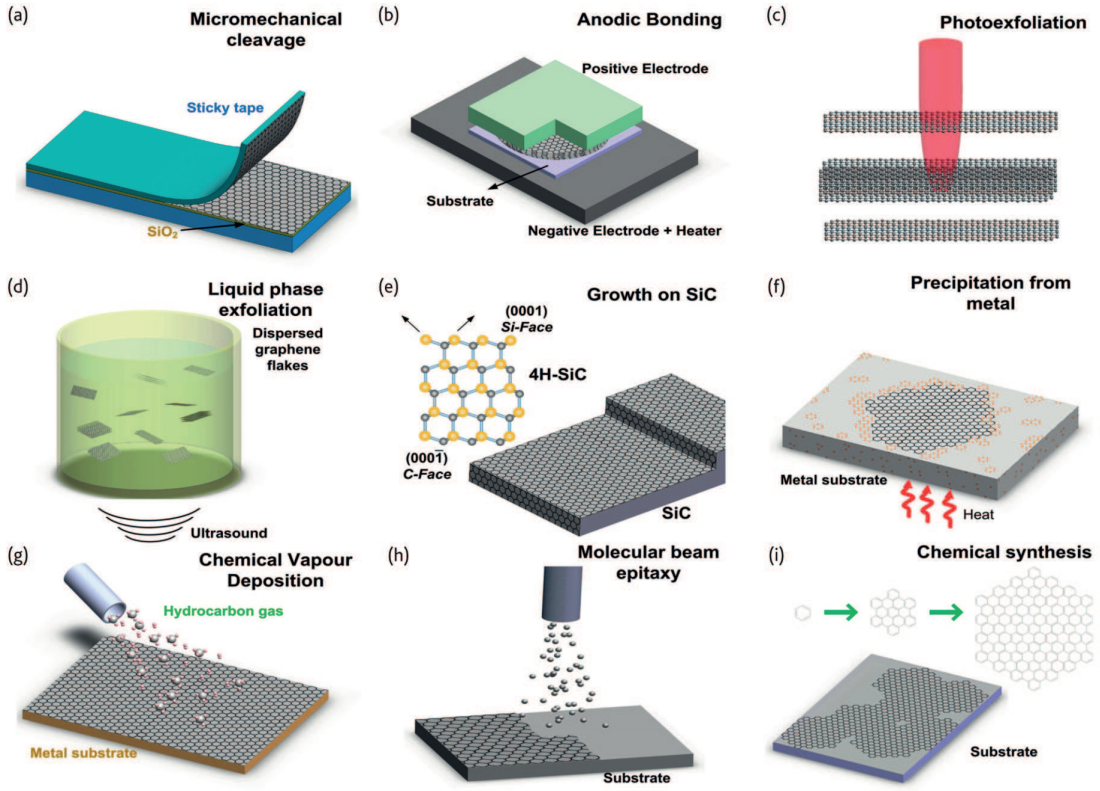

Figure 2.9: Schematic illustration of the most common graphene production methods. Most of them can also be extended to other layered materials. Taken from Ref.[26].

2.3.1 Micro-mechanical cleavage

Dry exfoliation methods comprehend a range of techniques that use mechanical and/or electromagnetic forces to cleave bulk crystals of layered materials at the interface between two adjacent atomic planes. Among these techniques, one of the most used is referred

to as micro-mechanical cleavage. This method, very well known to crystallographers, was the first utilized to isolate a flake of single layer graphene[13, 43]. It is based on the use of an adhesive tape to mechanically exfoliate bulk layered crystals, followed by a final exfoliation of the thin flakes attached to the scotch tape on the target substrate (Fig.2.9(a)). Micro-mechanical cleavage relies on the stark difference between in-plane (covalent) and plane-to-plane (Van der Waals) bonds, the latter being about two orders of magnitude weaker. The use of high purity bulk crystals as a starting material can lead to flakes of ideal quality for proof-of-concept/fundamental studies. However the maximum lateral size of single layer flakes is limited to hundreds of μm and the search of such flakes across the substrate relies on inspection by optical microscope, which can be time consuming[43, 44]. For this reason micro-mechanical cleavage is not a scalable technique and it struggles to find room in industrial applications, although it remains the best method for proof-of-concept in novel devices[26]. Some bulk crystals, such as graphite and molybdenite ones, are available in nature and can be mined. h-BN and most of other TMDs need to be synthesized[45, 46].

2.3.2 Chemical vapour deposition

Chemical vapour deposition (CVD) is one of the most widely used techniques to grow large-scale (wafer-size) thin films in the semiconductor industry. In this technique a substrate in a process chamber is exposed to one or more precursors which react and/or decompose to produce the film. There are different types of CVD processes: thermal, plasma-enhanced and many more [26].
Graphene growth has been demonstrated on various transition metals such as ruthenium (Ru), iridium (Ir), cobalt (Co), rhenium (Rh), nickel (Ni), platinum (Pt), palladium (Pd) via decomposition of hydrocarbon precursors[47]. One parameter that plays a key role in the growth of graphene films is the carbon solubility in the metal. Most of the mentioned metals are characterized by high carbon solubility: for Ni $\sim$0.6% in weight (wt) at 1326°C and for Co $\sim$0.9% wt at 1320°C[47]. This means that during the growth process carbon atoms segregate at the surface of the metal substrate, but they can also diffuse into it. Upon cooling at room temperature, the diffused atoms precipitate at the surface, yielding a final graphitic film with areas of different thickness, generally hard to control [47, 48].

The need to grow uniform large area single layer graphene for applications lead to the pursuit of new suitable substrates with lower carbon solubility[26]. Copper (Cu) has a carbon solubility of up to 0.008% wt at 1084°C, much lower with respect to Ni and Cu,

opening a path toward a self-limited growth process. The growth of graphene on Cu has indeed lead to exceptional results in terms of uniformity and defect concentration[49–53]. This is typically performed at temperatures around ∼1000°C, close to the Cu melting point (∼1085°C) and with methane (CH_4) used as a precursor in a gas mixture with hydrogen(H_2)[49]. Firstly carbon atoms nucleate at the Cu surface, then nuclei expand and merge to one another until full substrate coverage occurs. This generates a continuous graphene film with several crystal orientations (poly-crystalline graphene)[49]. Both Cu and H_2 play a catalytic role in the graphene growth. The surface of Cu is key: the presence of defects, edges or terraces are likely to be nucleation sites. H_2 also plays additional roles: an initial annealing treatment in H_2 at ∼1000°C removes the native oxides present at Cu surface and enables re-arrangement of the surface in large grains[47, 54].

Many refinements to the growth technique such as tuning the H_2/CH_4 partial pressures or applying surface pre-treatments to smoothen the Cu surface have lead to obtaining not only uniform, cm-sized layers of poly-crystalline graphene[50], but also mm-sized single crystalline domains, achieved by minimizing nucleation sites[52, 53]. This makes of CVD growth of graphene a more up-scalable method compared to micro-mechanical cleavage. The main weaknesses of CVD graphene growth on Cu reside in the use of high temperatures and in the necessity to transfer graphene to insulating substrates for applications. Yet, the quality achieved with CVD graphene paved the way to the realization of several state-of-the-art electronic and opto-electronic devices[47, 55].

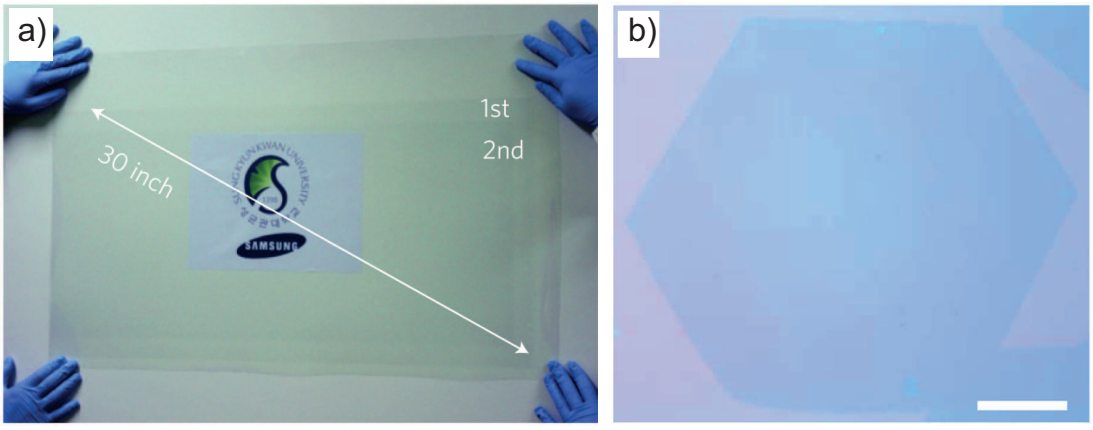

Figure 2.10: (a) A 30-inch CVD-grown graphene film transferred on flexible substrate by roll-to-roll process (from Ref.[50]) and (b) an optical image of graphene single-crystalline domain. Scale bar is 1mm (from Ref.[52])

The growth of CVD-h-BN and CVD-TMDs is not at a stage as advanced as for CVD graphene and therefore there is considerable room for improvement.

Mono- and multi-layer h-BN have been synthesized on metals such as iron (Fe), Ni, Cu, and Pt, and insulators such as SiO_2 and sapphire[56]. Most common precursors are the solid ammonia borane (BNH_6) or the liquid borazine ($B_3H_6N_3$). The difference relies in how the precursor is delivered to the growth chamber. Ammonia borane is sublimed at ∼120°C and carried into the reaction region by carrier gases[57]. In the case of borazine, a carrier gas is used to bubble into a cylinder which contains the liquid (bubbler) and the substrate is exposed to the outlet vapours[58]. The temperatures utilized to grown on Cu is similar to that used for graphene (∼1000°C), although they can vary significantly from report to report[57, 58]. The most suitable thickness of h-BN needed for applications is also now under the spotlight of the scientific community: on the one hand monolayer h-BN might not be enough to screen the influence of the underneath substrate roughness, on the other hand growing uniform, wrinkle free, multilayer h-BN has proven to be a tough challenge[57, 58]. More recently growth of wafer-scale, wrinkle-free uniform multilayer h-BN has been demonstrated on sapphire, however temperature had to be raised to ∼1400°C[56].

In most reports on growth of TMDs solid precursors are used, mainly due to the hazardousness of gaseous S and Se precursors, such as hydrogen sulphide (H_2S) and hydrogen selenide (H_2Se). For 1L-MoS_2 up to ∼120μm lateral size single-crystalline domains were first obtained directly on SiO_2/Si using powders of molybdenum trioxide (MoO_3) and S as solid precursors. These were placed in two separate ceramic boats heated at ∼650°C and the substrate was exposed to the vapours, while nitrogen was used as carrier gas[59, 60]. Continuous 1L-MoS_2 films have been obtained on sapphire with a similar method[61]. The growth of 1L-WSe_2 domains has been achieved by usage of tungsten trioxide (WO_3) and Se powders heated at ∼925°C and deposition on sapphire. In this case a mixture of argon (Ar) and H_2 was used, due to H_2 playing an active role in the formation of WSe_2[62]. Remarkably, growth of wafer-scale homogeneous films of TMDs on SiO_2/Si has been reported by Ref.[63]. They used CVD with metal-organic precursors (generally referred to as MOCVD). The use of such precursors allowed a control of the partial pressures, not possible with solid precursors. Ar and H_2 were used as process gases[63].

2.3.3 Other methods

Other top-down approaches for the production of graphene and layered material are[26]: *anodic bonding*, *photo-exfoliation* and *liquid phase exfoliation* (Fig.2.9 (b-d)). In these techniques either an electrical discharge (anodic bonding), laser light pulses (photo-exfoliation) or ultrasounds (liquid phase exfoliation) are used to break the layer

to layer bonds in bulk crystals and produce thin flakes. In the case of liquid phase exfoliation (LPE) this happens in a liquid environment.

Finally, among the bottom-up approaches a few other techniques can be listed[26]:

- *Growth on silicon carbide (SiC)*: This technique is quite well-established and it relies on the fact that heating SiC in ultra-high vacuum at temperatures above ∼1000°C, allows the surface to graphitize (Fig.2.9(e)) due to evaporation of silicon. Being covalently bonded with silicon, the graphene surface layer has to be decoupled from the substrate via hydrogen intercalation.

- *Growth on metals by precipitation*: A similar process to that used in the case of CVD graphene on metals with high carbon solubility is used. Carbon atoms can diffuse into the material at high temperatures and precipitate at the surface upon cooling(Fig.2.9(f)).

- *Molecular beam epitaxy (MBE)*: this is a widespread technique in the field of the III-V semiconductor industry (Fig.2.9(g)). It uses ultra-high vacuum environments to selectively deposit atomic species. This has been attempted both with graphene and with layered materials, so far with limited success.

- *Chemical synthesis*: Graphene and layered materials can also be chemically synthesized (Fig.2.9(h)): for example graphene can be synthesized by assembling polycyclic aromatic hydrocarbons (PAHs) through surface-mediated reactions.

2.4 Characterization

2.4.1 Optical microscopy

Optical microscopy represents one of the most rapid and non-destructive techniques for the identification of graphene and layered material flakes[43]. The choice of the inspection wavelength and of the substrate for the identification of flakes is crucial for obtaining a good optical contrast[20, 43, 64]. When light impinges on a structure composed by several layers, multiple reflections take place; what is read by the detection camera is a signal (I_{Det}) which correspond to the superposition of these reflections. If a layered material is exfoliated on the most common substrate SiO_2/Si, for instance, there are several contribution to I_{Det}: E_{LM}, E_{SiO_2} and E_{Si}. These represent the reflected fields from the air-layered material, the layered material-SiO_2 and the SiO_2-Si interfaces respectively. The intensity of the read signal is dominated by two factors, that are E_{LM}

and E_{Si} and thus I_{Det} can be approximated to the squared sum of the electric field amplitudes of the two reflected waves[20, 64]:

$$\mathrm{I}_{\mathrm{Det}} \approx |E_{LM} + E_{Si}|^2 = |E_{LM}|^2 + |E_{Si}|^2 + 2|E_{LM}||E_{Si}| \cos\phi \tag{2.17}$$

where ϕ represents the phase shift, a factor which includes the phase change due to the optical path in the oxide of thickness t_{SiO_2} and the one due to the reflection at each boundary[64]. The contrast can be calculated with respect to the strong field reflected by silicon when the layered material is not present. If the field reflected from the layered material is assumed to be a small quantity ($|E_{LM}|^2 \simeq 0$), the contrast δ will be given by the following equation[64]:

$$\delta = \frac{\mathrm{I}_{Si} - \mathrm{I}_{Det}}{\mathrm{I}_{Si}} \sim -2 \cdot \frac{|E_{LM}|}{|E_{Si}|} \cdot \cos\phi \tag{2.18}$$

The reflectance is defined as the ratio between the reflected power to the incident power. If silicon is considered so reflective that its reflectance is approximately equal to one, the reorganized equation of contrast in terms of reflectance will depend solely on the reflectance of the layered material[64]:

$$\delta = -2\sqrt{\mathrm{R}_{LM}} \cos\phi \tag{2.19}$$

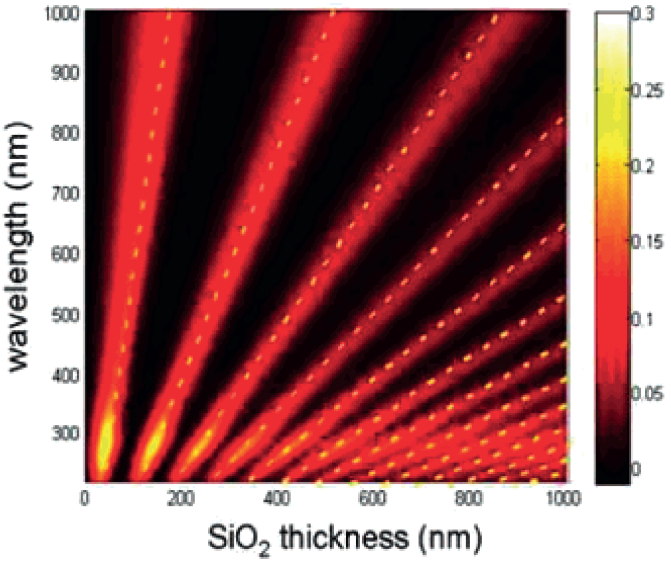

Figure 2.11: Optical contrast calculated for graphene. Taken from Ref.[64].

This analysis has been performed in reference [64] in the case of graphene, and then extended to other layered materials (Fig.2.11) [65, 66]. Since the variable part of equation

2.19 is embedded in the phase shift, the role of the SiO_2 is found to be that of a spacer, thus its thickness t_{SiO_2} can be adjusted for each wavelength and layered material to tailor the best optical contrast achievable [20, 64–66]. For example, the best t_{SiO_2} for graphene in the visible range is found to be at the values of ∼90nm and ∼300nm[20, 64].

2.4.2 Atomic force microscopy

Atomic force microscopes (AFMs) are important for measuring surface morphology of graphene and layered materials. Besides, the vertical resolution of modern atomic force microscopes (∼1Å) is theoretically high enough to measure the step height relative to a single layer of atoms. In earlier studies of graphene, AFM was considered the definitive method to measure the number of layers[43].

However, with this method, discrepancies arise from the fact that the tip-layered material and tip-substrate interactions are different. Furthermore the presence of a layer of water absorbed at the surface and substrate roughness, can significantly affect the step height measurements. For single layers an overestimation is likely, as for Fig.2.12. The real thickness of single layer graphene is ∼0.34Å, similar to that of h-BN, while it becomes ∼0.65Å for 1L-MoS_2, with similar values for other TMDs. Data on step height of a 1L can become more reliable when a comparison with a bilayer (2L) is performed on the same substrate.

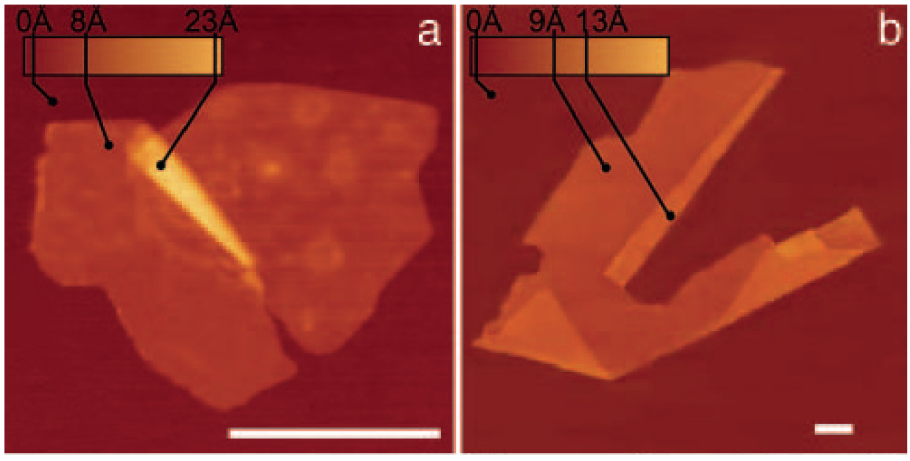

Figure 2.12: (AFM images of (a) 1L-$NbSe_2$ and (b) single layer graphene. All scale bars are 1μm. Taken from Ref.[43].

Furthermore an optimization of the tip-surface interaction and use of smooth substrates such as MICA can help improving the accuracy of the step height measurement[43].

2.4.3 Transmission electron microscopy

In transmission electron microscopy (TEM) a beam of electrons is used to produce images of thin (up to ∼100nm) samples with high spatial resolution (nowadays <0.5Å), exploiting the wave-particle electron duality and the smaller De Broglie wavelength of electrons compared to those used in light microscopes.

TEM was first used in the field of graphene by Refs.[67, 68] to unambiguously discriminate between mono- and bi-layer. When the beam impinges on a suspended graphene sheet a diffraction pattern is generated and then collected by a detector. The 3d reciprocal lattice of a single layer graphene is a set of rods lying in the positions corresponding to those of the 2d reciprocal lattice (see Fig.2.13(a)). These rods possess a slowly varying intensity in the direction perpendicular to the plane. The diffraction pattern in normal incidence corresponds to a section (blue surface) of the 3d reciprocal lattice. Tilting the sample in the TEM leads to probing the whole 3d reciprocal space, by changing the section plane. Tilting of angles <20° produces no significant changes in graphene due to the weak change in intensity of the rods (pink surface).

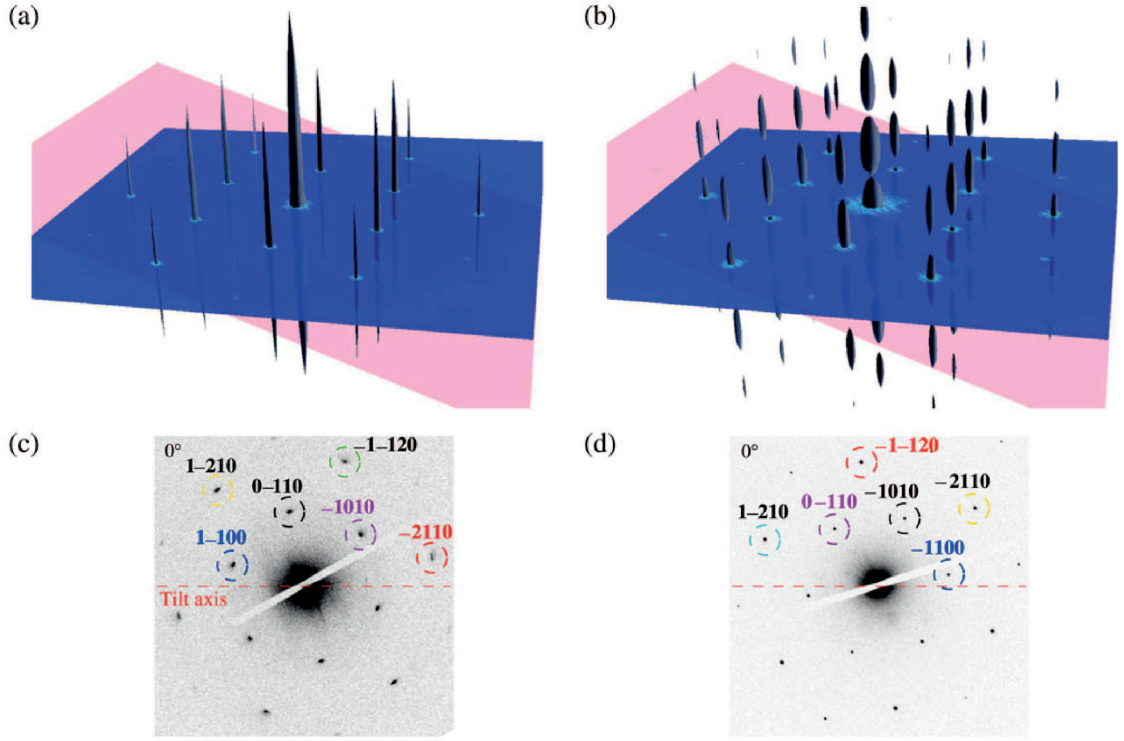

Figure 2.13: 3d reciprocal space of (a) single- and (b) bi-layer graphene. Diffraction pattern images of (a) single- and (b) bi-layer graphene in normal incidence. Taken from Ref.[68].

On the other hand, in the case of the bi-layer, a considerable modulation of the rods intensity is present. Therefore the intensity of the diffraction pattern spots can vary significantly with the probe angle (see Fig.2.13(b)).

The advent of graphene grown by chemical vapour deposition has also shifted the attention to grains and grain boundaries in graphene samples. TEM was indeed used to describe the poly-crystalline nature in CVD-graphene samples, as different grains lead to different orientations of the diffraction pattern[69]. Electron diffraction also remains the method currently used for proving the single crystalline nature of CVD graphene domains[51].

In order to use TEM graphene and layered materials have to be transferred on proper grids, which allow the material to be locally suspended or supported by thin membranes. This makes TEM a technique mostly used only for dedicated studies. Furthermore, voltages used to accelerate electrons have to be controlled: values of voltages >60keV would be enough, for instance, to start knocking out carbon atoms from the graphene lattice, degrading the sample quality.

2.4.4 Raman spectroscopy

Raman spectroscopy is probably the most powerful, non-destructive technique used to characterize graphene and layered materials[70]. This technique is based on the detection of photons inelastically scattered by phonons. When a photon of energy $\hbar\omega_{ph}$ impinges on a sample, an electron may be excited from the ground state at energy E_{GS} to a state at energy $E_{GS} + \hbar\omega_{ph}$. This excited state can be either real, leading to resonant Raman spectroscopy or virtual, leading to non-resonant Raman spectroscopy. Graphene is a broadband absorber, therefore Raman spectroscopy is always resonant. The radiative recombination of the electron, accompanied by emission of a photon with the same energy as that used for excitation, is defined as an elastic scattering phenomenon and referred to as "Rayleigh scattering". In an inelastic process, the electron interacts with a phonon before radiative recombination, gaining or reducing its energy of an amount $\hbar\Omega$. This process is termed "Raman scattering"[71]:

$$\hbar\omega_{sc.ph} = \hbar\omega_{ph} \pm \hbar\Omega \tag{2.20}$$

being $\hbar\omega_{sc.ph}$ the energy of the scattered photon. If the electron loses energy from the interaction with a photon before recombining, the sign in equation 2.20 is minus and the process is called "Stokes". On the opposite, if the electron gains energy, the process is referred to as "Anti-Stokes". The Raman spectrum is a plot of the energy difference

between the incident and scattered photon energies and the shift is usually expressed in cm^{-1}. Excitation frequencies used for Raman spectroscopy are typically in the infrared (IR) to ultraviolet (UV) spectral range[71].

Carbon atoms being active in the 800-2000cm^{-1} range make graphene a good candidate for showing prominent features in the Raman spectrum (Fig. 2.14(a))[70, 72]. The G peak is due to the stretching of carbon atoms bonds and it corresponds to the E_{2g} phonon (Fig. 2.14(b)), whereas the D peak is due to the breathing modes in six-atom rings and thus its origin is related to the A_{1g} mode. The D peak process is not Raman active in pristine graphene, hence it requires the presence of disorder, edges or defects to be activated[70].

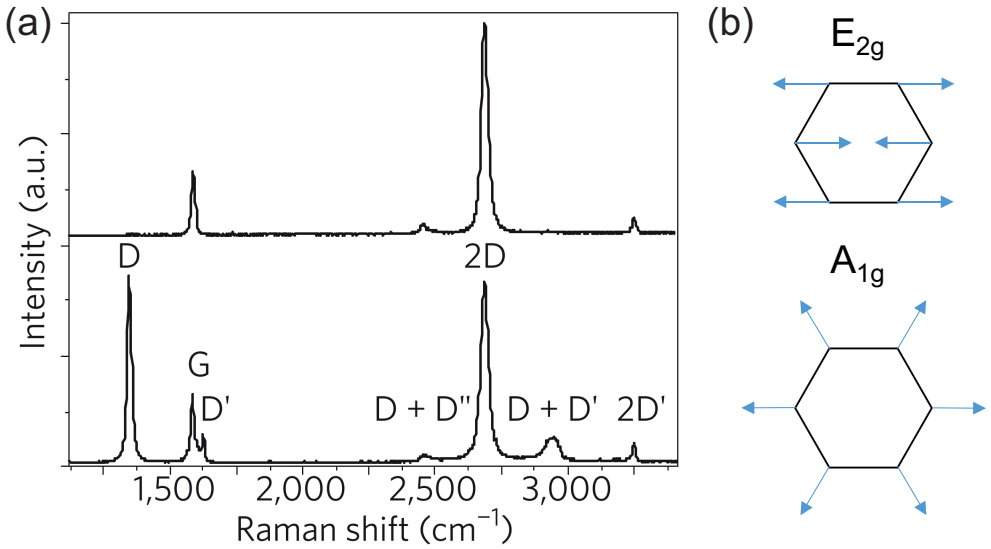

Figure 2.14: (a) Raman spectra of pristine (top) and defective (bottom) graphene (from Ref.[70]). (b) Representation of the E_{2g} and A_{1g} modes at the origin of the G and D Raman peak in graphene, respectively

The activation mechanisms are depicted in Fig.2.15. For the G peak there are three steps: a photon from the excitation beam induces the generation of an electron hole couple; consequently, a phonon of momentum $\mathbf{q} \sim 0$ may scatter the excited electron in a virtual state; this electron can therefore recombine by emitting a photon with different energy[70, 73]. The activation process for the D peak is an intervalley process and it involves a "double resonance" mechanism, described by the following steps[74, 75]: excitation through light of an electron-hole pair, scattering with phonon while exchanging a momentum $\mathbf{q} \sim \mathbf{K}$, defect scattering event and electron-hole recombination.

A similar process exists also as intravalley, in which case the peak that arises is called D′. The 2D and 2D′ peaks are the overtones of the D and D′ peaks, respectively. Since

they originate from a process where momentum conservation is satisfied by the presence of two phonons with opposite wave vectors, no defects are required for their activation and this suggests their presence also in the pristine graphene spectrum.

By analysing the Raman spectrum it is possible to immediately distinguish graphene from few-layer graphene and graphite because of the change in intensity and shape of the 2D peak[72]. Specifically, while the single-layer has a single, sharp 2D peak of Lorentzian shape, in multilayer graphene a shoulder appears in the 2D shape, suggesting that more components arise for the peak formation, due to the appearance of additional energy bands[72].

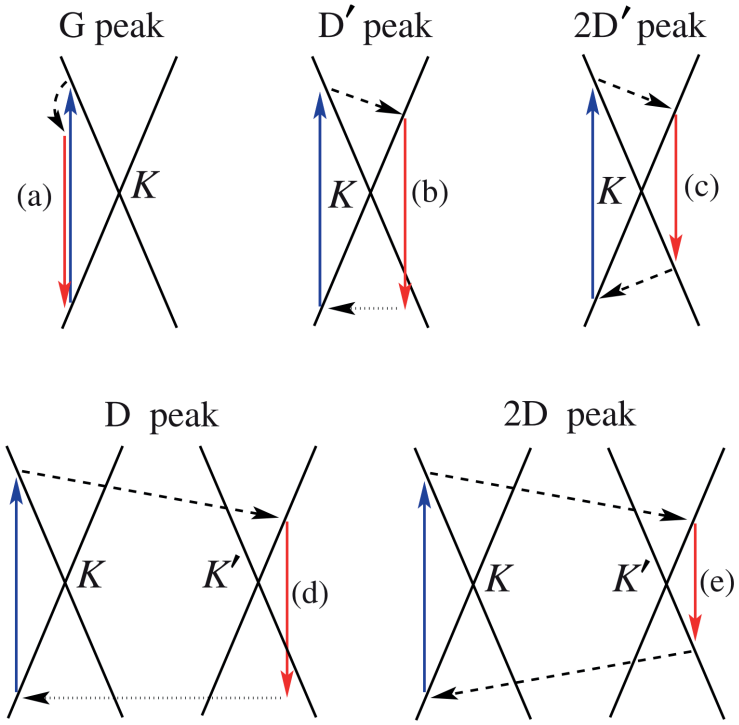

Figure 2.15: Activation mechanisms for peaks in the Raman spectrum of graphene. Solid black and red lines indicate photo-excitation of electron-hole pairs and radiative recombination, respectively, while dashed and dotted lines indicate phonon and defect scattering, respectively. Taken from Ref.[73].

Other information can be retrieved from the analysis of the position, shape, intensity and area of the peaks. For instance by studying the G peak position and width, and the variation of position, relative intensities and areas with the 2D peak it is possible to estimate the level of doping[73, 76]. The intensity of the D peak relative to that of the G peak and their positions and shape will describe the amount of defects in the sample and the presence of edges[64, 77].

The distinction between mono- and few-layer graphene is rather straightforward. However trying to determine the exact number of layers in few-layer graphene is challenging if only the G and 2D peaks are used. When atomic layers stack one on top of the other, new modes appear in the low frequency Raman spectrum (<200cm^{-1}). These are the shear (C) and layer breathing modes (LBM), corresponding to the relative motion of atoms in adjacent layer[78, 79]. A relation between C, LBM peak positions versus number of layers can be found if atoms within a layer are considered as a single atomic mass and that layers are connected by springs. This is referred to as the linear chain model. Spring constants are named $\alpha_{\parallel}$ for C and $\alpha_{\perp}$ for LBM. The following equations apply[78, 79]:

$$Pos(\mathrm{C})_N = \frac{1}{\sqrt{2}\pi c}\sqrt{\frac{\alpha_{\parallel}}{\mu_m}}\sqrt{1+\cos\left(\frac{\pi}{N}\right)} \tag{2.21}$$

$$Pos(LBM)_N = \frac{1}{\sqrt{2}\pi c}\sqrt{\frac{\alpha_{\perp}}{\mu_m}}\sqrt{1-\cos\left(\frac{\pi}{N}\right)} \tag{2.22}$$

where c is the speed of light in vacuum, μ_m is the single layer mass per unit area and N is the number of layers. In the case of C modes, for instance, Eq.2.21 can be applied in the bulk limit to calculate $\alpha_{\parallel}$ and then used to build a calibration curve for the number of layers. Eq.2.21 and Eq.2.22 can be extended to all other layered materials[78, 79].

In the high frequencies range h-BN has only one prominent G peak due to the in plane relative motion of boron and nitrogen atoms (E_{2g} phonon mode)[80]. In the same frequency range MoS_2 shows two prominent peaks: they are assigned to the E^1_{2g} mode, corresponding to the in-plane relative motion between molybdenum and sulphur atoms and the A_{1g} mode, due to the out-of-plane motion of sulphur atoms[81, 82]. Their frequency difference has been used to monitor the number of layers (Fig.2.17): E^1_{2g} shifts to lower frequencies while the A_{1g} blue shifts to higher frequencies with increasing N[83]. This method is quite powerful to determine thickness in 1L-MoS_2 and 2L-MoS_2, but the E^1_{2g}-A_{1g} frequency difference starts to fall within the instrumental precision for >3L-MoS_2 and it is therefore necessary to resort to the C and LBM peaks.

$NbSe_2$ has the same structure of MoS_2 and it also possesses E^1_{2g} and A_{1g} modes. However the sensitivity of the material to light when exposed to the environment, has made Raman measurements more complicated[84].

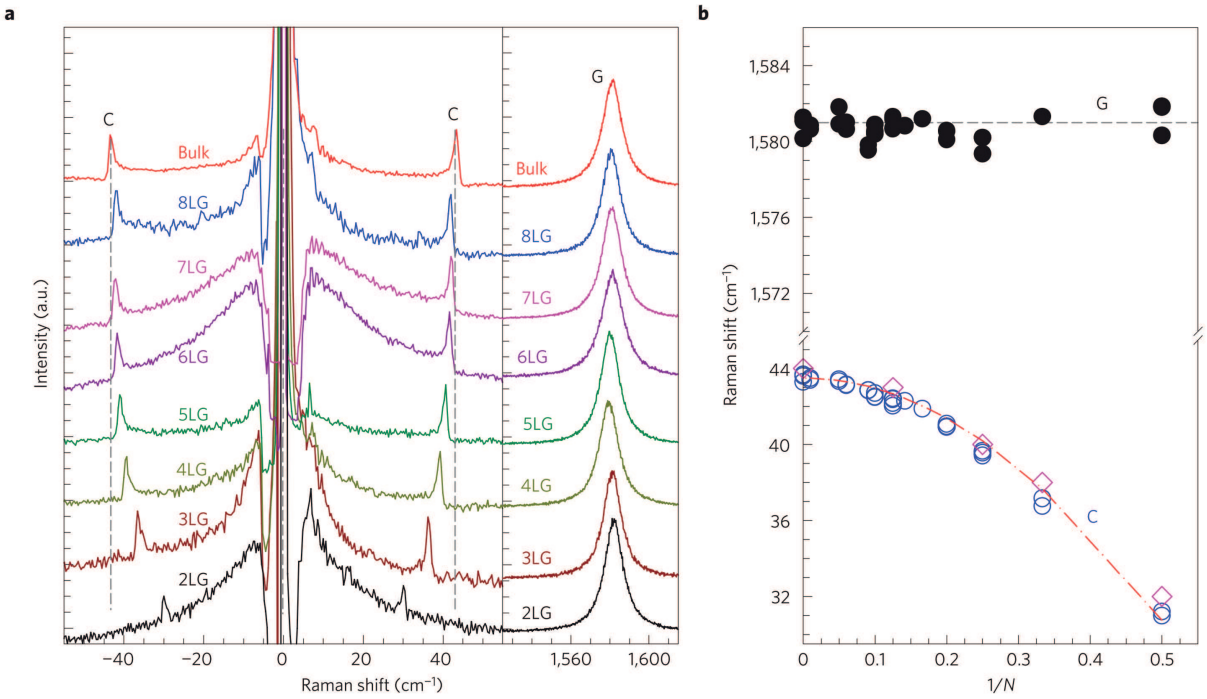

Figure 2.16: (a) Raman spectra of few layer graphene flakes in the frequency region of the C and G peaks. (b) Plot of the C and G peak positions as a function of the inverse number of layers $1/N$. Taken from Ref.[78].

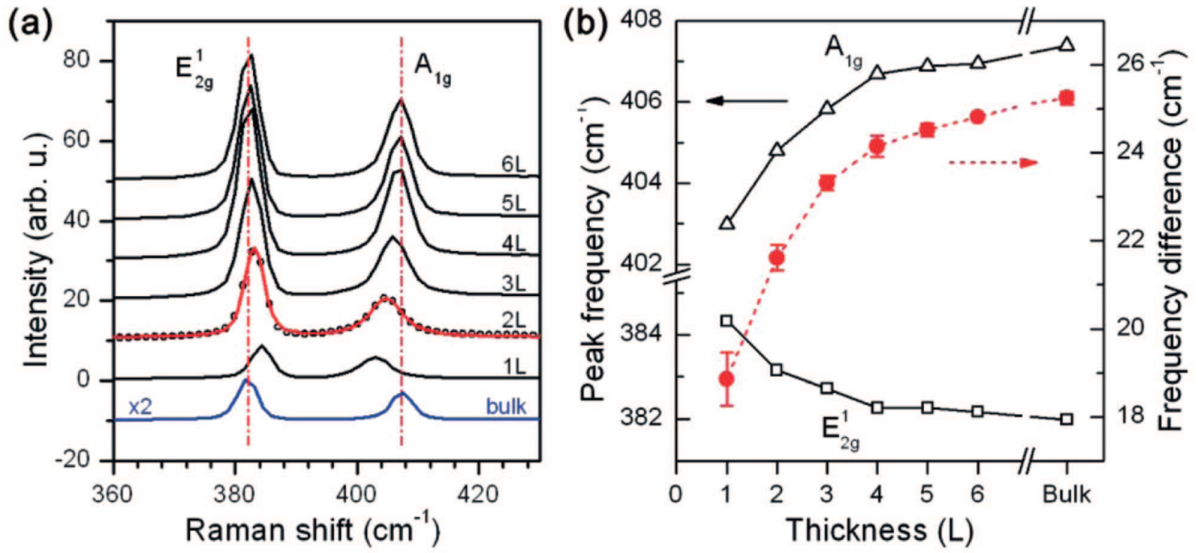

Figure 2.17: (a) Raman spectra of MoS_2 for flakes of different thickness. (b) Plot of the E^1_{2g} and A_{1g} peak positions (black line) and the relative frequency difference (red line) as a function of the number of layers. Taken from Ref.[83].

2.4.5 Photoluminescence spectroscopy

In a photoluminescence (PL) experiment a beam of light impinges on a sample and some of the photons are absorbed. Whenever radiative recombination occurs, photons are emitted back, detected and resolved in terms of their energy (wavelength). Indirect bandgap semiconductors are expected to show much lower quantum yield with respect to direct bandgap ones, the quantum yield being the ratio between the photons re-radiated by the material divided by the number of photons incident on it. This is due to the fact that absorbtion and emission processes in indirect bandgap material require phonons. TMDs such as MoS_2, $MoSe_2$, WS_2 and WSe_2 experience an indirect-to-direct transition when reduced to single layers (Fig.2.18)[34].

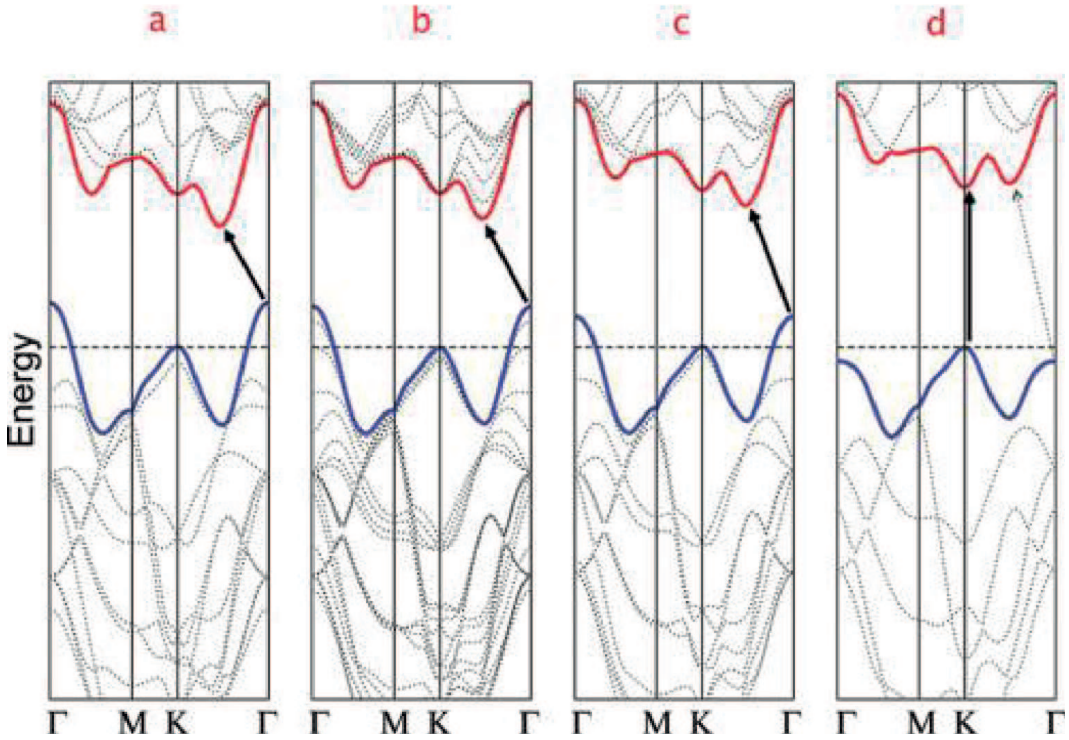

Figure 2.18: Band diagrams of (a) bulk, (b) 4L, (c) 2L and (d) 1L-MoS_2 showing the indirect (around Γ) to direct (at K) bandgap transition[34]

1L-MoS_2 is by all means a direct bandgap semiconductor and it shows a sharp PL peak at the energy which corresponds to its energy bandgap (Fig.2.19(a)). The quantum yield decreases by orders of magnitudes already in the bilayer sample, with the intensity of the PL peak being almost flat if compared with 1L-MoS_2. The signal gets progressively weaker when the thickness increases[32]. A careful analysis of the PL spectrum of 1L and few layer MoS_2 can reveal the presence of three peaks, which are labelled A, B and I in the normalized plot of Fig.2.19(b). The A and B peaks are originated by radiative

recombinations from the conduction band to the top (A) and bottom (B) of the spin-split valence band. These peaks are the signature of excitons. An exciton is a bound state between an electron and a hole which can be created when a photon is absorbed by a material. The binding energy of excitons is rather small (∼tens of meV) in most bulk semiconductors, whereas it reaches values of hundreds meV in ultra-thin layered materials due to the limited screening of Coulomb interactions[85, 86]. The process is the following: an electron-hole pair is generated by the absorption of a photon, the excitonic bound state is at a lower energy with respect to the unbound state, therefore an exciton can be formed; consequently radiative recombination can occur. Finally the I peak is related to an indirect transition, activated by a phonon, and is therefore more pronounced in thicker samples[32, 34].

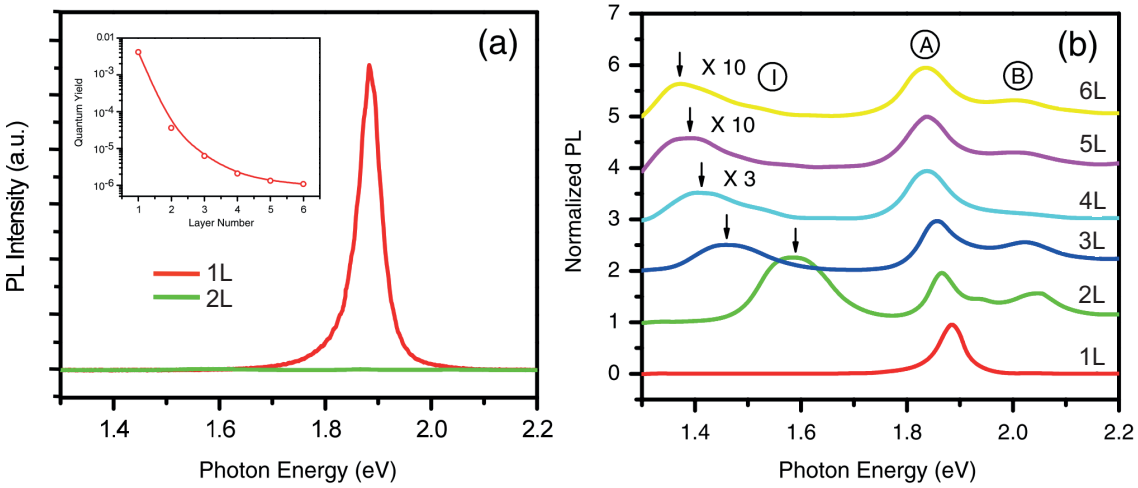

Figure 2.19: (a) Comparison of a photoluminescence spectrum between a single layer and bilayer MoS_2 and (b) normalized photoluminescence spectra from 1 to 6 layers MoS_2. Adapted from Ref.[32]

2.4.6 Absorption spectroscopy

Absorption spectroscopy is a technique helpful in understanding the amount of light that a material absorbs in a wavelength range generally spanning the near-infrared (NIR) to the UV. Samples are either suspended or prepared on quasi-transparent substrates. Light from a broadband source is routed toward the back side of the sample and partially absorbed, while the transmitted light impinges on a detector. The reflectance R (i.e. fraction of reflected light) of graphene and most of other atomically thin materials is of the order of 0.1% in the visible range. Energy conservation requires: R + A + T = 1, where T and A are the fraction of transmitted (transmittance) and absorbed (absorbtance)

light. If reflectance of ultrathin layered materials is thus neglected, the following equation applies:

$$A_{LM} \approx 1 - T_{LM} \approx 1 - \frac{I_{LM+sub}}{I_{sub}} \tag{2.23}$$

where A_{LM} and T_{LM} are the absorptance and transmittance of the layered materials respectively (in % unit), whereas I_{LM+sub} and I_{sub} are the transmitted light intensities across the layered material on the substrate and across the substrate alone, respectively. This is further simplified in the case of suspended samples. Absorption spectroscopy has been applied to graphene[23, 87] and layered materials[88]. The absorption of graphene is constant to ∼2.3% in the visible range[23, 87]. 1L-MoS_2 has negligible absorption at wavelengths corresponding to energies smaller than the bandgap >700nm to more than 10% at shorter wavelengths[88].

2.4.7 Pump probe spectroscopy

Pump probe spectroscopy can provide qualitative and quantitative information on the dynamics of photo-excited carriers in molecules and solids[89]. An ultra-short (∼femtosecond) laser pulse, of energy typically resonant with an electronic transition, excites the sample from a ground to an excited states. This pulse is referred to as the "pump pulse". With a tunable delay τ_{delay} a second pulse, with intensity much smaller than the pump, is used to probe the sample by monitoring changes in transmission or reflection. This pulse is referred to as the "probe pulse". The measured signal is therefore[89]:

$$\frac{\Delta T}{T}(\omega_{\text{probe}}, \tau_{\text{delay}}) = \frac{T_{\text{ON}}(\omega_{\text{probe}}, \tau_{\text{delay}}) - T_{\text{OFF}}(\omega_{\text{probe}})}{T_{\text{OFF}}(\omega_{\text{probe}})} \tag{2.24}$$

T_{ON} and T_{OFF} being the transmissions of the probe pulse across the sample when the pump pulse is on and off.

Pump probe spectroscopy allowed us to unveil the timings and nature of photo-carrier cooling in graphene. Excitation of hot electrons in the conduction band is followed by electron-electron collisions happening in timescales of ∼tens of femtoseconds (fs) and electron-phonon collisions in timescales of ∼1ps. This is followed by phonon cooling and reaching of equilibrium, which happens in few picoseconds (ps)[25, 90]. In 1L-MoS_2 timescales are longer (up to 100ps) due to the presence of a bandgap. The dynamics are further complicated by the contribution of excitons[91].

2.5 Conclusions

Graphene is a material with remarkable electrical and optical properties. It can be produced with multiple methods, some of which are scalable and reproducible. Due to broadband absorption, outstanding mobility at room temperature and flexibility, the use of graphene is highly desirable for optoelectronic applications. Research on layered materials is expanding with compounds showing properties which are complementary to those of graphene. Also the production of layered materials could potentially be up-scaled, but improvements are needed. The characterization techniques described in this chapter can give a massive amount of information on the properties of LM. Most of them are non-destructive. Information such as number of layers, morphology of the surface, amount of light absorbed and in some cases also the dopant and defect concentration can be retrieved.

Chapter 3

Layered Material Heterostructures

3.1 Introduction

After the isolation of graphene, research on layered materials has experienced a boom. More recently, the attention of the scientific community has also been directed toward the study of more complicated structures. The term "heterostructure" refers to a junction of two or more crystals with different bandgap. The assembly of heterostructures is widely established in the field of bulk semiconductors, where techniques such as CVD or MBE are being used for growth and precise control over the thickness of the various layers composing the heterostructure. The rise of layered materials with unprecedented control of the thickness down to the atomic scale has therefore prompted the idea to assembly layered heterostructures of atomically thin materials in a chosen sequence. The possibility to stack layered materials with atomic precision would indeed allow a fine-tuning of the properties of the resulting stack. This concept is nowadays far from being just a dream (Fig.3.1)[26]. The combination of conducting, semiconducting, insulating and superconducting layered materials can now result in the fabrication of heterostructures with novel and exotic properties that can be exploited in a vast range of applications, such as tunneling transistors[92, 93], p-n junctions[94] and light emitting diodes[95]. These heterostructures are often referred to as "Van der Waals heterostructures" recalling the nature of the interlayer bonds[96].

One possibility for heterostructure assembly is direct growth. However this has been proved to be rather complicated. Alternatively, techniques involving the transfer of layered materials have been developed. Layered material samples can either be moved to a new target substrate, or on top of another layered material or stack. Here we divide transfer in two classes: wet transfers, whenever the interface between layered materials in the heterostructure comes to contact with a liquid or solvent at same stage of the

assembly process, and dry transfers when the interface is never exposed to liquids or solvents[26, 55].

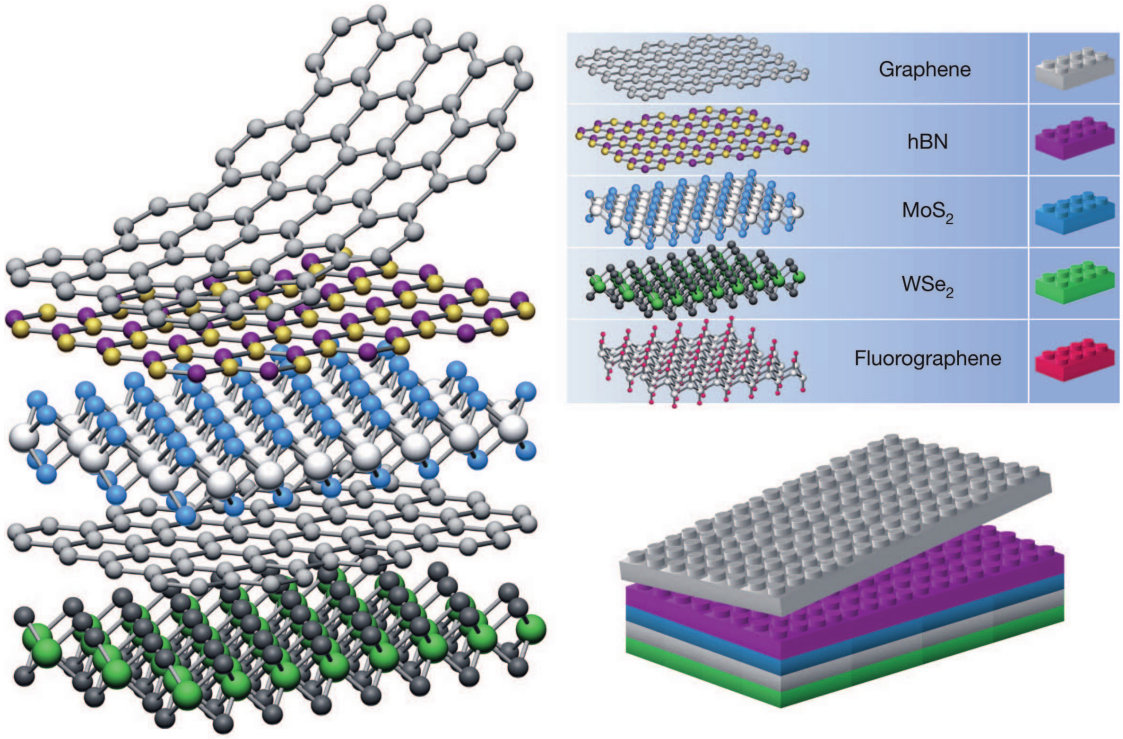

Figure 3.1: Concept of layered heterostructure assembly. Taken from Ref.[96]

A considerable effort has been put in the development of versatile, fast and clean techniques for the transfer of both exfoliated and grown materials. In this chapter these will be reviewed, focusing on their upsides and downsides.

3.2 Growth

Growth of layered heterostructures has been attempted with several methods including CVD and MBE[96]. h-BN was first grown on graphene by CVD on a Cu substrate with the sequential usage of n-Hexane (C_6H_{14}) and ammonia borane as precursors[97]. However samples were highly defected and discontinuous. Furthermore, growth of layered materials or heterostructures on metals intrinsically requires transfer on insulating substrates to enable the fabrication of the vast majority of electronic and opto-electronic devices. CVD was also used to grow graphene-TMD[98] and TMD-TMD heterostructures[99], with recent reports also showing growth of three- or few- layer heterostructures[63, 100, 101]. With rare exceptions[63] it would seem that the weak interlayer bonds in layered materials

hinder the formation of continuous layers, instead leading to the formation of crystalline islands of limited lateral size (up to few μm)[96].

3.3 Transfer

Wet and dry transfer techniques were applied both to exfoliated and to CVD grown layered materials. The common paradigm is the pursuit of a method which can minimize the amount of residual contaminants, with particular attention to interfaces in the case of layered heterostructures.

3.3.1 Wet transfer

The wet transfer was first applied to layered material-related technologies by Ref. [102]. Graphene was mechanically exfoliated on a SiO_2/Si substrate. A layer of polymethyl methacrylate (PMMA) was spin-coated on top of the substrate where the flake to be transferred was lying. The immersion in sodium hydroxide (NaOH) partially etched SiO_2 leaving the polymeric membrane, with the flake attached on the bottom, floating at the surface of the solution. The PMMA was then lifted with the target substrate and the polymer was later dissolved in acetone. More recently this technique has evolved and nowadays the use of an etchant in wet transfer of flakes is not necessary (Fig.3.2).

PMMA is indeed hydrophobic, whereas the SiO_2 layer is hydrophilic. If the substrate with the flakes and the spin-coated polymer is dipped in deionized water, intercalation of water bewteen PMMA+layered material and SiO_2 takes place due to capillarity and the polymer membrane can be detached and lifted with the target substrate. Moreover, a deterministic transfer can be performed by mounting the detached polymeric membrane, for instance fished with a plastic frame, on a micro-manipulator. It is thus possible to align two flakes or a flake on top of a pre-patterned device on the target substrate with μm precision[26].

The transfer of CVD graphene has so far mostly relied on etching of the underlying growth substrate[48, 49]. As for the case of flakes a sacrificial PMMA layer is spin coated on the growth substrate, the sample is then left floating at the surface of an aqueous solution for metal etching. Chemicals such as hydrogen chloride (HCl) are used for Ni [48] and iron chloride ($FeCl_3$) or ammonium persulfate ($NH_4S_2O_8$) for Cu[49, 50]. Similar techniques have also been adapted for the transfer of CVD MoS_2 films grown on sapphire[103]. PMMA can be substituted by thermal release tapes laminated on the grown surface, especially while dealing with flexible substrates sensitive to solvents. After

etching of the metal substrate, the tape/graphene is re-laminated on the target substrate and heat (∼120°) is applied for tape release[50].

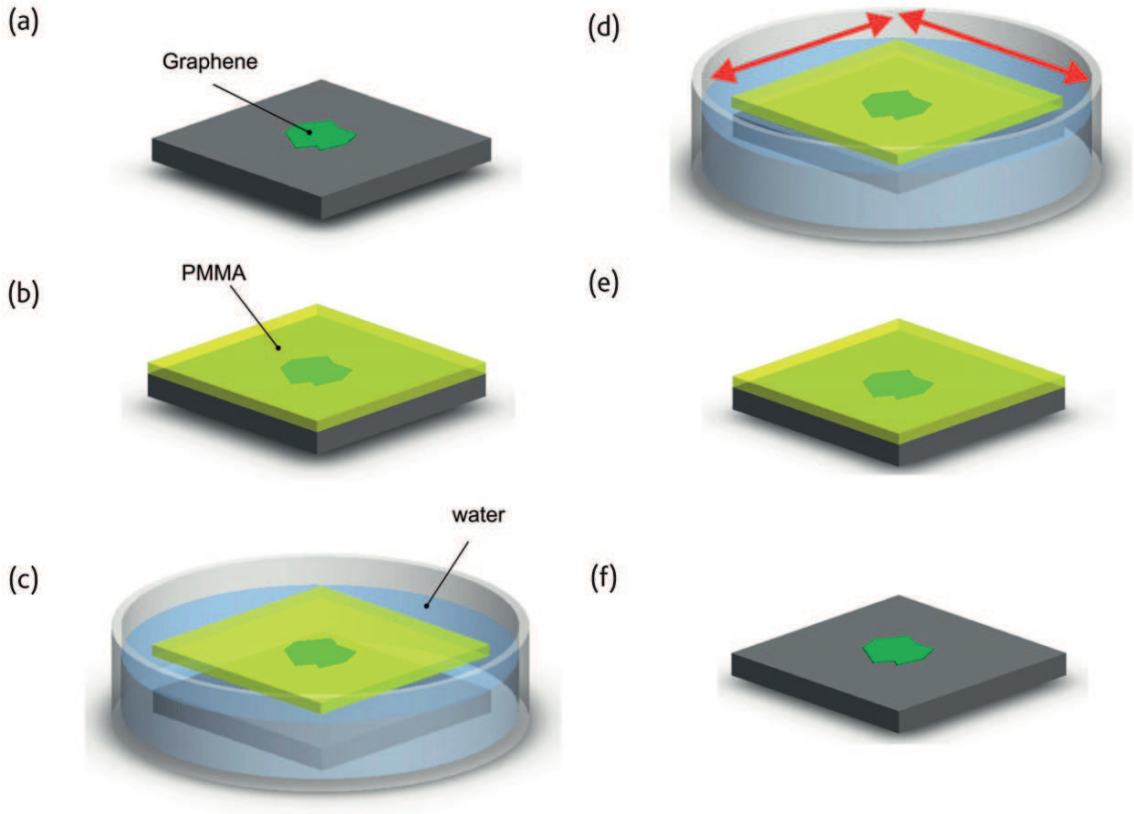

Figure 3.2: Wet transfer of mechanically cleaved flakes. (a) Exfoliated flakes of layered materials, (b) spin coating of PMMA layer, (c) dipping in water for polymer detachment (d-e) transfer on the target substrate and (f) polymer removal. Adapter from Ref.[26]

The etching of the growth substrate can be avoided by usage of electrochemical solutions for delamination of the graphene layer. PMMA is still used as a sacrificial layer and the PMMA/graphene/Cu stack is now employed as cathode in an electrolytic cell. A metallic foil can serve as anode. The two electrodes are immersed in an aqueous solution with an electrolyte (e.g. potassium peroxodisulfate, $K_2S_2O_8$) . Whenever the cathode is polarized at a negative voltage, bubbles are induced at the graphene/Cu interface due to the reduction of water, accompanied by the formation of H_2. This induces the detachment of the PMMA/graphene membrane[104]. However using this method can be detrimental for the quality of the transferred film.

The disadvantage of wet transfer processes is the involvement of water and solvents. Residuals of these can contaminate the surface of layered materials and interfaces in layered heterostructures.

3.3.2 Dry transfer

Dry transfer methods started to be developed shortly after the first works on wet transfer techniques and were initially focused on the transfer of graphene on h-BN. The procedure reported by Ref.[28] consists in the preparation of a double polymeric layer on top of SiO_2/Si substrate (Fig.3.3). The first layer is a water-soluble polymeric layer such as polyvinyl alcohol (PVA) and the second layer is the standard PMMA. Graphene is mechanically exfoliated on top of this double layer membrane and h-BN flakes are exfoliated on a separate SiO_2/Si substrate. Water can gently be added to the edges of the substrate with graphene or by performing a scratch around the flake to penetrate beneath the graphene flake and dissolve the PVA layer. Now the graphene/PMMA is released at the surface of a beaker with water, lifted with a glass slide and tilted up-side down to be mounted on a micro-manipulator. Alignment to the h-BN flake can then be performed with a microscope. It would seem that water is still involved in the process and indeed this is the case. However it is worth nothing that the top surface of graphene, which is the one then brought in contact with h-BN, never touches water or solvents if the substrate is not completely immersed in the water for PVA dissolution.

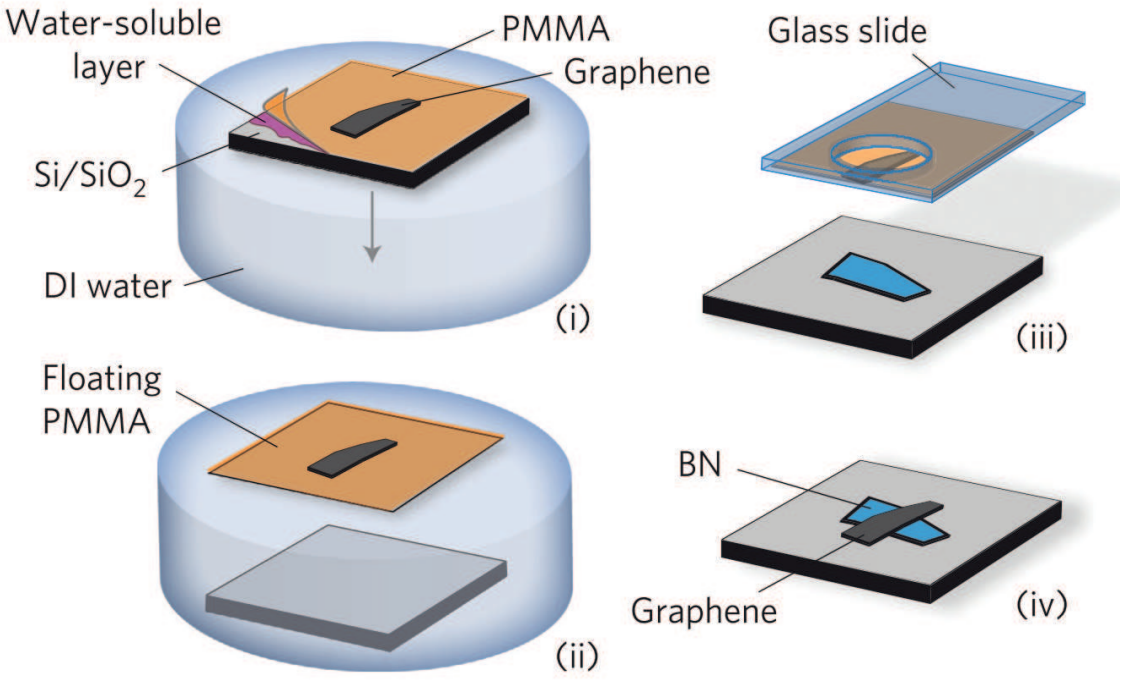

Figure 3.3: Transfer of graphene on h-BN by water dissolution of PVA layer. (i) exfoliation of graphene on the PMMA/PVA/SiO_2/Si stack, (ii) dissolution of PVA with the graphene/PMMA membrane left floating at the water surface, (iii) lifting with glass slide and (iv) heterostructure formation. Taken from Ref.[28].

More recently, an all-dry transfer method that relies on viscoelastic stamps has been reported[105]. The novelty is represented by the fact that the use of wet chemistry is not necessary at any step of the transfer. The working principle is based on the concept of viscoelasticity and Van der Waals interactions: the stamp behaves as an elastic solid over short timescales, while it can slowly flow over longer timescales. A polydimethylsiloxane (PDMS) stamp is deposited on a glass slide and a layered material is mechanically exfoliated on top. The stamp is brought in contact with the target substrate where a second layered material is lying. Adhesion forces, dominated by Van der Waals interactions, take place at the interface between the layered materials. The adhesion between the flakes and the stamp is instead rate-sensitive due to the viscoelastic behaviour of the PDMS stamp. Pulling the stamp away from the source substrate with high peel velocity leads to adhesion strong enough to pick up both flakes to the surface of the stamp, lifting them away from the substrate. If the stamp is peeled away with sufficient low peel velocity, the flakes tend to be released to the target substrate and separate from the stamp, forming the heterostructure[105, 106].

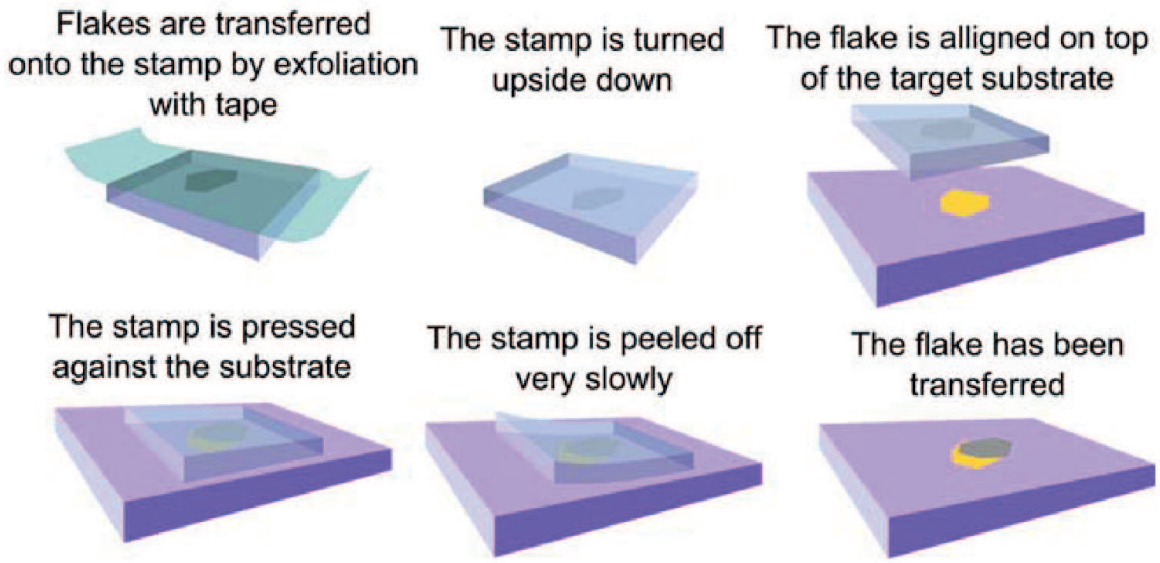

Figure 3.4: Step by step schematic of the dry transfer process employing a viscoelastic PDMS stamp. Taken from Ref.[105].

In following reports an extra thermoplastic polymer, typically polycarbonate (PC) or polypropylene carbonate (PPC), was added on the surface of the PDMS stamp[107, 108]. These polymers allow a further degree of control of the heterostructure assembly through the temperature, as both PC and PPC are softened by heating. Exfoliation of all flakes forming the heterostructure can be done on SiO_2/Si. A PDMS layer is deposited on a

glass slide and covered by a PPC or PC film. This stack is brought into contact with the source substrate, containing the first flake to be transferred. After contact with PDMS, the substrate is heated to temperatures from 60°C up to 90°C to soften the PPC-PC and the flake is picked up from the source substrate. The pick-up of a new layered material can then be performed, now also exploiting the Van der Waals interaction between the flake already present on the PPC or PC film and the next one to be picked up from SiO_2 (see Fig.3.5). When the heterostructure is completed, the PPC and PC are softened by heating (>90°C). PPC and PC are then finally dissolved with chloroform. Here it is also worth noting that the usage of chloroform to dissolve the polymeric film happens at the last step, when the heterostructure is already formed. Therefore the solvent never comes in contact with the interface.

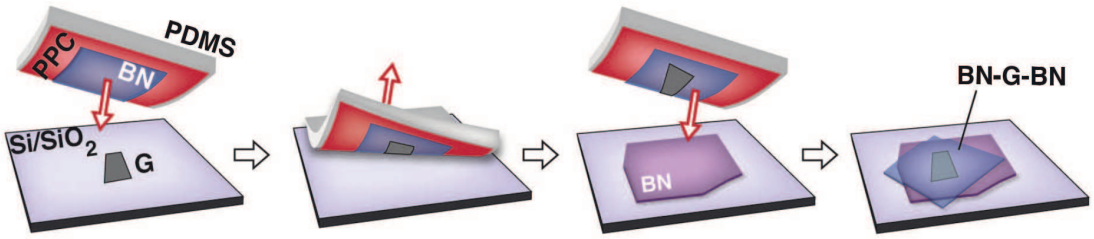

Figure 3.5: A schematic of the pick up process of the graphene and last h-BN layer in a h-BN/graphene/h-BN heterostructure, followed by final release of the heterostructure on the target substrate. Taken from Ref.[107].

This transfer technique is so powerful that a variant has been used to dry pick up CVD graphene island from the grown Cu substrate with exfoliated h-BN flakes on PMMA/PVA/PDMS stamps, to make the first dry transfer involving CVD grown materials[109]. However this was only enabled by oxidation of Cu beneath the graphene islands.

Despite all the effort put in the development of contaminant-free transfer techniques, it has been reported by several groups that blisters of contaminants still tend to randomly form at the interfaces of dry-transferred layered heterostructures[110]. Recent techniques have suggested that temperature is crucial to avoid the formation of blisters. Ref.[111] has shown that an increase of the temperature to >110°C on PPC while fabricating encapsulated graphene (h-BN/graphene/h-BN) heterostructures may hinder the formation of blisters in heterostructures.

3.4 Characterization

The microscopy and spectroscopy characterization techniques described in the previous chapter can be extended to layered heterostructures. In the past few years these have been utilized not only to study heterostructures layer-by-layer, but also to investigate interlayer effects, suggesting that stacked layers can also influence each other. For example, new phonon modes can appear in Raman spectra of layered heterostructures[112]. PL and pump probe have instead been employed for probing interlayer excitons, which are bound states formed by an electron leaving in the conduction band of one semiconducting TMD and a hole leaving in the valence band of the other TMD composing the heterostructure[113, 114].

3.5 Conclusions

Layered heterostructures represent the unprecedented possibility to engineer devices atomic layer by atomic layer. Direct growth of heterostructures is at an early stage and many key issues need to be unravelled. Wet and dry transfer techniques are instead now well developed, especially for μm size layered material flakes. The minimization of residual contaminants could be critical to exploit the functionality of each material, leaving its characteristic intact. The transfer of continuous large area CVD layered materials still mostly relies on the use of wet techniques, although fundamental steps toward dry CVD heterostructures have been made. Scaling-up of wet and dry transfer techniques will also be a fundamental target toward the integration of layered materials at an industrial level.

Chapter 4

Optoelectronics

4.1 Introduction

Optoelectronics is the branch of photonics related to the study and implementation of electronic devices for sourcing, manipulating and detecting optical signals. These comprehend a vast range of photodetectors, optical modulators and light emitting devices. Optoelectronic devices are nowadays used everywhere: interconnects, motion sensors, imaging, security and night-vision are only a few areas of the ones targeted by optoelectronics[115]. Over the years, the optoelectronic platform has been established relying mainly on silicon, germanium and III-V semiconductors. Nowadays, graphene related materials (GRM) are attracting attention due to their promising properties and quickly climbing the ladder toward integration in existing technologies[55].

Silicon is an indirect bandgap semiconductor with a bandgap of ∼1.1eV. The presence of an indirect bandgap requires the assistance of phonons for absorption and emission processes, inevitably affecting the efficiency. Nonetheless, the reduced costs and advanced knowledge of silicon components still leave silicon as the best choice for photodetectors at wavelengths which correspond to energies above the bandgap (1.1eV correspond to λ ∼1100nm). Germanium has an indirect bandgap of ∼0.67eV and it is considered as a solid choice for photodetection in the near infrared and at the telecom wavelength ∼1550nm. Although possible, the integration with silicon can be costly and not ideal due to the large lattice mismatch between the two materials (∼0.4%).

III-V semiconductors such as gallium arsenide (GaAs), or indium arsenide (InAs) have a direct bandgap and offer an alternative to silicon in light emitting devices. They can be grown with remarkable precision through MBE. Growth of ternary compounds also allows tuning of their bandgap to tailor applications at specific wavelengths. However the production costs are high and the integration with silicon is difficult to achieve.

Graphene is a broadband absorber as a single layer absorbs ∼2.3% of light in the visible and near-IR, including at the telecom wavelength λ=1550nm[23]. Moreover, the graphene Fermi level can be efficiently tuned through electrostatic doping, which enables an additional degree of control on its optical properties[13]. Despite being a remarkable number for a single layer of atoms, the ∼2.3% absorption is clearly not enough for the fabrication of efficient photodetectors or modulators, therefore its responsivity to light has to be enhanced. Integration of graphene with silicon-based technologies has been demonstrated in several works[116–118]. It is important to remark that graphene should not be thought as a competitor of silicon, but rather as a medium which can enable some functionalities through integration with silicon technologies that would not be available otherwise.

Single layer Mo- and W- based TMDs can complement the property of graphene with the presence of a bandgap and offer an alternative to III-V semiconductors in light emitting devices[95]. They cannot however compete with silicon as photodetectors at visibile wavelengths on rigid platform due to the early stage of their fabrication technology[39]. $NbSe_2$ is instead a superconductor with a critical temperature (T_C) in the bulk of ∼7.2K and its use in low temperature photodetection could be investigated.

The huge potential of GRM also lies in their flexibility which is hardly achieved both with silicon/germanium and with III-V semiconductors.

4.2 Photodetectors

Photodetectors are a class of devices needed to convert optical signals into electrical signals. Generally the conversion process requires three steps: absorption of photons and creation of photo-generated carriers, transport of photo-carriers to the electrodes and extraction of an electrical signal. Photodetectors can be divided in several classes, each of which has its own key figures of merits. Definitions can slightly vary from report to report. Overall, the key parameters are linked to: sensitivity (which is defined in a specific range of λ), speed and noise level[1].

4.2.1 Photoconductors

In photoconductors, absorption of photons and consequent generation of photo-carriers produces a change in conductivity $\Delta\sigma$ (Fig.4.1). Conductivity in semiconductors is defined as[1]:

$$\sigma = q(\mu_n n + \mu_p p) \tag{4.1}$$

where μ_n and μ_p are electron and hole mobilities, respectively, while n and p are electron and hole concentrations, respectively. The role and significance of mobility will be discussed later on in this chapter.

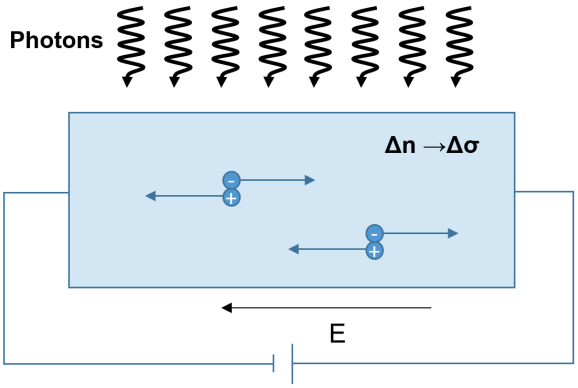

Figure 4.1: Schematic of a photoconductive detector. Generation of electron-hole pairs creates an unbalance in charges Δn, which modifies the conductivity and the current circulating in the circuit.

In photoconductors the optical power P_o is partially absorbed. The absorbed fraction P_{abs} generates a photocurrent I_{ph} being the absolute difference of the output currents registered upon illumination and in the dark state $I_{ph} = |I_{light} - I_{dark}|$. The external quantum efficiency (EQE) of a photoconductor is measured in % units and defined as the rate of photo-excited carriers divided by the number of incident photons[1]

$$EQE = \left(\frac{I_{ph}}{q}\right)\left(\frac{P_o}{h\nu}\right)^{-1} \tag{4.2}$$

where q is electron elementary charge, h is the Planck constant and $\nu = c/\lambda$ is the frequency of the incident photon. The definition of internal quantum efficiency only differs by taking into account the fraction of absorbed photons:

$$IQE = \left(\frac{I_{ph}}{q}\right)\left(\frac{P_{abs}}{h\nu}\right)^{-1} \tag{4.3}$$

Likewise the external and internal responsivities are measured in A/W units and can be defined as follows:

$$R_{ext} = \frac{I_{ph}}{P_o} \qquad R_{int} = \frac{I_{ph}}{P_{abs}} \tag{4.4}$$

EQE and R_{ext} are generally smaller than IQE and R_{int} as P_{abs} is a fraction of P_o. Furthermore all these relations are sometimes renormalized by a factor which takes into account the fact that the photosensitive area is generally different with respect to the spot size of the light beam. Photoconductors are also generally categorized based on their photoconductive gain G_{ph}, which is a dimensionless quantity. Indeed, any incident photon can result in more carriers being detected, if the latter can recirculate in the circuit without recombining[55, 115].

$$G_{ph} = \frac{\tau}{t_{transit}} \tag{4.5}$$

where τ is the lifetime of photo-generated carriers and $t_{transit}$ is the time that carriers need to travel from the source to the drain electrode[2]. If there is gain, $G_{ph} > 1$. Some photoconductors can achieve G_{ph} as high as 10^6[1]. Despite being able to achieve remarkable responsivities, photoconductors typically exhibit large dark currents I_{dark}. This increase can affect the noise equivalent power (NEP), which is expressed in units of $W{\cdot}Hz^{-1/2}$ and it represents the minimum optical power necessary for the signal to noise ratio to be equal to 1 [55].

Another key performance indicators for photoconductors and other photodetectors is the speed. This is commonly defined as the frequency at which I_{ph} drops to half (-3dB) with respect to its peak value. It is expressed as:

$$f_{-3dB} = \frac{1}{2\pi RC} \tag{4.6}$$

R and C being the total resistance and capacitance of the device, respectively.

Photoconductors with remarkable properties have been fabricated both with graphene and with layered materials. In graphene the conductivity is very sensitive to electrostatic perturbations and a gain mechanism is achieved by decorating the surface with sensitizing centres such as colloidal quantum dots[119]. Quantum dots absorb light in spectral ranges which can vary depending on their size and then transfer photogenerated charges to graphene, modifying its conductivity. With this method it was possible to achieve responsivities R_{int} $\sim 10^7$A/W and gains G_{ph} up to 10^8 in the visible range[119]. 1L-MoS_2 was also used to absorb light and transfer charge to the graphene layer. R_{int} $\sim 5{\cdot}10^8$A/W[120] and G_{ph} $\sim 10^8$ were also achieved on rigid substrates[121]. Layered materials such as MoS_2[122] and gallium sulphide (GaS)[123] photodetectors also showed reasonable responsivities 10^2-10^3A/W, without the aid of hybrid structures.

4.2.2 Photodiodes

A diode is a two-terminal electronic component, typically formed by the junction between a p-type and an n-type semiconductor, or a metal and a semiconductor (Schottky). The presence of a different doping level at the interface induces a charge transfer (depletion) and the establishment of a built-in electric field in the depletion region[1]. In a photodiode, electron-hole pairs are generated upon absorption of photons in the depletion region of an inversely polarized p-n junction, *i.e.* the positive pole is on the n-side. In Fig.4.2 three different regions of the inversely polarized p-n junction are marked.

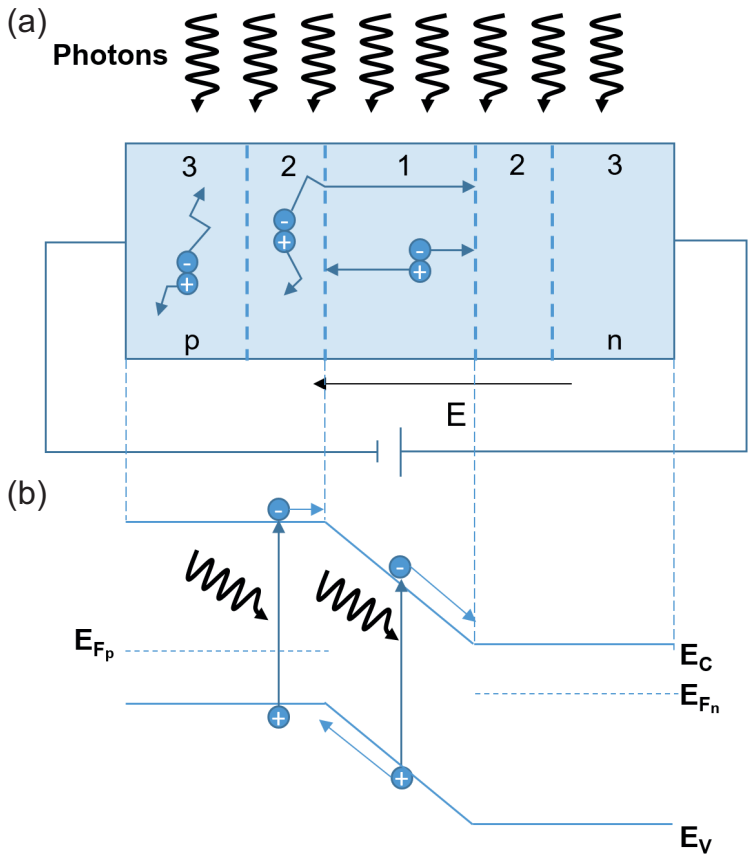

Figure 4.2: (a) Schematic of absorption processes and photo-carrier separation in different regions of a p-n photodiode and (b) corresponding band-diagram. Transitions shown for electrons on the p-side can symmetrically happen for holes in the n-side.

Region 1 is the depletion region where the built-in electric field is present. Charges photo-generated in this region are separated by the built-in electric field and move toward the electrodes where they are collected. Charges generated in region 2 may diffuse in the depletion region, in which case they are dragged by the electric field to the depletion region edge and also participate to the photocurrent. Electrons and holes in region 3 are

too far from the region where the electric field is present, therefore they diffuse randomly and recombine without participating to the signal. Increasing the reverse bias has several positive effects, such as making the depletion region wider, which increases the chances of absorption, but also increasing the electric field dragging the carriers, shortening their transit time[2].

Photodiodes are generally benchmarked with the same figures of merit of photoconductors. Here we will discuss about two other important types of photodiodes[2]:

- *Schottky photodiodes*: these are photodiodes formed by junctions between a metal and a semiconductor. The advantage of these photodiodes is that they can be used to detect photons with energies smaller than the semiconductor bandgap (see Fig.4.3).

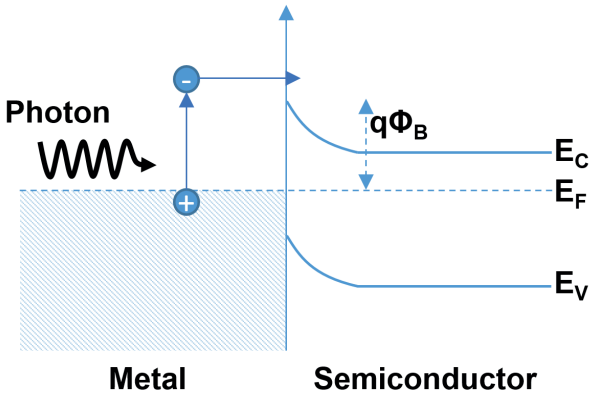

Figure 4.3: Schematic working principle of a Schottky photodiode with photon energies greater than $q\Phi_B$ and smaller than the semiconductor bandgap $E_{BG} = E_C - E_V$

  If the photon is absorbed close enough to the junction and it has energy at least $q\Phi_B$, an electron can overcome the barrier formed with the semiconductor and diffuse in the region where electric field is present to participate to the I_{ph}. A typical Schottky junction is made of gold (Au) thin films on doped Si. One disadvantage of Schottky junctions is that the yield of electrons being transferred from the metal to the semiconductor is rather poor.

- *Avalanche photodiodes*: in avalanche photodiodes (APD) an intense reverse bias applied to a p-n junction produces a strong electric field in the depletion region. The impact of drifting charges with high kinetic energy knocks out electrons in bound states (impact ionization) from the valence to the conduction band, generating additional carriers contributing to I_{ph} (avalanche multiplication). This

gain mechanism is so efficient that some avalanche photodiodes are used as single photon detectors.

In graphene an I_{ph} can be produced by electric field separating photo-induced charges in junctions between areas of p-type and n-type doping, or different doping in general[55]. Selective-area doping can be achieved by the use of chemicals[124], by electrostatics through the use of split-gates[125] or by taking advantage of the charge transfer from metals with different work function with respect to that of graphene[126–128]. The work function is the distance between the Fermi level and the vacuum level or, in other words, the minimum energy needed to knock out an electron from the solid. The first graphene photodetectors were made exploiting the latter concept and they were the first to be explored, by using basic metal-graphene-metal (MGM) configurations. Achieved responsivities in these detectors were of the order of ∼10mA/W at 1550nm[128]. p-n photodiodes were also realized with TMDs by using split-gate configurations[129, 130].

4.2.3 Bolometers

Bolometers, also known as thermal detectors, mostly work in the mid-IR and far-IR, *i.e.* in the range of wavelengths from 3μm to 1mm. Their working mechanism is not based on the generation of electron-hole pairs, therefore bolometric detectors are not limited to λ corresponding to energies higher than the bandgap.

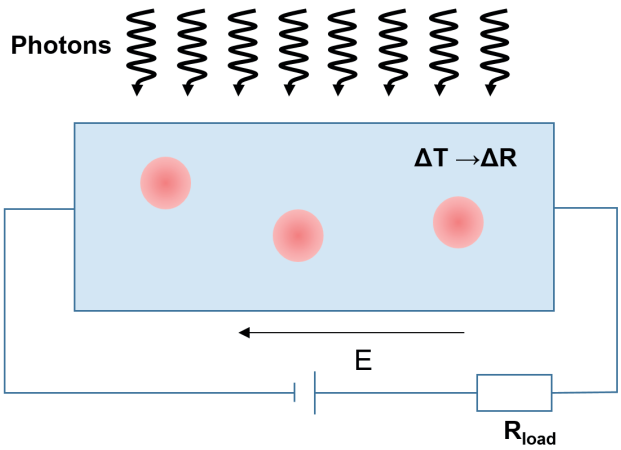

Figure 4.4: Working principle of a bolometric photodetector

The incoming radiation impinges on the detector, causing generation of heat, *i.e.* a change of temperature ΔT. As the resistance of the detector is sensitive to T variations, heating causes variations of the output signal. This variation of T in terms of incident power P_o is ruled by the heat flow equation[131]:

$$C_T \frac{d(\Delta T)}{dt} + G_T \Delta T = \eta P_o e^{j\omega t} \tag{4.7}$$

where C_T is the heat capacity of the sensitive element (unit J/K), G_T is the thermal conductance of the element supporting the detector (unit W/K), η is a factor which takes into account the fraction of absorbed photons (i.e. quantum efficiency) and ω is the frequency of incoming radiation. This equation has the following solution:

$$\Delta T = \frac{\eta P_o e^{j\omega t}}{G_T + j\omega C_T} \tag{4.8}$$

In order to maximize the ΔT, G_T and C_T have to be optimized to be as low as possible. On the one hand C_T is minimized by reducing the mass of the sensing element; if the area of the element is fixed by the pixel size, the only parameter left for optimization of C_T is the thickness, which is the reason why thin films are generally used for bolometric applications. On the other hand the thermal conductance G_T of the supporting element has to be controlled in order to avoid dissipation of heat; this is achieved by using suspended structures as for Fig.4.5[131, 132]. A wide range of thin-film materials can be used from metals, to semiconductors and superconductors[131]. The latter will be discussed in the next subsection.

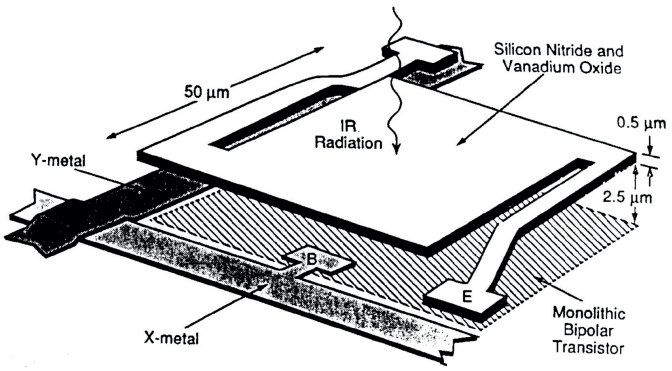

Figure 4.5: Example of suspended structure utilized to suppress the conductance G_T of the supporting material and avoid heat dissipations. Taken from Ref.[131]

New figures of merit have to be introduced for bolometers. The most important figure of merit is the temperature coefficient of resistance (TCR), which assumes that temperature changes due to the incoming radiation produce linear variations in the resistance:

$$\Delta R = \mathrm{TCR} \cdot R \Delta T \tag{4.9}$$

The TCR is measured in %/K units. Its rigorous definition is therefore:

$$\mathrm{TCR} = \frac{1}{R}\frac{dR}{dT} \tag{4.10}$$

TCR of ∼0.4%/K can be obtained with metallic bolometers[133], up to 4.3%/K with semiconducting bolometers[134] and values above ∼200%/K with superconducting bolometers which however require cooling to be operated[131]. Bolometers are typically biased in current (I_{bias}), while changes in voltage are detected. A photovoltage V_{ph} is produced by changing the temperature and the responsivity is quoted in V/W instead of A/W. Adding up the equations written so far, the responsivity for bolometers can be calculated by the following equation[131]:

$$R_{int} = \frac{I_{bias} \cdot \mathrm{TCR} \cdot R\Delta T}{P_o} = \frac{I_{bias} \cdot \mathrm{TCR} \cdot R\eta}{|G_T + j\omega C_T|} \tag{4.11}$$

An important class of thermal detectors are the one based on the use of pyroelectric crystals, whose working principle is depicted in Fig.4.6[135].

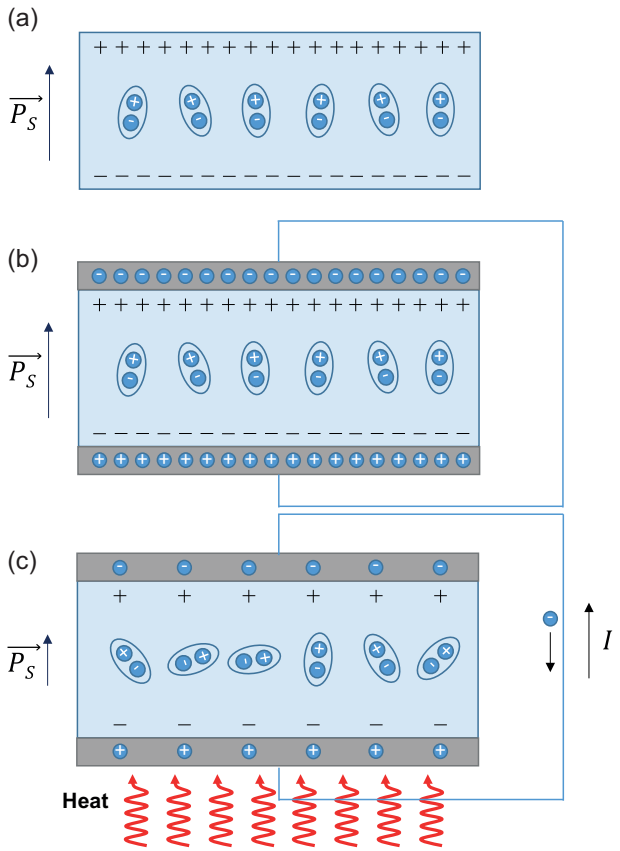

Figure 4.6: Working principle of a pyroelectric crystal (a) at rest, (b) short-circuited by two connected electrodes and (c) when heat is applied.

Pyroelectric crystals are materials in which each unit cell has a net preferential electric dipole orientation perpendicular to the surface, generating an overall spontaneous polarization of the crystal $\mathbf{P_s}$. At each surface this results in a layer of bound charge. When at rest, charges at the surface of the crystal simply attract ions of opposite sign from the environment. If two metals are deposited at the opposite sides of the crystal and a short-circuit is made, charges of opposite sign accumulate at the electrode surface but no net current flows in the circuit, because P_s remains constant and the electrode charges compensate those at the surface. Heat can perturb and alter the dipole order, causing a decrease in the intensity of P_s, with consequent flow of current in the circuit, compensating the change in bound charge[135]. The pyroelectric constant p_c regulates the change in P_s with temperature[136]:

$$dP_s = p_c \cdot dT \tag{4.12}$$

If heat is generated by electromagnetic radiation, the photocurrent I_{ph} can be calculated as[135, 136]:

$$I_{ph} = \frac{dQ}{dt} = A\frac{dP_s}{dt} = A \cdot p_c \cdot \frac{dT}{dt} \tag{4.13}$$

where A is the electrode area. The value of p_c in lithium niobate ($LiNbO_3$), which is a typical pyroelectric crystal, is of the order of $83\mu Cm^{-2}K^{-1}$.

The resistance of graphene is weakly dependent on temperaure[137] and conventional bolometers have only achieved responsivities as low as 0.2mA/W at $\lambda \sim 10\mu$m[138]. This suggests that alternative solutions are needed to circumvent this issue.

4.2.4 Superconducting photodetectors

Superconductors are materials whose resistance drops to zero below a certain critical temperature T_C. Superconducting photodetectors are extremely sensitive objects that can resolve down to single photons with unequalled performance[139]. The energy of a photon in the visible and near-IR is as low as $\sim 10^{-19}$J. The price to pay for this sensitivity is however the need of cooling down to temperatures near the superconducting transitions. Here two types of superconducting photon detectors will be described: transition edge sensors (TES) and superconducting single photon detectors (SSPD).

For TES the operation is straightforward: the transition (drop) in resistance from the metallic state to the superconducting state in some materials can be so sudden to be completed in a temperature span of few mK. In TES a superconductor is biased and kept

at a temperature on the cusp of the superconducting transition so that any absorption of photons results in a substantial change in resistance[139, 140].

The working principle of SSPDs is more complicated and it is explained by the "hotspot model" depicted in Fig.4.7. Superconductivity in conventional superconductors originates from phonon-mediated pairing up of electrons, which form the so called bosonic Cooper pairs[141]. The superconducting state can be broken not only by heating above the T_C, but also by flowing a current with density J above a critical current density J_C[141]. In SSPDs a superconducting thin film is kept at a temperature well below the T_C and biased with a current density smaller, but close to J_C. The binding energy of a Cooper pair is of the order of 1meV, whereas that of a phonon at $\lambda = 1550$nm is about $\sim$0.8eV therefore a photon can break hundreds of Cooper pairs, creating a hot resistive region, which is named a hotspot[142, 143].

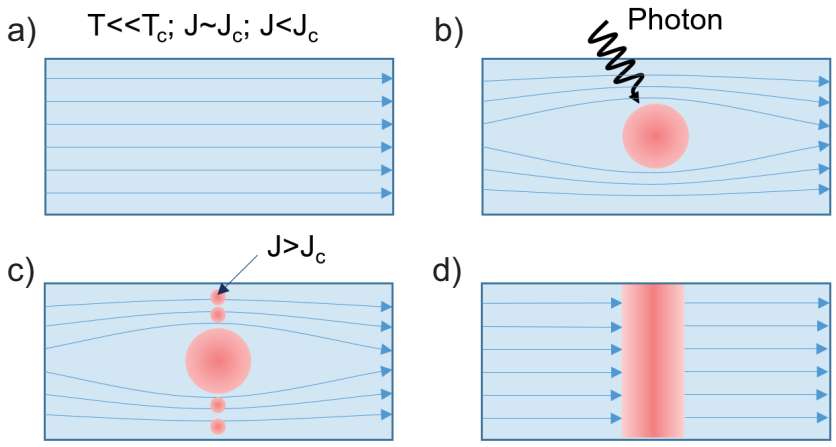

Figure 4.7: Different steps in the hotspot mode. (a) The superconductor is biased with a $J \sim J_C$, (b) a photon impinges on the superconductor causing the formation an hotspot, (c) current diverts from the resistive area, causing the formation of additional resistive spots on the adjacent region until (d) a resistive barrier is formed.

The flowing current would divert from the resistive spot to flow in the adjacent regions, thereby increasing the current density above J_c. This creates additional resistive regions, which continue to form until there is a barrier across the entire width of the superconductor[142, 143]. The current is now forced to pass through the resistive region causing a voltage drop to the output signal (pulse) which can be detected[144]. The responsivity has thus units of V/W. Superconductivity is restored after cooling by electron-electron and electron-phonon interactions, leaving the device ready to detect other photons[142, 143].

In order to assess the performances of these detectors new figures of merit need to be introduced[139]. The first discriminant factor is whether a detector has or does not have the ability to resolve single photons. If a detector is able to distinguish single photons an important parameter becomes the dead time τ_d, that is the time after the absorption of a photon in which the detector is unable to sense a new one. τ_d influences the overall speed of the detector, *i.e.* the maximum detected count rate. Superconducting detectors also normally show a non-zero dark count rate D_C (measured in Hz), meaning that the detector has a finite probability of recording dark counts; this may depend for instance on the susceptibility of the material to noise from the environment or on the biasing conditions. The detection efficiency DE (in % units) generally replaces the quantum efficiency, although the meaning is practically the same. The DE is defined as:

$$DE = \frac{R_{det}}{R_{inc}} \tag{4.14}$$

where R_{inc} and R_{det} are the rate (photons per unit time) at which photons arrive and are detected, respectively. As the dark counts are a direct measurement of the noise, the NEP in SSPDs can be measured by the formula[139]

$$NEP = \frac{h\nu}{DE}\sqrt{D_C} \tag{4.15}$$

In TES the most commonly used material is tungsten (W), operated at temperatures T ∼100mK. A DE of 95% at 1550nm was achieved with a maximum count rate of 100kHz[145]. These numbers are remarkable however 100mK require complicated systems for cooling. SSPDs are generally fabricated with niobium nitride (NbN), which has a T_C in the bulk of ∼16K. This allows operation at 1K to few K. Typical numbers of DE are around ∼60% at ∼1550nm with a maximum count rate of 1GHz[146].

SSPDs and TES reports with GRM are scarce, which leaves space to research in this field.

4.2.5 Other photodetectors

Multiple additional photodetection mechanism are nowadays known. Here we will focus on two mechanisms which are particularly relevant for graphene.

- *Photo-thermoelectric (PTE) effect:* The thermoelectric effect is the generation of a voltage upon heating of a junction of two different metals. The produced voltage is linked to the applied temperature gradient by the Seebeck coefficient, which has V/K units. Graphene sheets with different doping level possess different Seebeck

coefficients[115]. Photons incident at the junction between two graphene sheets with different doping can result in heating of the local electronic temperature T_e (Fig.4.8(a))[55, 115, 125, 147]. In graphene electron-electron interactions are strong and hot electrons are well decoupled from the surrounding phonon bath; this means that T_e can remain much higher than that of the lattice for many ps[55, 115, 125, 147]. The difference of T_e between the hot region and the surroundings is converted in a photovoltage V_{PTE} by the following equation[115]:

$$V_{PTE} = (S_1 - S_2)\Delta T_e \tag{4.16}$$

The signal generated upon absorption of photons in a p-n diode is therefore a combination of photovoltaic (photodiode with 0V bias) and PTE effect[125].

- *Plasma-wave assisted mechanism:* This effect was theoretically proposed by M. Dyakonov and M. Shur. A photovoltage appears in response to an oscillatory radiation (Fig.4.8(b))[55, 115]. This originates from the fact that the source and drain electrons in a graphene field effect transistor (FET) can act as a cavity for collective oscillations of the high mobility electron gas[148, 149]. These detectors allow detection of THz radiation from 0.1THz to 10THz, corresponding to $\lambda \sim 30\mu\text{m} \div 3\text{mm}$. Thus far the Dyakonov-Shur effect has been employed to achieve room temperature detection in a graphene-FET at 0.3THz[150].

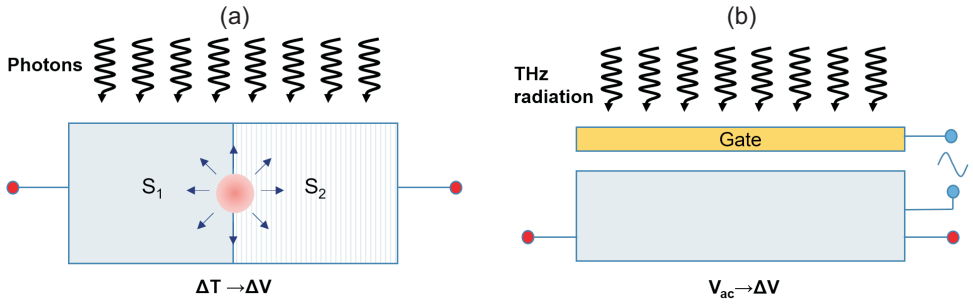

Figure 4.8: Schematics of (a) the PTE and (b) the plasma-wave assisted mechanism. Photovoltages are generated at the red poles in both cases.

4.3 Modulators

Light-matter interaction can be exploited to manipulate light. Electric fields, magnetic fields and acoustic waves can be used to modify the positions, orientations, or shapes of the molecules composing the material, influencing the light passing through[2]. The propagation of light in a material is well described by its complex refractive index $\tilde{n}$:

$$\tilde{n} = \mathrm{n} + j\kappa \tag{4.17}$$

The real part of $\tilde{n}$ is the optical refractive index n and it is connected to the phase velocity v of the wave travelling through the medium (n= c/v). Indeed n expresses how light slows down in a medium with respect to propagating in vacuum. The imaginary part κ is known as the extinction coefficient and it expresses how light is attenuated passing through the material due to absorption. This allows a first distinction between two categories of optical modulators, which are the refractive modulators and the absorptive modulators, depending on whether n or κ is being manipulated, respectively (Fig.4.9).

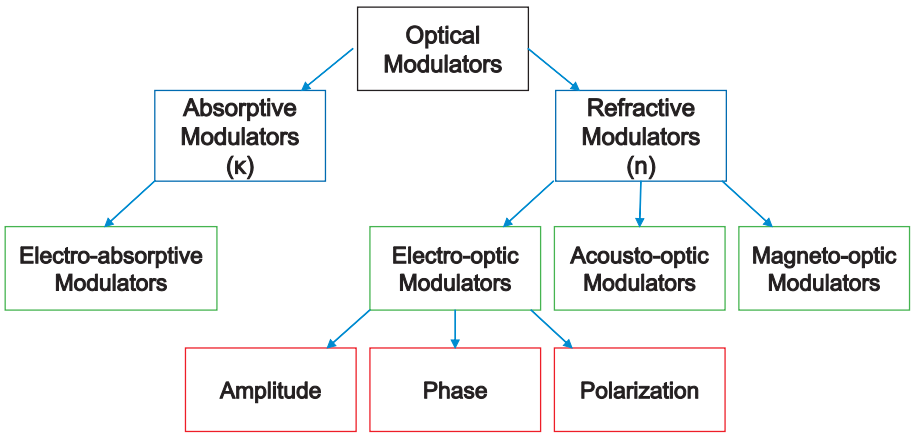

Figure 4.9: Chart with the different categories of modulators.

Modulators can further be categorized based on two other factors. On the one hand a classification can be made based on the nature of perturbation applied to the material, such as electrical, magnetic or acoustic. On the other hand the type of change on the incoming wave can be considered, since the light signal can be modulated in amplitude, phase or polarization[2].

Modulation of κ in electro-absorptive (also known as electro-absorption) modulators can be obtained performing electric field induced perturbation of the energy bandgap (Franz-Keldysh effect), free carriers concentration (plasma dispersion effect) or quantum confined states in quantum wells (Stark effect)[151, 152]. Differently, electro-optic

modulators rely on the fact that n is a function of the applied electric field E. The function n=n(E) is slowly varying, so it can be expanded in a Taylor series about $E \to 0$[2]:

$$\mathrm{n}(E) = \mathrm{n} + a_1 \cdot E + \frac{1}{2} a_2 \cdot E^2 + ... \tag{4.18}$$

The linear dependence of n on E is called the Pockels effect, whereas the quadratic dependence is named the Kerr effect. All materials exhibit the Kerr effect, whereas only some crystalline materials exhibit the Pockels effect[153].

Several figures of merit can be defined for modulators and here the most common ones will be listed[2, 154]:

- *Modulation depth:* measured in decibels (dB) or in %, it is the ratio between the light intensity being adjusted for maximum and minimum transmission:

$$M_d = 10 \log \frac{I_{max}}{I_{min}} \tag{4.19}$$

  It is sometimes reported including dividing by unit length (e.g. dB/μm)

- *Modulation speed:* also called bandwidth, the definition of speed in modulators is similar to that found in photodetectors. It is indeed expressed in Hz or bit/s and defined as the frequency at which the output power of the modulated optical signal is reduced by half.

- *Insertion loss:* also in dB unit, it represents the optical power lost because of the insertion of the modulator in a photonic circuit, taking into account reflections, absorption and coupling losses.

- *Half-wave voltage:* this parameter is specific for electro-optic phase modulators. It is measured in V and it represents the voltage needed to shift the phase of the incoming wave of $\lambda/2$ (π).

- *Power consumption:* it is expressed in J/bit and it is the energy needed for the modulator to produce one bit of data, *i.e.* to accomplish a single operation.

Silicon is largely used in modern modulators by exploiting the plasma dispersion effect[152, 154], whereas lithium niobate ($LiNbO_3$) is used due to its strong Pockels effect[155]. Modern modulators achieve speeds of several tens of Gbit/s, with a power consumption of tens of fJ/bit and modulation depths of tens of dB[154].

Electro-absorptive modulators can be fabricated with graphene owing to the possibility to shift the Fermi level by electrostatic doping. By means of a gate voltage, the absorption through the graphene layer can be efficiently modulated taking advantage of the Pauli blocking[156]. A 0.1dB/μm electro-absorptive graphene modulator was first demonstrated at 1550nm with 1GHz speed[156] and these values were further improved a few years later[157]. The broadband absorption of graphene allows modulators to work from the visible to THz wavelengths[156, 158]. These properties boosted the integration of graphene modulators in silicon photonics[55]. Other layered material based modulators are also under investigation, although considerable performance improvement is needed for integration in modern technologies[39, 159].

4.4 Light emitting devices

In a semiconductor, three fundamental processes exists as a consequence of interaction between an electron and a photon: absorption, spontaneous emission and stimulated emission[1]. In order to visualize these processes we can consider an atom in a two-level system (4.10). At equilibrium the atom lives on the ground state E_1. The absorption of a photon of energy E_{12}=E_2-E_1 would bring the atom to the excited state E_2. The excited state is unstable and the atom would want to return to the ground state. Two radiative process are then possible. In the case of spontaneous emission the atom simply relaxes to the ground state by emitting a photon of energy E_{12}. Alternatively the emission can be stimulated by a photon of energy E_{12} and emission of a photon with the same energy, phase and polarization of the stimulating one (coherent)[1].

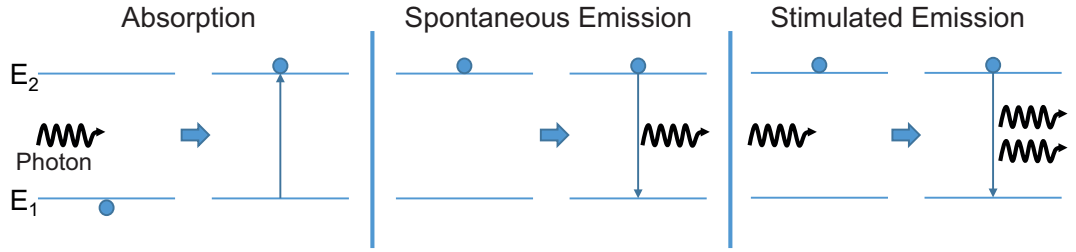

Figure 4.10: The three fundamental transitions when a photon interacts with a particle in a two level system

The instantaneous populations on level E_1 and E_2 can be named n_1 and n_2, respectively. If a constant of proportionality is assigned to each of the transitions, *i.e.* absorption (B_{12}), spontaneous emission (A_{21}) and stimulated emission (B_{21}), then the following balance equation for the rates of the three transitions can be written:

$$B_{12}n_1\rho(E_{12}) = A_{21}n_2 + B_{21}n_2\rho(E_{12}) \tag{4.20}$$

where $\rho(\mathrm{E}_{12})$ is the density of photons with energy E_{12}. In order to favour the rate of stimulated emission over that of absorption and spontaneous emission, an high density of stimulating photons $\rho(\mathrm{E}_{12})$ and $n_2 > n_1$ are needed. The latter condition is satisfied when an inversion of population is performed and more atoms are in the excited states than those in the ground state. Spontaneous and stimulated emission lie at the heart of the two fundamental light emitting devices in optoelectronics, which are light emitting diodes (LEDs) and lasers, respectively[2]. Laser is indeed an acronym for light amplification by stimulated emission of radiation[1].

Solid-state LEDs and laser diodes are realized with forward-biased p-n junctions of direct bandgap semiconductors. p-n junctions of heavily doped semiconductors allow to achieve population inversion in the carrier depletion region. A cavity can be built around the diode to confine the photons emitted by spontaneous emission and make them recirculate to stimulate new photons, establishing a gain mechanism. If gain overcomes the losses, stimulated emission dominates and lasing starts to occur[1, 2].

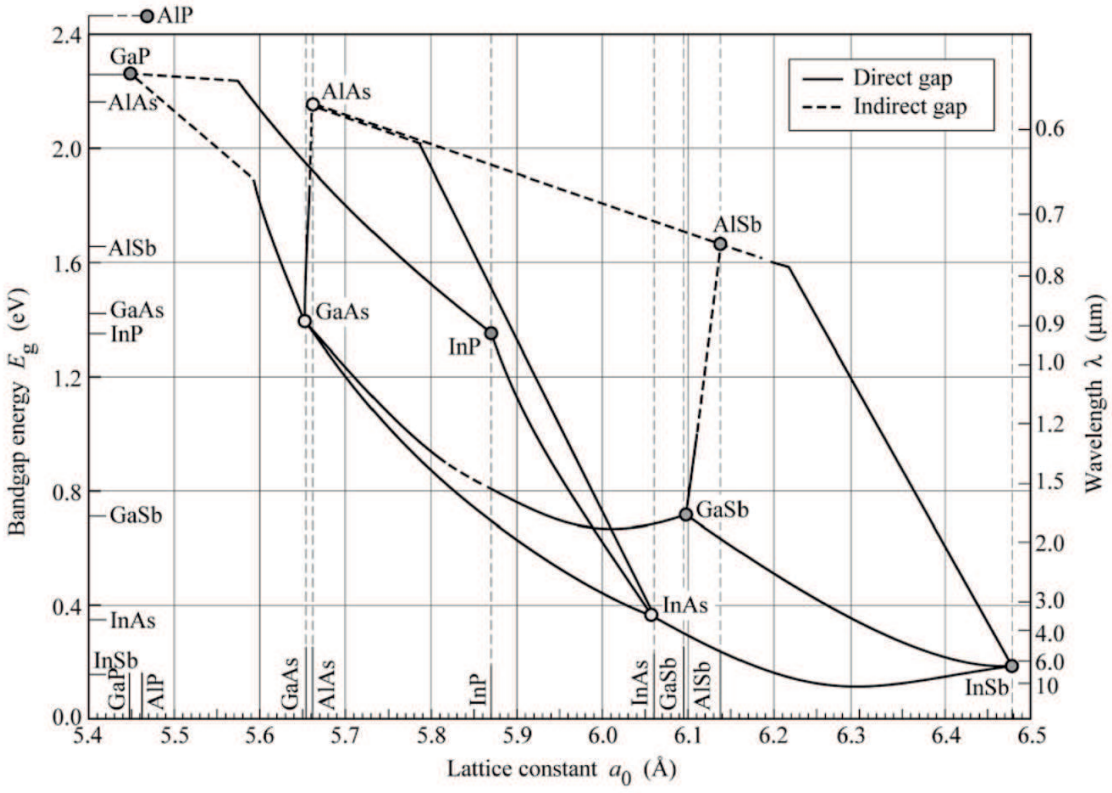

Figure 4.11: Energy bandgap and lattice constant of III-V semiconductors[160]

The scene of LEDs and lasers is nowadays dominated by III-V semiconductors and their compounds as engineering their bandgaps can help covering emission at wavelengths spanning the visible to the IR (Fig.4.11)[160].

Graphene is a zero bandgap material and it is therefore not suitable as an active material in LEDs and lasers. Light emitting devices were first demonstrated with MoS_2[88]. More recently all-GRM LEDs were fabricated by using graphene/h-BN/TMD heterostructures[95]. Graphene is used as an electrode to source and tunnel carriers in the TMD through an h-BN insulating barrier. Carriers are thus injected in the TMD, available for radiative recombination and light emission[95]. As of today, lasing from TMDs is yet to be demonstrated.

4.5 Key material requirements for optoelectronic devices

4.5.1 Mobility

Since its isolation, graphene has attracted attention due to its outstanding mobility at room temperature. The mobility can be calculated by using several methods, such as field-effect or Hall measurements. At least four contacts need to be deposited on single layer graphene (SLG) to reliably extract a meaningful value of the mobility. A Hall bar can be fabricated as for Fig.4.12(a) so that both field-effect and Hall measurements can be performed on the same device.

In the field effect (FE) case a current I_{DS} flows between the source (electrode 1) and the drain (electrode 4), whereas the voltage drop (V_{23}) across the graphene sheet is measured between electrodes 2 and 3. The resistance of graphene can be modulated through electrostatic doping by means of a gate voltage[13]. The typical substrate of graphene is Si with a layer of SiO_2 on top. If Si is heavily doped, it can work as an electrode, with the SiO_2 acting as a gate oxide. This measurement configuration is known as back-gate(BG). Here I define W as the width of the graphene channel and L as length, *i.e.* the distance between electrodes 2 and 3 (or 5 and 6). The measured resistance of graphene is $R = V_{23}/I_{DS}$, whereas its resistivity is $\rho = R \cdot W/L$ by using Ohm's law in the 2d limit. Fig.4.12(b) plots ρ as a function of the back gate voltage V_{BG}. For this sample the Dirac point or charge neutrality point (CNP) is at V_{CNP} ~28V. This means that with no gate voltage the sample is p-doped and the transport is dominated by holes for V_{BG} <28V and by electrons for V_{BG} >28V. The starting point to understand how to calculate the field effect mobility μ_{FE} is Eq.4.1. If we want to measure mobility where

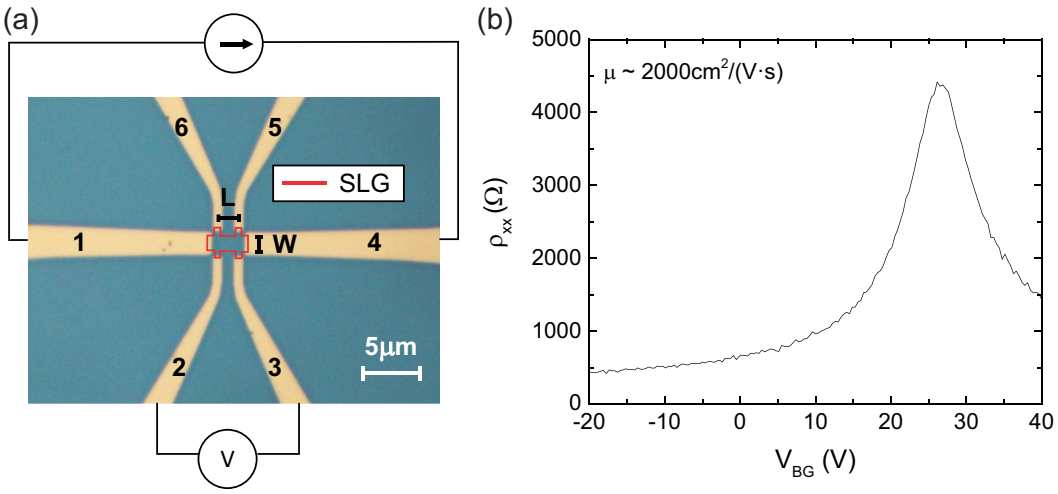

Figure 4.12: (a) Optical microscope image of a graphene Hall bar with a scheme of the four terminal measurement setup. (b) Longitudinal resistivity as a function of the gate voltage in a SLG sample on a Si substrate with 90nm of SiO_2.

one carrier conduction prevails, such as in the electron branch, the formula for σ can be simplified to:

$$\sigma = q\mu_n n \tag{4.21}$$

If we now differentiate σ with respect to the charge carrier concentration n, the following equation is obtained:

$$\frac{\mathrm{d}\sigma}{\mathrm{d}n} = q\left(\mu_n + \frac{\mathrm{d}\mu_n}{\mathrm{d}n}n\right) \tag{4.22}$$

Close to the CNP carrier concentration is small as it is equal to the concentration of charged impurities n^* and the second term on the right hand side of Eq.4.22 can therefore be neglected. If the variation of charge carrier concentration $\mathrm{d}n$ is associated with charges electrostatically induced by a gate voltage V_{BG}, then:

$$\mathrm{d}n = \frac{C_{ox} \cdot \mathrm{d}V_{BG}}{q} \tag{4.23}$$

where C_{ox} is the capacitance per unit area of the oxide. Therefore an equation for the mobility can be extended also to holes and written in the form:

$$\mu_{FE} = \frac{1}{C_{ox}} \frac{\mathrm{d}(1/\rho_{xx})}{\mathrm{d}V_{BG}} \tag{4.24}$$

as $\sigma = 1/\rho$. Furthermore here I specify $\rho = \rho_{xx}$ as being the longitudinal resistivity of the channel. As explained, the estimation of μ with Eq.2.24 is particularly valid in regions close to the Dirac point. Alternatively μ_{FE} can be measured simply by using Eq.4.21 and assuming that n is only represented by the electrostatically-induced charge:

$$n = \frac{C_{ox}(V_{BG} - V_{CNP})}{q} \tag{4.25}$$

Since this method does not take into account the presence of residual charge n^*, it is more valid far from the Dirac point where the induced n is much greater than n^*.

The Hall effect is the appearance of a voltage difference in the direction transverse to that of the electrical current flow. This effect is due to the deflection of charges from their trajectories due to the Lorentz force $\vec{F}$ in the presence of a magnetic field $\vec{B}$:

$$\vec{F} = q(\vec{E} + \vec{v} \times \vec{B}) \tag{4.26}$$

where $\vec{v}$ is the velocity vector of the charges. In the Hall measurement configuration (Fig.4.13(a)) a current I_{DS} is still sourced from electode 1 to electrode 4, but the voltage drop V_{35} across electrodes 3 and 5 (or 2 and 6) is monitored.

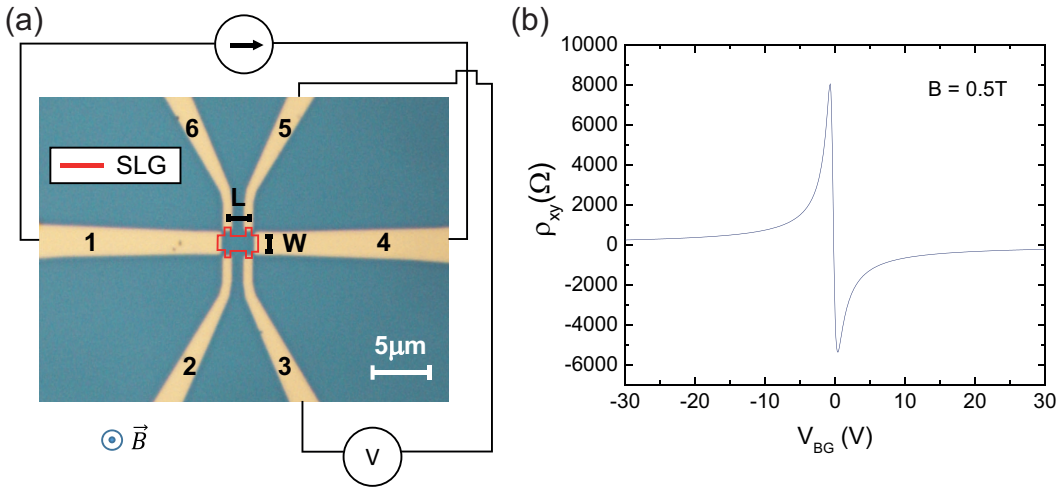

Figure 4.13: (a) Optical microscope image of a graphene Hall bar in Hall measurement configuration. (b) Representative transversal resistivity as a function of the gate voltage in a SLG sample different from that in Fig.4.12(b). B=0.5T.

The carrier density is measured directly at each V_{BG} by the following relation:

$$n = \frac{B}{qR_{xy}} \tag{4.27}$$

where R_{xy}=$\rho_{xy}L/W$ and B is the magnetic field intensity. The Hall mobility μ_H can therefore be calculated as:

$$\mu_H = \frac{1}{qn\rho_{xx}} \tag{4.28}$$

This method has the advantage that the n is measured directly, however it is also not valid close to the Dirac point, *i.e.* when ρ_{xy} changes sign and the conduction in the channel switches from electrons to holes or vice-versa (Fig.4.13(b)). In this work mobility is also sometimes referred to as μ, without specifying the measurement method or the carrier type. This happens especially when the maximum value of an experiment is reported.

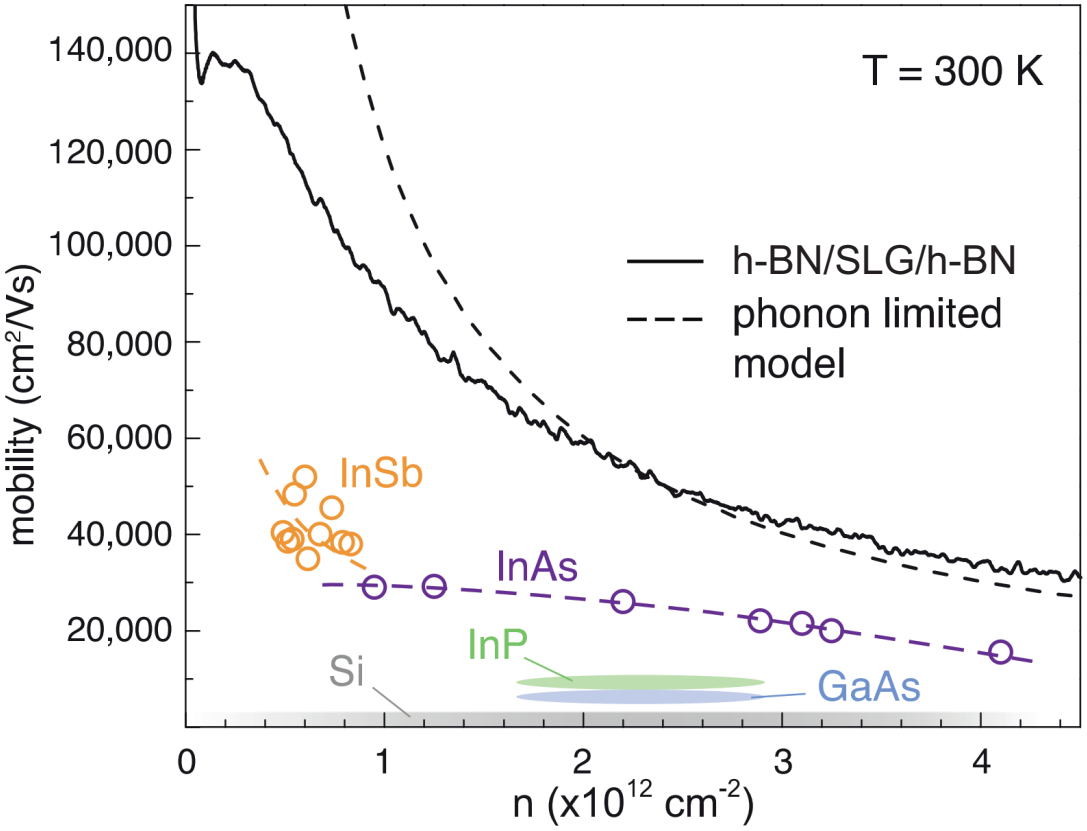

Figure 4.14: The mobility of a h-BN/graphene/h-BN device (solid line) compared to the theoretical limit (dashed line) and to that of other most common semiconductor compounds. Adapted from Ref.[107]

The room temperature (RT) μ in graphene flakes produced by micro-mechanical cleavage on SiO_2 is limited to values $< 10\,000\ cm^2V^{-1}s^{-1}$ by charged surface states, impurities and surface roughness[161]. Atomically-flat flakes of hexagonal boron nitride

(h-BN) used both as a substrate and as a capping layer have enabled the RT μ of exfoliated graphene to be increased by an order of magnitude to values exceeding 100 000 $cm^2V^{-1}s^{-1}$[107, 162], close to the theoretical limit imposed by scattering of carriers with acoustic phonons[163, 164]. h-BN is currently considered the primary candidate for the fabrication of devices overcoming the $\sim$ 10 000 $cm^2V^{-1}s^{-1}$ mobility limit associated with SiO_2 substrates.

The significance of mobility in photodetectors can now be discussed. In photoconductors the gain G_{ph} is inversely proportional to the transit time (Eq.4.5). If the distance between the source and drain electrode in a photoconductor is L, the transit time is $\tau_{transit} = L/v_d$ where v_d is the carrier drift velocity. If carriers move to a source-drain voltage bias V_{DS}, then[115]

$$\tau_{transit} = \frac{L^2}{\mu V_{DS}} \tag{4.29}$$

the higher the carrier mobility, the shorter is the transit time and consequently, the higher is G_{ph}. In photoconductors however, one carrier type recirculates in the circuit, delaying the recombination. This means also that recirculating carriers are not available for detecting the next photon, reducing the device speed. The higher the gain G_{ph}, the lower the device speed: this is the reason why photoconductors generally have a response time in the range of ms[2].

On the other hand, photodiodes (except for APDs) are not governed by a gain mechanisms. The mobility, through $\tau_{transit}$, directly influences the device speed as it relates to how fast carriers are separated in the presence of electric field. High mobilities can allow photodiodes to work in the GHz regime, with a response time of ns[2].

In bolometers, temperature changes the resistance of a material. These changes affect the mobility which degrades at higher temperatures due to increased scattering with phonons. However, temperature changes could be used indirectly to induce a doping of the graphene channel. In such case a change of carrier concentration would imply a movement toward left or right in the curve of Fig.4.12(b). We have seem in Eq.4.24 how mobility can be related to the slope of this curve. High mobility leads therefore to steeper curves of σ or ρ versus applied electric field and consequently to more sudden changes of the resistance even in the presence of small perturbations. A device exploiting this concept will be presented in Chapter 7.

4.5.2 Scattering time

The scattering time τ_{sc} is the average time between two consecutive scattering events of a charge carrier drifting in a material. In the Boltzmann treatment the mobility is related to the scattering time by the following relation[1]:

$$\mu = \frac{q\tau_{sc}}{m^*} \tag{4.30}$$

Intuitively, the more the scattering events (i.e. shorter τ_{sc}), the more complicated the drifting of charges becomes. Several scattering phenomenon are possible and the average timing in each mechanism contributes to the final τ_{sc} following the Matthiessen rule for scattering time[1]:

$$\frac{1}{\tau_{sc}} = \frac{1}{\tau_{\text{phonons}}} + \frac{1}{\tau_{\text{impurities}}} + \frac{1}{\tau_{\text{defects}}} + ... \tag{4.31}$$

At low temperatures (<200K) the dominant scattering mechanisms limiting the mobility in graphene are two: one is the scattering of carriers with unintended charged impurities (Coulomb scattering), mostly present due to the substrate if graphene is deposited on SiO_2[163]. The other mechanism is the scattering of carriers by defects[163]. At higher temperatures (>200K) the scattering by phonons also starts to play an important role and ultimately limits the carrier mobility[163]. An atomically-flat substrate, such as h-BN, free of dangling bonds, and a graphene with low defect concentration can thus positively impact on the mobility of graphene[28], and consequently to the performance of the optoelectronic device[55, 115].

4.5.3 Doping

Doping is the process of the introduction of impurities or extra-charges in or at the surface of a material with the purpose of modifying its electrical properties. Doping can be achieved in several ways. For example, in silicon dopants can be added in the growth process. At a later stage doping can be achieved through atomic implantation by impacting ions on the surface of the solid or by diffusion, exploiting the random motion of atoms from regions with high concentrations to regions of lower concentrations. Alternatively doping can be attained by electrostatics: this can be unintended as for the presence of charged impurities or environmental contaminants at the surface, or induced on purpose by using a field effect transistor. The surface of atomically thin layered materials is by definition completely exposed to the environment and can thus strongly

be influenced by extra charges. The doping can be p-type if the material is hole doped, or n-type for doping by electrons[1].

Methods to calculate the charge carrier concentrations have been shown in the previous subsection, in particular by the use of field effect (Eq.4.25) or Hall effect (Eq.4.27). The latter is the most accurate method to measure the doping level as it is a direct measurement. In the absence of electrical contacts to measure the device trans-characteristics (I_{DS} vs V_{BG}) or Hall effect, Raman has become a powerful tool to give an indication of the doping level in graphene[70, 73, 76, 165]. Position and full width at half maximum of the G peak (Pos(G) and FWHM(G)), position of the 2D peak (Pos(2D)), area and intensity ratios (A(2D)/A(G) and I(2D)/I(G)) are all sensitive to doping[73, 76, 165]. Calibration curves from experimental and theoretical studies are then present, which correlate each of the mentioned features with the position of the Fermi level of graphene. The Fermi level E_F is then related to the charge carrier concentration by the formula[18]:

$$E_F(n) = \hbar v_F \sqrt{\pi n} \tag{4.32}$$

which can be reorganized to give the following equation for estimation of the charge carrier concentration:

$$n = \frac{E_F^2}{\hbar^2 v_F^2} \pi \tag{4.33}$$

The doping level is fundamental in GRM photodetectors and optoelectronic devices. In graphene the doping level establishes a cut-off absorption wavelength due to Pauli blocking. Absorption of photons with energies E below $<2E_F$ are indeed inhibited due to the absence of available states or of carriers available for the transition (Fig.2.5). On the other hand the doping level and Pauli blocking can be exploited to build graphene-based electro-absorption modulators[156].

Besides, the doping level influences the mobility (Fig.4.14). The presence of more charge carriers can indeed degrade the mobility because of an increase in the number of scattering events[1]. Therefore operating at high carrier concentrations in graphene ($n \sim 10^{13}\text{cm}^{-2}$) means sacrificing the sample mobility.

4.5.4 Defects

Defects can influence the electrical, optical and mechanical properties of a solid. There are several categories of defects and specifically: point, line, surface and volume defects. Here we will focus on the former three[1].

- *Point defects:* there are several types of point defects. For instance, vacancies are missing atoms in the lattice, whereas interstitial defects are instead atoms occupying extra sites, which would not be occupied otherwise. A substitutional defect refers to the presence in the lattice of an atom of a different atomic species with respect to that forming the lattice. Finally an interstitial atom plus a vacancy form a Frenkel defect.

- *Line defects:* Line defects are also called dislocations. They are extra atomic planes or chains (in 2d materials) which add to the lattice.

- *Surface defects:* Surface defects are of paramount importance, especially in the field of layered materials grown by chemical vapour deposition. These defects refer to sudden changes of orientation of the lattice, with the two areas merging together at the so-called grain boundary. Materials grown with a single lattice orientation are generally called single crystals, whereas if several orientations are presence the material is defined as poly-crystalline.

In graphene the D peak in the Raman spectrum is activated by the presence of defects[72, 75]. Assuming point- or Raman active defects, their concentration n_D (in cm^{-2} units) can be estimated with the following empirical formula for samples with negligible (<100meV) doping[70, 77]:

$$n_D = 7.3 \cdot 10^9 (E_L)^4 \frac{I(D)}{I(G)} \tag{4.34}$$

where E_L is the Raman excitation wavelength (in eV) and $I(D)$ and $I(G)$ are the intensities of the D and G peak respectively. The formula has to be corrected for samples with non-negligible doping[166]:

$$n_D = 2.7 \cdot 10^{10} (E_L)^4 \frac{I(D)}{I(G)} (E_F)^{0.54} \tag{4.35}$$

In high quality samples the concentration of defects is of the order of $n_D \sim 10^{10}\mathrm{cm}^{-2}$ or below and the I(D)/I(G) ratio is almost negligible. The calculation of such relationship (Eq.4.35) is more complicated in layered materials such as MoS_2 due to the presence of more atomic species and the absence of evident defect-activated peaks. The presence of surface (or area) defects in graphene has been extensively studied[69, 167, 168] although the role of grain boundaries in high mobility devices is yet to be unravelled. It was found that the electrical properties of CVD poly-crystalline graphene were not as drastically affected by grain boundaries as those of other materials, such as complex oxides[69, 168].

Overall the presence of defects is still somehow detrimental to the sample mobility, defects being an important source of scattering. Graphene samples with a high D peak are thus unlikely to be used for applications where high mobility is required. The presence of defects can also influence the optical properties of materials due to the creation of mid-gap states in the bandgap of semiconductors. This generates an additional channel for absorption and recombination, which could be an advantage or a disadvantage depending on the application. For example on the one hand defect states can enable absorption at sub-bandgap energies, but on the other hand they can degrade (broaden) the emission linewidth in light emitting devices.

4.6 Conclusions

The field of optoelectronics has been introduced. The working principles of most common photodetectors, modulators and light emitting devices have been explained along with a discussion on their figures of merit. Layered materials offer an opportunity to implement functionalities in optoelectronic devices. The demonstration of possible integration of graphene with silicon photonics should further encourage the research in this field. The influence of sample mobility, scattering time, doping and defects has been discussed.

Photodetectors can take advantage of the high mobility in graphene and of its potential broadband absorption. Regarding TMDs, the direct bandgap absorption of 1L-MoS_2 and other Mo- and W- sulphides and selenides can be explored as efficient absorbers. Photodetectors with layered superconductors such as $NbSe_2$ could also be investigated and compared with current superconducting single photon detectors and bolometers.

Chapter 5

Fabrication of Graphene, Layered Materials and Hybrid Structures

5.1 Introduction

The fabrication of advanced photodetectors required the synthesis of graphene and layered materials by different methods and in some cases the assembly of their heterostructures.

Here I will show the synthesis technique adopted for micro-mechanical cleavage of layered materials on arbitrary substrates. The large variety of possible transfer methods has been outlined in Chapter 3. I will explain that I developed a method for wet assembly and encapsulation of CVD graphene in h-BN flakes for high mobility applications. Here it will be shown how this method, despite being wet, does not hinder the mobility of graphene, minimizing the presence of contaminants by using elevated temperatures during the production of the hetero-stack. Additionally, I adapted growth techniques to our lab facilities and perfected the wet transfer of CVD graphene and CVD MoS_2 to arbitrary substrates. I will also describe the fabrication of an all-CVD layered material heterostructure and its attractive properties.

The characterization of the synthesized materials is a key issue. I will here show the characterization of flakes, CVD materials and heterostructures by microscopy and spectroscopy techniques. Electrical characterization will also be performed in the case of wet-encapsulated CVD graphene as a proof of its considerable potential.

5.2 Micro-mechanical cleavage of graphene, MoS_2, h-BN and $NbSe_2$

I produced flakes of graphene and layered materials by micro-mechanical cleavage using the scotch tape method discussed in Chapter 2. Fig.5.1 shows μm-sized flakes of SLG, MoS_2, h-BN and $NbSe_2$ on a Si substrate + ~300nm SiO_2.

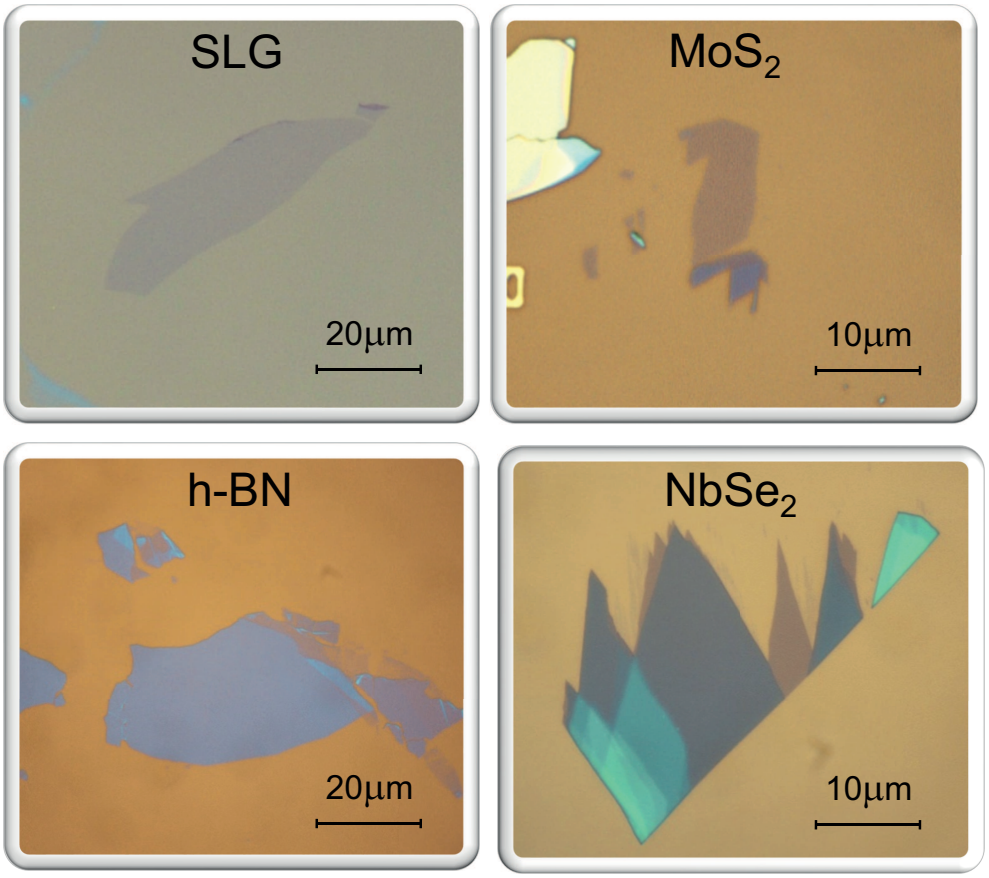

Figure 5.1: LM flakes produced by micro-mechanical cleavage.

The exfoliation of graphite can yield large single layer graphene flakes, up to hundreds of μm in lateral size. h-BN is instead used in this thesis work as a material for the encapsulation of graphene. In such case, h-BN does not need to be exfoliated down to the 1L, which would make the identification more challenging[66]. Flakes of 1L, 2L and few layer- (FL) MoS_2 and $NbSe_2$ typically show a maximum lateral size of few tens of μm, smaller compared to graphene. I found that exfoliating $NbSe_2$ on a PDMS stamp[105], with subsequent transfer (stamping) on the target substrate, yields larger flakes.

All produced materials are characterized by Raman spectroscopy. Fig.5.2 shows Raman spectra of the materials treated in this work. In graphene the D peak is absent, as commonly happens for micro-mechanically cleaved flakes, confirming the good quality.

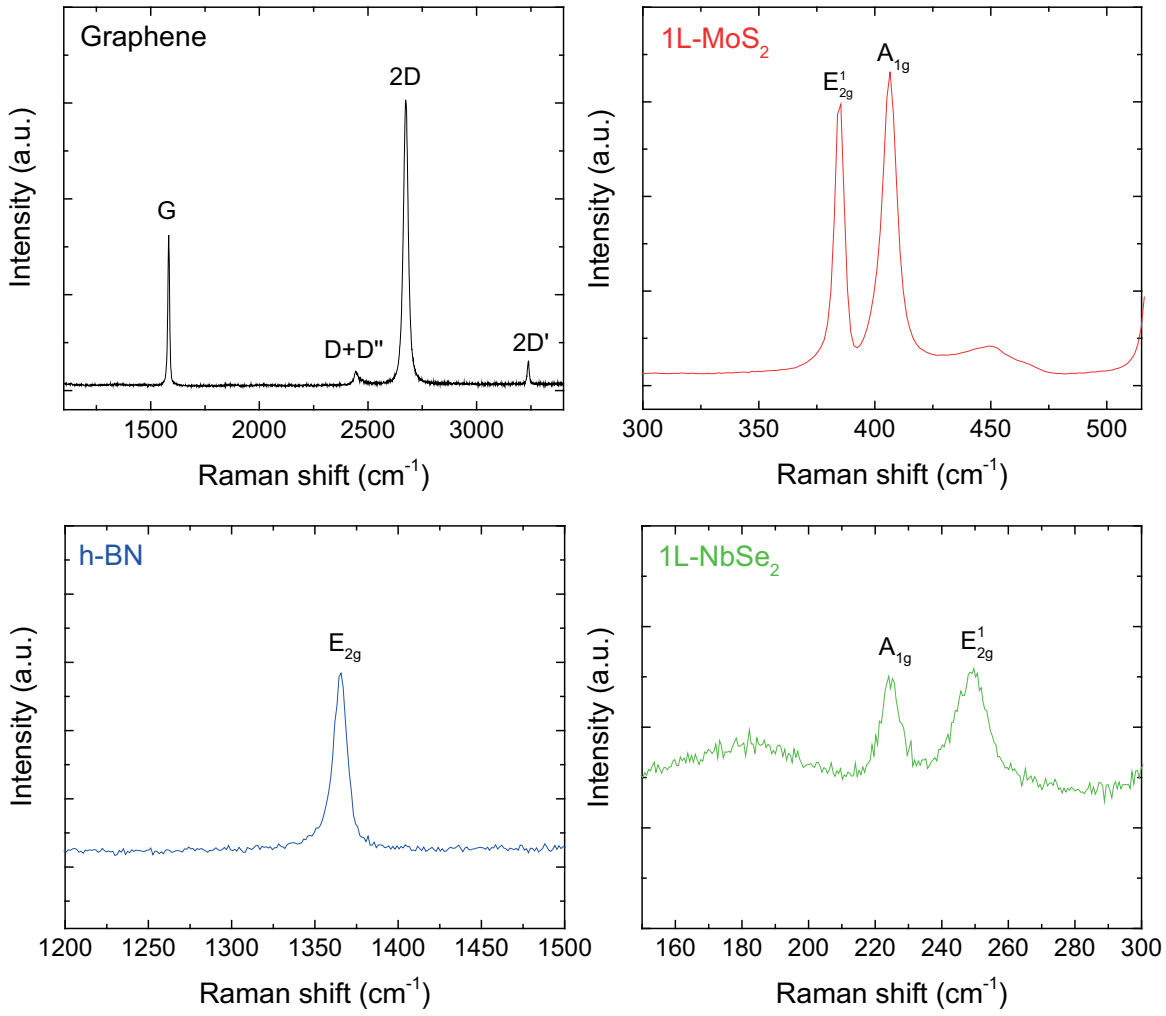

Figure 5.2: Raman spectra measured with an excitation wavelength λ=514nm of single layer graphene, 1L-MoS_2, few layer h-BN and 1L-$NbSe_2$.

The spectrum of 1L-MoS_2 is also accompanied by its photoluminescence (Fig.5.3) to show the strong emission from the direct transition of the A exciton, typical of the 1L.

The characterization of $NbSe_2$ was much more challenging. The material is indeed sensitive to air and shining light from a laser even with few tens of μW power, induces damaging on the sample, as shown in Fig.5.4, probably because of photo-assisted oxidation. I took full (high- and low-frequency) Raman spectra in vacuum, where laser-induced damaging of the sample did not occur. This allowed me to perform a systematic study

and determination of the number of layers (Fig.5.5), mainly by using the shear mode E^2_{2g} as discussed in Chapter 2.

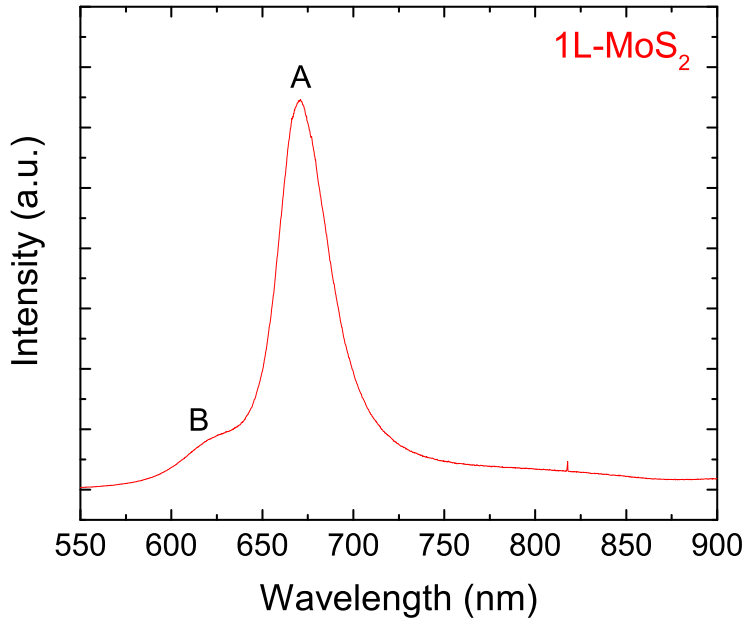

Figure 5.3: Photoluminescence of 1L-MoS_2 taken at λ=514nm.

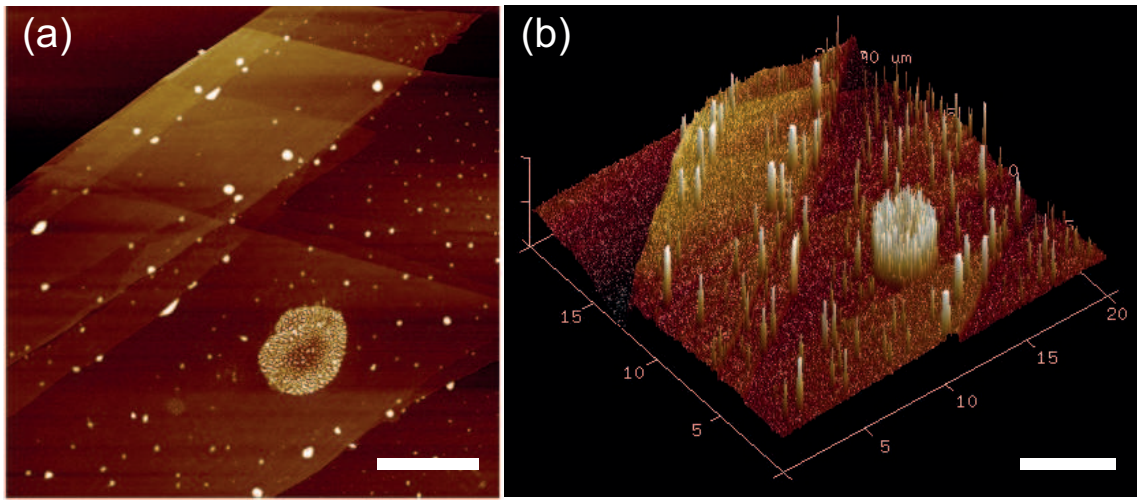

Figure 5.4: (a)-(b) AFM images of a $NbSe_2$ flake hit by a laser beam in air at 514nm with a power of $\sim$100μW. Scale bar is 5μm.

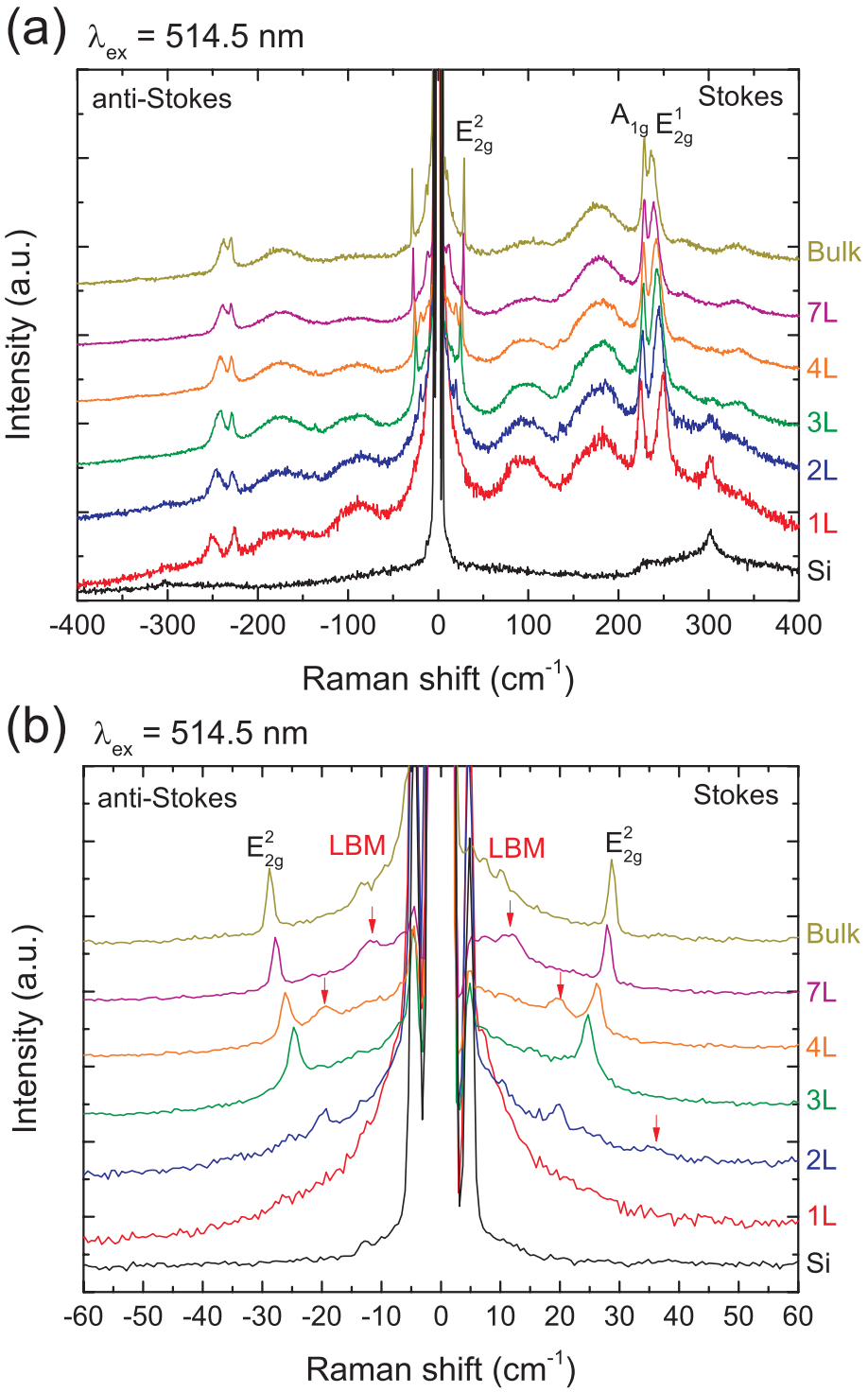

Figure 5.5: (a) Full Raman spectra and (b) close-up to the low frequency modes of $NbSe_2$ flakes with different thickness.

5.3 Growth of graphene by CVD

I grew graphene in a ∼4-inch tube chemical vapour deposition (CVD) system (Fig. 5.6) on 35μm-thick Cu foils. Sheets of Cu of ∼9cm ×6cm are cut by using the blade of a sharp cutter. Vacuum is made (< 4mTorr) in the furnace tube and in the gas lines, then CH_4 and H_2 are switched on to purge the lines (50:50sccm). In the meantime, the Cu foil is cleaned in acetic acid for 10 minutes, transferred in deionized water for additional 10 minutes and dried with nitrogen (N_2). The Cu sheet is rolled to fit into a ∼4cm diameter quartz tube which is then inserted in the main tube of the furnace: this is to avoid contaminations of the main tube with residuals deriving from Cu being heated at 1000°C. After reaching again a vacuum below 4 mTorr, the temperature is increased from room temperature (RT) to 1000°C in 20 sccm of H_2 in 60 minutes (see Fig.5.6), temperature is then kept constant at 1000°C for additional 30 minutes in order to perform annealing of the Cu foil. 5sccm of CH_4 are then added for 30 minutes for the growth of graphene to take place. After that, the heater coils are quickly turned away from the Cu foil position for fast cooling down.

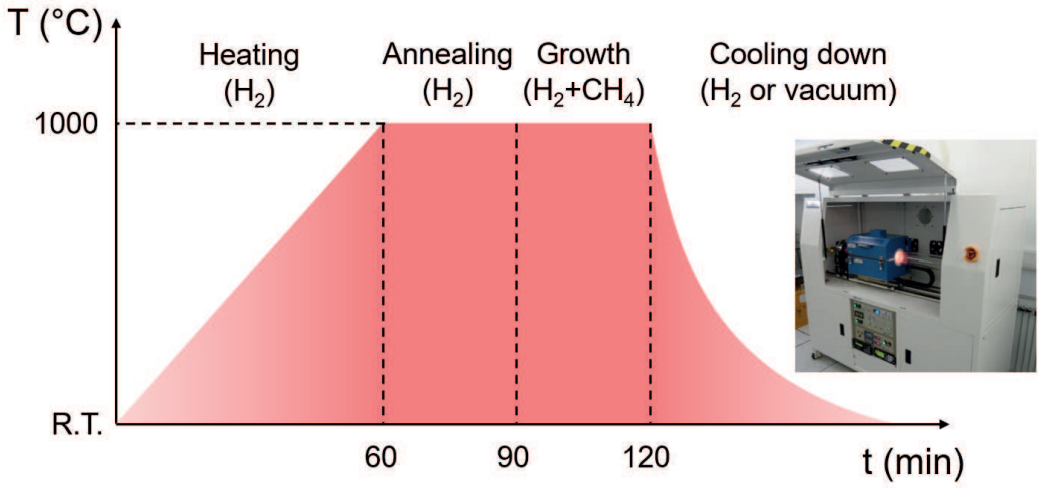

Figure 5.6: A scheme which shows the temperatures, gases and timing for the growth of CVD graphene. On the right: a picture of the furnace during a growth process.

This recipe was based on that of Ref.[49] and it yields poly-crystalline graphene. A representative Raman spectrum of poly-crystalline CVD graphene is shown in Fig.5.7. At 514nm excitation wavelength Cu shows a background photoluminescence signal (black curve). This can be removed by subtraction of the baseline to better appreciate the features of graphene (red curve). The most intense features are the G and the 2D peak. The D peak intensity is negligible, indicating the good quality of the grown samples.

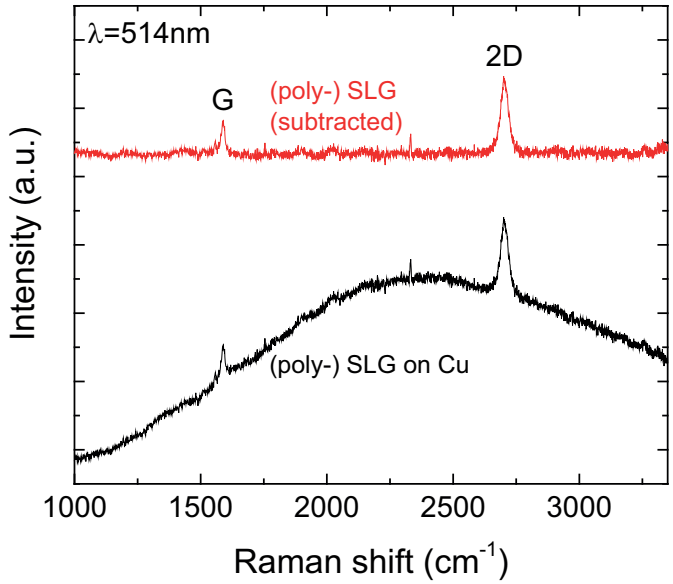

Figure 5.7: Raman spectra of poly-crystalline graphene before (black curve) and after (red curve) the subtraction of Cu PL.

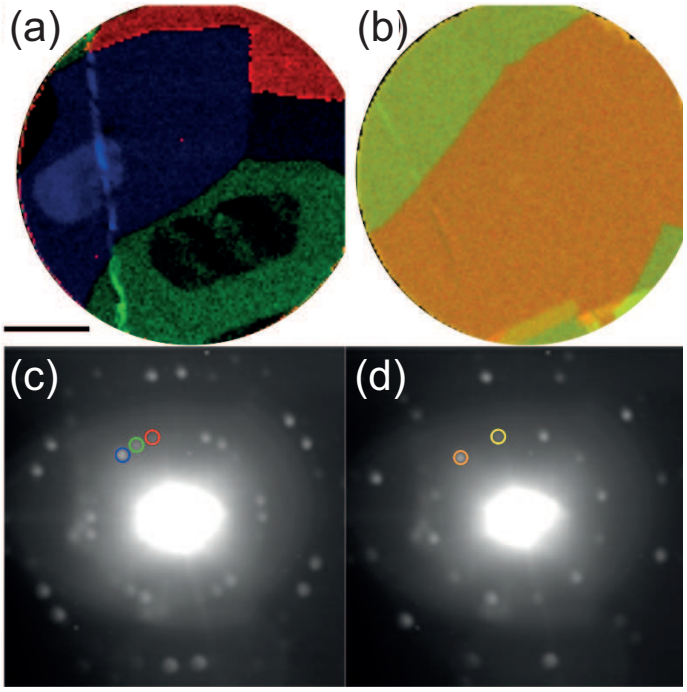

Figure 5.8: TEM diffraction maps (a-b) and patterns (c-d) of two circular poly-crystalline graphene areas. The scale-bar is ∼500nm.

TEM characterization of CVD graphene unveils a grain size of the order of a few μm. False-colour image maps of the crystal orientations (Fig.5.8(a-b)) are built by taking diffraction patterns at multiple points across holes of diameter $\sim$1.5μm. The overlap of all diffraction pattern images across the hole (a) and (b) are shown for clarity in Fig.5.8(c) and (d), respectively.

For the purpose of fabricating encapsulated CVD graphene devices single crystalline graphene was also used. Single crystals were grown on Cu foil at a temperature T $\sim$1065°C, closer to the melting temperature of Cu ($\sim$1085°C), with a similar method to that just explained. The crystals have regular hexagonal shapes and can be visualized under the microscope by oxidation of the Cu foil (Fig.5.9(a)). TEM diffraction images (Fig.5.9(b,1-5)) show identical patterns in several positions of the crystal, confirming the presence of a unique grain[169].

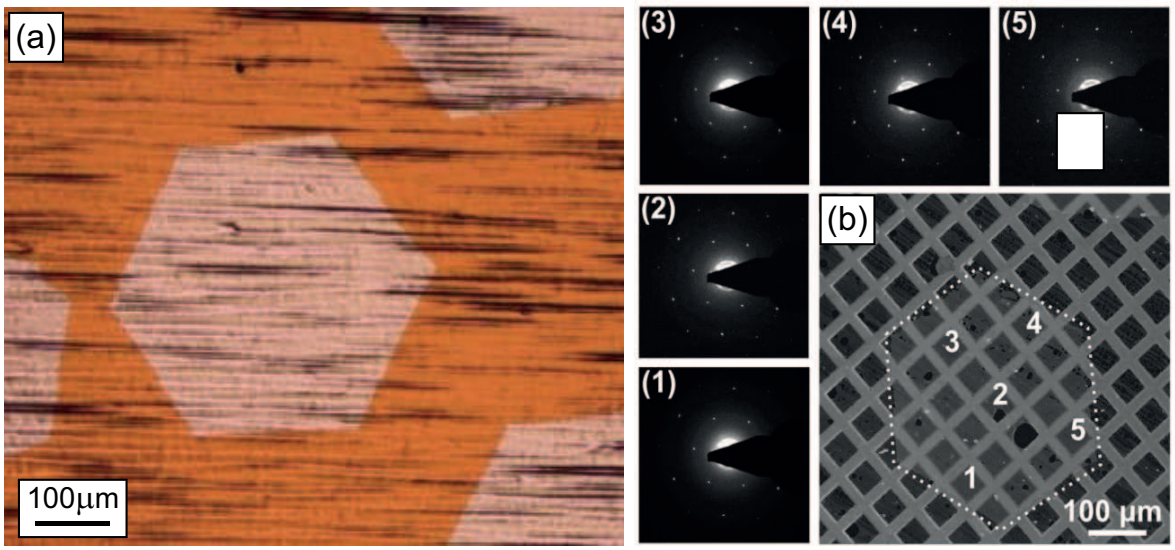

Figure 5.9: (a) Graphene single crystal on Cu, oxidized in air at $\sim$250°C for 1 minute. (b) Microscope image of a graphene single crystal transferred on a TEM grid adapted from Ref.[169], along with diffraction patterns, measured at positions (1-5).

5.4 Wet transfer of CVD graphene on arbitrary substrates

The results presented in this dissertation required CVD graphene to be transferred on several substrates such as: SiO_2, Si, lithium niobate ($LiNbO_3$), praseodymium cerium copper oxide (PCCO) films and poly-ethylene terephthalate (PET) foils. I accomplished

this by using the following wet transfer technique, also shown in Fig.5.10: the Cu foil on which SLG has been grown is cut in pieces according to the final target substrate dimensions (a) and taped from the edges on a 125μm-thick PET foil, which acts as a mechanical support. A poly-methyl methacrylate (PMMA) resist is spin coated on top of the SLG/Cu/PET stack at 4000 rounds per minute (rpm) for 40 seconds, then the PET support is removed by cutting the edges (b). The graphitic film grown on the side uncoated by PMMA is removed with a reactive ion etcher (RIE) by means of a 20W oxygen (O_2) plasma for 20 seconds at 200mTorr. The PMMA/SLG/Cu stack is then dropped at the surface of a solution of ~2.0g of ammonium persulfate (APS) in 150 ml of deionized water for Cu etching (c). When the Cu is entirely dissolved (d), the remaining PMMA/SLG stack is lifted with a PET substrate and transferred to a beaker filled with deionized water for diluting APS residuals. The procedure is repeated twice and then the PMMA/SLG is finally lifted with the target substrate (e) and left to dry overnight in a slanted position with respect to the worktop. The sample (PMMA/SLG/target substrate) is then transferred in a beaker with acetone for PMMA removal for few hours, then moved to a beaker with isopropyl alcohol (IPA) for 5 minutes and dried with N_2, leaving the SLG film on the target substrate.

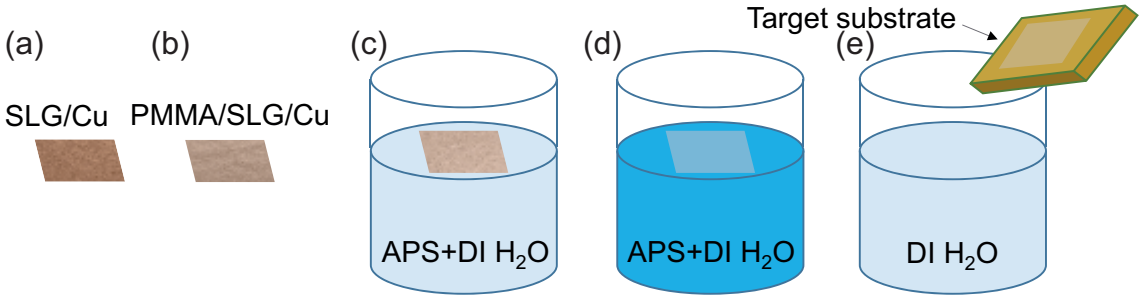

Figure 5.10: Some fundamental steps of the wet transfer of CVD graphene. The starting point is SLG on Cu foil (a), followed by spin coating of a PMMA layer (b). The stack is then transferred at the surface of an aqueous APS solution (c) for Cu etching. After few hours Cu is etched (d) and the solution turns blue due to the etching reaction with Cu. Graphene can be picked up with a target substrate (e), which is then followed by removal of PMMA in acetone.

Raman characterization of the transferred films on the target substrates relevant for this work are shown in Fig.5.11(a-d). The background signal of SiO_2/Si is flat and no subtraction is required. In all other spectra point-to-point subtraction was performed to better visualize the features of graphene and estimate doping. In all cases, the D peak is negligible, indicating that the transfer has not induced a considerable concentration

of defects. Characterization of CVD graphene on PET will be shown in a following dedicated section.

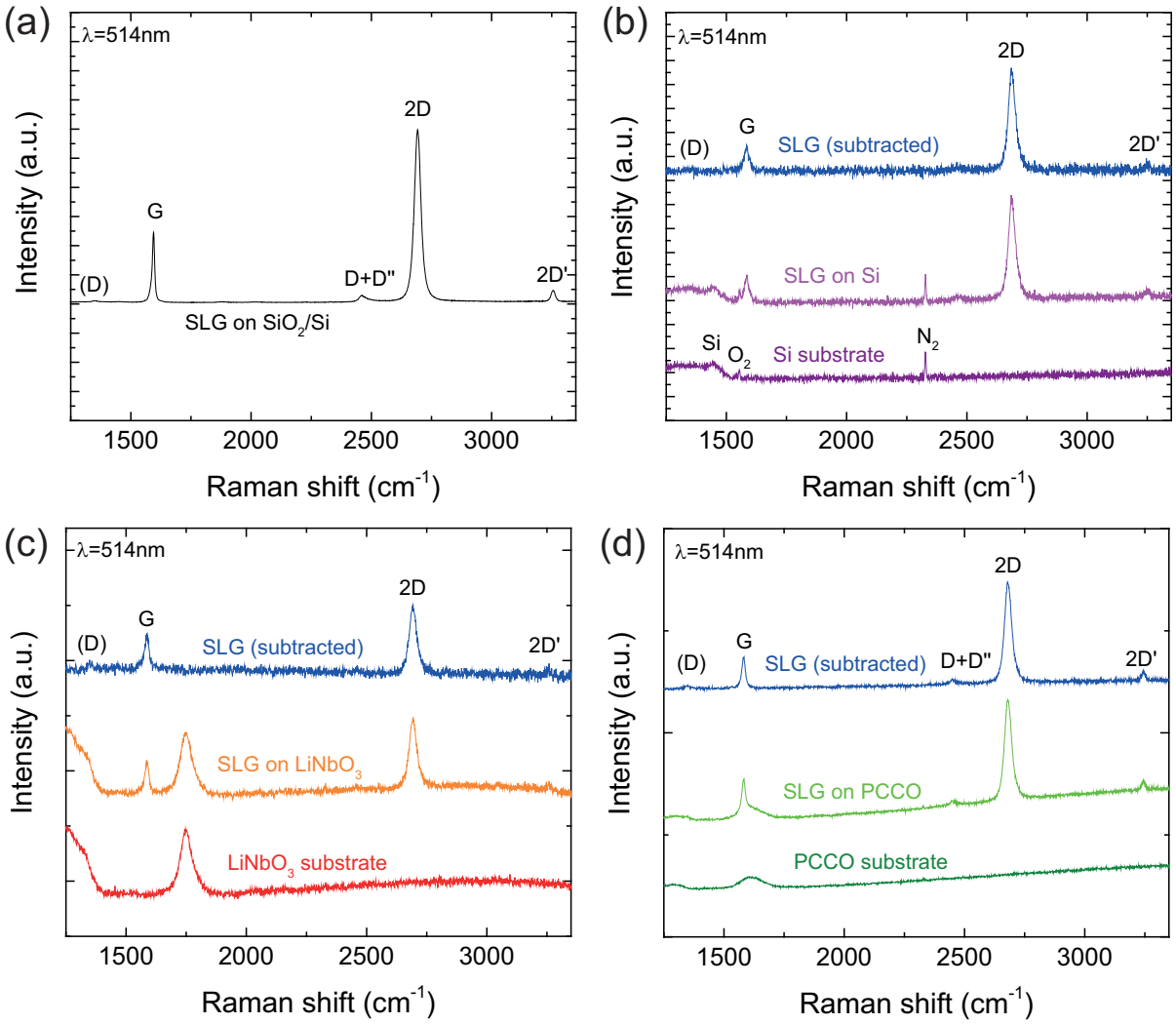

Figure 5.11: Raman spectra of CVD graphene on (a) SiO_2/Si, (b) Si, (c) $LiNbO_3$ and (d) PCCO before and after substrate subtraction. A λ=514nm has been used for excitation.

5.5 Encapsulation of CVD graphene in h-BN by wet transfer

Several methods have been employed for targeting high mobility with CVD graphene grown on metals and transferred to arbitrary substrates. These include wet and dry

techniques, sharing the need of minimizing residual contaminations from the transfer[26]. The highest mobilities with wet transfer methods have been achieved when transferring CVD graphene films on h-BN flakes[170–172], however the measured values of RT μ in these cases is less than 20 000 $cm^2V^{-1}s^{-1}$[170, 172]. In these cases μ was mainly limited by the top surface of graphene being exposed to environmental contaminants and residuals from the transfer[170–172].

As previously mentioned, recently a full-dry transfer technique for CVD graphene has been reported by Ref.[109]. This consists in picking up graphene with an h-BN flake directly from the copper (Cu) substrate on which it has been grown, and transferring it on a bottom h-BN layer for encapsulation. This dry procedure allows remarkable RT μ of up to 80 000 $cm^2V^{-1}s^{-1}$ to be achieved, comparable to exfoliated graphene[111, 162]. However it relies on the ability to pick up/detach graphene from the growth substrate using exfoliated h-BN. This is enabled only by oxidation of the metal below the graphene layer.

Here I developed a viable alternative to the dry transfer in Ref.[109]. Graphene single crystals are grown on Cu by CVD, as shown in Fig.5.9(a). These are then transferred on Si coated with 285nm oxide (SiO_2) as for Fig.5.12 using the wet transfer method described earlier.

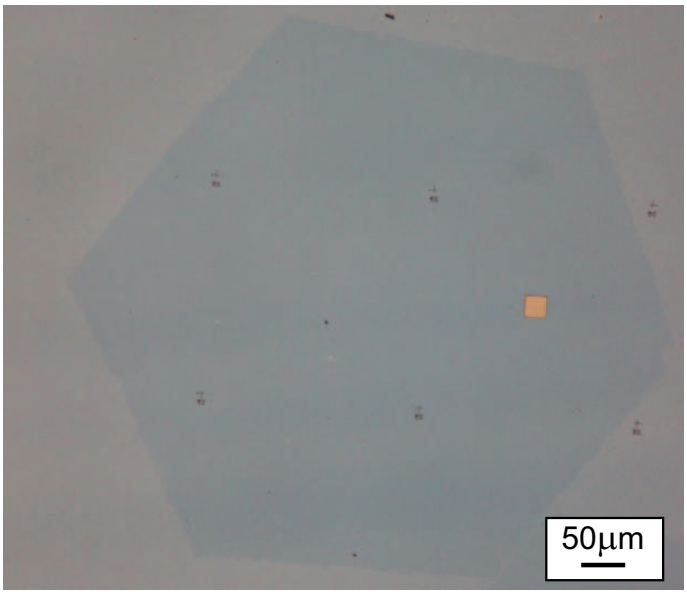

Figure 5.12: Single crystal transferred on SiO_2/Si by wet method.

After wet transfer onto SiO_2, graphene was encapsulated in h-BN using a dry transfer process, in which a polymer stamp is used to pick up and drop-down the layered materials (Fig.5.13).

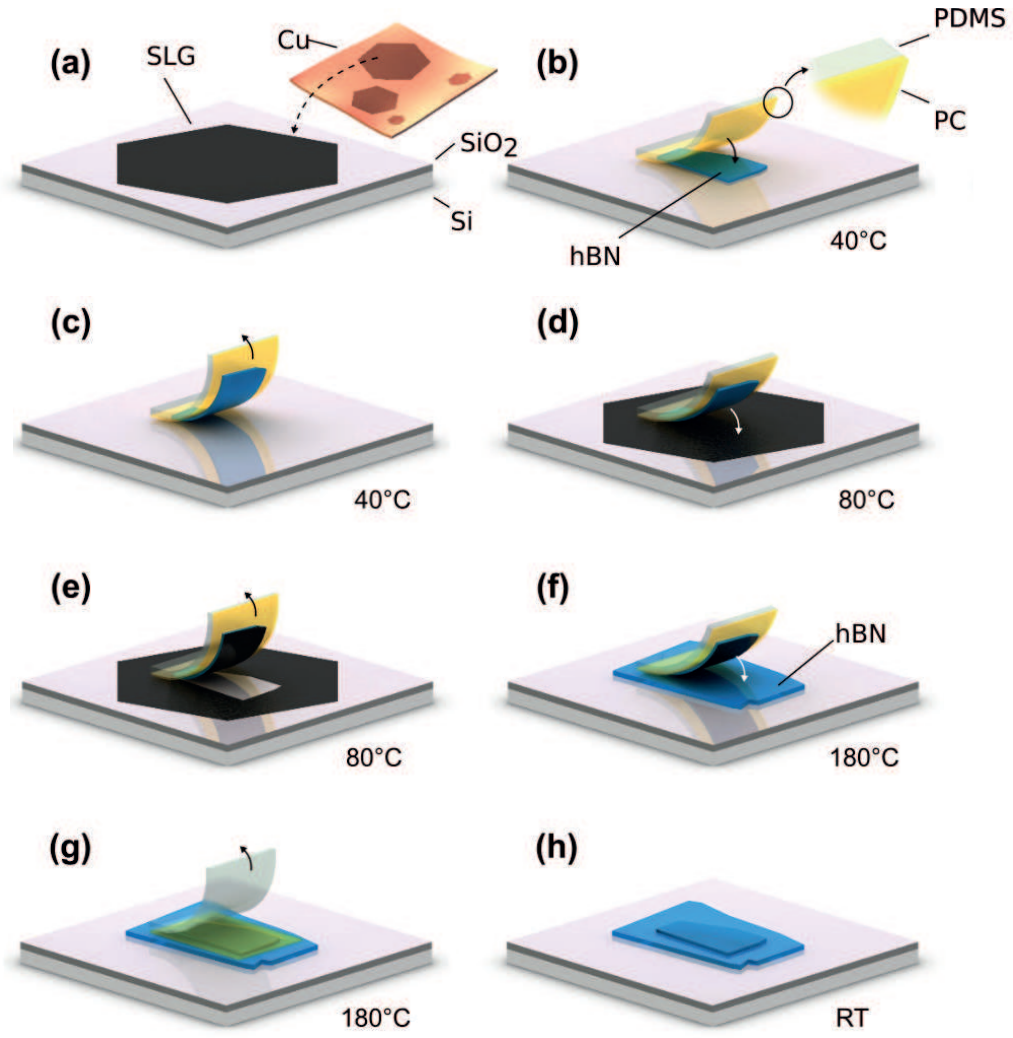

Figure 5.13: Depiction of the transfer processes used to assemble the encapsulated graphene heterostructures, involving first a wet transfer of graphene from the Cu growth foil onto SiO_2 (a), followed by encapsulation in h-BN using a hot-release technique (b)-(h).

h-BN is prepared via micro-mechanical cleavage from bulk crystals onto silicon (Si) substrates with 285nm SiO_2. The encapsulation of graphene within h-BN typically results in blisters containing trapped adsorbates and contaminants[110], which must be avoided during sample fabrication as they locally degrade transport properties[110]. It has recently been shown by Ref.[111] that it is possible to exclude contamination blisters by using a "hot pick-up/release" technique. This transfer method uses a raised temperature during encapsulation, above the glass transition temperature T_g, of the polymer stamp, allowing the interface of the layered materials to be brought together in a directional,

conformal manner. I have developed a similar process, but in contrast to Ref.[111], which uses a polypropylene carbonate (PPC) stamp ($T_g \sim 40°$), here polycarbonate (PC) was used, for which T_g is $\sim$ 150°C. The encapsulation temperature is T ~180°C. Here it is worth noting that using this transfer process to encapsulate mechanically exfoliated graphene in h-BN enables us to produce blister free material over the entire sample dimensions, with areas over 1000μm^2 achievable, limited only by the size of the exfoliated flakes.

The utilized transfer stamp consists of a film of PC mounted on a polydimethylsiloxane (PDMS) block for mechanical support, which in turn is placed on a glass slide attached to a micro-manipulator, enabling fine spatial control in x,y,z. The temperature of the sample is set using a heated stage. The complete transfer process is depicted in Fig.5.13. The transfer begins by positioning the stamp above a flake of h-BN, and then lowering it into contact, with the stage temperature set to 40°C. As the stamp is withdrawn the h-BN adheres to the surface of the PC, and is delaminated from the SiO_2 substrate (Fig.5.13(b-c)). The picked-up h-BN flake is then positioned above the wet transferred graphene and brought into contact at 80°C. After waiting for $\sim$ 5 minutes to promote adhesion between the h-BN and graphene, the stamp is lifted, picking up the portion of the SLG in contact with the h-BN (Fig.5.13 (d-e)). For the final stage of the transfer, in which the top h-BN/SLG is brought into contact with the bottom h-BN, a temperature of 180°C is used, and the stamp is carefully tilted to ensure that contact occurs first on one side, and then conformally advances across the substrate (Fig.5.13 (f)). At 180°C withdrawing the stamp releases the PC onto the substrate (Fig.5.13 (g)), which is dissolved by placing the sample in chloroform (Fig.5.13 (h)).

Fig.5.14(a) and Fig.5.14(b) show bright and dark field microscope images of the final h-BN/SLG/h-BN heterostructure. Scans of the heterostructure by atomic force microscopy (AFM) (Fig.5.14(c)) reveal that some blisters of contaminants are present in the heterostructure. They tend to aggregate in specific areas/lines, which could be attributed to residual wrinkles from the wet transfer.

Fig.5.15 shows representative Raman spectra of single crystals of SLG on Cu (red curve), then transferred on SiO_2/Si (blue curve), and encapsulated in h-BN (magenta curve). The spectrum on Cu is shown after subtraction of the Cu photoluminescence (PL)[173]. As a standard fingerprint of SLG graphene, the 2D peak is a single sharp Lorentzian with FWHM(2D)$\sim$27cm^{-1}. No D peak is observed indicating negligible defects [70, 77]. After wet transfer on SiO_2/Si, the 2D peak retains its single-Lorentzian lineshape with FWHM(2D)$\sim$30cm^{-1} and the D peak is still negligible indicating that no significant defects are induced by the wet transfer process. After the pick up and

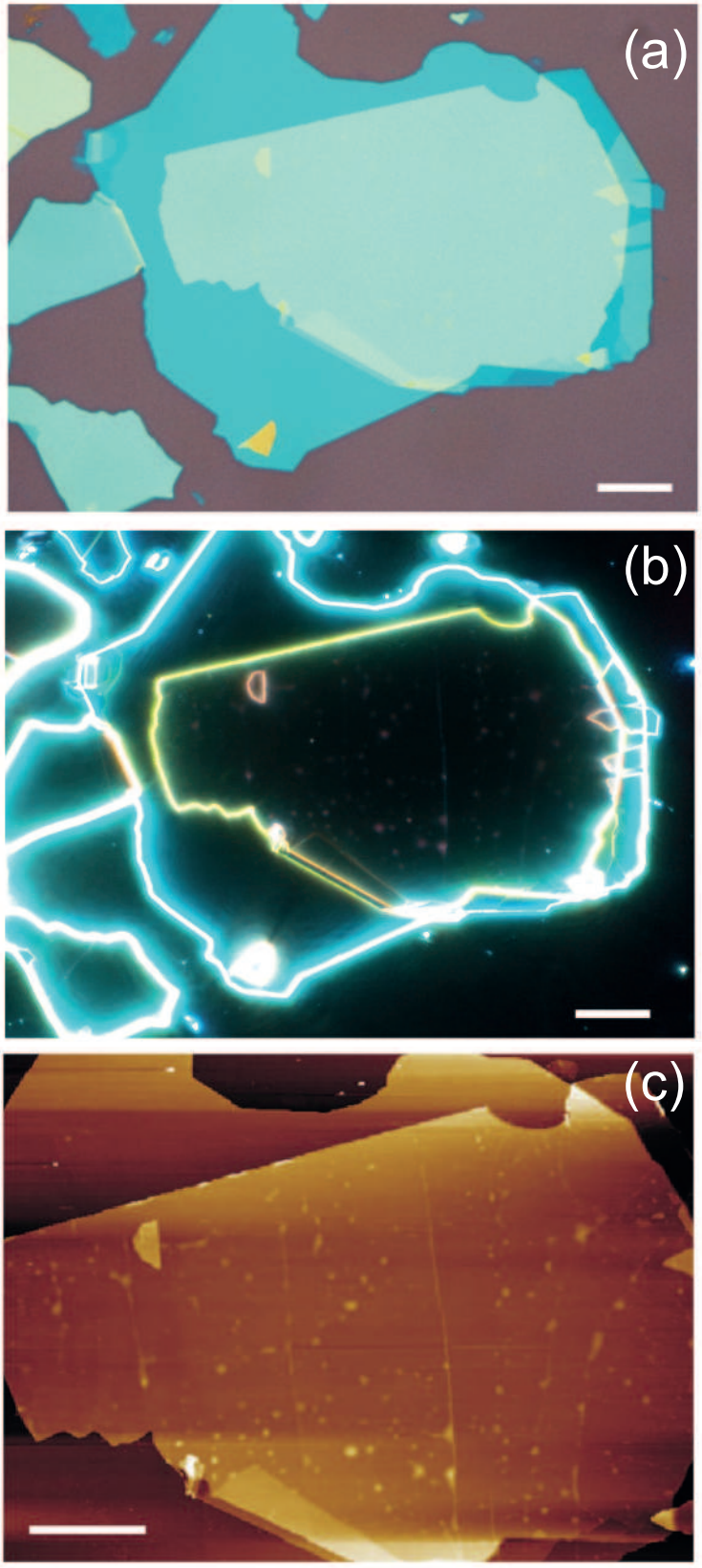

Figure 5.14: (a) Bright field, (b) dark field and (c) AFM image of a CVD graphene single crystal encapsulated in h-BN. Scale bars are 10μm.

encapsulation the 2D peak, now at $\sim$2693cm^{-1}, shows a FWHM(2D)$\sim$17cm^{-1}, similar to those obtained in Ref.[109] with all-dry transfer. Ref.[109] identified a narrow linewidth for the 2D peak as an hallmark sufficient (but not necessary) to expect high mobility from a specific sample; this is due to the FWHM(2D) being proportional to the amount of random strain fluctuations across the sample, which represent a dominant source of scattering[174]. The D peak is still negligible. Another key aspect is given by Pos(G) being $\sim$1583cm^{-1}, FWHM(G)$\sim$15cm^{-1}, and I(2D)/I(G) and A(2D)/A(G), being $\sim$14.8 and $\sim$15.3, respectively. These features all point toward a negligible doping <100meV[73, 76], which is expected for encapsulated graphene.

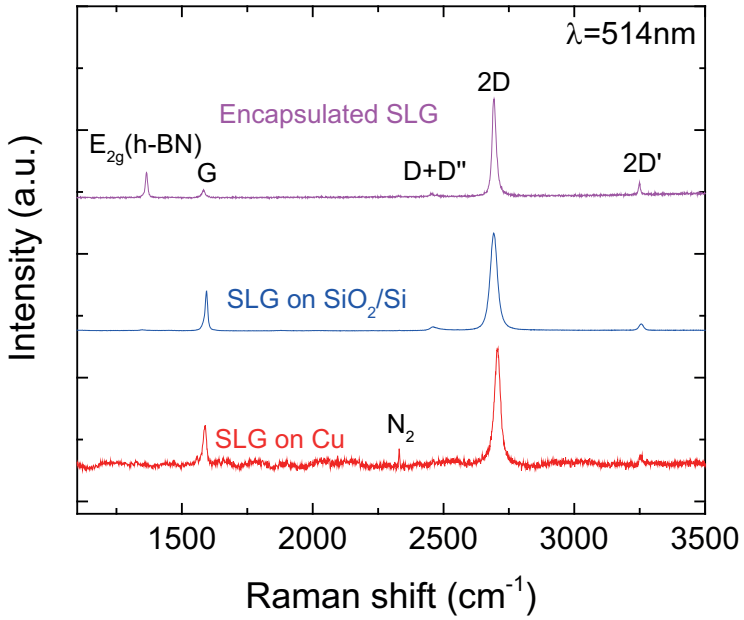

Figure 5.15: Raman spectra of SLG as grown on Cu (red curve), transferred on SiO_2 (blue curve) and after encapsulation by hot-release technique (magenta curve).

In order to probe the quality of these encapsulated CVD graphene heterostructures electrically I processed them into Hall-bar geometries to perform four terminal transport measurements. To form electrical contacts to the encapsulated graphene I followed the method of Ref.[107]: a portion of the heterostructure is first dry etched, exposing an edge of the graphene, onto which metal is then evaporated to achieve a "one-dimensional" or "side" contact. I etched the heterostructures in a reactive ion etcher (RIE) using a plasma formed from a mix of tetrafluoromethane (CF_4) and oxygen (O_2) (ratio 4:1) under a forward power of 20W. Metal contact leads are deposited by e-beam evaporation of 5/70 nm of chromium/gold (Cr/Au).

An optical image of one of the Hall bars is shown in the inset of Fig.5.16(a), with the extracted resistivity of the sample as a function of the back gate voltage V_{BG} shown in the main figure. The corresponding conductivity σ is shown in Fig.5.16(b). I first extracted a value for field effect mobility μ_{FE} by using Equation 4.24. C_{ox} $\sim$1.1·10^{-4}F/m^2 is estimated by the following equation:

$$C_{ox} = \left(\frac{1}{C_{\text{h-BN}}} + \frac{1}{C_{\text{SiO}_2}}\right)^{-1} = \left(\frac{t_{\text{h-BN}}}{\epsilon_0 \epsilon_{\text{h-BN}}} + \frac{t_{\text{SiO}_2}}{\epsilon_0 \epsilon_{\text{SiO}_2}}\right)^{-1} \tag{5.1}$$

where ϵ_0,$\epsilon_{\text{h-BN}}$ and ϵ_{SiO_2} are the permittivity of vacuum, the relative permittivity of h-BN and that of SiO_2, respectively; whereas $t_{\text{h-BN}}$ and t_{SiO_2} are the thickness of the bottom h-BN layer and the SiO_2 oxide layer, respectively. This yields peak values of μ_{FE} = 49 000 cm^{2}V^{-1}s^{-1} and 54 000 cm^{2}V^{-1}s^{-1} for electrons and holes respectively at T = 290K. I also calculated the density dependent Hall mobility for Fig.5.17(a) by using Equations 4.27 and 4.28, thus extracting n from Hall measurements. The peak μ_H at room temperature reaches $\sim$ 70 000 cm^{2}V^{-1}s^{-1} close to the neutrality point, while remaining above 30 000 cm^{2}V^{-1}s^{-1} even at densities n >1.5·10^{12}cm^{-2}. At T = 9K the peak μ_H exceeds 120 000 cm^{2}V^{-1}s^{-1}. μ_{FE} as a function of temperature is shown in Fig.5.17(b), reaching 86 000 cm^{2}V^{-1}s^{-1} at T = 9K.

Such mobility values are consistent with those reported for heterostructures formed from CVD grown graphene on h-BN substrates, but prepared by dry rather than wet stacking techniques [109, 175]. For example, CVD graphene encapsulated by dry transfer in h-BN, also measured in Hall bar geometries, was reported with a peak μ varying between 70 000 − 350 000cm^{2}V^{-1}s^{-1} at T = 1.6K [109]. The wet transfer method used in Ref.[171] enabled mobilities up to 50 000cm^{2}V^{-1}s^{-1}, but only at low temperature [171]. Furthermore the latter mobility is also a factor of $\sim$ 2.5 lower then the results presented here, in addition to requiring high temperature annealing to remove residuals.

In addition to their mobility, our sample exhibits further hallmarks associated with encapsulated graphene prepared using dry transfer techniques. From Fig.5.16(a), the sample is highly intrinsic [28, 107, 110] with the charge neutrality point occurring close to zero gate voltage, at $V_{CNP} = -1.8V$, indicating a doping of $\sim$ 1.2·10^{11}cm^{-2}. Furthermore, the resistivity peak of our sample is extremely narrow, with a FWHM of 1V at 9K.

In order to investigate the variation in mobility of our material a total of twenty-two individual Hall bar channels from five different heterostructures were fabricated and measured. The variation in μ_{FE} at RT between the different channels is shown in Fig.5.18, varying from a minimum of $\sim$ 10 000 cm^{2}V^{-1}s^{-1} up to a maximum of $\sim$ 55 000 cm^{2}V^{-1}s^{-1}.

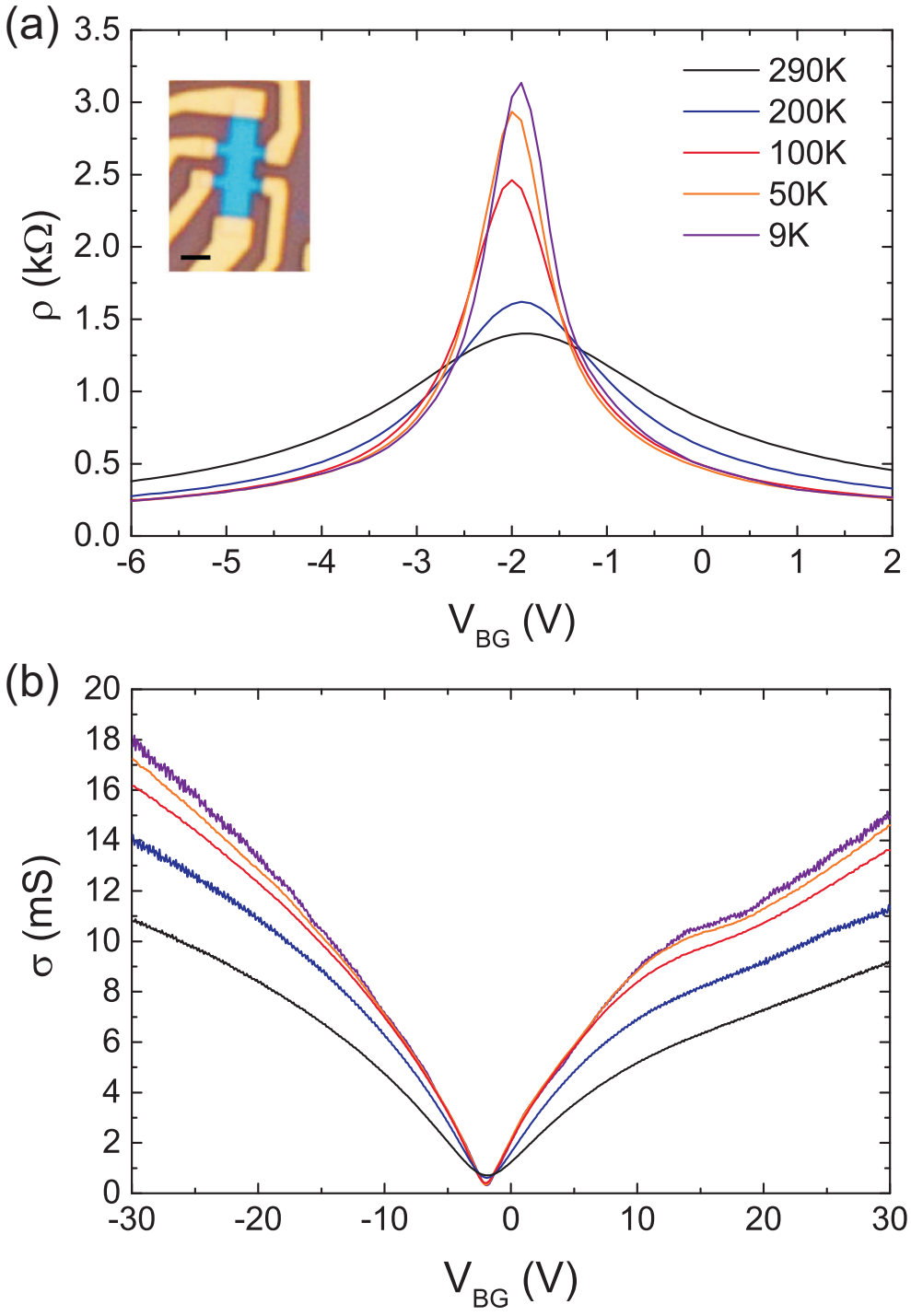

Figure 5.16: Electrical transport measurements of Hall bar geometries. (a) Extracted resistivity (ρ_{xx}) vs. gate voltage for a Hall bar measured at temperatures between $T = 9$K and 290K. Inset: an optical image of the device. The scale bar corresponds to 1.5μm. (b) Conductivity vs. gate voltage for the device shown in (a).

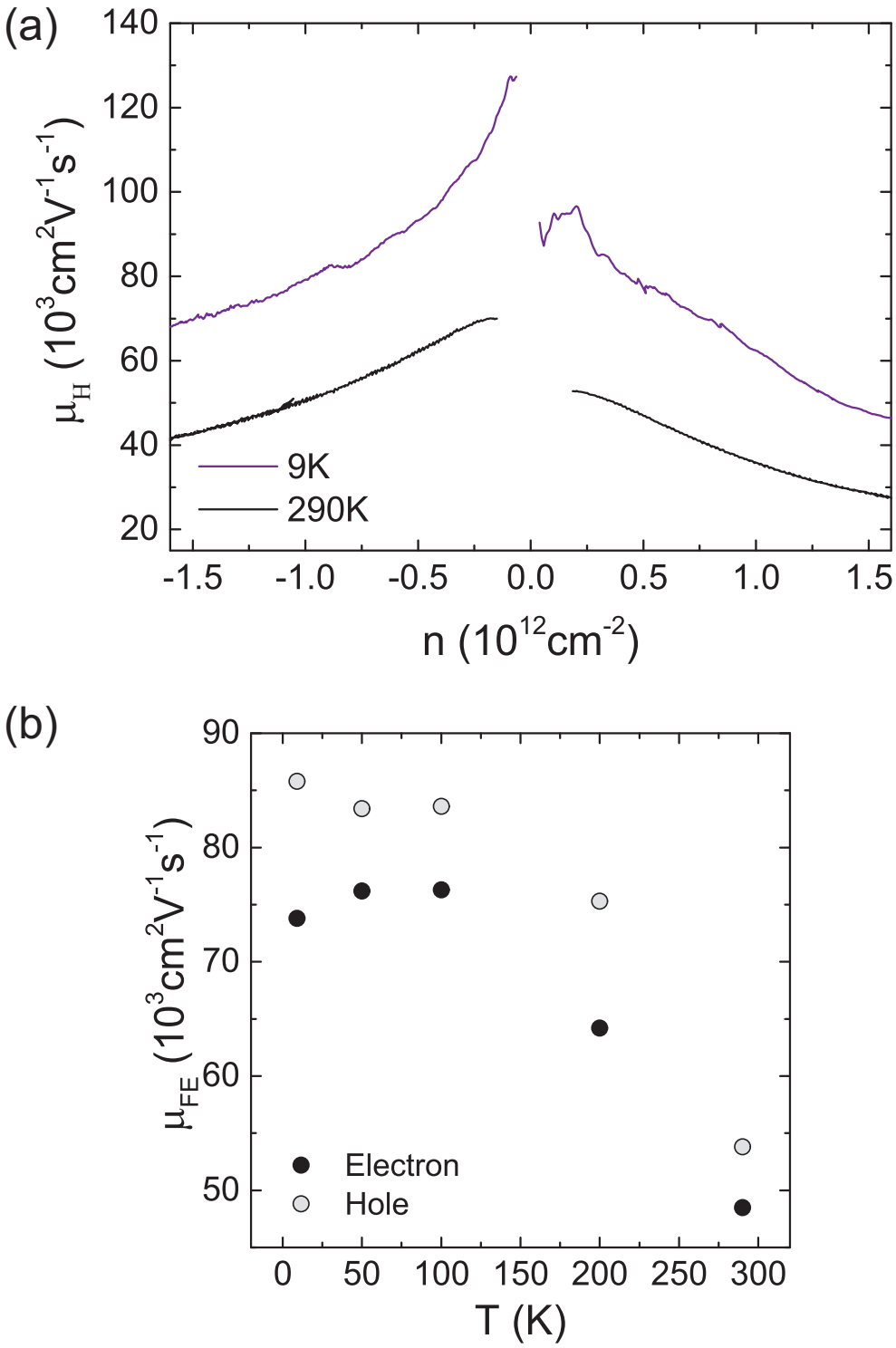

Figure 5.17: (a) Density dependent Hall mobility of the device in 5.16(a), extracted assuming the Drude model of conductivity $\mu = 1/ne$, and shown for $T = 9$K and 290K. (b) Field effect mobility vs. temperature for the device in 5.16(a).

A similar statistical analysis of exfoliated graphene encapsulated in h-BN prepared by dry stacking methods yielded mobilities in the range $15\,000 - 110\,000\,\mathrm{cm^2V^{-1}s^{-1}}$[111].

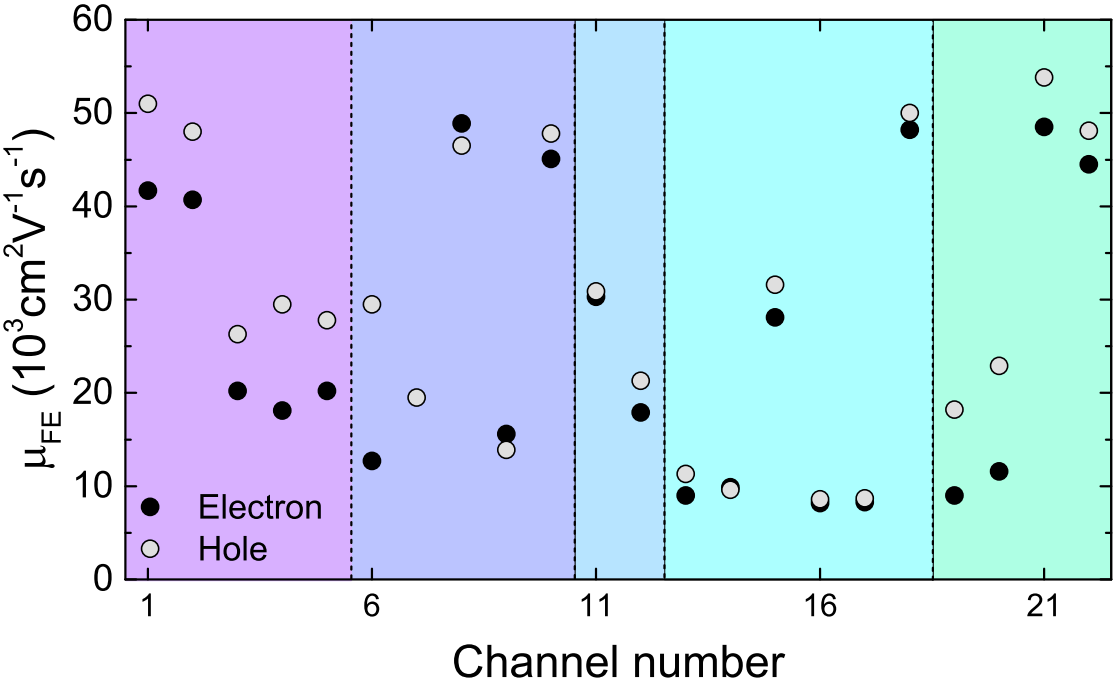

Figure 5.18: Field effect electron and hole peak mobilities extracted from twenty-two different Hall bar channels. The five shaded regions (S1-S5) correspond to devices fabricated from five different heterostructures.

Fig.5.19 shows representative data of samples fabricated from CVD-grown polycrystalline graphene for comparison with single crystals. Fig.5.19(a) is an optical image of h-BN/polycrystalline-SLG/h-BN heterostructure. Detaching polycrystalline from SiO_2 with h-BN was more challenging and temperature had to be raised from $T = 80°C$ to $T = 180°C$ in the pick up step. The resistivity of a sample as a function of the back gate voltage V_{BG} is shown in 5.19(c). The field effect mobility is extracted again by using Eq.2.24 close to the charge neutrality point (CNP) at $V_{BG} \sim 4V$[13]. I calculated a mobility of $\mu_{FE} = 7\,000\,\mathrm{cm^2V^{-1}s^{-1}}$ and $5\,000\,\mathrm{cm^2V^{-1}s^{-1}}$ for electrons and holes respectively at $T = 290K$. It has to be mentioned that the "bump" in the resistivity vs V_{BG} at $V_{BG} \sim -8V$ suggests the presence of an additional neutrality point in the graphene channel, indicating inhomogeneous doping across the sample[176].

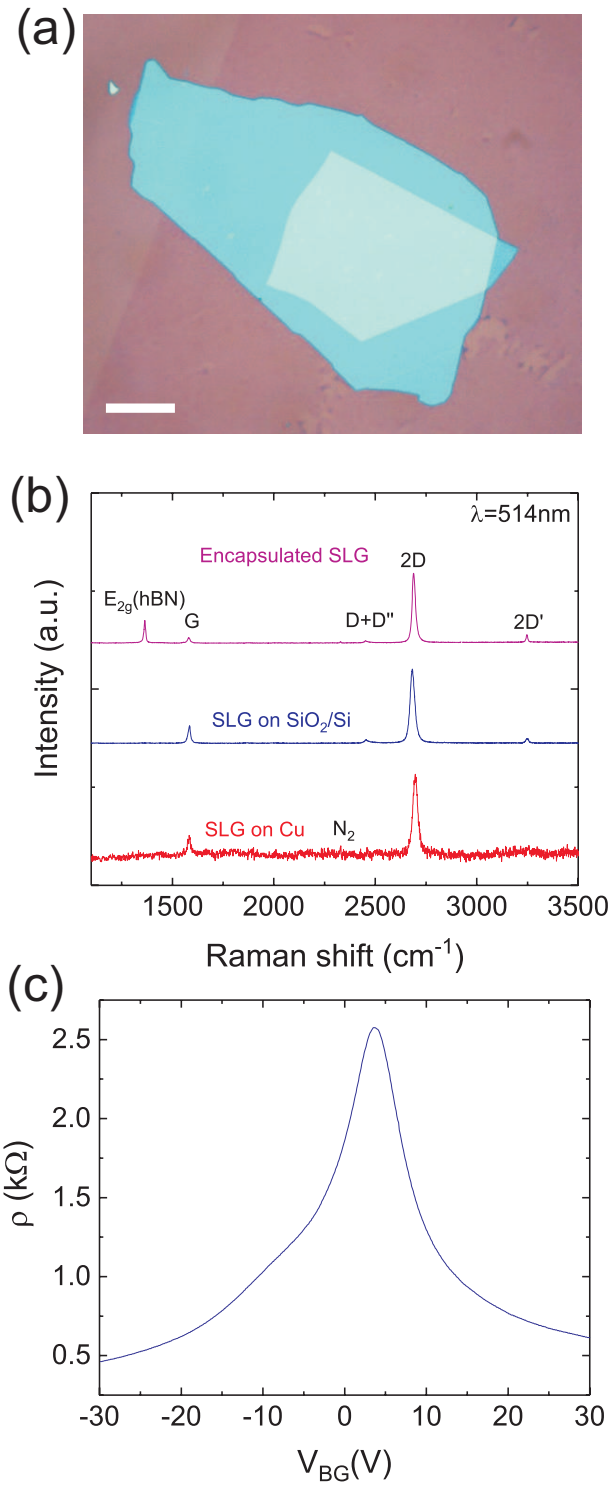

Figure 5.19: (a) Optical image of an encapsulated polycrystallyne graphene sample. Scale bar is 10μm. (b) Representative Raman spectrum of polycrystalline graphene as grown on Cu, whereby the PL of Cu has been removed (red curve), Raman spectrum of polycrystalline graphene when wet transferred on SiO_2/Si (blue curve) and final spectrum of the sample encapsulated in h-BN (magenta curve). (c) Electrical transport measurement of resistivity vs gate voltage in a Hall bar geometry at 290K.

5.6 Growth of MoS_2 by CVD

1L-MoS_2 for this dissertation was grown at Ecole Polytechnique Federale de Lausanne (EPFL) in the group of Prof. Andras Kis by CVD on sapphire substrates using solid precursors as discussed in Ref.[103]. In short, sapphire substrates are annealed at 1000°C in air for 1 hour after cleaning by acetone, isopropyl alcohol and deionized (DI) water. They are then placed face-down above a crucible containing ~5mg MoO_3 (≥99.998% purity). This is loaded into a 32mm outer diameter quartz tube placed in the growth furnace. A second crucible containing 350mg sulfur (≥ 99.99% purity) is located upstream from the growth substrates. Ultrahigh-purity argon (Ar) is used as carrier gas at atmospheric pressure. Temperature is ramped to 300°C with 200sccm Ar flow, then it is hold constant to 300°C for 10 minutes. It is then ramped to 700°C at an increased ramp rate of 50°C/min with 10sccm Ar flow. Temperature is then kept constant at 700°C for 10 minutes, followed by a first cooling step to 570°C with 10sccm of Ar and a final rapid cooling down performed by increasing the gas flow to 200sccm and opening of the furnace[103, 177].

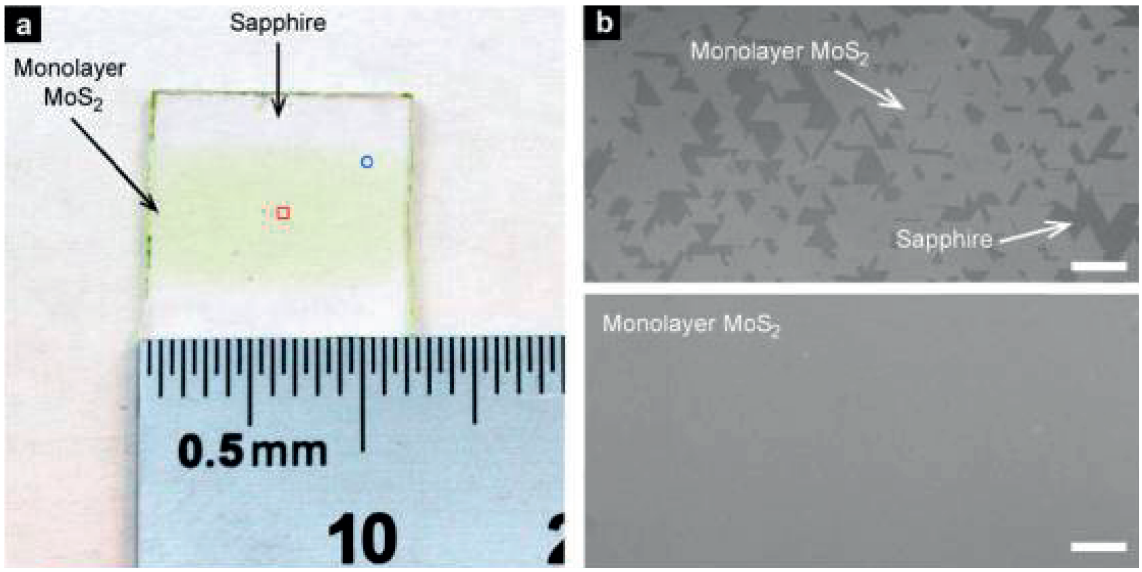

Figure 5.20: (a) Picture of a MoS_2 film grown by CVD on sapphire. (b) Magnification of a central and side area. 1L-MoS_2 crystals merge in the central area to form a uniform poly-crystalline film. At the edges stitching does not occur and it is possible to observe the typical MoS_2 crystal triangular shape. Scale bar is 20μm. Taken from Ref.[103].

This growth recipe yields large area uniform 1L-MoS_2 films as shown in Fig.5.20. I characterized these films by Raman and PL and the results are shown in Fig.5.21. The laser power is kept below 100μW (spot size < 1μm in diameter) to avoid possible heating

effects or damage. Fig.5.21(a) plots the Raman spectrum of CVD MoS_2 on sapphire for 514nm excitation. The two characteristic peaks of MoS_2 are present, with the in-plane E^1_{2g} mode at$\sim$ 385cm^{-1} and the out of plane A_{1g} mode at$\sim$404cm^{-1}[81, 82]. They possess a FWHM(E^1_{2g})=2.5 and FWHM(A_{1g})=3.6cm^{-1}, respectively. As shown in Chapter 2, the E^1_{2g} mode softens, whereas the A_{1g} stiffens with increasing layer thickness, so that their frequency difference can be used to monitor the number of layers[83, 178]. Here the peak position difference of $\sim$20cm^{-1} is an indicator of 1L-MoS_2[83]. The peak at$\sim$ 417cm^{-1}, marked by asterisk in Fig.5.21(a), corresponds to the A_{1g} mode of sapphire[179].

Another evidence for 1L-MoS_2 comes from the PL spectrum in Fig.5.21(b), showing a strong A excitonic peak at $\sim$658nm ($\sim$1.88eV), due to band-to-band radiative recombination in 1L-MoS_2[32]. The B exciton is at $\sim$610nm ($\sim$2.03eV).

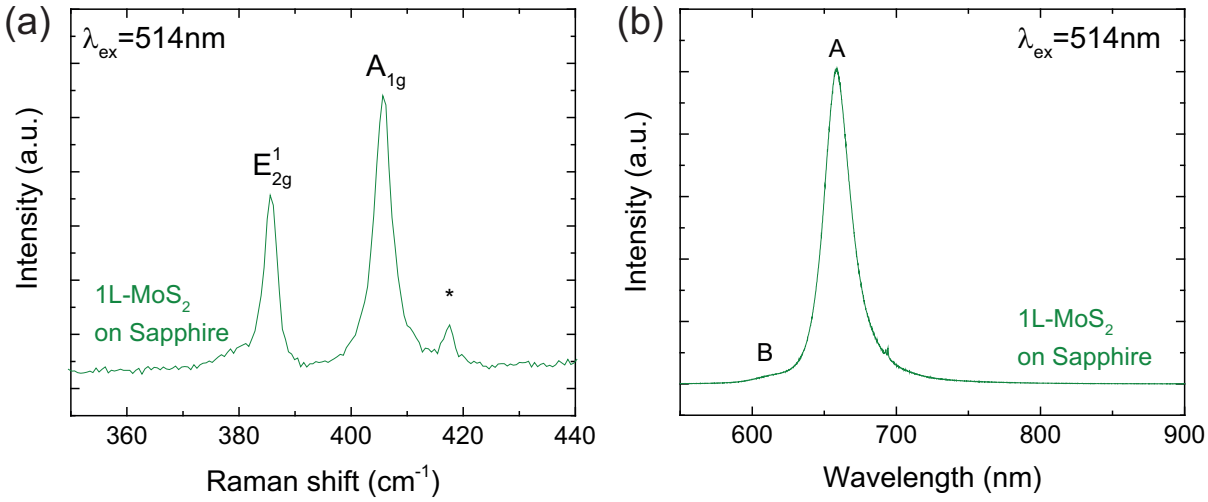

Figure 5.21: (a) Raman and (b) PL spectra of 1L-MoS_2 grown by CVD on sapphire.

5.7 Wet transfer of MoS_2 on arbitrary substrates

In order to transfer MoS_2 from sapphire to arbitrary substrates a wet transfer procedure was adopted as for Ref.[103]. A layer of PMMA is spin coated on the MoS_2/sapphire sample. The PMMA is soft-baked at 120°C for 20 minutes or left overnight in a desiccator to let the solvent evaporate. The edges of the sapphire substrate are scratched to create a frame around the sample area to be transferred by means of a cutter. A 30% (in weight) potassium hydroxide (KOH) aqueous solution is prepared. The sample is dipped in the solution, which is then transferred to a hot plate at about 70°C to promote the etching reaction: the chemical formula of sapphire is α-aluminium

oxide (α-Al_2O_3), which is etched by KOH. After 30 minutes the PMMA/MoS_2/sapphire sample of the solution and slowly re-immersed into it with a tilt angle of 70°/80° with respect to the water surface, to help the PMMA membrane with 1L-MoS_2 detaching from the sapphire substrate. If this does not happen the etching is prolonged for further 15 minutes and the temperature is increased in steps of about 10°C. Once the membrane is floating at the surface of the solution, it can be lifted with a PET carrier substrate, washed approximately three times in water beakers and finally lifted with the target substrate. The target substrate (e.g. SiO_2/Si) can be cleaned with a O_2 plasma treatment or just immersed in the same KOH solution to smooth the surface. Characterization by Raman and PL can now be performed again. However, conversely to the case of SLG, in 1L-MoS_2 there are no evident peaks activated by defects, therefore detection of changes in the film properties is much more challenging.

If the target substrate of the transfer is SiO_2/Si, I found that a re-transfer of the 1L-MoS_2 film can be performed with relative simplicity and without the need of wet etching. I indeed used a water-based method similar to that discussed in the Section 3.3.1. A PMMA layer can be spin coated on top of 1L-MoS_2/SiO_2/Si. The sample is then immersed in water and placed in an hot plate at 90°C for 1 hour. Water intercalates at the PMMA/1L-MoS_2 - SiO_2 interface due to capillarity. The PMMA/1L-MoS_2 can then be slowly peeled off the substrate with tweezers and lifted with the new target substrate.

5.8 Fabrication of graphene/MoS_2 heterostructures

The assembly of graphene/MoS_2 heterostructures required the use of most of the growth and transfer techniques described in this chapter[177]. The fabrication of the heterostructure starts with growth of CVD SLG on Cu and CVD 1L-MoS_2 on sapphire. MoS_2 is then wet transferred to a PET substrate and SLG is transferred on top of it to form the heterostructure.

Raman and PL characterizations are performed at each step of the SLG/1L-MoS_2 assembly on PET, *i.e.* on 1L-MoS_2 transferred on PET, and on SLG on 1L-MoS_2[177]. This is to confirm that no degradation occurred during the fabrication process. A summary of the Raman data is shown in Fig.5.22[177]. In the panel (c) full spectra are shown; however the presence of several peaks originating from the PET substrate make a clean analysis impossible, especially for graphene[180]. Close ups are thus shown in the panels (a) and (b), specifically addressing regions of prominent peaks from 1L-MoS_2 and SLG. For 1L-MoS_2 on PET (red curve) and also after SLG transfer on top, the frequency

difference between E^1_{2g} and A_{1g} and the FWHM of the peaks are preserved, suggesting no degradation.

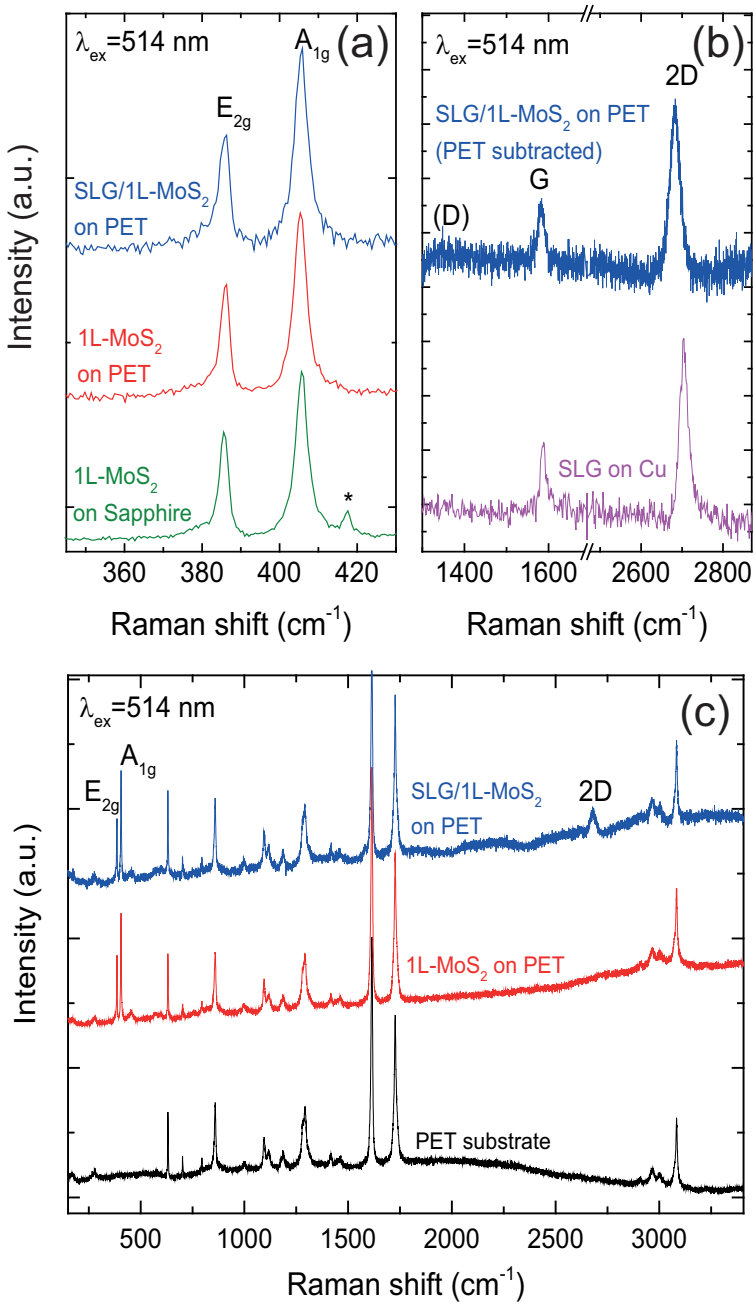

Figure 5.22: (a) Raman spectra at 514nm for 1L-MoS_2 on sapphire, 1L-MoS_2 on PET, and SLG/1L-MoS_2 on PET. (b) Comparison at 514nm of the Raman spectra of as-grown SLG on Cu (magenta curve) with SLG/1L-MoS_2 after transfer on PET. (c) Raman spectra at 514nm of PET substrate (black curve), 1L-MoS_2 on PET (red curve) and SLG/1L-MoS_2 on PET (blue curve).

For SLG, again a point-to-point subtraction is implemented, normalizing the spectra to the intensity of the PET peak at∼1615cm^{-1} The result is in Fig.5.22(b) (blue curve). The 2D peak retains its single-Lorentzian line-shape with FWHM(2D)∼28cm^{-1}, validating the transfer of SLG. The negligible D peak indicates that no significant defects are induced during transfer. Doping can be estimated by analysing the position and linewidth of the G and 2D peaks and the empirical curves in Refs.[76] and [73]. Pos(G) is∼1583cm^{-1}, FWHM(G)∼17cm^{-1}, Pos(2D)∼2683cm^{-1} and A(2D)/A(G)∼4.8, indicating a *p*-doping∼4·10^{12}cm^{-2} (∼250meV)[73, 76].

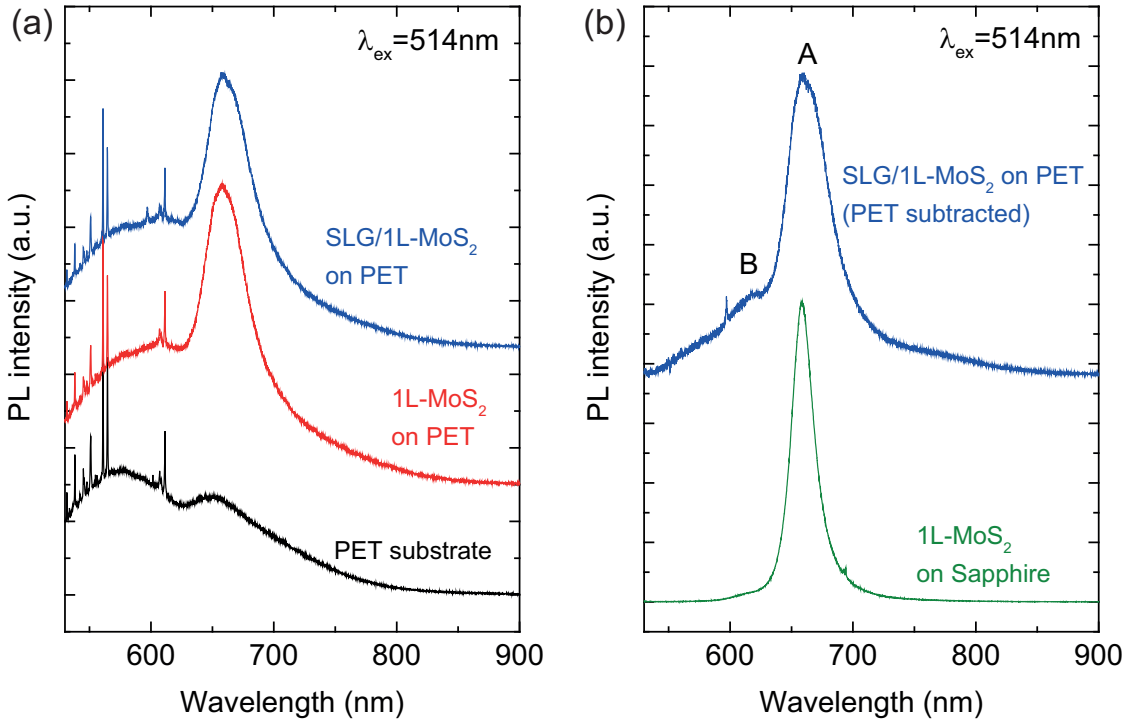

Figure 5.23: (a) PL spectrum at 514nm (2.41eV) of 1L-MoS_2 on sapphire, and SLG/1L-MoS_2 after transfer on PET. (b) PL spectra of PET substrate (black curve), 1L-MoS_2 on PET (red curve) and SLG/1L-MoS_2 on PET (blue curve).

The PL spectrum of 1L-MoS_2 on PET is shown in Fig.5.23(a) (red curve) and no significant changes are registered with SLG on top (blue curve). The signal from 1L-MoS_2 is convolved within the background due to the PET substrate (black curve) and can be revealed by subtraction, upon normalization to the intensity of the Raman peak at∼1615cm^{-1}, corresponding to the peak at∼560nm in Fig.5.23(a). As a result, the PL signal of 1L-MoS_2 can be seen in Fig.5.23(b), showing similar excitonic peak shape and positions to those observed on the sapphire substrate (green curve).

In order to estimate the R_{int} of the photodetector made with a SLG/1L-MoS_2 stack a further characterization step is needed, represented by the absorption spectroscopy. I then measured the absorption and transmission of SLG/1L-MoS_2 using broadband (400-1300nm) white light from a tungsten halogen lamp. The transmitted light is collected by a 10x objective lens with a spectrometer equipped with a 300 grooves/mm grating and a detector. Fig.5.24(a) plots the optical transmittance of bare PET (T_{PET}, black line), 1L-MoS_2 on PET (T_{MoS_2}, red line) and the final SLG/1L-MoS_2 stack on PET (T_{Hetero}, blue line) measured in the 400-800nm wavelength range. Fig.5.24(b) plots the absorption of 1L-MoS_2 on PET (A_{MoS_2}, red line) and of SLG/1L-MoS_2 on PET (A_{Hetero}, blue line). This is calculated applying Eq.2.23 to the present case to give:

$$A_{MoS_2} = \frac{T_{PET} - T_{MoS_2}}{T_{PET}} \qquad A_{Hetero} = \frac{T_{PET} - T_{Hetero}}{T_{PET}} \tag{5.2}$$

The three peaks in Fig.5.24(b) at ∼650nm (1.91eV), ∼603nm (2.06eV), and ∼428nm (2.90eV) correspond to the A, B, C excitons of 1L-MoS_2[32, 181]. The positions of the A, B and C peaks remain unchanged after SLG transfer. The offset difference between the two curves (red and blue) is ∼2.6%, consistent with the additional SLG absorption in this wavelength range[23].

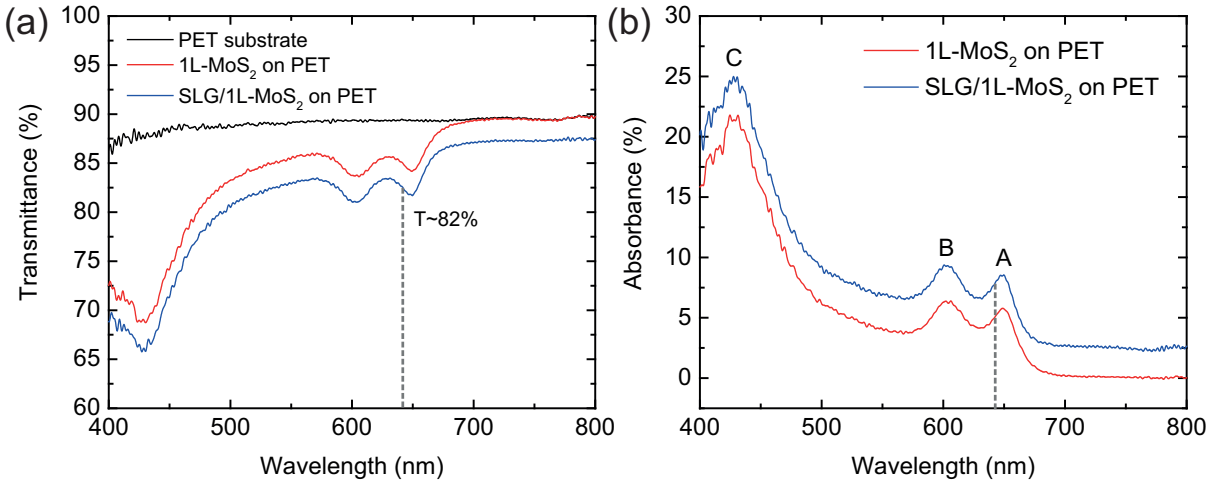

Figure 5.24: (a) Transmittance of PET (black curve), 1L-MoS_2 on PET (red curve) and SLG/1L-MoS_2 on PET (blue curve). (b) Absorbance of 1L-MoS_2 and SLG/1L-MoS_2 as derived from the transmittance measurements. Dashed lines indicate our test wavelength.

5.9 Conclusions

In this chapter the techniques I used to prepare materials for optoelectronic devices are shown. Graphene, MoS_2, $NbSe_2$ and h-BN can be prepared by micro-mechanical cleavage. Graphene and 1L-MoS_2 are also grown by CVD on Cu and on sapphire, respectively. I used mainly wet methods to transfer graphene and MoS_2 from the grown substrate to arbitrary target substrates. I demonstrated that encapsulation of single crystals of CVD graphene by a wet method can yield mobilities comparable to those obtained with dry methods and not far from those obtained with exfoliated samples. I also fabricated a graphene/MoS_2 heterostructure by sequential wet transfer of the two grown films. I characterized all the as-synthesized and transferred materials by Raman spectroscopy and, when needed, also by PL and absorption spectroscopy.

Chapter 6

Graphene-Silicon Schottky Photodetectors

6.1 Introduction

Near infrared (NIR) photodetection at 1550nm is of paramount importance for a variety of applications. These are not limited only to the already-cited optical communications[182–185], but can also span also the fields of imaging[186] and sensing[187, 188]. In modern telecom systems, operation at 1550nm benefits from a reduced light absorption in optical fibers[182].

Many photodetectors (PDs) for 1550nm have been proposed[1, 182, 189, 190]. For telecommunication and data transfer applications, light is guided on chip and photodetector geometries typically rely on a waveguide configurations[191–200]. Here optical confinement contributes to enhanced light absorption and photodetection. On the other hand, for other applications such as free-space optical communication (FSO), light radar (LIDAR) or medical imaging, NIR PDs for free-space illumination are required[183–188].

At present, III-V compound (*e.g.* indium gallium arsenide (InGaAs) or indium phosphide (InP))[201, 202] and germanium (Ge)[191–194] semiconductors are the materials of choice for vertically-illuminated NIR PDs, due to their high (>90%)[1] NIR absorption. The ever growing demands for miniaturization of photonic components and development of photonic integrated circuits make the integration of PDs with on chip silicon technologies crucial[1, 182]. Since modern microelectronics relies on mature complementary metal-oxide-semiconductor (CMOS) technology, the development of NIR PDs on Si is promising for integrated microsystems, combining both optical and electronic functionalities. III-V materials are not compatible with standard CMOS fabrication processes because of cross-contamination and dopant redistribution effects[3], and are

typically manufactured in separate facilities[3]. Epitaxially grown Ge on Si provides a competitive platform to InGaAs and InP based NIR photodetection[193, 203, 204]. Nevertheless, due to defects[3] and dislocations-like recombination centers at the Si-Ge interface[193, 203, 204], these PDs typically show larger leakage current[204] compared to III-V devices, resulting in increased noise[193]. To reduce the defects density, a two-step Ge deposition is commonly used[193, 203, 204], however it involves high (>650°C) temperature processes, which sacrifice the "thermal budget"[204].

An alternative and promising approach for monolithic integration of NIR PDs with silicon technologies is to perform sub-bandgap photodetection in Si exploiting the internal photoemission process (IPE) in a Schottky junction as shown in Fig.4.3[1, 205–207]. In short, photoexcited carriers from the metal electrode can be emitted into Si over the Schottky barrier $q\Phi_B$, allowing NIR detection for photon energy $h\nu > q\Phi_B$[1, 205, 206]. The advantages of the Schottky junction configuration over other PD types stem from its simple structure[1], easy fabrication and possibility of integration with silicon technology[1]. One of the main drawbacks is the limited ($< 1\%$)[208, 209] internal quantum efficiency (IQE) of the IPE process, in this case related to the the number of carriers emitted into Si per absorbed photon. As a result, limited IQE leads to limited responsivity, so that the highest R_{ext} reported so far in vertically-illuminated Si Schottky PDs operating at 1550nm is$\sim$5mA/W[210], much lower than the 0.5-0.9A/W for III-V[1] and Ge[1] based PDs.

Graphene photodetectors at 1550nm were first obtained with metal-graphene-metal (MGM) configurations and responsivities R_{ext} up to 10mA/W[128, 211]. The low responsivity is due to weak absorption of graphene ($\sim$2.3% at 1550nm) and limited active area in proximity to the electrodes[128].

On a different note, the interface between Graphene and Si provides a Schottky junction which can be exploited to absorb NIR photons with energy below the Si bandgap[118, 211, 212]. Fig.6.1 depicts the photodetection mechanisms in SLG/Si interfaces, assuming p-doped graphene and n-doped Si. At photon energies greater than the silicon bandgap E_{BG} the internal photo-emission from graphene to Si competes with interband absorption in Si, with the latter dominating between the two. At energies below E_{BG} but greater than the Schottky barrier $q\Phi_B$ (*e.g.* $h\nu$=0.8eV$\rightarrow$ λ=1550nm), interband absorption in Si is negligible and internal photo-emission from SLG to Si dominates.

Nonetheless the limit of graphene absorption still needs to be overcome. In this chapter I show three different approaches to tackle the necessity to enhance absorption in Graphene/Si PDs at 1550nm, two for vertical illuminations (free space) and one for

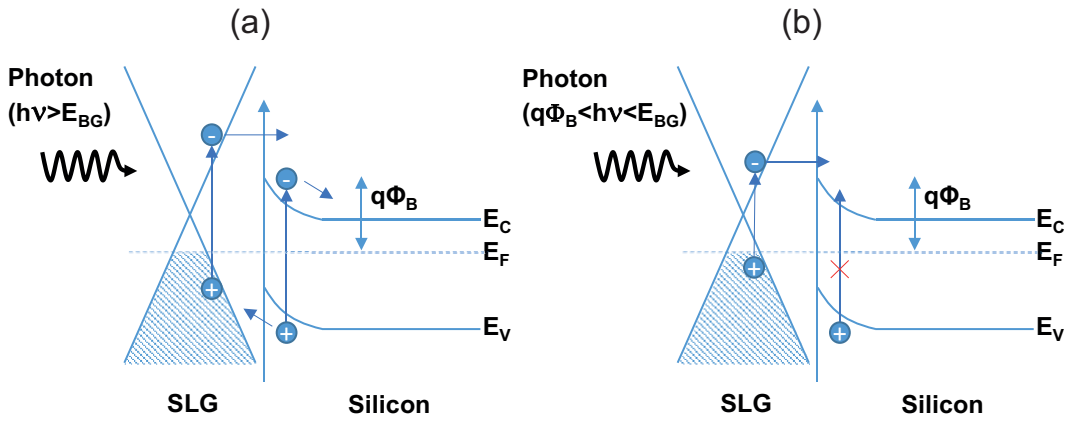

Figure 6.1: Schematic illustration of photodetection mechanisms in a SLG/Si Schottky junction illuminated by photons with energy (a) $h\nu > E_{BG}$ and (b) $q\Phi_B < h\nu < E_{BG}$

on chip applications. These results have lead to three manuscripts, two of which are published in Refs.[213, 214] and one is now in preparation.

6.2 Resonant cavity enhanced graphene-silicon Schottky photodetectors

The first approach used to enhance the absorption of graphene in vertical illuminated graphene/Si Schottky PD is by combining a Schottky junction with an optical Fabry-Perot (F-P) cavity to enhance light interaction and absorption at the SLG/Si interface. I will refer to this PD as RCE-PD (resonant-cavity enhanced photodetector). A F-P cavity is formed by two reflecting surfaces facing each other at the two ends of a medium of refractive index n. Light coupled with the resonator undergoes multiple reflections, suffering from amplitude reduction in each round trip. With L being the cavity length, the spectral response of the device made out of the F-P cavity typically shows resonance peaks at frequencies spaced by a factor $c/(\mathrm{n}\cdot 2L)$, *i.e.* the inverse of the time needed for a round trip[2]. Here I show that the PD responsivity peaks coincides with F-P resonances, with R_{ext} increasing with the number of light round trips inside the cavity. Taking advantage of multiple light reflections at resonance, a spectrally-selective photoresponse with maximum R_{ext} ~20mA/W is obtained.

The two examples of vertically illuminated Schottky PD share a similar fabrication process line. Here I will describe the fabrication steps for the RCE-PD and in the next section I will only highlight the differences with the avalanche PD. The fabrication process is presented in Fig.6.2. The RCE-PDs are fabricated on double-polished, low-doped

($\sim 10^{15}$cm^{-3}), 200μm thick Si substrates to minimize free carrier absorption in the F-P cavity. The substrates are also cleaned by immersion in acetone and isopropyl alcohol, followed by a Piranha cleaning solution, *i.e.* a mixture 4:1 of sulphuric acid (H_2SO_4) and hydrogen peroxide (H_2O_2). A 100nm-thick layer of SiO_2 is deposited on the Si substrate by e-beam evaporation.

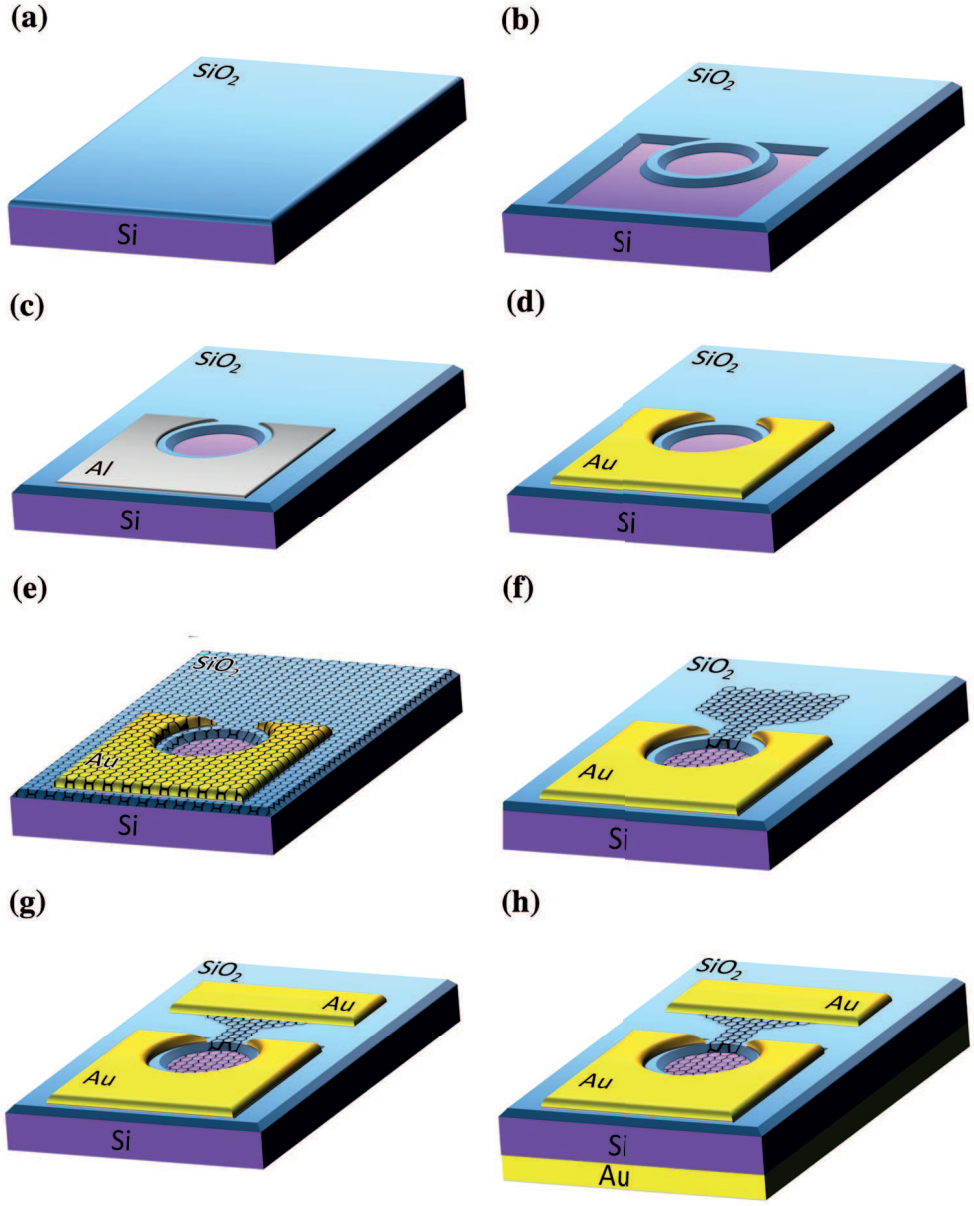

Figure 6.2: Fabrication process of RCE Si-SLG Schottky PD. (a) SiO_2 layer deposition. (b) Schottky and Ohmic contacts area definition. (c) Al ohmic contact formation. (d) Au protection layer deposition. (e) SLG transfer. (f) SLG shaping. (g) Au contact to SLG deposition. (h) Au Back mirror deposition.

Next, the SiO_2 is patterned with a shape as for Fig.6.2(b) by optical lithography using a laser-writer (photoresist mask S1805). After defining the mask, the sample is baked at 120°C for 2 minutes and the oxide is then wet etched in a buffer-oxide-etch (BOE) solution. In the following step, Al ohmic contacts to the p-type Si are realized by an additional lithography step, evaporation of a ∼120nm Al layer, lift-off and thermal treatment (alloying) at 460°C for 30min in a forming gas (5.7% H_2 in N_2). Before evaporation the native Si oxide is removed by dipping again the sample in BOE for 10 seconds. To protect the Al pads from subsequent treatments involving BOE, an additional Au layer is fabricated on top of Al using optical lithography, Cr/Au (3nm/50nm) evaporation and lift-off. CVD graphene is then grown by CVD and transferred on the structure as discussed in Sections 5.3 and 5.4. In order to ensure a contact between graphene and silicon in the central circular area, the formation of native Si oxide is hindered by performing the last transfer step, involving the lifting of the PMMA/SLG stack, in a solution of (very) diluted hydrofluoric acid (HF) in water (2mL HF in 400mL deionized water). The photoactive area of graphene in Fig.6.2(h) is defined by another laser-writer lithography, followed by a 20W oxygen (O_2) plasma treatment for 20 seconds at 200mTorr to remove SLG from unwanted areas. A final laser-writer lithography is performed to make a Cr/Au contact (3nm/50nm) on SLG. The back metal mirror is then fabricated by simply evaporating a film of Cr/Au (3nm/100nm) on the back side.

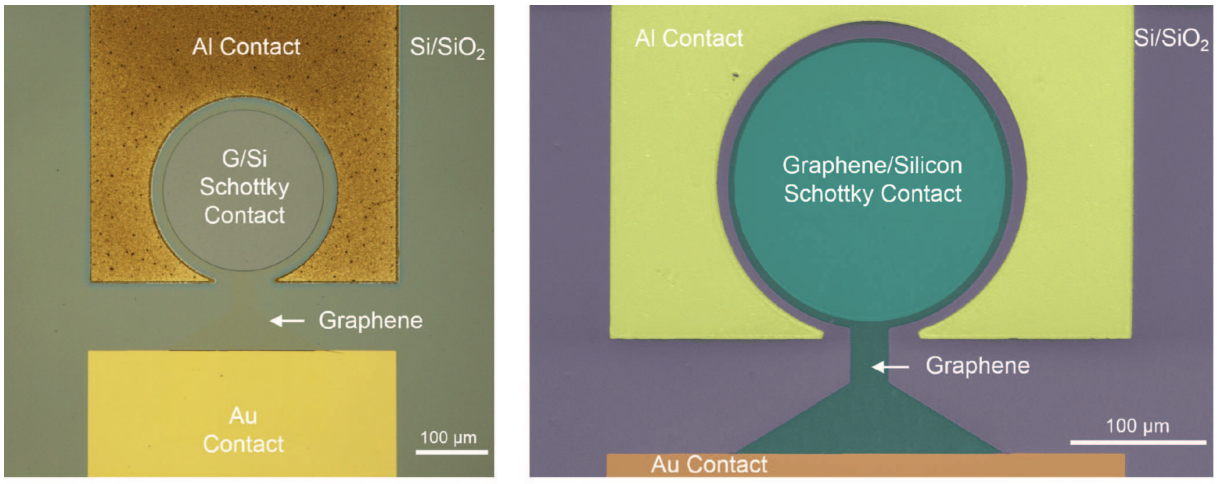

Figure 6.3: (a) Optical image of vertically illuminated graphene/Si Schottky PD and (b) false-colour SEM image, also highlighting the area of SLG.

Raman characterization of SLG on Si substrates has been shown in Section 5.4. Raman maps at 514nm of the G and 2D peak intensities over the circular area show

uniform coverage of SLG (Fig.6.4). These have been collected by selecting a grid of points with steps along x and y of 5μm.

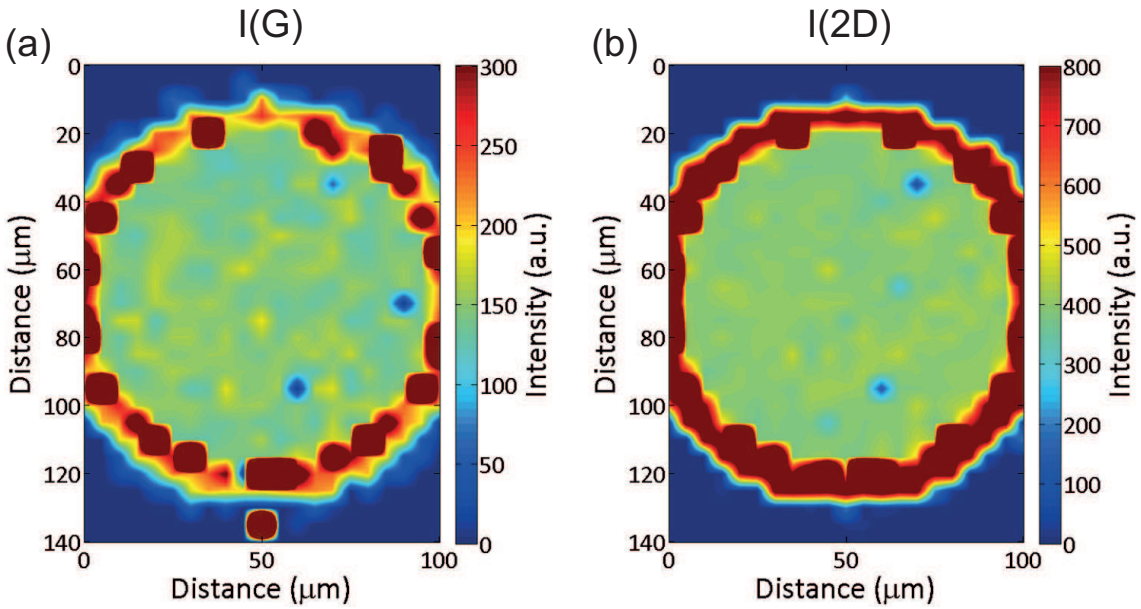

Figure 6.4: Raman maps of (a) G peak intensity (I(G)) and (b) 2D peak intensity (I(2D)) of a vertically-illuminated Graphene-Si Schottky PD. Excitation wavelength is λ=514nm

The resonant structure consists of a $\lambda/2$ Si slab layer confined between SLG/Si top and Au bottom mirrors. When vertically-illuminated at resonance, light circulates inside the cavity leading to increased absorption at the SLG/Si interface, resulting in enhanced internal photoemission (IPE) from SLG to Si.

To electrically characterize the PD, the current-voltage (I-V) characteristics of the SLG/Si Schottky junction is first measured, Fig.6.5(a). The device shows rectifying I-V diode behavior, which follows the Schottky diode equation[1, 215]:

$$I = AA^*T^2 e^{-\frac{q\Phi_B}{k_B T}} \left(e^{\frac{qV_a}{\eta_D k_B T}} - 1 \right) \tag{6.1}$$

where $q\Phi_B$ is the Schottky barrier height (SBH), A^* is the Richardson constant (32 A/cm^{2}K^2 for p-type Si[1]), A is the junction area (~7854μm^2), $k_B\,T$ is 26meV at room temperature, η_D is the diode ideality factor, defined as the deviation of the measured I-V curve from the ideal exponential behavior[1], and V_a is the applied voltage. The difference of this equation with respect to standard metal-semiconductor junctions lies in $q\Phi_B$. In graphene/Si Schottky junctions the SBH depends on the applied voltage:

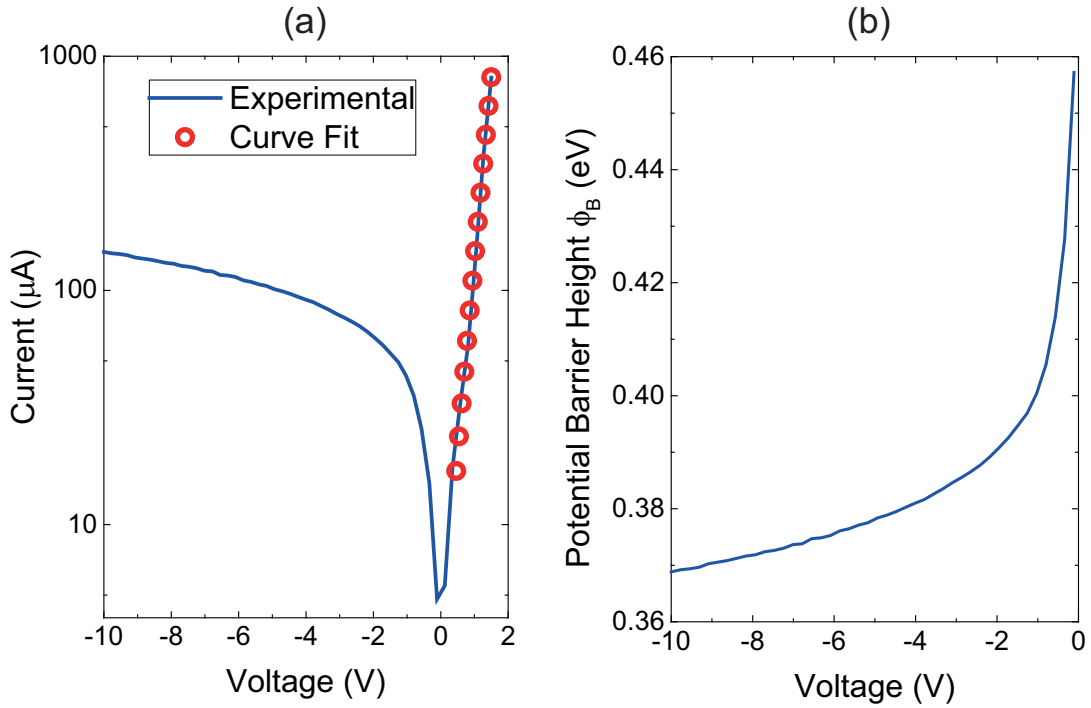

Figure 6.5: (a) I-V characteristic of SLG/Si Schottky PD (semi-log scale). Experimental data and fit are shown. (b) Potential barrier height as a function of reverse bias.

$$q\Phi_B = q\Phi_{B_0} + q\Delta\Phi_B(V_a) \tag{6.2}$$

where $q\Phi_{B_0}$ is the Schottky barrier height (SBH) at zero voltage and $q\Delta\Phi_B(V_a)$ is the SBH change due to applied voltage bias. $\Delta\Phi_B$ is typically dominant in reverse bias because of the higher potential drop of the Schottky junction, resulting in a more pronounced barrier-lowering Schottky effect[1, 215] and SLG Fermi level shift[212, 215, 216]. On the other hand, in forward bias the potential drop is limited by the built-in voltage (V_{bi} <1V)[1], so that $\Delta\Phi_B$ can be neglected and $\Phi_B \sim \Phi_{B_0}$. The SBH is estimated in forward bias by fitting the experimental data with Eq.6.1 and using Φ_B and η_D as fitting parameters. This results in: $q\Phi_B$ ~0.46eV and η_D ~11. These results are in the range of previously reported values (0.41< $q\Phi_B$ <0.47 and 2< η_D <30) for SLG/Si Schottky diodes[118, 211–213, 216, 217]. By fitting the I-V curve in reverse bias the SBH dependence on applied reverse voltage is obtained and $q\Delta\Phi_B$ is found to be up to~80meV at -10V, Fig.6.5(b).

The opto-electronic characterization has been carried out by Dr Maurizio Casalino at CNR-IMM, Italy, using the set-up of Fig.6.6(a). Light at telecom wavelengths is generated by a tunable laser (ANDO AQ4321D). The optical signal is chopped and split

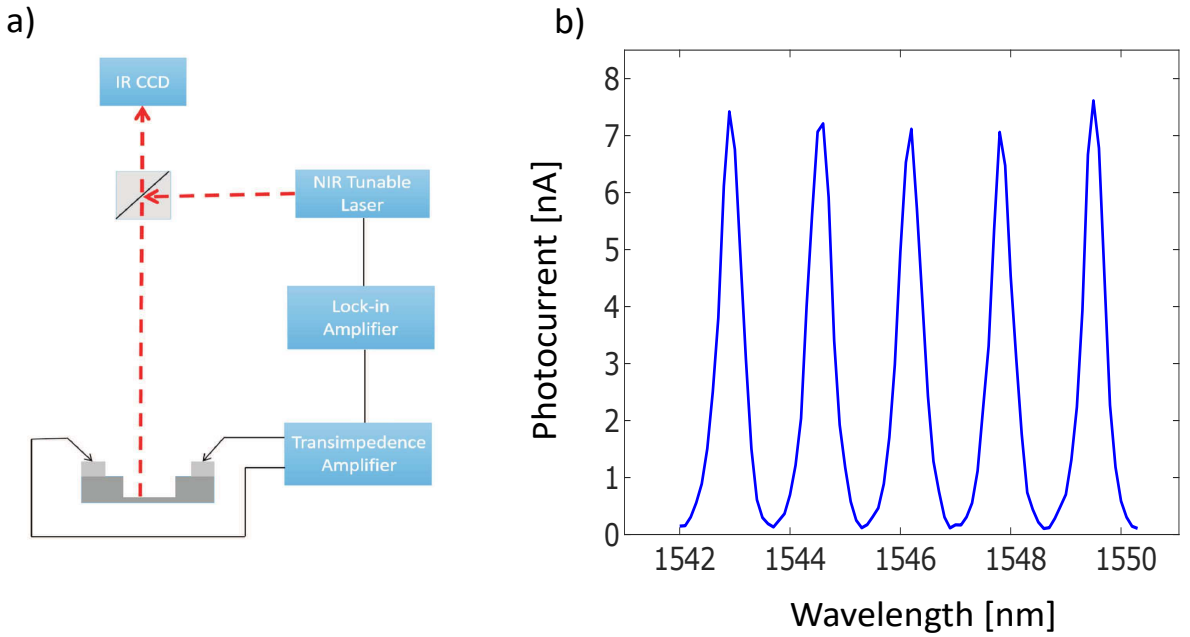

Figure 6.6: (a) Opto-electronic measurements setup. (b) Spectral response (photocurrent) of RCE SLG/Si Schottky PD without backside Au (V_a=-1V).

by a beam splitter between the reference, used for continuous power monitoring, and the device under test. The PD illumination is inspected by an infrared camera (IR CCD). The transimpedence amplifier has a double role: it is used both to generate a reverse voltage bias to polarize the junction and to amplify the photocurrent then fed to a lock-in for measuring the photoresponse. The incident optical power P_{inc} is measured separately with a commercial InGaAs PD (R_{ext} ∼1A/W).

Fig.6.6(b) plots the PD responsivity as a function of λ under reverse voltage V_a=-1V. The device demonstrates spectral selectivity, exhibiting wavelength dependent and periodic I_{ph} peaks upon illumination. The spectral separation $\Delta\lambda$ between the peaks is∼1.7nm. This is an important parameter in F-P cavities which goes under the name of free spectral range (FSR). This can be estimated as:

$$FSR = \frac{\lambda_0^2}{2n_g \cdot L} \tag{6.3}$$

where λ_0 is the illumination wavelength, $n_g = \mathrm{n} - \lambda_0 \cdot d\mathrm{n}/d\lambda$ is the group index of Si around 1550nm. This is as a refractive index but calculated using the group velocity, instead of the phase velocity of the wave. n_g is estimated to be ∼3.61[218], n=3.45 is the refractive index of Si at 1550nm[218], and $d\mathrm{n}/d\lambda$ is the dispersion.

To confirm the cavity effect on PD responsivity and the device response around 1550nm, R_{ext} is calculated with and without the Au mirror, Fig.6.7(a).

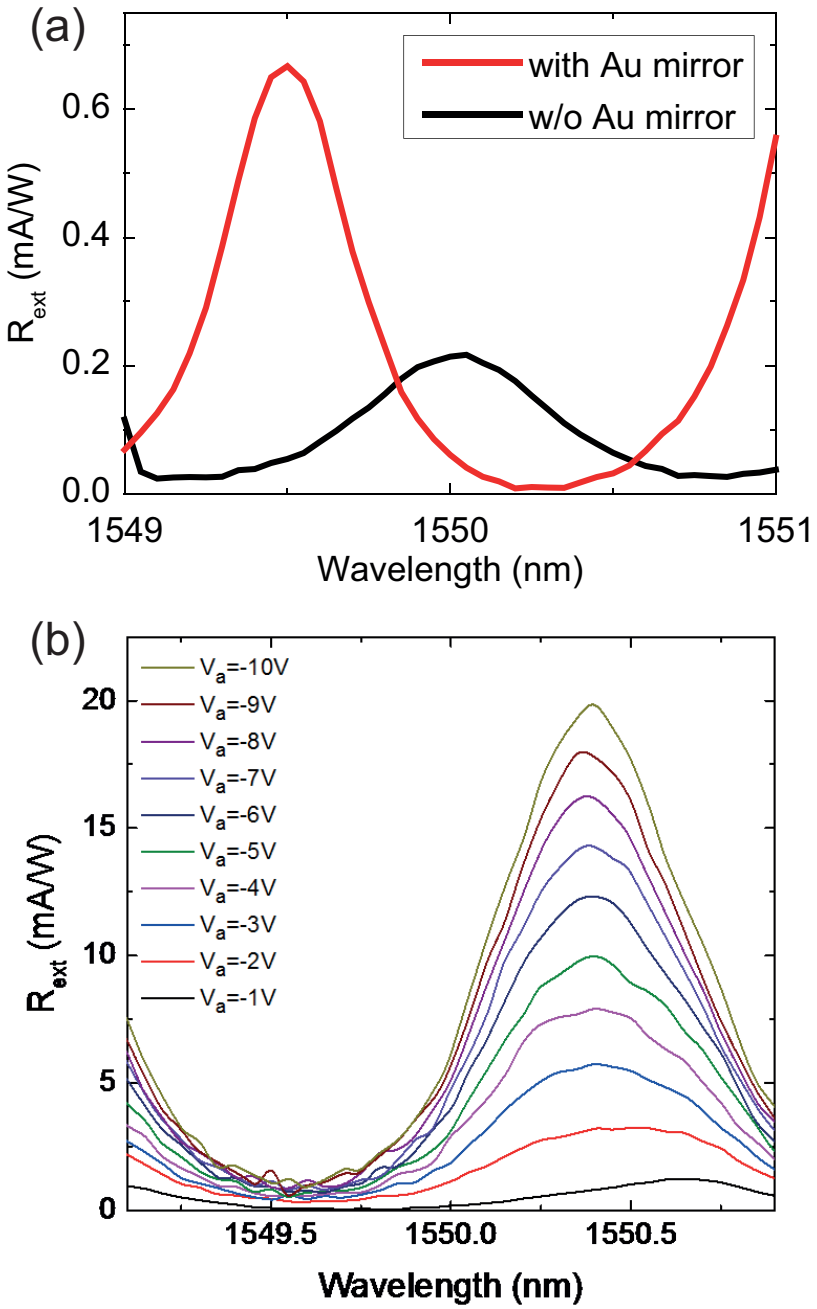

Figure 6.7: (a) R_{ext} of a SLG-based RCE PD with a (red curve) and without a (black curve) Au mirror at -1V. (b) R_{ext} as a function of increased reverse voltage registered in a device different from that shown in (a)

Whenever light impinges on the interface between two materials with different refractive index, a Fresnel reflection occurs[2]. The Si/air interface provides already for a

Fresnel reflection which is enough to generate a cavity structure. This induces a peak in R_{ext} at resonance, *i.e.* around 1550nm. A factor of 3× R_{ext} enhancement is observed with the Au mirror compared to the bare Si/air interface. The slight (up to 1nm) variation in resonant wavelengths among the two devices is also attributed to the different refractive index of gold and air (Fig.6.7(a-b)).

Another important parameter to define the optical energy built-up in a F-P cavity is the finesse F, associated with the wavelength selectivity of the device. This is defined as the ratio between the FSR and the FWHM of the responsivity peaks. The introduction of a mirror in the cavity does not change any parameter in Eq.6.3 of the FSR. However as we see from Fig.6.7(a) the FWHM(R_{ext}) is affected by the presence of the mirror and F goes from ∼3 (without) to ∼5.3 (with) Au mirror, respectively.

To further enhance R_{ext}, the Schottky barrier lowering effect can be exploited by applying a larger (up to 10V) reverse bias to the PDs with integrated Au mirrors. Fig.6.7(b) plots R_{ext} for different V_a. R_{ext} can be pushed up to ∼20mA/W at V_a=-10V. This is the highest value reported so far for vertically-illuminated Schottky Si PDs at 1550nm.

6.3 Graphene-silicon Schottky avalanche photodetectors

The second approach for a vertically illuminated PD at 1550nm is based on the avalanche gain mechanism discussed in Section 4.2.2. The principle of operation of this device relies on driving the PD at high reverse biases ($< -3V$) to trigger impact ionisation in the Si depletion region and lead to carrier multiplication. This process yields a significant photogain, resulting in an enhancement of the photoresponsivity at 1550nm illumination from the mA/W regime to $>$ 1 A/W.

For the fabrication of avalanche PDs the last evaporation step of the back side mirror in RCE-PDs is not performed. Furthermore, highly-doped (∼$5{\cdot}10^{18}$cm^{-3}) Si is used in order to set the avalanche breakdown voltage around ∼-4V. Electrical characterization is initially performed by taking the current-voltage I-V characteristics and confirming rectifying behaviour (Fig.6.8).

Another rigorous approach for the evaluation of the SBH is to use the "Arrhenius plot" as depicted in Fig.6.8(b). I-V curves are taken at different temperatures (Fig.6.8(a)). The expression of saturation current I_S in reverse polarization can be extracted from Eq.6.1[1]:

$$I_S = AA^*T^2e^{-\frac{q\Phi_B}{k_BT}} \tag{6.4}$$

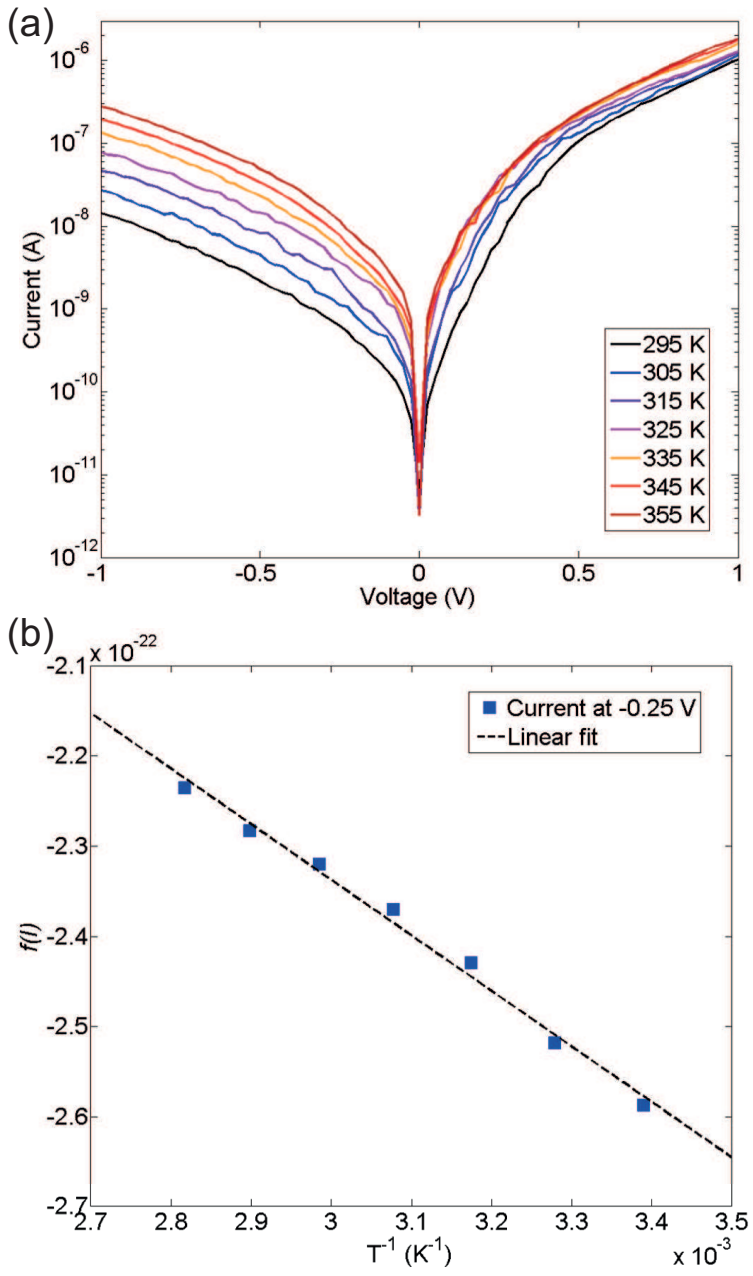

Figure 6.8: (a) I-V characteristics (semi-log scale) of the SLG/Si Schottky avalanche PD measured at different temperature and (b) plot of $f(I)$ versus T^{-1} at the temperatures measured in (a) and by fixing the applied voltage at a V_a=-0.25 V; $q\Phi_B$ ~0.39 eV is extracted by performing a linear fit.

By taking the logarithmic of both equation sides and reorganizing, we obtain:

$$\ln\left(\frac{I_S}{AA^*T^2}\right) = f(I) = -\frac{q\Phi_B}{k_BT} \tag{6.5}$$

therefore at a fixed bias voltage, which here has been chosen at V_a=-0.25V, the relation between T^{-1} and $f(I)$ is linear as shown in Fig.6.8(b). The slope of the curve is related to the SBH. For this device a SBH $q\Phi_B$ ∼0.39 eV has been measured. The reason for larger currents at higher temperatures in the dark is due to increased emission of carriers from SLG to Si overcoming the Schottky barrier (thermionic emission).

The optoelectronic characterization is carrier out by illuminating the PD with a laser source at 1550nm, having a spot size (diameter) of ∼2mm and a P_o of 3mW. *I-V* curves are taken in the dark and under illumination in Fig.6.9. Possible hysteresis are checked by taking multiple I-V curves in dark and upon illumination. Curves taken in the same regime widely overlap with minor shifts allowing us to disregard hysteresis issues. The current slowly increases with increasing the reverse voltage until the avalanche regime is reached at V_a ∼-3.5V. Here the current increases more rapidly due to avalanche multiplication by impact ionization of carriers in Si, after being injected over the Schottky barrier through IPE.

Consequently, the I_{ph}, *i.e.* the distance between the curve in dark and at 1550nm, also increases in module as clear from the linear plot in Fig.6.9(b). The photo-responsivity R_{ext} can be calculated using a slightly modified version of Eq.4.4 [1]:

$$R_{ext} = \frac{I_{ph}}{P_o \cdot A_{PD}/A_o} \tag{6.6}$$

A_{PD}/A_o is indeed a scaling factor that takes into account the fact that only a fraction of the optical power impinges on the PD. Specifically : A_o is the laser spot area, A_{PD} is the PD area. Considering a P_o= 3mW, a laser spot diameter of 2mm and the diameter of the photoactive area being 100μm, R_{ext} is reported in Fig.6.10(a). R_{ext} jumps from the mA range to values exceeding 1A/W for V_a ∼-4V in the avalanche regime. This R_{ext} is similar to those obtained in current state of the art Ge-Si photodetectors at 1550nm, whose integration on the Si platform is however more complicated[191, 194].

The avalanche multiplication gain factor M is defined as:

$$M = \frac{1}{1-(V_a/V_{bd})^n} \tag{6.7}$$

where V_{bd} is the breakdown voltage, *i.e.* the value for which M approaches infinity, and n is a constant, typically 2< n <6 in Ge- or InGaAs-based avalanche PDs[195, 219].

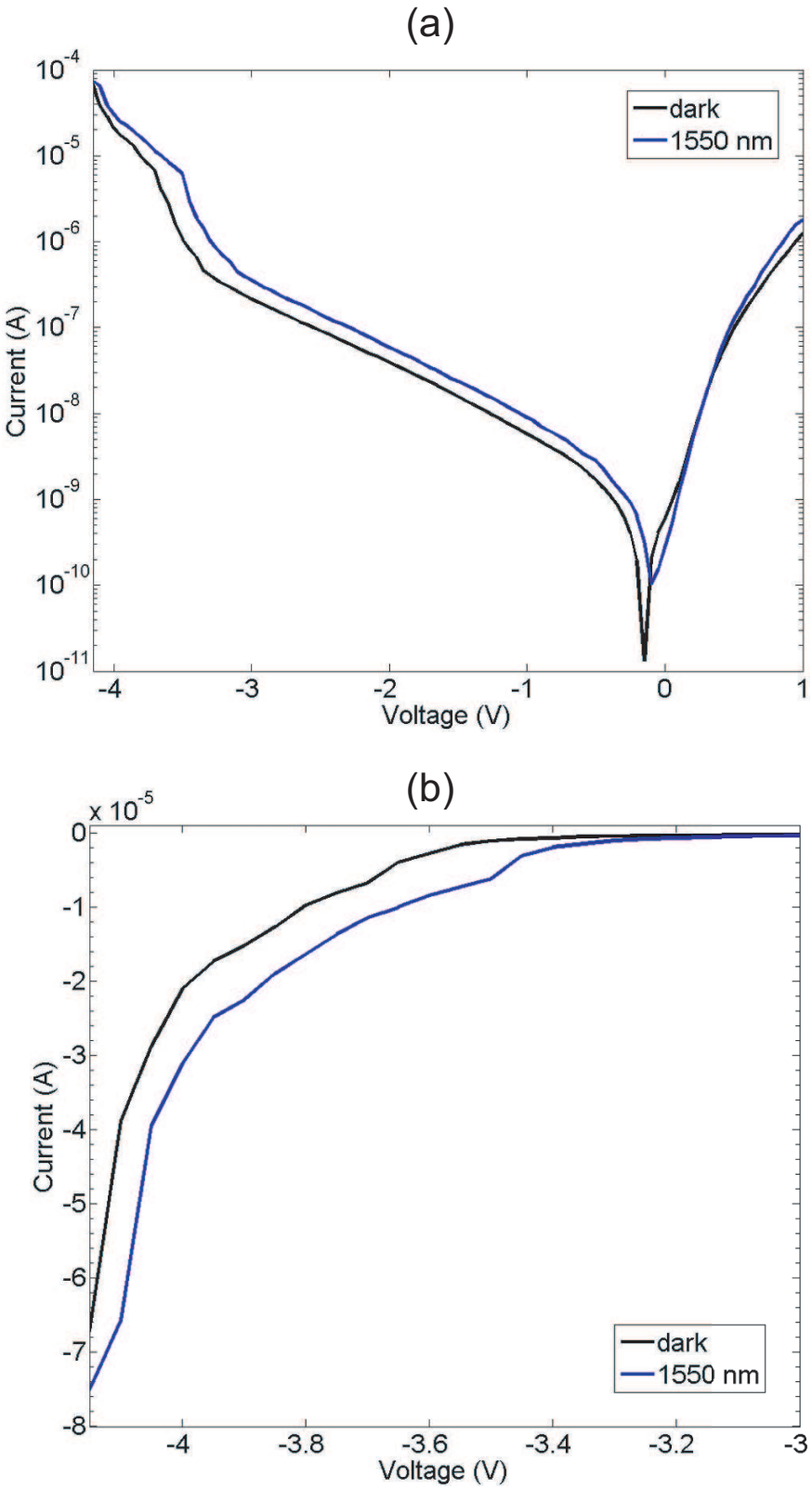

Figure 6.9: (a) *I-V* characteristics (semi-log scale) of the SLG/Si Schottky avalanche PD in the dark and upon illumination at λ-1550nm and (b) a close-up to the avalanche regime in linear scale.

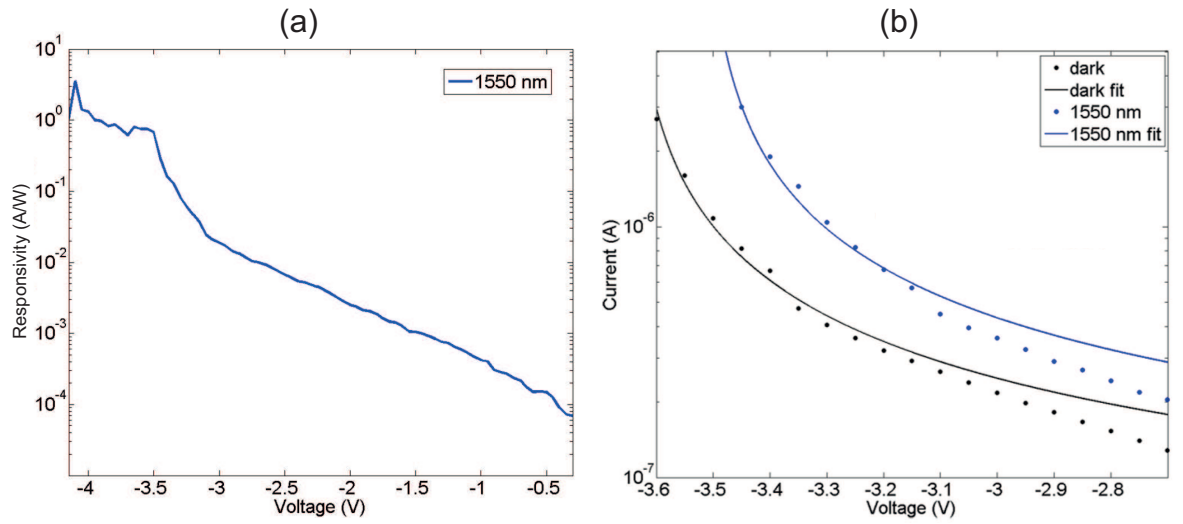

Figure 6.10: (a) Semi-logarithmic plot of the photo-responsivity R_{ext} as a function of reverse bias of an SLG-Si Schottky avalanche PD, measured at 1550nm. (b) I-V characteristics in the dark and upon illumination with fits.

To confirm that avalanche multiplication is responsible for the behaviour measured at V_a <-3V, data of the current measured in dark and upon illumination are fitted with Eq.6.7 by choosing breakdown voltages V_{bd} ∼-3.5V as shown in Fig.6.10(b). The fits are in good agreement with experimental data, confirming the presence of an avalanche mechanism. An M approaching infinity would be expected for $V_a \sim V_{bd}$, which would let the current increase exponentially, eventually breaking the device; however the current (Fig6.9(a)), as well as R_{ext} (Fig6.10(a)), saturate for $V_a < V_{bd}$. This is attributed to in-series resistances such as the contact resistance, which limit the flowing current.

Finally, it is worth mentioning that the avalanche multiplication is not the only phenomenon playing a role at high reverse biases. Indeed, field emission through the Schottky barrier for carriers with energy lower than the SBH could potentially modify the I-V curve.

6.4 Waveguide-integrated graphene-silicon Schottky photodetectors

In the last section of this chapter I then report the results obtained on a compact (5μm length), waveguide integrated, SLG/Si Schottky PD with $R_{ext} \sim$ 85mA/W at 1550nm for on-chip photodetection. Here I will describe how the metal-SLG-Si structure

benefits from optical confinement at the Schottky interface. The results obtained in this section have been published in Ref.[213], which I co-authored.

Obtaining optical confinement is in principle a rather facile task to be achieved. For example, the light travelling in a medium with a certain refractive index, surrounded by a medium with lower refractive index, can be trapped and guided from one point to another due to multiple total reflections at the boundaries[2]. Waveguides provide interconnections between optical components such as light sources, modulators and photodetectors and thus represent an essential building block in optical interconnects[2].

Different methods and geometries can be employed for achieving optical confinement. For the fabrication of a waveguide integrated photodetector (WI-PD), here the geometry shown in Fig.6.11(a) was chosen. The device consists of a Si-waveguide coupled to a SLG/Au contact that electrically forms a Schottky diode. Here light is confined at the interface between Au/SLG and Si in order to enhance the absorption. This is achieved by exploiting Surface Plasmon Polaritons (SPPs). SPPs are travelling waves at the interface between a metal and a dielectric or semiconductor, with intensity exponentially decaying in each medium in the direction perpendicular to the interface[220]. The electromagnetic field associated to SPPs is obtained from solving the Maxwell equations in each medium of the metal-semiconductor junction. A set of boundary conditions have to be accounted for: the continuity of the transversal components of the electric and magnetic field across the interface and the vanishing of their amplitudes infinitely far from the interface[220]. The simulations of the structure have been carried out by Dr Ilya Goykhman and the results are shown in Fig.6.11(b). By adjusting the device dimensions, the SPP guiding can provide optical confinement at the Au-SLG-Si interface, where the IPE process takes place. This can increase light absorption in SLG, adjacent to the Schottky interface and, as a result, enhance R_{ext}.

Fig.6.12 outlines the fabrication process of the WI-PD. The starting material is a commercial silicon on insulator (SOI) substrate with a 340nm p-type ($7 \cdot 10^{17}\text{cm}^{-3}$) Si layer on top of a 2$\mu$m buried oxide (BOX). First, a 100nm silicon nitride (SiN) mask is deposited by plasma enhanced chemical vapor deposition (PECVD) onto the SOI substrate at 300°C (Fig.6.12(b)). Next, a Si photonic waveguide and the PD area are defined by electron beam lithography. The EBL pattern is subsequently impressed onto SiN by performing reactive ion etching (RIE) with a gas mixture of fluoroform (CHF_3) and O_2.

Then, the SOI substrate is (locally) wet oxidized in a furnace at 1000°C, to grow a SiO_2 layer only in patterns defined by EBL where Si is exposed to O_2, while at the same time a SiN mask prevents O_2 diffusion into the Si in protected areas (Fig.6.12(c)). After

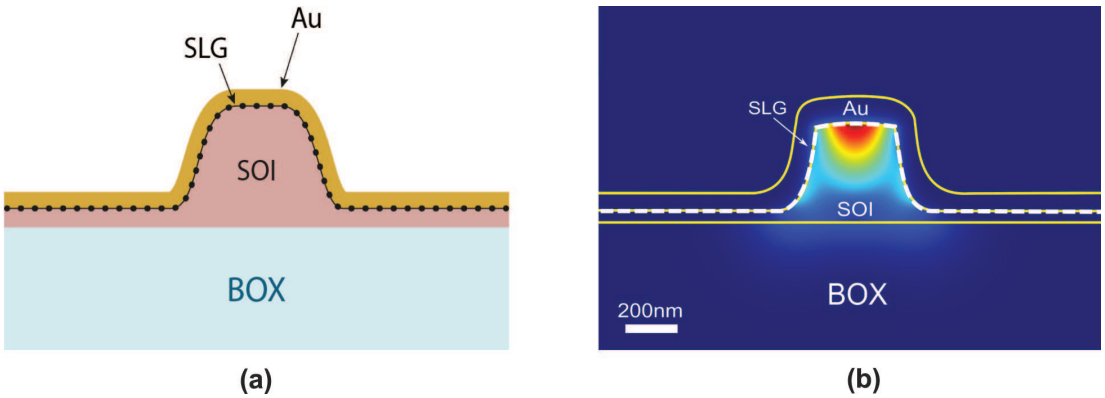

Figure 6.11: (a) Schematic drawing of Au-SLG-Si Schottky PD. SOI stands for silicon-on-insulator, and BOX stands for buried oxide; (b) Finite element (COMSOL Multiphysics)[221] simulated optical intensity profile of an SPP waveguide mode supported by a Au-SLG-Si structure.

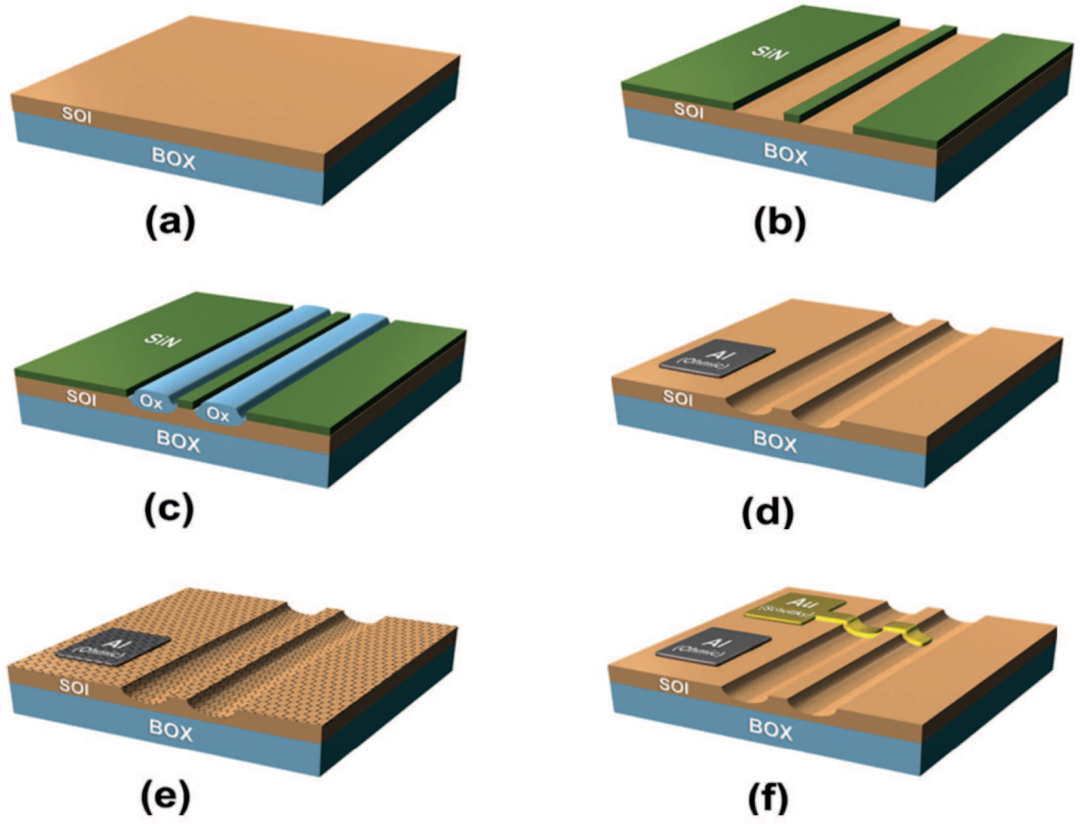

Figure 6.12: Fabrication process of Si-SLG Schottky PD integrated with a photonic waveguide. (a) Planar SOI substrate; (b) PECVD deposition and patterning of SiN mask; (c) Local oxidation; (d) Etching of SiN and SiO_2. Al ohmic contact to Si; (e) SLG transfer; f) Formation of Schottky contact and consequent SLG etching.

oxidation, the sacrificial SiN mask layer is etched in phosphoric acid (H_3PO_4, 180°C), followed by SiO_2 removal in a buffered oxide etch (BOE) solution. This fabrication process is based on the technique of local-oxidation of Si (LOCOS), in which a Si waveguide is defined by oxide spacers[222] rather than by reactive ion etching (RIE). The LOCOS process enables the realization of low-loss (∼0.3dB/cm) Si photonic waveguides minimizing scattering phenomena by achieving smooth waveguide profiles. The ohmic contact to Si is realized by Al evaporation, followed by metal lift-off and thermal alloying at 460°C in a forming gas (H_2/N_2, 5%/95%) environment, similar to the previous RCE and avalanche PD.

SLG is grown and transferred onto the SOI with Si waveguides as discussed in Sections 5.3 and 5.4. To obtain a Schottky interface between the Si waveguide and SLG without the native oxide layer the transfer is performed, as in RCE and avalanche PDs, in diluted hydrofluoric acid (HF)and DI water (1:100). Control samples are always transferred in parallel to SiO_2/Si substrates. Then, a Schottky contact is realized by evaporation and liftoff of an 3nm/100nm Cr/Au metal strip intersecting the Si waveguide with SLG on top (Fig.6.12(f)) (or without SLG for reference devices) and forming a Schottky interface for photodetection. A final lithography step, followed by reactive O_2 plasma is performed in order to remove superfluous SLG. Fig.6.13 shows a scanning electron microscope (SEM) micrograph of the resulting WI-Schottky PD integrated with locally-oxidized[222] Si waveguides. The PD length is$\sim 5\mu$m and the Si waveguide width is$\sim 310nm$.

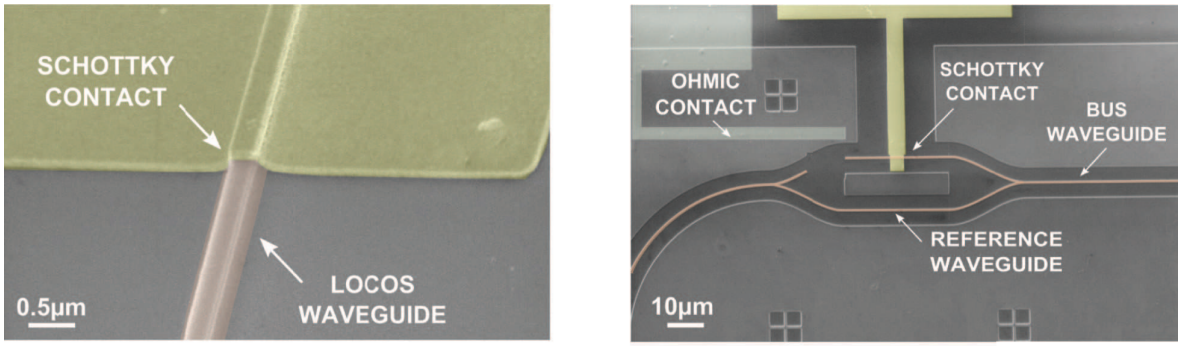

Figure 6.13: (a) SEM micrograph of Schottky PD coupled to Si photonic waveguide. False colors: brown-Si, yellow-Au; (b) Layout of waveguide integrated Schottky PD.

Fig.6.14 plots the I-V characteristic of a WI-PD, measured using a probe station and a parameter analyzer. The device shows typical rectifying diode behaviour. The current in forward bias is limited by series resistance[1], while at reverse bias the leakage/saturation current I_S is governed by thermionic emission from Au/SLG to Si. In reverse bias, I_S grows

with increasing temperature, consistent with the thermionic-emission theory of Schottky diodes, explained in Section 6.3[1]. Using the same procedure from Section 6.3 and Equations 6.4 and 6.5 the SBH in Au-SLG-Si devices can be extracted: $q\Phi_B \sim 0.34$eV and diode ideality factor $\eta_D \sim 1.8$[1]. For the reference Au-Si devices instead $q\Phi_B \sim 0.32$eV and $\eta_D \sim 1.7$, similar to Au-SLG-Si. This indicates that SLG does not significantly affect the electrical properties of the Schottky contact.

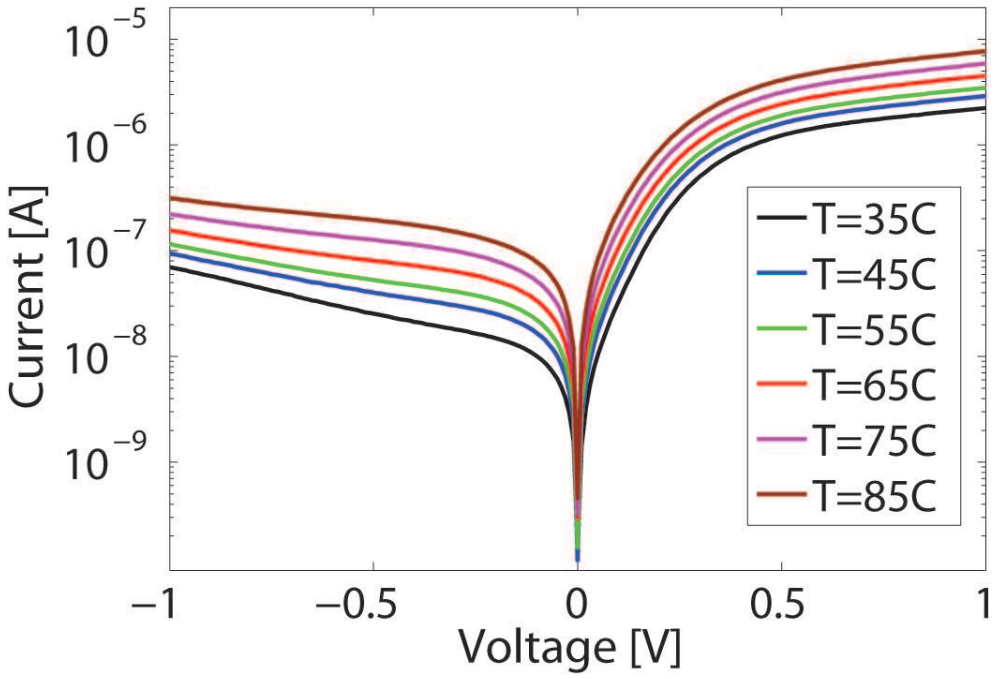

Figure 6.14: Semi-log *I-V* characteristics of WI SLG-Si Schottky PD at various temperatures.

For opto-electronic characterization, λ =1550nm transverse-magnetic (TM) polarized light from a laser source is used (Agilent 81680A). The optical signal is coupled to the waveguide using a polarization-maintaining (PM) tapered fiber. The device under test is placed on a fixed vacuum holder, while the fiber is aligned with respect to the waveguide facet under microscope using a high precision (0.1μm step) XYZ translation stage. Fig.6.13(b) shows that the device has a symmetric Y-branch to split the optical signal between the active arm with integrated Schottky PD and a reference waveguide. This is for continuously monitoring possible power fluctuations during the measurements. At the output facet of reference waveguide the light is collected with a similar fiber and detected by an external InGaAs power meter. After optimizing the optical coupling conditions by adjusting the positions of both the input and the output lensed fibres, and maximizing the optical power reading in the InGaAs power meter the *I-V* characteristics

of the Schottky photodetector. For I-V measurements, electrical probes are brought in contact with the electrical pads of the Schottky device under a microscope using micromanipulators. The I-V curves of Au-SLG-Si WI-PD (Fig.6.15(a)) and reference Au-Si WI-PD devices (Fig.6.15(b)) at different P_o are measured. A P_o increase results in larger reverse current, since I_{ph} acts as an external current source added to the Schottky diode current I_S .

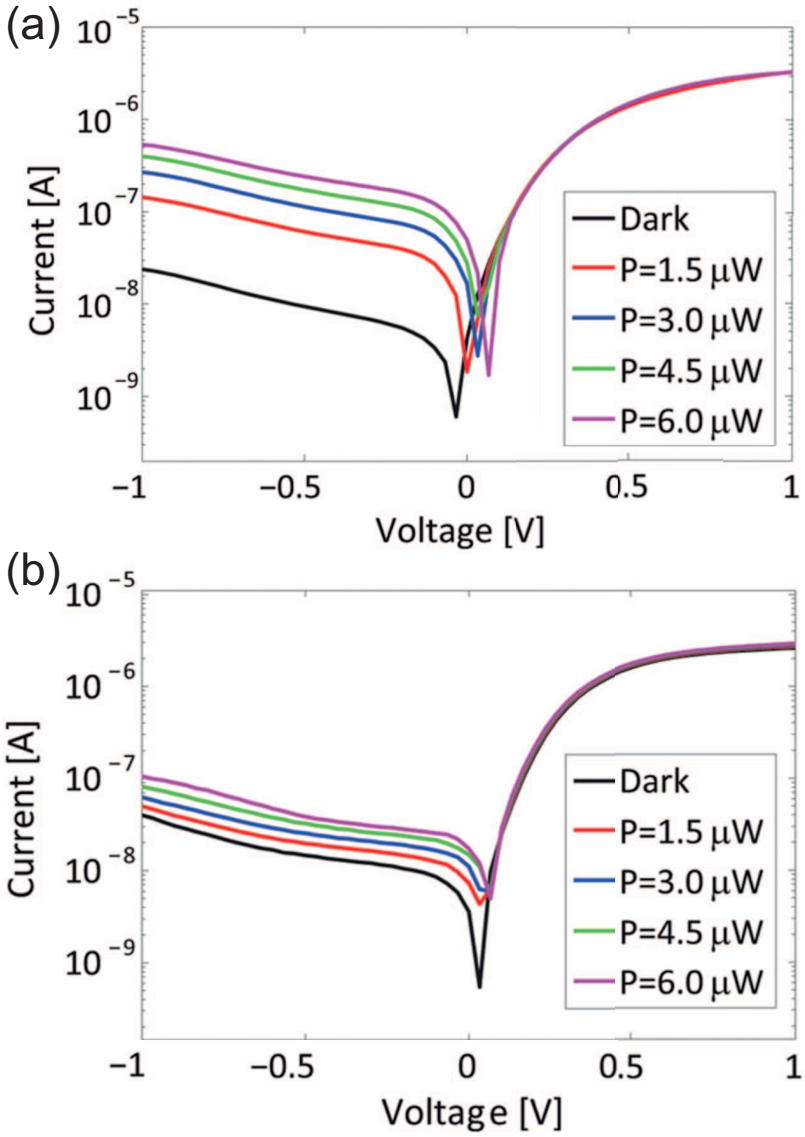

Figure 6.15: I-V characteristics of (a) graphene-integrated and (b) reference Au-Si PDs for different optical powers coupled to the Schottky region.

Fig.6.16(a-b) show plots of I_{ph} as a function of P_o as derived from the I-V curves in Fig.6.15. I_{ph} grows linearly with P_o and the slope corresponds to R_{ext}. P_o inside the

Schottky PDs is estimated by taking into account a coupling loss of ∼ 18.5dB (98.5%) between the external tapered fiber and the Si waveguide (as measured by monitoring the output signal in the reference waveguide), a propagation loss ∼ 1.5dB/mm (29% per mm) in the waveguide, a ∼ 3dB (50/50) power splitting, and ∼ 1.5dB (29%) power loss in the Y-branch.

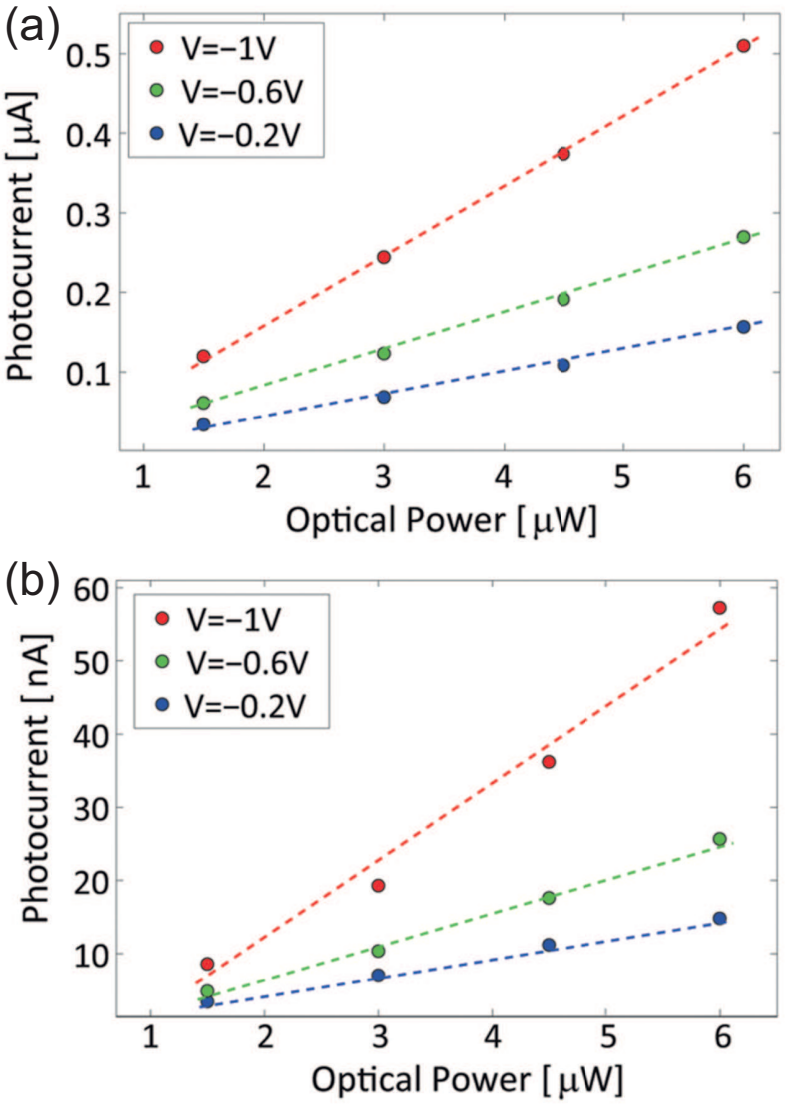

Figure 6.16: Measured photocurrent in (a) graphene-integrated and (b) reference Au-Si PDs as a function of optical power coupled to the Schottky region.

Consequently, based on I-V measurements and P_o estimation, R_{ext} is plotted in Fig.6.17 as a function of applied voltage V_a. The maximum achieved responsivity is R_{ext} ∼85mA/W with $I_S \sim 20nA$ at V_a =-1V. The presence of SLG at the Schottky interface improves R_{ext} by one order of magnitude compared to the reference device. This

is confirmed by consistent results in at least three devices. The enhancement of R_{ext} is attributed to improvement in light absorption in the SLG adjacent to the Schottky barrier, where the IPE process takes place, probably due to higher transmission probability of "hot" carriers from SLG to Si when compared to the Au-to-Si photoemission process. In avalanche mode R_{ext} can be further increased up to$\sim 0.37 A/W$ at V_a=-3V.

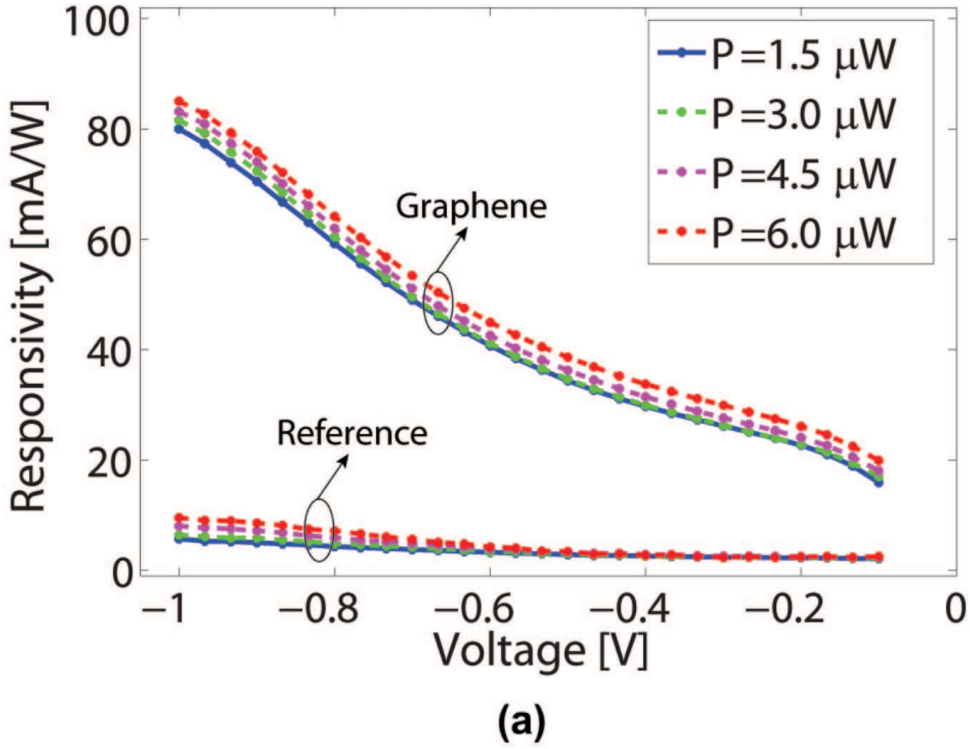

Figure 6.17: (a) Calculated R_{ext} of Au-SLG-Si and reference Au-Si PDs as a function of reverse bias for different optical powers coupled to the Schottky region

6.5 Conclusions

I showed three types of graphene-based Schottky PDs, either working in vertical illumination or integrated on-chip. In all three PD configurations the photodetection mechanism is based on internal photoemission.

The RCE-PD is spectrally-selective at λ around 1550nm. The photodetection is enhanced by integration in a F-P cavity, which increases the SLG absorption due to multiple reflections at the cavity resonance. As a result, the photoresponse R_{ext} is $\sim$20mA/W at V_a=-10V. The resonance wavelength may be further tuned by varying the Si cavity thickness, while the spectral-selectivity can be increased by taking advantage of

more complex high-finesse microcavities. With appropriate selection of the Si substrate, the SLG/Si Schottky interface can be driven and utilized in avalanche mode to build Schottky avalanche PDs. These yield R_{ext} in the order of ∼1A/W at V_a=-4V.

In parallel, on-chip, compact, WI Au-SLG-Si Schottky photodetectors operating at 1550nm have been shown. The presence of graphene at the Schottky interface significantly improves the PD responsivity. The device has 85mA/W responsivity at V_a=-1V. This is one order of magnitude higher compared to a reference metal-Si PD under the same conditions. This improvement is attributed to the combined effect of light confinement and graphene absorption at the metal-graphene-silicon Schottky interface.

These devices pave the way for developing high-responsivity graphene-Si free-space illuminated and integrated PDs for NIR, challenging state-of-the art Si/Ge photodetectors.

Chapter 7

Graphene Pyroelectric Bolometers

7.1 Introduction

After having discussed PD examples at 1550nm, we now direct our attention towards another wavelengh range: the mid-IR (MIR). This is the spectral range in which the radiation from objects at room temperature has a peak (at $\lambda \sim 10\mu$m)[131]. There is a growing number of fields demanding highly sensitive photodetectors in this range, such as applications in astronomy[223], medicine[224, 225], security[226], night vision[227] and motion tracking[228]. In Section 4.2.3 I introduced bolometers, along with their key figures of merit, as a class of thermal PDs able to sense light at mid-IR wavelengths. Bolometers that are able to operate at room temperature (RT) with no need for cooling are obviously highly desirable. I have also introduced pyroelectric materials in Sect.4.2.3 as a simple opportunity to work as transducers of a thermal signal to an electrical signal.

Here I show a RT PD for MIR by integrating a dual-gated SLG sheet with a pyroelectric material. The device resistance changes proportionally to temperature T, mimicking a bolometric resistor[229], allowing us to use TCR as a metric for its net electrical output. Internally, the PD comprises a floating metallic structure that concentrates the charge generated by the pyroelectric substrate over an integrated graphene field effect transistor (GFET). The total pyroelectric charge generated on a variation in T increases with area, delivering effective TCRs up to $\sim$900%/K for a footprint of 300×300 mm^2. The results shown in this chapter have been published in Ref. [230], which I co-authored.

7.2 Fabrication

Figure 7.1 shows the desired layout of a single device and the corresponding electrical model. A SLG channel with source and drain contacts is fabricated on the pyroelectric substrate lithium liobate ($LiNbO_3$), LN in short (Fig.7.1(a)). A dielectric layer isolates the SLG from an H-shaped floating Au structure designed to overlap the oxide-coated SLG in the centre, whereas lateral pads are placed in direct contact with the substrate. Finger-like structures can be used to enhance light absorption at selected wavelengths. With such a design the conductivity of SLG can be modulated by a dual-gate capacitive structure. From the bottom, there is the pyroelectric polarization (and associated electric field) generated directly by the substrate, C_1 in Fig.7.1(a), which can be referred to as the "direct effect"[231].

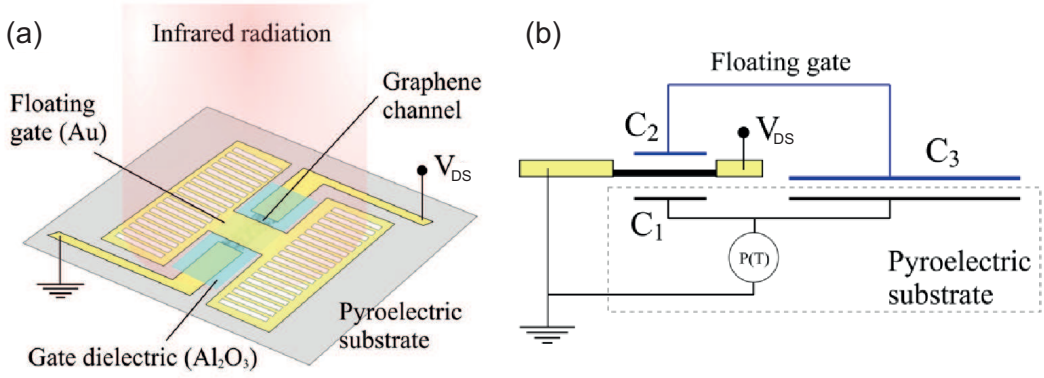

Figure 7.1: (a) Scheme of a device illuminated by infrared radiation. The conductance of the SLG channel is modulated by the pyroelectric substrate and by a floating gate. This is driven by two metallic pads in contact with the substrate, with a total area much larger than the overlap with the SLG channel. Such pads can be either uniform or patterned. (b) Circuit diagram for the device in (a).

From the top, there is a gate C_2 connected in series with capacitor C_3 as a floating circuit branch, with $A_{C_3} > A_{C_2}$. The perimeter of the pads defining C_3 sets the overall pixel size, from which only the source and drain contacts stem out to be connected to electrical probes.

As a first approximation, the generated pyroelectric charge ΔQ is uniformly distributed on the substrate[131, 229]. Therefore, the direct effect from C_1 does not depend on the channel area A_{C_1}. Conversely, for the floating gate in Fig.7.1, ΔQ accumulating on C_3 does depend on area. Based on Eq.4.12 we have:

$$\Delta Q = p \Delta T A_{C_3} \tag{7.1}$$

Being the structure electrically floating, the same charge would accumulate on C_2. Therefore the charge on C_2 generates for the SLG channel an effective top-gate voltage V_{TG} (in module):

$$\Delta V_{TG} = \frac{\Delta Q}{C_2} = \frac{p_c \Delta T t}{\epsilon_0 \epsilon_r} \frac{A_{C_3}}{A_{C_2}} \tag{7.2}$$

where ϵ_0 and ϵ_r are the vacuum and relative permittivity, and t is the oxide thickness. Hence, for fixed t and ΔT, the geometrical ratio A_{C_3}/A_{C_2} controls the gain of the integrated SLG amplifier and therefore the TCR.

SLG is grown by CVD and transferred on 500 mm-thick z-cut LN as discussed in Sections 5.3 and 5.4. The quality of the SLG film is monitored at each step by Raman spectroscopy as shown in Sect.5.4. During the fabrication process heating of the substrate is necessary in steps such as the polymer baking or the deposition of the top-gate oxide. Owing to the pyroelectric nature of LN, a significant static charge can build on both surfaces. To preserve the devices from discharge-induced damage, all metallic features, *i.e.* source, drain and floating gate on the LN surface are prepared as an electrically connected pattern. In this configuration, the device can undergo all the required heating (up to 120°C) processing steps without failing. The shorts are removed only at the last step, when no further heating is required aside from normal sensor operation.

The complete device fabrication process is depicted in Fig.7.2. First, SLG channels are patterned (Fig.7.2(b)) using optical lithography by laser writer and etching of exposed unwanted areas in O_2 (20W for 20seconds). A second lithographic step defines the metal contacts (source and drain), as well as the floating gate pads directly in contact with the substrate (Fig.7.2(c)). All features are shorted together as explained above. Before the deposition of a 40 nm-thick Au layer via thermal evaporation, a mild Ar plasma (0.5W, 20 seconds) is used on the exposed SLG areas. This is used to improve the contact resistance as defects induced by the plasma treatment ensure a good bonding with the metal[232]. Next, a 10nm aluminium oxide (Al_2O_3) layer is deposited by atomic layer deposition (ALD) at 120°C, to serve as gate dielectric (Fig.7.2(d)). Two nm of aluminium (Al) are used as a seed layer for atomic layer deposition[233]. Optical lithography is again used to define windows in the Al_2O_3, to expose the contact pads (source and drain), part of the shorting lines and a small section of the lateral pads where the top electrode needs to be anchored. The Al_2O_3 is then wet-etched in an alkaline solution (Decon90:DI Water 1:3) for ∼6 minutes, leaving the structure in Fig.7.2(e). Another lithographic step is then used to finalize the top-gate via thermal evaporation and lift-off of 2/60 nm of Cr/Au. Bonding pads are also prepared in this step, overlapping those deposited with the contacts (Fig. 7.2(f)). Finally, the electrical shorts are removed with

a last lithographic step followed by wet-etching of the Au lines in an aqueous solution of potassium iodide (KI) and iodine (I_2) (Fig.7.2(g)). An optical picture of the final device is shown in Fig.7.2(h), where the black arrows indicate where the Au shorts have been etched.

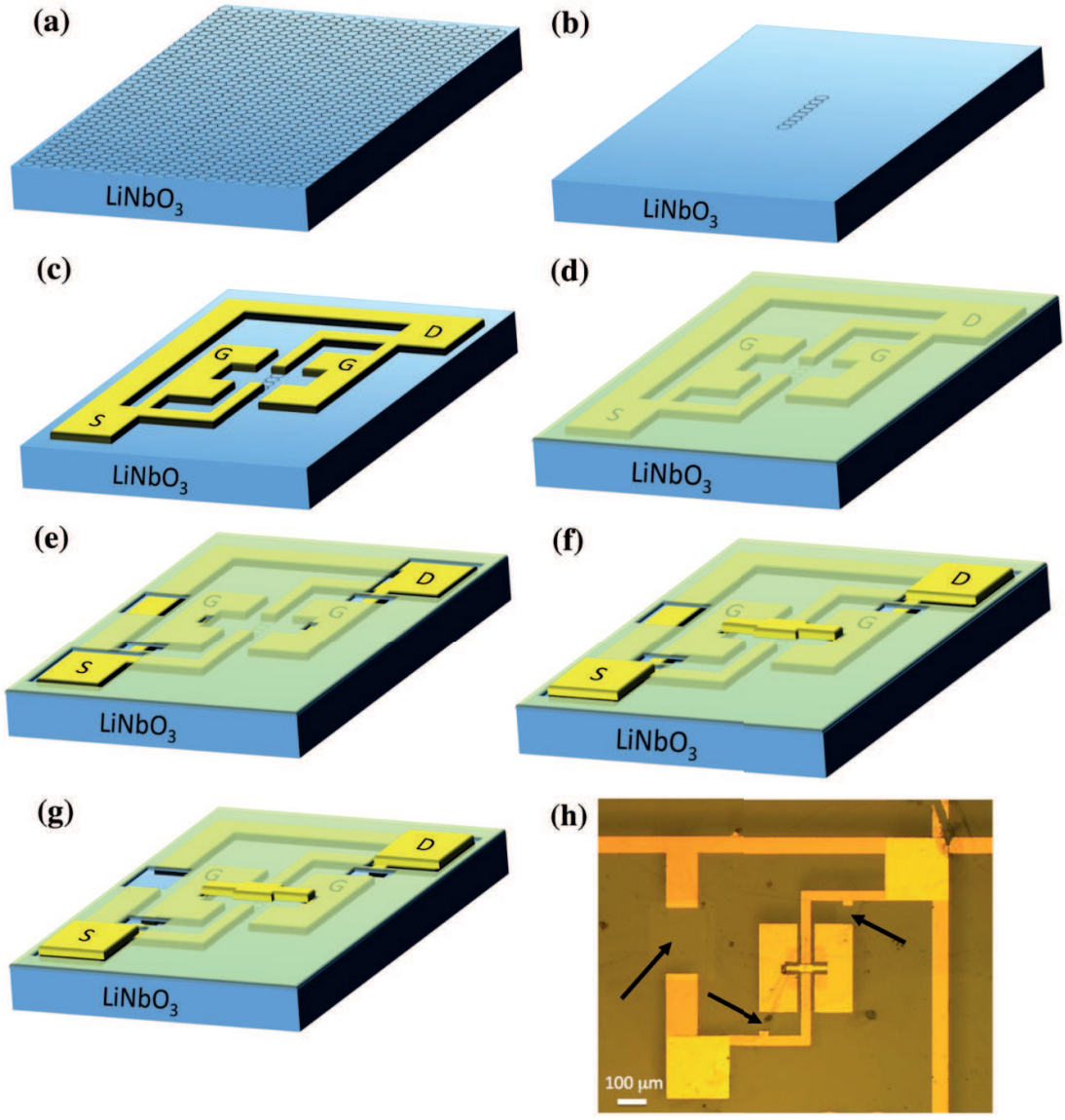

Figure 7.2: (a)-(g) Step by step fabrication process of the SLG-based pyroelectric bolometer and (h) final optical picture of the device with indicators on the areas where short-circuits have been removed by etching.

7.3 Results

The characterization of the properties of the pyroelectric bolometer is divided in two parts. The first part will cover the optoelectronic characterization as the device is illuminated with MIR light and an electrical signal is produced. These measurements were taken by Prof. Frank Koppens and co-workers at ICFO, Spain. The second part will instead consider a thermo-electrical characterization, being in this case heat the cause of a change in the electrical signal. In the latter, heat is seen as a quantity independent from a conversion from photons.

As shown in Fig.7.3 the device is first illuminated with λ ~9μm light and a spot size matching the pixel size of 300μm×300μm. A drain-source bias V_{DS}=10mV is used. The resulting modulation of the channel drain current is shown over nine ON/OFF laser cycles. The responsivity is R_{ext} ~0.27mA/W. A larger V_{DS} can be used to increase the responsivity, but this in turn increases also the dark current I_{dark} (I in the OFF state).

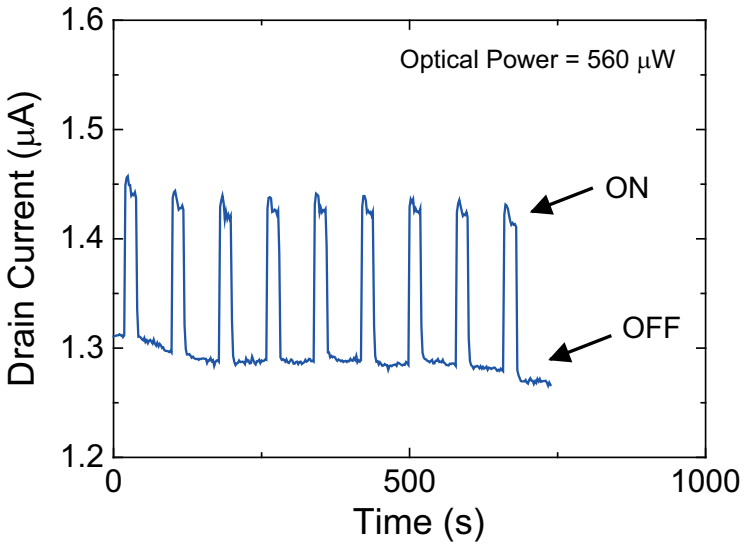

Figure 7.3: Drain current I_{DS} as a function of time circulating in a pyroelectric bolometer biased with a V_{DS}=10mV and illuminated with 9μm MIR light. The laser is switched ON and OFF for nine times.

The responsivity in bolometers is sometimes normalized as follows:

$$R_{ext,N} = \frac{\frac{I_{ph}}{I_{dark}} \cdot 100}{P_o} \tag{7.3}$$

here the unit is %/W and, for the device in Fig.7.3, $R_{ext,N}$ ~$2{\cdot}10^4$%/W, over two orders of magnitude higher with respect to Ref.[231], where only the direct effect of the pyroelectric substrate was exploited.

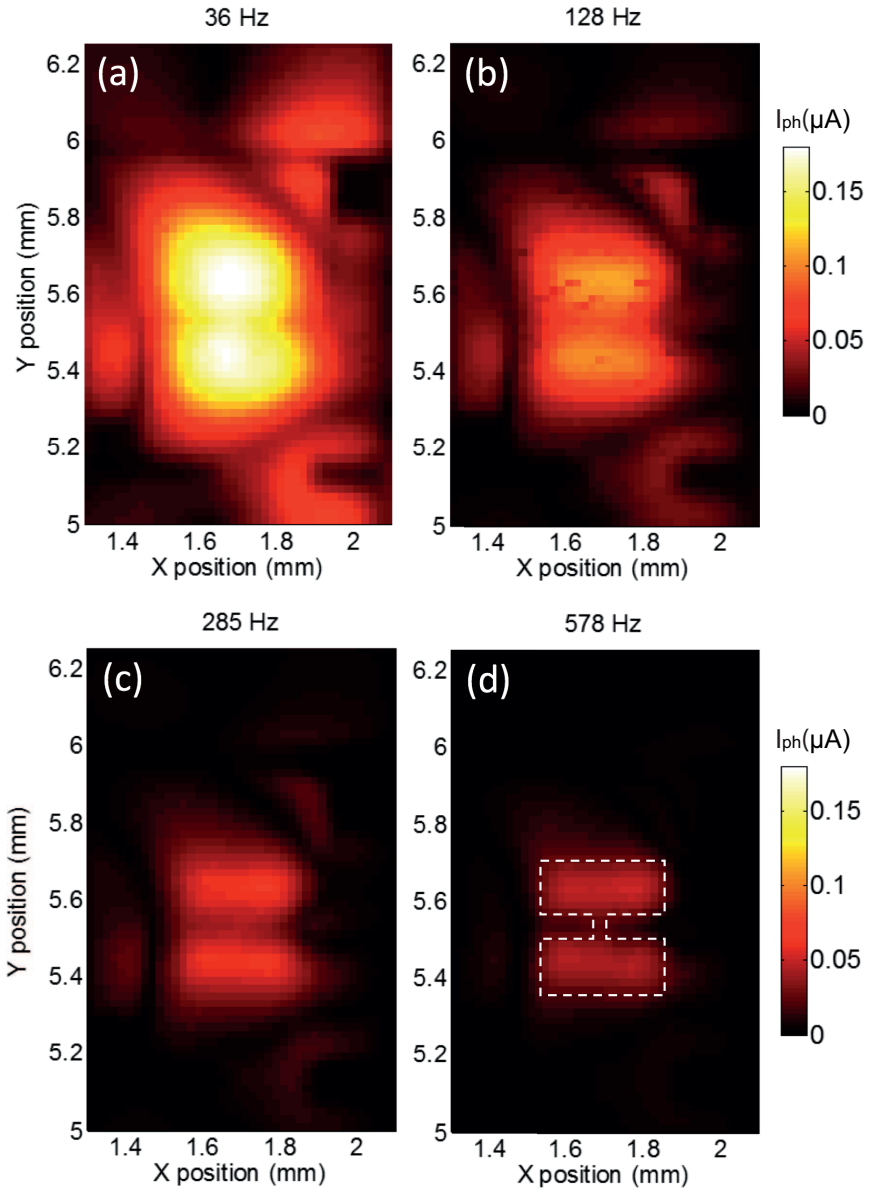

Figure 7.4: (a-d) I_{ph} profiles of a representative device for different ν and a beam P_o ~1.8mW at 9μm. The peak intensity decreases at higher μm, but the map is more resolved. The dashed white lines in (d) indicate the location of the device features.

In order to take photocurrent maps of the device and assess where the maximum signal is generated, the spot size is reduced to 10μm diameter. The signal is collected by

a lock-in amplifier, with light beam being chopped at several frequencies. At the slowest chopper frequency (ν ~36 Hz; Fig.7.4(a)) the photocurrent map shows two broad bright areas, which largely overlap and extend beyond the pixel area. When ν is increased, the two peaks become progressively resolved until, above ~500Hz (Fig.7.4(d)), they match the location of the lateral pads defining the pixel highlighted with a dashed line.

Analysing Figures 7.4(a-d) it becomes clear that the signal decreases at higher ν. To investigate the trend of I_{ph} with frequency, here I show I_{ph} on full illumination ($300\times300\mu m^2$ spot size) in Fig.7.5 as a function of ν. I_{ph} scales with ν and is measurable up to 1kHz. This result is intuitive as for slow chopping speeds there is more time both for heating up and for heat to laterally spread away from the illuminated spot, inducing a more homogeneous temperature distribution.

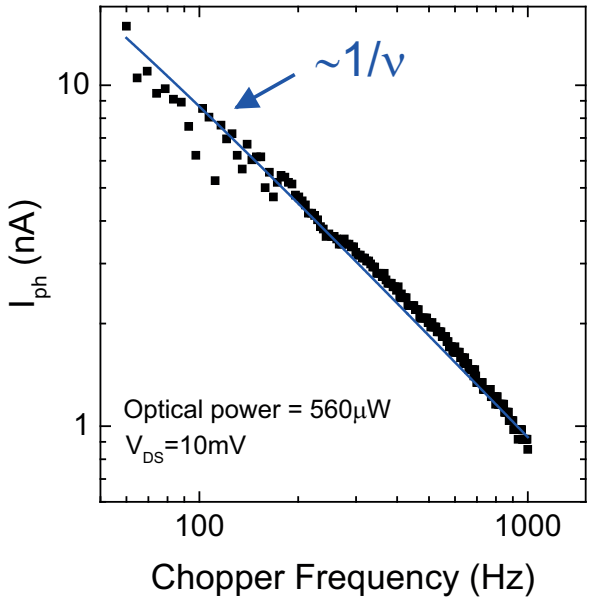

Figure 7.5: Logarithmic plot of the photocurrent as a function of the chopper frequency when using 9μm light, showing $1/\nu$ scaling at ν over 60Hz (solid blue line).

We now move on to the thermo-electrical characterization, considering the performance of the device as a local thermometer, independent from the conversion of photons to T[136, 229]. Each pixel is a two-terminal device whose resistance represents a readout of the local T. As for bolometers, the TCR is considered as the key figure of merit. Being a normalized parameter (see Eq.4.10), the TCR does not depend on V_{DS}. In Figures 7.6(a) and (b) the thermo-electrical characteristics of a representative device is shown, taken in a probe station with a T-controlled chuck, connected to a source-meter. The device has a pixel size of $100\times100\mu m^2$ and area ratio A_{C_3}/A_{C_2} ~22. The sample is placed on a chuck with T control and it is in thermal equilibrium in the dark, hence photon absorption

is disregarded. A gate voltage (V_{GS}) is applied to the device and Fig.7.6(a) shows the typical Dirac curve at an equilibrium temperature of 20°C. Whenever an active electrical probe is connected to the gate pad, it acts as a sink neutralizing all the charge generated by the pyroelectric material (C_3) on any T change. The vast majority of devices are slightly p-doped. Because of the passivation offered by the Al_2O_3 gate dielectric, the initial SLG doping does not show significant variations over several weeks. The gate probe is then removed to leave the gate structure floating. The GFET drain current I_{DS} is monitored, while T is raised by 0.2°C, kept constant for 10 minutes and then decreased to its original value. The resulting plot in Fig.7.6(b) shows that the drain current increases by ∼50% for a 0.2°C change (TCR∼250%/K), it is rather stable over time and then it returns to its original value with negligible hysteresis. The red star markers on the electrically driven Dirac curve in Fig.7.6(a) show how the SLG conductivity evolves when the gate is thermally driven as in Fig.7.6(b). This stable response over several minutes indicates that no appreciable leakage occurs through the pyroelectric crystal and/or the GFET gate within a practical measurement timeframe. The initial bump to 3.6μA in Fig.7.6(b) is due to the small overshoot of the chuck T at the end of the ramp.

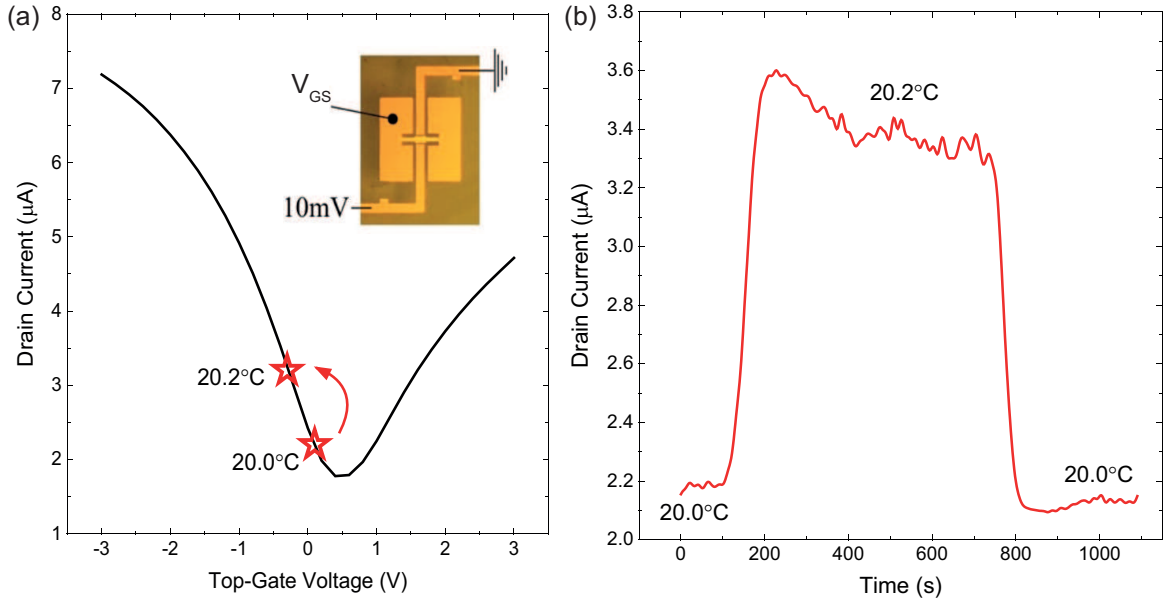

Figure 7.6: (a) Transfer characteristics of a typical device acquired by driving V_{TG}. (b) Response to a T change of the same device under floating gate conditions. Once plotted over the GFET Dirac curve in (a), the change in drain current shows that a T variation of 0.2°C corresponds to a ΔV_{TG} ∼0.44V

The NEP and the noise equivalent substrate temperature (NEST) is then calculated. The NEST is similar to the NEP, but it represent the device temperature change needed

to produce a signal comparable to the noise. To evaluate the NEST the normalized noise power spectrum for a representative device is measured as for Fig.7.7(a). The spectral density of the current fluctuations (S_I) is the Fourier transform of the drain current recorded during 100s with a sampling time of 1ms. The spectrum is dominated by a noise inversely proportional to the inverse of the frequency (ν^{-1}) up to 1 kHz, as reported for other SLG-based devices[234]. The channel area (L×W) normalized noise (S_I/I^2)(L×W) is $\sim 5 \cdot 10^{-7} \mu m^2/Hz$ at 10Hz, considering a $20 \times 30 \mu m^2$ SLG channel. This number slightly exceeds the typical range ($\sim 10^{-8} \mu m^2/Hz$) reported for SLG devices on SiO_2 (Ref.[234]). The NEST in bolometers can be measured as:

$$NEST = \frac{\sqrt{S_I/I^2}}{TCR} \tag{7.4}$$

thus, considering a pixel size of $100 \times 100 \mu m^2$ and a TCR of $\sim 214\%/K$, the device in Fig.7.6(b) shows a NEST$\sim$40mK$\cdot$Hz$^{-1/2}$ at 1Hz. For the biggest pixel size ($300 \times 300 \mu m^2$, TCR$\sim$600%/K), the minimum NEST is $\sim$15mK$\cdot$Hz$^{-1/2}$. For the MIR PD in Fig.7.3, this T resolution translates into a NEP$\sim 5 \cdot 10^{-7}$W$\cdot$Hz$^{-1/2}$ at 1Hz, where the NEP is calculated as:

$$NEP = \frac{\sqrt{S_I/I^2}}{R_{ext,N}} \tag{7.5}$$

this is almost one order of magnitude better than previous reports on graphene pyroelectric detectors[235].

To appreciate what these numbers mean in practice, Fig.7.7(b) depicts the response of a large device ($300 \times 300 \mu m^2$, TCR$\sim$600%/K) illuminated by the IR radiation emitted by a human hand at a distance of $\sim$15cm. In one test the sample is placed directly on a large (200mm diameter) metal chuck (with heat sink, blue data) and in another it is placed in a concave plastic box that keeps it suspended, thus more thermally isolated (without heat sink, black data). Without heat sink, the PD heats up more (hence larger device responsivity), but its response and recovery are much slower. Even with heat sink, the proximity of the hand is easily detected. It has to be noted that this result is achieved on a bulk (500μm-thick) LN substrate with a resistive measurement in air, indicating the huge potential of SLG-based pyroelectric bolometers.

Finally, here I discuss how TCR scales with A_{C_3}/A_{C_2}. Disregarding C_1, from Eq.7.2 a linear dependence is expected. However Figure 7.8 plots the measured TCR for several devices fabricated by keeping A_{C_2} constant ($22 \times 20 \mu m^2$) and varying A_{C_3} from $25 \times 25 \mu m^2$ to $300 \times 300 \mu m^2$. TCR up to 900%/K have been achieved in $300 \times 300 \mu m^2$ pixels. Data-

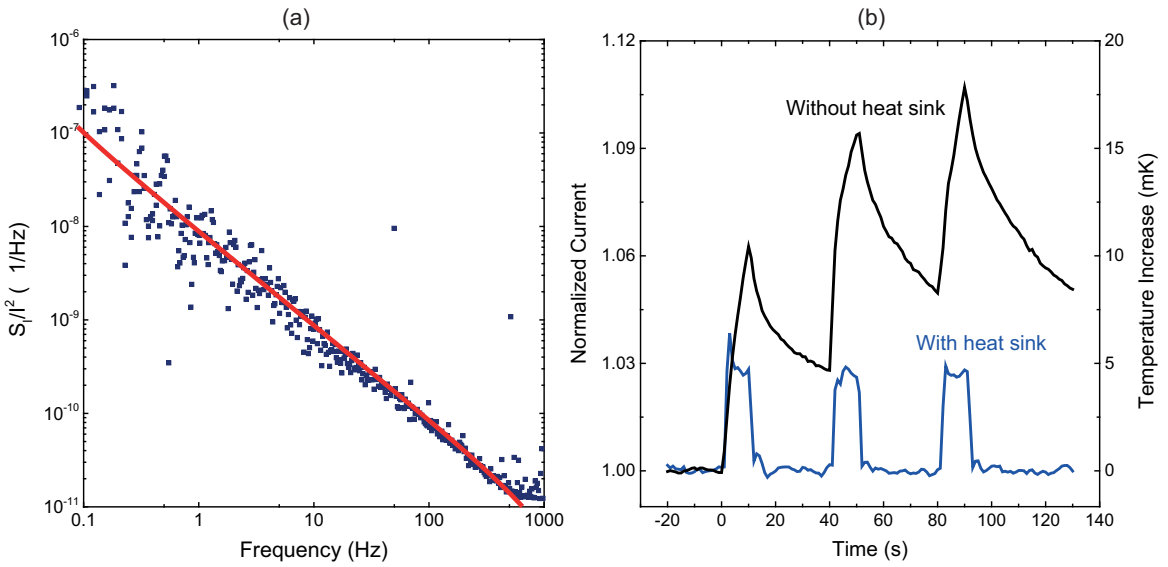

Figure 7.7: (a) Normalized noise spectrum density for a representative device at constant T, showing the typical ν^{-1} behaviour for SLG channels.(b) Normalized current response of a SLG pyroelectric bolometer to thermal body radiation (human hand at a distance ∼15cm). The local T increase is estimated from the TCR. The T transients change in amplitude and speed according to the heat sink efficiency.

points fit a square root dependence, indicated by the blue line. This behaviour cannot be explained by invoking the direct effect, whose contribution appears on a much smaller scale (TCR∼5%/K). Rather, we have to consider that the pyroelectric substrate does not end at the pads edge. Such pads are thus not driven just by the crystal below them (as assumed by a linear dependence on area), but can also be affected by the exposed polarization of their surrounding areas (an effect scaling linearly with perimeter, hence the square root dependence on area).

To better quantify this behaviour, Au pads of different sizes (0.01–0.3mm^2) were prepared on LN and the total charge generated on heating was measured (Fig.7.8(b)). This is accomplished by placing an electric probe on each pad, connecting the probe to ground and integrating the pyroelectric current flowing through the probe over the whole temperature ramp. In one case, the pads are kept isolated on the 1×1cm^2 pyroelectric surface and independent from each other. In another case, the whole surface around the pads is coated with Au and grounded during all measurements (with only a gap of 5μm uncoated around the pads). This is meant to suppress any contribution from areas beyond the pad footprint. Fig.7.8(b) shows that a square root dependence on the pad area is observed in both cases. The total pyroelectric charge decreases by a factor ∼2–3 on screening, but is still above what would be expected from a simple model

$\Delta Q/\Delta T = p_c A$, as for Eq.7.1[229]. This result has major technological implications, as it proves that a substantial contribution to the observed TCR enhancement for small A_{C_3} arises within the first few micrometres from the pad edge. It is then possible to harvest an enhanced pyroelectric charge in a dense array of small pixels, with only a tiny gap of few micrometres separating two adjacent devices.

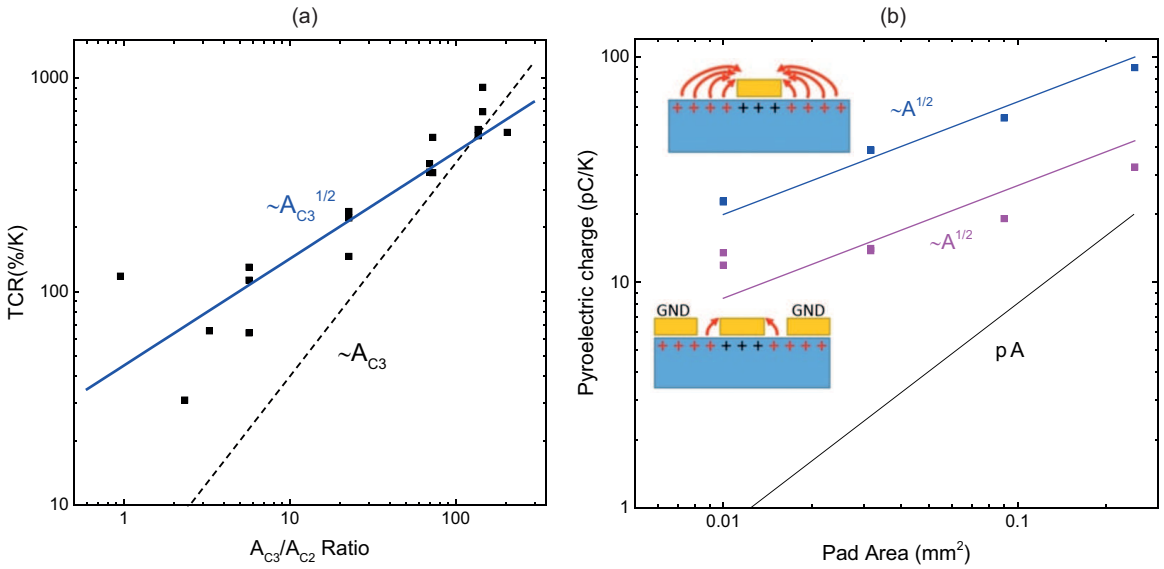

Figure 7.8: (a) TCR for several devices with different A_{C_3}/A_{C_2}, extracted from thermo-electrical measurements as in Fig.7.6(b). For decreasing A_{C_3}, the TCR follows a square root law (blue line) instead of a linear dependence (black dashed line). (b) Integrated pyroelectric charge per K measured for unscreened (blue) and screened (magenta) Au pads on z-cut LN. A square root scaling law with area is found in both cases, which explains the behaviour observed in (a). The black line represents the expected value without contribution from surrounding areas.

7.4 Conclusions

In conclusion, here I presented a graphene-based pyroelectric bolometer operating at room temperature with TCR up to ∼900%/K for a device area ∼300×300μm^2 able to resolve temperature variations down to 15mK at 1Hz. For smaller devices, the TCR scales sub-linearly with area, due to an enhancement of the collected pyroelectric charge in close proximity to the metallic edges. When used as MIR PDs, these devices deliver very promising performance (in terms of responsivity, speed and NEP) even on bulk substrates and are capable of detecting warm bodies in their proximity. This technology

is competitive on a number of levels, ranging from high-resolution thermal imaging (small pixel limit) to highly sensitive spectroscopy in the MIR.

Chapter 8

Flexible Graphene/MoS_2 Photodetectors

8.1 Introduction

Modern electronic and opto-electronic systems such as smart phones, smart glasses, smart watches, wearable devices and electronic tattoos increasingly require ultra-thin, transparent, low-cost and energy efficient devices on flexible substrates[236]. The rising demand for flexible electronics and optoelectronics requires materials which can provide a variety of electrical and optical functionalities, with constant performance upon application of strain[237]. A wide range of optoelectronic devices on flexible substrates have been reported to date, such as photodetectors (PDs)[238, 239], light emitting diodes (LEDs)[240], optical filters[241], optical interconnects[242, 243], photovoltaic devices[244, 245] and biomedical sensors[246, 247].

Major challenges in the development of flexible optoelectronic devices stem from the limitations associated with the high stiffness of bulk semiconductors[248, 249]. In the case of flexible PDs, the current approaches primarily rely on thin (μm-thick) semiconductor membranes[238, 250] and compound semiconductor nanowires (NWs)[239, 251–253], mainly because of their ability to absorb light throughout the whole visible range (0.4-0.7μm) and the possibility to adapt their fabrication techniques from rigid to plastic, or deformable substrates[236].

We have mentioned previously in the text the significance of responsivity in photodetectors and the possibility to split the definition in R_{ext} and R_{int}. In flexible PDs, R_{ext} up to $\sim$0.3A/W was reported for crystalline semiconductor membranes (InP, Ge)[238, 250] with integrated p-i-n junctions, showing photocurrent up to$\sim$ 100μA, with$\sim$ 30% degradation upon bending at a radius r_b $\sim$3cm[250]. PDs made of a single semiconductor NW

on flexible substrates[239, 251–253] demonstrated R_{ext} up to$\sim 10^5$A/W, for r_b down to 0.3cm[239]. Yet, these provide limited I_{ph} in the order of nA[239, 252, 253] up to less than 1μA[251]. For flexible devices exploiting NW-arrays by drop-casting, rather than based on single-NWs, R_{ext} degrades significantly from$\sim 10^5$A/W to the mA/W range, due to photocurrent loss at multiple junctions in the NW network[239, 252, 253].

Graphene and related materials (GRMs) have great potential in photonics and optoelectronics[25, 55, 115, 254]. A variety of GRM-based devices have been reported, such as flexible displays[255], photovoltaic modules[129, 130], photodetectors[115, 122, 127, 128], optical modulators[156], plasmonic devices[256–260], and ultra-fast lasers[254]. Heterostructures, obtained by stacking layers of different materials were also explored[55, 115], *e.g.* in photovoltaic[261] and light emitting devices[95].

Flexible PDs based on graphene and related materials (GRM) were studied for ultraviolet[123, 262], visible[263–268] and near infrared bands[269, 270]. In these devices, different materials and heterostructures produced by mechanical exfoliation[263, 264], CVD[265, 266, 269], and LPE[267, 268, 270] were employed. The flexible PDs produced by mechanical exfoliation[263, 264] have a small (μm^2) photoactive area, and they cannot be scaled up to mass production. LPE-based PDs have low (<mA/W)[267, 268] responsivity. Ref.[270] showed that thick (μm) films of chemically modified and charge-transfer optimized LPE/polymer composites can provide$\sim$A/W responsivity[270] at near infrared bands. Nevertheless, these PDs require high (10V) operation voltage and are non-transparent. Flexible PDs at 450nm using CVD MoS_2 transistors[265] and MoS_2/WS_2 heterostructures[266] were previously reported, and PDs at 780nm were prepared from doped SLG pn-junctions[123]. However, these devices have responsivity in the mA/W range. CVD-based SLG/MoS_2 heterostructures[121] showed good photodetection on rigid Si/SiO_2 substrates, with back-gate dependent R_{int} $\sim 10^8$A/W for optical intensities <0.1pW/μm^2.

Here I demonstrate a polymer electrolyte gated, CVD-based flexible PD for visible wavelengths with large (mm^2) photoactive area combined with high responsivity (hundreds A/W), high (>80%) transparency, gate tunability, low (<1V) operation voltage and stable ($\pm$12%) I_{ph} upon multiple (>30) bending cycles with bending radius <1.4cm. The device is assembled by stacking on a PET substrate a centimetre-scale CVD SLG on top of a CVD-grown single layer MoS_2 (1L-MoS_2). Given the responsivity, flexibility, transparency and low operation voltage (below $1V$), these PDs may be integrated in wearable, biomedical and low-power opto-electronic applications[246, 247, 251]. The results presented in this chapter have been published in Ref.[177].

8.2 Fabrication

Fig.8.1 plots a schematic drawing of the flexible PDs. In total I fabricated 4 PD arrays with 10 devices each, with channel lengths of 100μm, 200μm, 500μm and 1mm. Each device consists of a 1L-MoS_2 layer film used as an absorber covered by a SLG channel, clamped between source and drain electrodes. We chose PET as a flexible substrate due to its ∼90% transparency in the visible range[271] and ability to withstand solvents (*e.g.* acetone and isopropyl alcohol)[272] commonly used in the transfer processes of layered materials grown by CVD. A 1L-MoS_2 is used as absorber in order to preserve a >80% transparency, considered suitable by industry for wearable applications[273]. The assembly of the heterostructure has been discussed in Chapter 5.

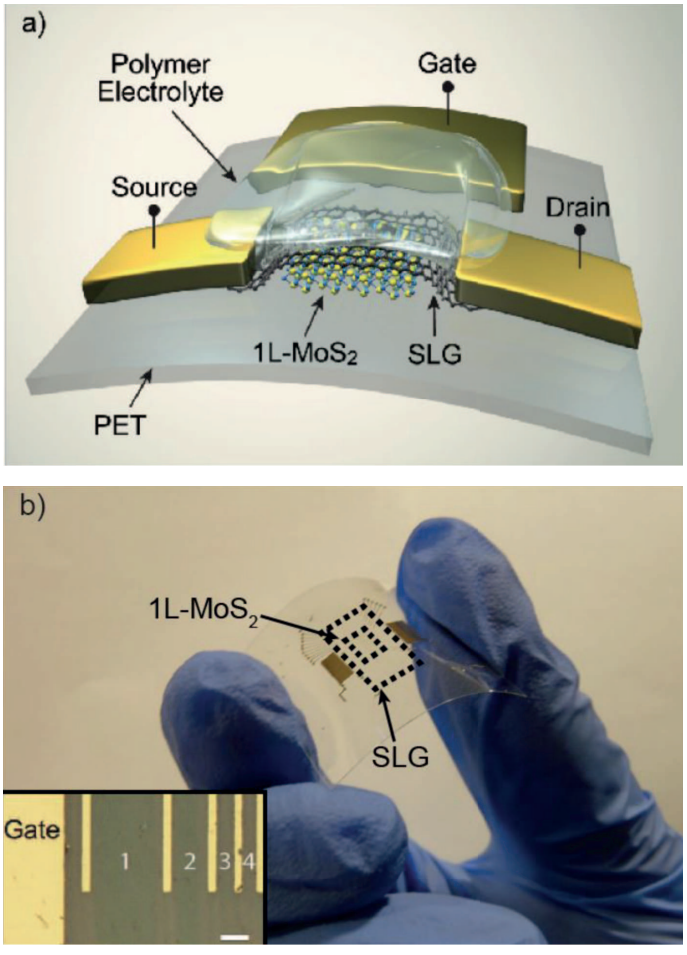

Figure 8.1: (a) Schematic SLG/MoS_2 flexible PD, side-gated with a polymer electrolyte. (b) Picture of a typical PD, showing transparency and flexibility. (Inset) Optical image of 4 PDs with different channel lengths and common side gate electrode. Scale bar is 200μm

The PD area is shaped by etching, whereby SLG extending beyond the 1L-MoS_2 layer is removed in an oxygen plasma, using a home-made shadow mask. The source-drain and gate electrodes are then defined by patterning the contacts area, followed by Cr/Au (6nm/60nm) evaporation and lift-off. PDs with different channels lengths (100μm-1mm), 2mm channel width and common side-gate electrodes (1cm $\times$ 0.5cm) are built (Fig.8.1(b)). The SLG/1L-MoS_2 heterostructure is gated using a polymer electrolyte[76, 165].

Ref.[121] showed that the responsivity of SLG/MoS_2 PDs can be enhanced by gating. This induces a stronger electric field at the SLG/MoS_2 interface and promotes charge transfer from the MoS_2 absorber to the SLG channel. Various gating techniques have been exploited for GRM-based devices, including conventional Si/SiO_2 back-gates[18], high-k dielectrics (Al_2O_3, HfO_2)[274], chemical dopants[275], ionic liquids[276] and polymer electrolytes (PE)[76, 166]. In order to gate our SLG/1L-MoS_2 on PET, we employ the latter due to its compatibility with flexible substrates[277] and the ability to substantially dope SLG ($\pm 0.8eV$)[76, 166] using small gate voltages (up to 4V), unlike other gating techniques, which would require higher biases to reach the same doping[18, 275].

The polymer electrolyte (PE) gating technique is based on the concept of an electrical double layer (EDL). To form the EDL in a transistor geometry an electrolyte is filled between a gate electrode and the sample. Whenever, for example, a positive voltage V_{GS} is applied, ions of opposite sign present in the electrolyte start migrating in opposite directions due to the electric field and accumulate at the surface of the gate electrode and that of the sample (Fig.8.2). When steady state is reached an EDL capacitor at the gate electrode surface is formed by the sheet of ions and a layer of accumulated space charge in the solid. The same happens at the surface of the sample[278]. These EDLs are typically $\sim$1nm thick and they thus show a very high capacitance, which I estimate later on in this chapter, enabling the possibility of achieving doping concentrations up to $n \sim 10^{14}$-10^{15}cm^{-2}.

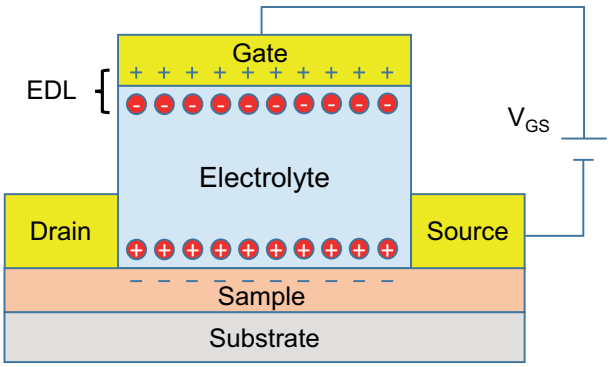

Figure 8.2: Schematic working principle of an electric double layer transistor

I used a PE consisting of lithium perchloride ($LiClO_4$) and polyethylene oxide (PEO)[76, 166]. The PE is placed over both the SLG channel and the side-gate electrode as for Fig.8.1. I evaluated the effect of PE deposition on the SLG channel doping by means of Raman spectroscopy and found negligible variation of the doping level with no bias applied. For electrical measurements low voltages need to be applied $-1V < V_{GS} < 1V$ in order to avoid electrochemical reactions, such as hydrolysis of residual water in the electrolyte[279, 280]. These reactions may permanently modify the graphene electrode[279, 280], and compromise the stability and performance of the device. To control the stability of the PE gating the gate leakage current (I_{gate}) is continuously monitored and kept below 1nA throughout the experiments. The devices were measured many times, showing no degradation in the leakage current over at least six months.

The expected operation principle of these devices is depicted in Fig.8.3. For energy bands alignment, the electron affinity of 1L-MoS_2 and the Dirac point of SLG are assumed to be∼4-4.2eV[281, 282] and∼4.6eV[283, 284], respectively. SLG is assumed to be initially p-doped (Fig.8.3(a), as reported in previous works involving SLG transferred on PET[285, 286]. At zero voltage the device is in thermodynamic equilibrium with a constant Fermi level (E_F) across the structure and zero current flow between the layers. SLG is initially p-doped (Fig.8.3(a)), so that E_F is initially located below the Dirac point. During illumination and photon absorption in MoS_2, part of the photo-generated electrons would be injected from the 1L-MoS_2 conduction band into the lower energy states in p-doped SLG[121], leaving behind the uncompensated charge of photogenerated holes. The latter would be trapped in 1L-MoS_2 and act as an additional positive gate voltage, V_{GS}, applied to the SLG channel, resulting in a shift of the charge neutrality point (V_{CNP}) to more negative voltages. In p-doped SLG, the injected electrons from 1L-MoS_2 would occupy energy states above E_F (Fig.8.3(b)), thus reducing the holes concentration and decreasing the holes current in the SLG channel. Electron injection can be further promoted by gating. When negative V_{GS} is applied, higher p-doping of the SLG channel would induce a stronger electric field at the SLG/1L-MoS_2 interface[121], thus favoring electron transfer from 1L-MoS_2 (Fig.8.3(b). Hence, for negative V_{GS}, R_{ext} is expected to increase, due to injection of more photo-electrons to SLG and consequent more pronounced PD current reduction.

The opposite should happen for positive V_{GS}, where the gate-induced negative charge in SLG would reduce the p-doping and shift E_F towards the Dirac point. In this case, the photogenerated electrons in 1L-MoS_2 would experience weaker electric fields at the SLG/1L-MoS_2 interface[121], and would become less attracted by the SLG channel. Thus, we expect R_{ext} to decrease. For high enough positive V_{GS}, E_F crosses the Dirac

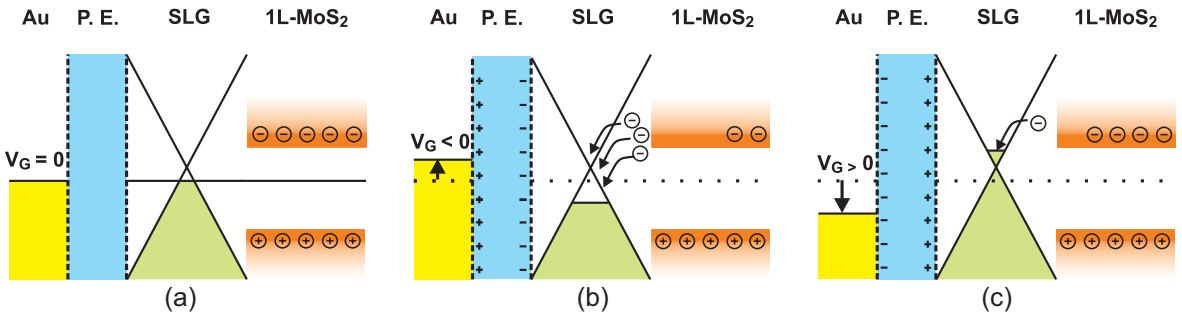

Figure 8.3: Schematic band diagram of polymer electrolyte (PE) gated SLG/1L-MoS_2 PD at (a) zero, (b) negative and (c) positive V_{GS}

point, and SLG becomes n-doped (Fig.8.3(c)). As a result, only a weak electron injection from 1L-MoS_2 would be possible, if E_F in SLG remains below the 1L-MoS_2 conduction band, retaining a weak electric field at the interface. In this regime, the transferred electrons increase the free carrier concentration in the n-doped channel, hence only minor increments of R_{ext} and I_{ph} are expected.

8.3 Results

The responsivity is characterized at 642nm (∼1.93eV), slightly above the A exciton peak, where absorption of 1L-MoS_2 is maximized (Fig.5.19(b)). At 642nm the SLG/1L-MoS_2 heterostructure shows ∼8% absorption and the device retains ∼82% transparency (Fig.5.19(a)).

The $I_{DS} - V_{GS}$ measurements in Fig.8.4(a) are taken at room temperature using a probe station and a parameter analyzer (Keithley 4200). The PD is illuminated at normal incidence by a collimated laser with P_o ranging from 100μW to 4mW. At these P_o and with $V_{DS} = 0.1$V we measure a positive V_{CNP} ranging from∼ 0.39V to 0.47V, indicating an initial SLG p-doping∼220meV (n∼$3{\cdot}10^{12}$cm^{-2}), consistent with the Raman estimate. The doping is calculated from Eqs.4.25 and 4.33, by using V_{GS} as gate voltage and C_{tot} as the polymer electrolyte gate capacitance calculated below.

Fig.8.4(a) shows that, for -1V$<V_{GS} < 0.5$V where SLG transport is hole dominated, the current decreases under illumination (∼ 10μA at $V_{GS} = -1$V), because of the SLG becoming more intrinsic, as anticipated from the band-diagram of Fig.8.3. For $V_{GS} > 0.5$V, where SLG is electron-doped, the PD shows a small (up to∼ 0.2μA) current increase under illumination. Fig.8.4(b) plots R_{ext} as a function of V_{GS}, as derived from transconductance measurements using Eq.6.6. As expected from the band-diagram in Fig.8.3, R_{ext} tends to increase for more negative V_{GS}, up to∼ 5.5A/W at $V_{GS} = -1$V,

$V_{DS} = 0.1$V for $P_o = 100\mu$W. By taking into account that only 8% of light is absorbed ($P_{abs} = 0.08 \cdot P_o$), it is possible to derive $R_{int} = R_{ext}/0.08 = 69$A/W. A bolometric effect could be at the origin of minor changes in the slope of the $I_{DS} - V_{GS}$ curve, due to a light-induced change in mobility of SLG.

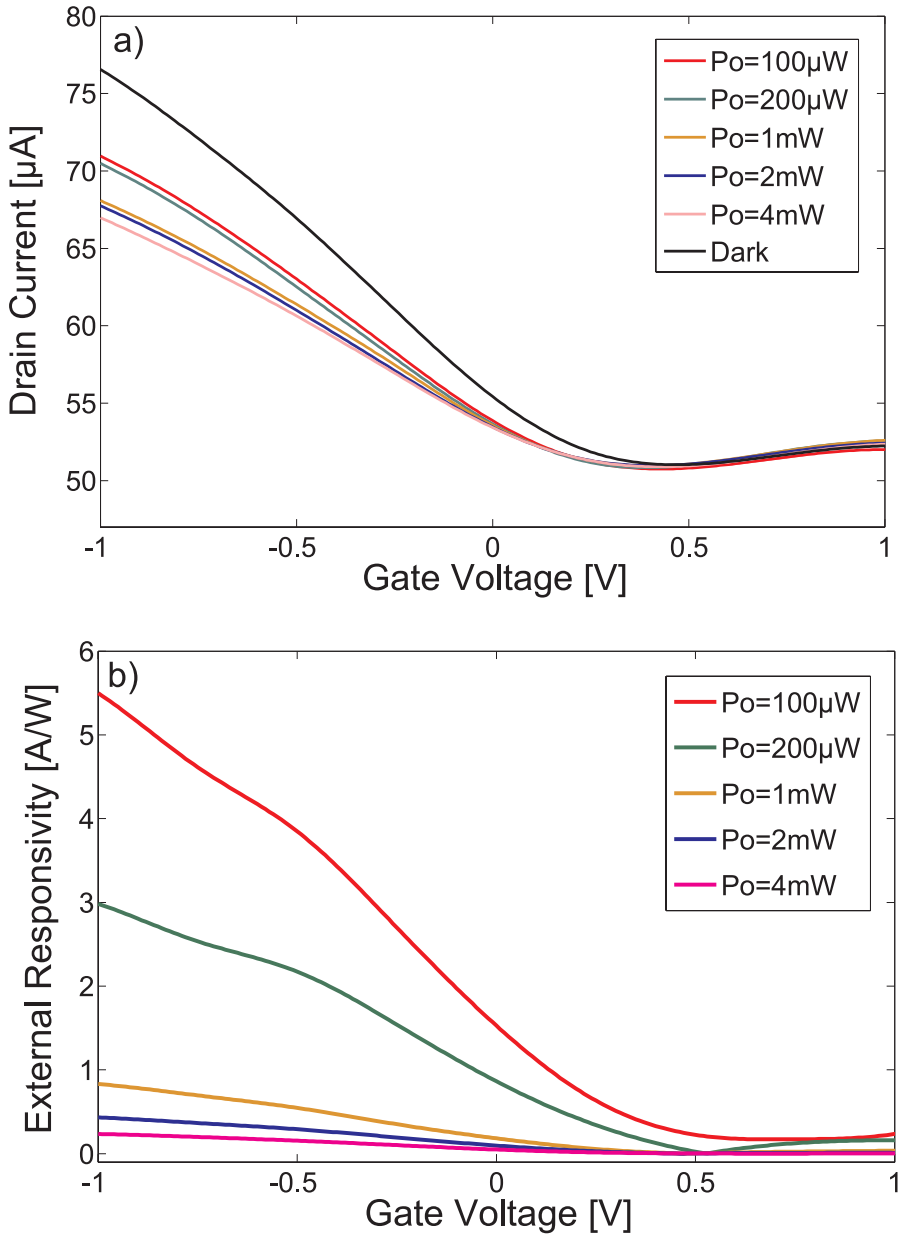

Figure 8.4: (a) Transfer characteristics as a function of P_o. (b) R_{ext} as a function of V_{GS} and P_o. Channel length and width are 100μm and 2mm respectively.

Fig.8.4(b) implies that the higher P_o, the lower R_{ext}. This can be explained considering that the more photo-generated electrons are injected into the p-doped channel, the lower

the electric field at the SLG/1L-MoS_2 interface, therefore a reduced injection of electrons causes R_{ext} to decrease.

Given that $R_{ext}, R_{int} > 1$A/W, the presence of a photoconductive gain (G_{ph}) is expected, as anticipated in Chapter 4[1, 119], whereby absorption of one photon results in multiple charge carriers contributing to I_{ph}. These PDs act as optically-gated photoconductors, where the SLG conductance is modulated by optical absorption in the 1L-MoS_2. In this configuration, the presence of G_{ph} implies that the injected electrons in SLG can recirculate multiple times between source and drain, before recombining with trapped holes in 1L-MoS_2. Consequently, G_{ph} can be estimated as the ratio of electron recombination (τ) and transit ($t_{transit}$), as for Eq.4.5 [1, 55, 115, 119]. For higher V_{DS}, the free carriers drift velocity v_d in the SLG channel increases linearly with bias (Ohmic region) until it saturates, because of carriers scattering with optical phonons[287]. The linear increase in v_d results in shorter $t_{transit}$, with $t_{transit} = L/v_d$, where L is the channel length[1, 55, 115, 119]. Therefore, G_{ph} is also expected to grow linearly with V_{DS}, providing higher R_{ext}. To confirm the photoconductive nature of G_{ph} in our devices and test the dependence of R_{ext} on V_{DS}, I measured $I_{DS} - V_{DS}$ under illumination at $P_o = 100\mu W$ for $V_{GS} = -1V$ and calculate R_{ext} using Eq.6.6. The $I_{DS} - V_{DS}$ characteristics of the PD show linear dependence, confirming Ohmic behavior of the metal-SLG-metal channel[288]. I used $V_{DS} < 1$V to keep the device operation in the linear (Ohmic) regime and minimize the effects of the non-linear dependence of v_d on V_{DS} (such as velocity saturation) that might appear for $V_{DS} > 1$V[287].

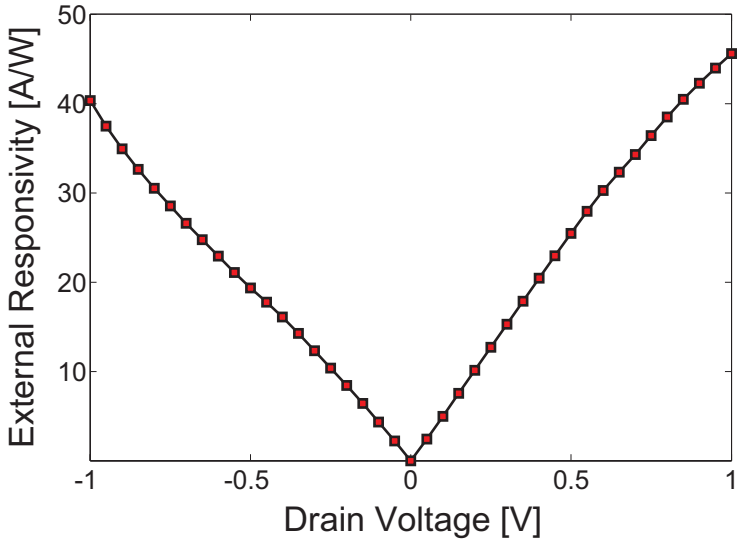

Figure 8.5: R_{ext} as a function of V_{DS} for $P_o = 100\mu$W at $V_{GS} = -1$V.

As shown in Fig.8.5, R_{ext} scales with V_{DS} and reaches$\sim$ 45.5A/W ($R_{int} \sim$ 570A/W) at $V_{DS} = 1$V. This is almost one order of magnitude higher than at $V_{DS} = 0.1$V, consistent with the similar increase in V_{DS}. These results are at least two orders of magnitude higher than semiconductor flexible membranes[238, 250]. Furthermore, such a combination of high (hundreds A/W) responsivity with μA range photocurrent surpasses that found in other GRM-based PDs in the visible range[263–268, 270]. I also fabricated a control device with a 1L-MoS_2 channel only, without SLG. This device has $R_{ext} \sim$ 2mA/W, which is four orders of magnitude smaller than that of the SLG/1L-MoS_2 heterostructure. It is thus possible to conclude that SLG/1L-MoS_2 heterostructures are necessary to achieve high (hundreds A/W) responsivity, due to the presence of photoconductive gain.

To assess the photoresponse uniformity in SLG/1L-MoS_2 heterostructures, photocurrent mapping was performed using the same laser source (642nm) as for opto-electronic characterizations. Scan areas of 80μm $\times$ 140μm (pixel size 3μm $\times$ 3μm) were taken at different locations. At each position (pixel) the device photocurrent is measured (Fig.8.6(a)), while V_{DS}=0.3V is applied. Backscattered light is also collected to give a reflection map (Fig.8.6(b)). Fig.8.6(a) indicates that the entire channel area confined between the source-drain electrodes is photoactive and shows uniform photocurrent photoresponse with standard deviation $\pm$15%. Interface imperfections (*e.g.* bubbles, polymer residuals, *etc.*) have minor effect on the charge transfer process from MoS_2 to graphene.

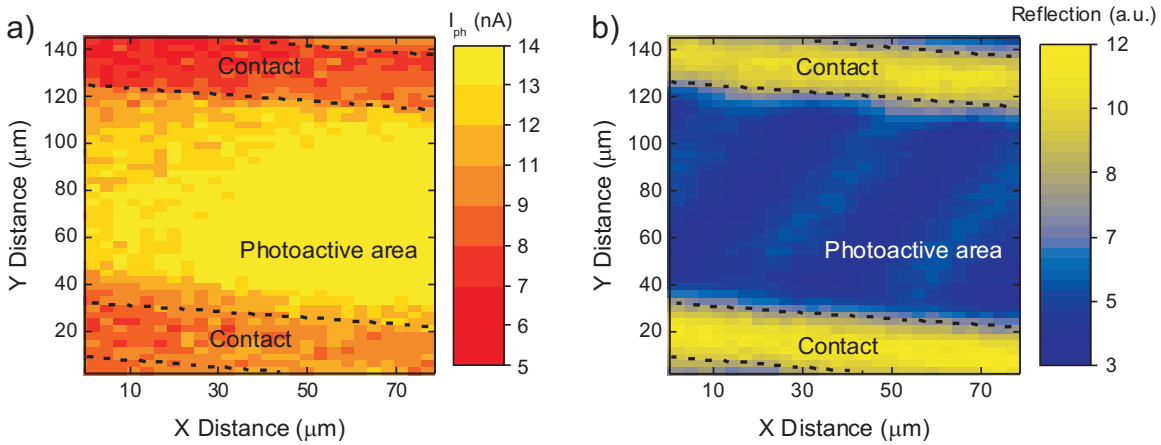

Figure 8.6: (a) Photocurrent map of channel area, simultaneously measured with backscattered light map. A uniform signal is observed in the channel area (between the electrodes). (b) Reflection map of backscattered light from the device channel. The yellow areas, corresponding to the contact areas, show higher reflectance than the substrate (in blue).

G_{ph} in this PD can also be calculated as the ratio between the electrons recirculating in the SLG channel, thus sustaining I_{ph}, and the initial electron concentration injected into SLG from 1L-MoS_2[121]:

$$G_{ph} = \frac{I_{ph}/q}{A_{PD} \cdot \Delta n_{ch}} \tag{8.1}$$

where q is the electron charge and Δn_{ch} is the concentration per unit area and per unit time of the injected electrons. Δn_{ch} is equal to the trapped-hole concentration in 1L-MoS_2, which is related to a charge neutrality point shift $\Delta V_{GS} = \Delta V_{CNP}$ in the transfer characteristics. To calculate Δn_{ch}, we can first write the potential balance in the metal-dielectric-SLG structure. When V_{GS} is applied, it creates a gate-to-channel potential drop (V_{diel}), and it induces a local electrostatic potential in the graphene channel ($V_{ch} = E_F/q$)[1, 76]:

$$V_{GS} = V_{diel} + V_{ch} = \frac{Q_G}{C_G} + V_{ch} \tag{8.2}$$

where Q_G and C_G are the charge concentration and the geometrical capacitance per unit area associated with the gate electrode respectively. $|Q_G| = |q \cdot n|$, with n the charge carrier concentration per unit area in the channel. Any variations of Δn change ΔV_{GS}. As a result:

$$\frac{dV_{GS}}{dQ_G} = \frac{1}{C_G} + \frac{dV_{ch}}{dQ_G} \tag{8.3}$$

which leads to:

$$\Delta Q_G = (1/C_G + 1/C_Q)^{-1} \cdot \Delta V_{GS} \tag{8.4}$$

where $C_Q = dQ_G/dV_{ch}$ is the SLG quantum capacitance[289, 290] that characterizes the changes of the channel potential ΔV_{ch} as a result of additional gating ΔQ_G, and $C_{tot} = (1/C_G + 1/C_Q)^{-1}$ is the total capacitance .

To calculate Q_G we first need to find C_G and C_Q. In PE gating, C_G is associated with the EDL at the SLG/electrolyte interface[76, 290–292]. The EDL acts like a parallel-plate capacitor with a dielectric layer thickness of the order of the so-called "Debye length" λ_D, so that $C_G = C_{EDL} = \epsilon\epsilon_0/\lambda_D$, where ϵ is the PE dielectric constant, and ϵ_0 is the vacuum permittivity. In principle, for a monovalent electrolyte, λ_D can be explicitly calculated[293] if the electrolyte concentration is known. However, in the presence of a polymer matrix, the electrolyte ions can form complexes with polymer chains[294], therefore the precise ion concentration is difficult to measure. For PE gating, different

EDL thicknesses in the range$\sim$ 1-5nm have been reported[76, 165, 291, 292]. To estimate C_{EDL} in these devices I took $\lambda_D \sim 2$nm[76] and the dielectric constant of the PEO matrix to be $\epsilon \sim 5$[295], as done in Ref.[76]. As a result, a $C_{EDL} = 2.2 \times 10^{-6}\text{F/cm}^2$ is obtained. This is the same order of magnitude as the SLG C_Q[290]. Therefore the latter cannot be neglected in Eq.8.4. C_Q is given by[290]:

$$C_Q \approx \frac{2q^2}{\hbar v_F \sqrt{\pi}} \cdot \sqrt{n} \tag{8.5}$$

Using Raman I estimated $n \sim 3 \cdot 10^{12}\text{cm}^{-2}$ at zero bias. From Eq.8.5 $C_Q = 4 \cdot 10^{-6}\text{F/cm}^2$. The absolute shift between the charge neutrality point V_{CNP} in dark and upon illumination at each optical power is extracted from 8.4(a) and plotted in Fig.8.7(a). Δn_{ch} can then be obtained relying on the following equation:

$$\Delta n_{ch} = \frac{C_{tot} \Delta V_{CNP}}{q} \tag{8.6}$$

from Eq.4.23. These result in a Δn_{ch} ranging from $4 - 8 \cdot 10^{11}\text{cm}^{-2}$ for P_o going from 100μW to 4mW. As a result, a $G_{ph} \sim 5 \times 10^4$ is obtained at $V_{DS} = 0.1V$ for different P_o as shown in Fig.8.7(b). The gain is constant at fixed V_{DS} in the optical power range used for measurements (100μW-4mW). This is because at high optical powers most charge traps in MoS_2 are saturated and I_{ph} grows proportionally with the number of induced charges in SLG. As discussed previously, G_{ph} becomes larger for higher V_{DS}. Thus, an increase of almost one order of magnitude is measured ($G_{ph} \sim 4 \cdot 10^5$ at $P_o = 100\mu$W) for V_{DS} going from 0.1V to 1V.

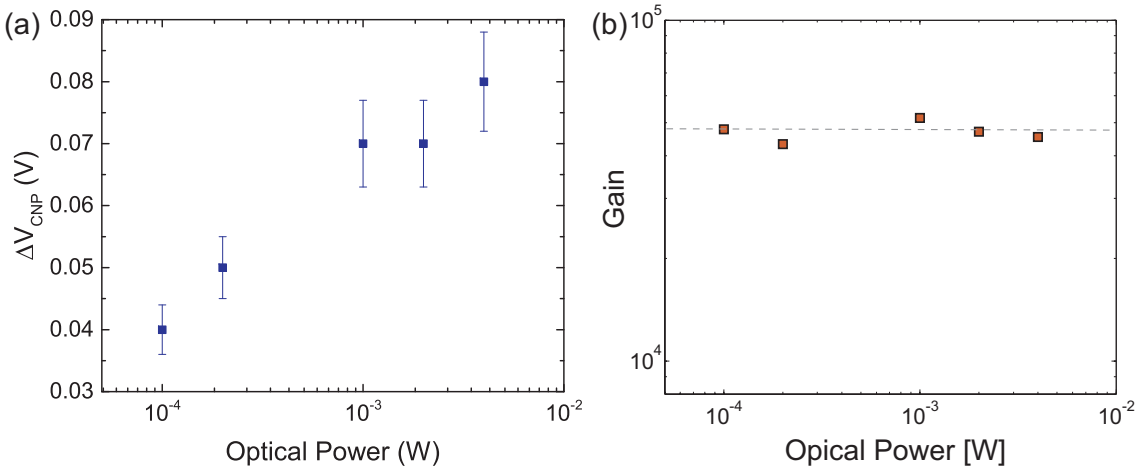

Figure 8.7: G_{ph} as a function of P_o at $V_{GS} = -1V$ and $V_{DS} = 0.1V$.

In order to further assess the performance of the SLG/1L-MoS_2 heterostructure I studied the timescale of the charge transfer process. This study has been performed by pump-probe spectroscopy. Fig.8.8(b) shows normalized differential transmission ($\Delta T/T$) dynamics, as discussed in Chapter 2, with a 400nm ($\sim$3.1 eV) pump and a 660nm probe ($\sim$1.9eV), while increasing V_{GS} from -1V to 0V.

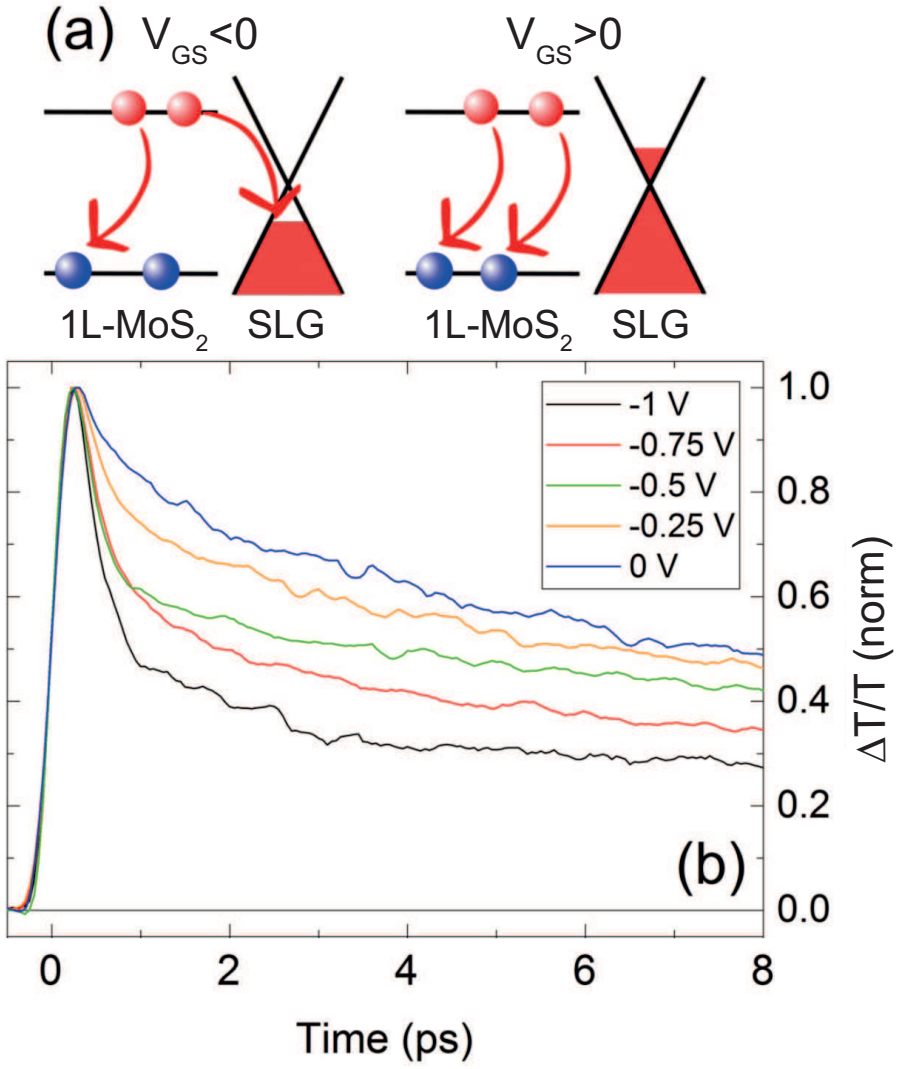

Figure 8.8: Pump-probe signature of ultrafast charge transfer in the layered heterostructure. (a) Sketch of the charge transfer process. At V_{GS}<0 the charge transfer is promoted, but it becomes progressively hindered due to smaller electric field between 1L-MoS_2 and SLG toward more positive V_{GS} (b) Pump-probe dynamics as a function of the top-gate voltage for 400nm pump and 660nm probe. The pump fluence is $\sim 1.8 \mu J/cm^2$

The pump photon energy lies well above the MoS_2 band-gap while the probe photon energy is chosen to be resonant with the A-exciton transition. The positive $\Delta T/T$ signal

is generated by absorption of MoS_2 (photo-bleaching). The absorption of photons and consequent generation of photo-carrier indeed blocks (Pauli blocking) further transitions and increases the transmission ($\Delta T/T > 0$). The contribution to the differential optical changes due to excitation of graphene is negligible: the decay of the signal in graphene would indeed decay to zero in ∼2ps, much faster than MoS_2. The thermalization of photo-carriers from the excited state to the edge of the conduction band happens in a timescale below the setup resolution. From a bi-exponential fit, for all the gate voltages between -1V and 0V, a fast recombination time of $\tau_1 \sim 300$fs and a slower one of $\tau_2 \sim$ 6ps is obtained. While the two recombination times are independent from the gate voltage, their relative weights show a strong V_{GS}-dependence. In particular, the fast component represents ∼80% of the total signal at -1V and it drops down to less than 50% at 0V. The slow component τ_2 is consistent with the recombination dynamics observed in monolayer MoS_2 [296]. The ultrafast component τ_1 is related to charge transfer from MoS_2 to graphene, which is hindered in the case of more positive voltages as shown in the concept of Fig.8.8(a). The efficiency of the transfer of photogenerated charges in this device is therefore up to 80% in the case of -1V V_{GS}.

Finally, I tested I_{ph} as a function of bending using a Deben Microtest three-point bending setup (Fig.8.9(a)). The bending radius r_b is estimated as:

$$r_b = \frac{h^2 + (L/2)^2}{2h} \tag{8.7}$$

where L is the chord of circumference connecting the two ends of the arc, and h is the height at the chord midpoint. The plotted values of I_{ph} in the bent state at each r_b ($I_{ph,bend}$) are normalized to the value of I_{ph} measured at rest with the sample in flat position ($I_{ph,rest}$). Fig.8.9(b) plots the normalized $I_{ph,bend}/I_{ph,rest}$ for different r_b, showing deviations within 15% for r_b down to 1.4cm. Our value of r_b is comparable to that reported for semiconductor membrane PDs[238, 250], yet the latter show two orders of magnitude lower (< 0.3A/W) responsivities[238, 250]. Although r_b is five times larger than the one reported by flexible single NW devices[239, 251–253], the device area of the tested PD ($> 40\text{mm}^2$) is at least six orders of magnitude larger compared to the single NW devices ($< 5\mu\text{m}^2$). To test the device performance upon bending cycles, photocurrent is re-measured at rest ($I_{ph,rest}$, flat position) and then at the maximum bending (*i.e.* smallest bending radius) allowed by our setup ($I_{ph,bend}$ bending radius 1.4cm), repeating these measurements for 30 bending cycles. Fig.8.9(c) plots $I_{ph,bend}/I_{ph,rest}$ as a function of bending cycles. This shows that our PDs retain stable photocurrent after multiple bending tests with a $I_{ph,bend}/I_{ph,rest}$ standard deviation ±12%.

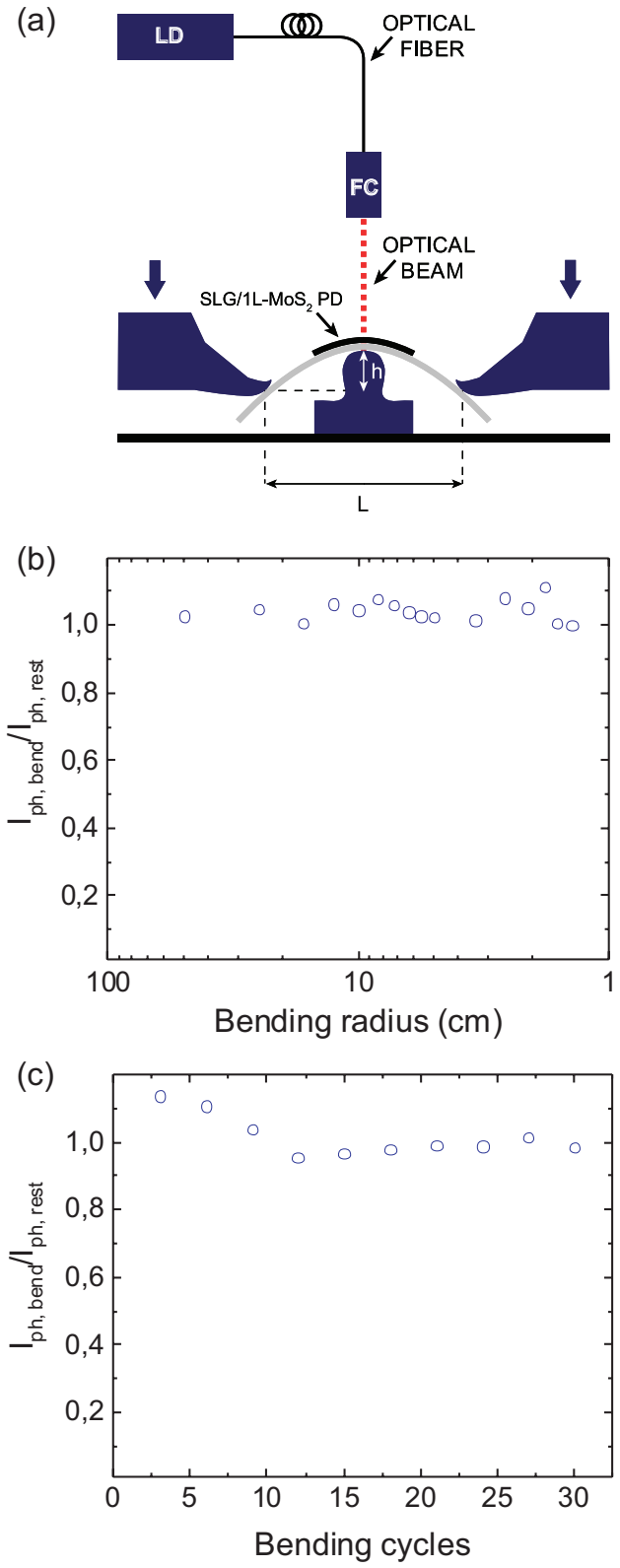

Figure 8.9: (a) Schematic three-point bending setup. LD = laser diode; FC= fiber collimator; (b) $I_{ph,bend}$ normalized to the value at rest $I_{ph,rest}$ as a function of r_b; (c) $I_{ph,bend}$ normalized to the value at rest $I_{ph,rest}$ upon several bending cycles

8.4 Conclusions

In this chapter I report polymer electrolyte gated flexible photodetectors for visible wavelengths with external responsivity up to$\sim$45.5A/W, photoconductive gain of 4×10^5, operation voltage < 1V and optical transparency $> 82\%$. The responsivity is at least two orders of magnitude higher than in semiconductor flexible membranes. The devices show stable performance upon bending for radii of curvature larger than $\sim$1.4cm. Owing to their responsivity, flexibility, transparency and low operation voltage, SLG/1L-MoS_2 flexible photodetectors can be an attractive candidates to be integrated in wearable, biomedical and low-power opto-electronic applications[246, 247, 251].

Chapter 9

Superconducting Transport in Layered Materials

9.1 Introduction

Superconductivity (SC) is an intriguing phenomenon first discovered in 1911 by H. K. Onnes, while studying mercury at low temperatures, and only a few years after that helium was successfully liquefied[141]. The name given to this phenomenon was inspired by one of its most important hallmarks, *i.e.* the abrupt disappearance of the electrical resistance of the cooled material below a certain critical temperature T_C[141]. Since the discovery of SC many theories have been formulated and, in parallel, many new superconductors where unveiled with T_C even exceeding 200K ($\sim$-73°C) at high pressures (155GPa)[297]. The Bardeen-Cooper-Schrieffer (BCS) theory describes well the origin of SC in conventional superconductors: at sufficiently low temperatures an electron would be able to attract positive ion cores in the surroundings, creating a positively-charged region. A second electron, typically with opposite momentum and spin, would be attracted by this charged region forming a so-called "Cooper pair" (CP). The interaction of CPs is a long-range interaction (up to hundreds of nm). Being formed by a bound state of two electrons, CPs have a total integer spin and behave as bosons, rather than as fermions. This implies that, unlike fermions (*e.g.* electrons), CPs can occupy and condense in the same ground state, leaving a energy gap 2Δ in the density of states. Δ is related to the binding energy of CPs, and it has been experimentally measured that $2\Delta(0) \simeq 3.5 k_B T_C$ at $T \rightarrow 0$K, with k_B being the Boltzmann constant[141]. This gap is therefore the energy required to break a Cooper pair apart and, as mentioned in Section 4.2.4, it is typically of the order of 1meV in conventional superconductors[141].

For many years scientists have tried to unravel the relation between thickness of a material and superconductivity[8, 298–300]. Although a definitive conclusion has not yet been found, there is consensus over the fact that properties of superconductors are expected to be deeply different at the two dimensional limit, due to the confinement of motions of electrons and the formation of discrete electronic states[299, 300]. Most studies in ultra-thin films have reported a reduction of the T_C with decreasing thickness[301–304]. However, typically structural defects in the films were at the origin of the T_C reduction[299, 300]. Ref.[305] showed that growing a high-quality monolayer film of iron selenide (FeSe) by MBE on strontium titanate can yield a film with a T_C ∼109K, more than 10 times higher with respect to that of the bulk, proving the great potential of high-quality ultrathin films.

The rise of layered materials, has enabled the possibility to isolate high-quality, ultra-thin layered flakes with unprecedented control on thickness[43]. This chapter, serving as preamble for Chapter 10, summarizes the studies I performed on the superconducting properties of SLG, MoS_2 and $NbSe_2$, *i.e.* a semimetal, a semiconductor and a superconductor, respectively. This dissertation is applications-oriented, therefore SC will mostly be addressed from a phenomenological point of view, rather than a theoretical one.

9.2 Proximity effects in graphene on PCCO

Conventional superconductors possess a gap Δ independent from momentum $\mathbf{k}$, thus with a spherical symmetry (s-wave) in the momentum space. From a practical point of view, this implies that an equivalent amount of energy has to be generated for each random direction of a superconducting crystal lattice to break a CP apart. Unconventional superconductors however do exist. They are characterized by a momentum-dependent Δ=$\Delta(\mathbf{k})$ and classified similarly to atomic orbitals (p-,d- and f-wave), depending on the symmetry of $\Delta(\mathbf{k})$ in the momentum space. In this case, the energy required to break CPs can be different, as well as zero, in some crystallographic directions, which are called "nodal directions".

When cooled down to low temperature SLG does not show superconducting properties [306]. However SC has been induced in SLG either by doping with lithium (Li) atoms[307], or by intercalating SLG sheets with calcium (Ca) atoms[308], or by proximity with another superconductor[309]. PCCO is an high-temperature cuprate superconductor. Its chemical formula is $Pr_{2-x}Ce_xCuO_4$ and the symmetry of $\Delta(\mathbf{k})$ and T_C can vary depending on the composition/doping (x). In particular for hole-doping (x <0.13) PCCO shows a d-wave symmetry, which leaves the way to an isotropic s-wave symmetry for electron

doping (x >0.13). In this disseration I report a scanning tunnelling microscopy (STM) investigation of SLG placed on the electron-doped superconductor PCCO to probe the possibility of inducing unconventional superconductivity in SLG via a proximity effect. The results here discussed are published in Ref.[310], which I co-authored. A PCCO film (200-nm-thick) was grown on (001) oriented $SrTiO_3$ (STO) by Dr Angelo Di Bernardo and co-workers. The film showed a T_C of ∼20K. I grew SLG by CVD and transferred it on top of PCCO/STO as explained in Sect.5.3 and 5.4. Furthermore characterization by Raman spectroscopy has also been discussed in Sect.5.4.

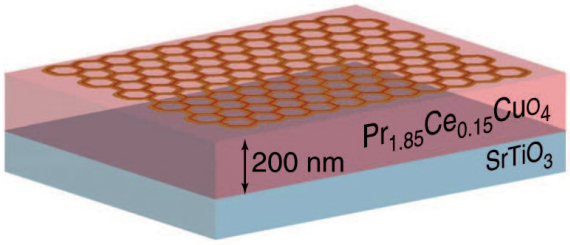

Figure 9.1: Schematic picture of the SLG/PCCO/STO structure.

STM or Scanning Tunneling Spectroscopy (STS) can be used to acquire topographic maps of a given sample and correlate them to its local density of states as a function of energy. In a STS experiment, a conducting tip is brought very close to the sample (at a distance typically less than 1 nm), and a voltage V is applied between the tip and the sample, which allows a current I to flow across due to quantum tunneling. Topographic images of the surface can be obtained by rastering the tip across the sample, while maintaining a fixed current and varying the sample-tip distance. Alternatively, by using the tunneling spectroscopy mode (STS), one can fix the tip position and locally measure the variation of the current ($\mathrm{d}I/\mathrm{d}V$) flowing in the tip as a function of the applied V bias. Electrons can indeed tunnel in unoccupied states (V >0) or out of occupied states (V <0) at energy $E \sim qV$[311]. This gives a quantification of the local density of states (LDOS). When probing conventional superconductors at $T \to 0$, $\mathrm{d}I/\mathrm{d}V$ is ∼0 at small biases V. Indeed we are in the SC gap Δ and there are no available states for electrons to tunnel in or out from. If the sample is fed with enough energy to break CPs (*i.e.* $E = qV \simeq \Delta$) a variation in $\mathrm{d}I/\mathrm{d}V$ is recorded. At finite temperatures these spectra assume a classical U-shape, which progressively disappears toward reaching the T_C.

STS measurements were performed by Prof. Oded Millo at the Hebrew University of Jerusalem, Israel. STS spectra were measured at 4.2K and correlated with the surface topography (Fig.9.2). On the one hand, spectra of PCCO/STO always show

V-shaped gaps[312, 313]. On the other hand, spectra recorded in different regions of SLG/PCCO/STO show either V-shaped gaps (Fig.9.2 (a)) or a sub-gap structure, including the so called zero-bias conductance peaks (ZBPCs) and split ZBCPs (Fig9.2(b-c)). V-shaped gaps are observed in about ∼45% of the scans, while in all the other areas either ZBCPs (∼30%) or split peaks (∼25%) are observed.

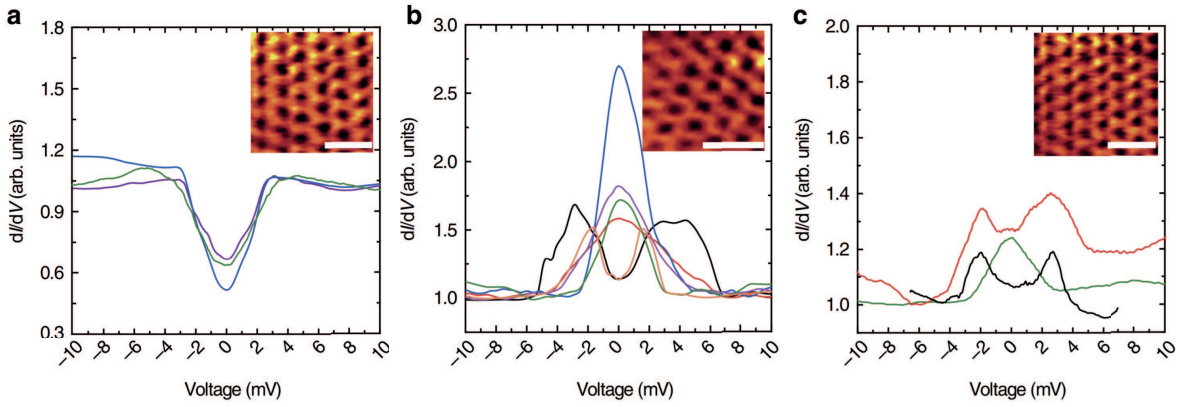

Figure 9.2: (a) Proximity-induced V-shaped gaps, (b-c) ZBCPs and split ZBCPs. Different colours in (a-c) are used to distinguish between spectra recorded in different sample areas. Insets in (a-c) show the typical topography of a sample area where the corresponding spectra in (a-c) are obtained (the scale bars in the insets have a length of 0.5 nm).

The spectra are different one from the other as the roughness of PCCO allows us to probe SLG on different facets (crystal orientations) of the underlying substrate. In the normal state none of these spectral features is observed, which rules out the possibility that these are due to electronic inhomogeneities in the sample. Furthermore ZBCPs are found (below T_c) only in regions where the STM images show clear SLG topography and not in defected regions. The modifications of the superconducting LDOS on SLG/PCCO/STO compared with the presence of just V-shaped gaps in bare PCCO/STO, suggests the emergence of an unconventional p-wave or d-wave superconducting state in SLG, different from that of the superconducting PCCO underneath and therefore intrinsic to SLG itself. This has therefore been induced in SLG by proximity. The early stage of these findings however makes the fabrication of devices still impractical.

9.3 Superconductivity in $NbSe_2$

As anticipated in Sect.2.2.3, $NbSe_2$ is a metal which becomes a superconductor with a T_C in the bulk of ∼7.2K[314]. The material represents an interesting research platform

due, mainly due to the coexistence of SC and a CDW order[42]. In one of the early studies on cleaved layered crystals (Ref.[8]) it was shown that the T_C of $NbSe_2$ progressively decreases with thickness. Refs.[40, 41] have recently reported on a persistence of the superconducting state down to the 1L, putting a final esclamation mark on the existence of SC in two dimensions. It was also reported that the electrical properties of $NbSe_2$ tend to degrade when the material is exposed to the environment[315]. The solutions to overcome this issue were either represented by minimizing the exposure time (<1 hour) during the fabrication process [41] or by preparing the sample in an inert atmosphere[40].

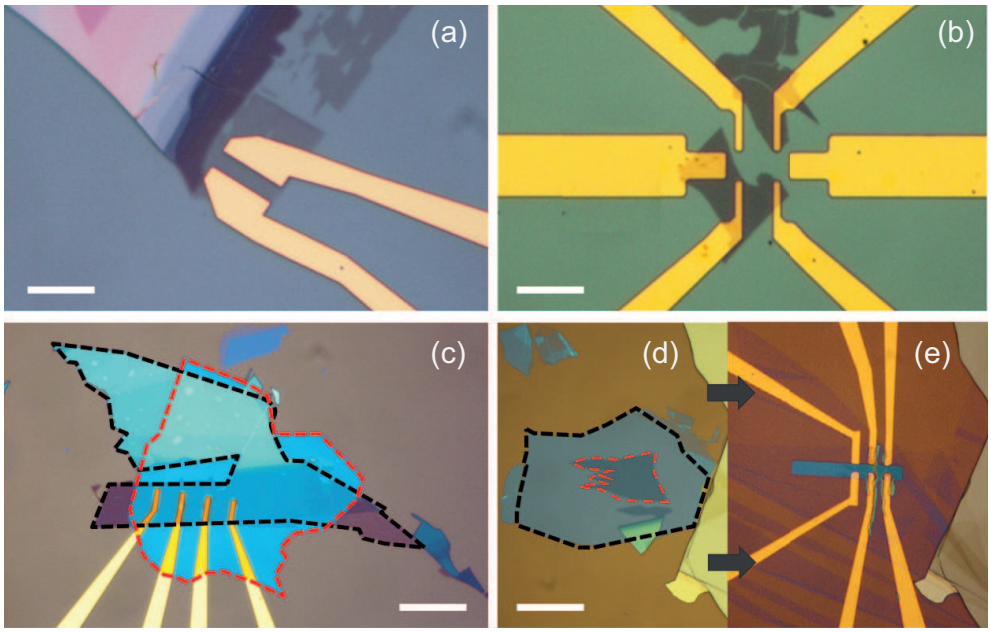

Figure 9.3: (a) $NbSe_2$ exfoliated on SiO_2/Si with top contacts. (b) $NbSe_2$ transferred on pre-patterned bottom contacts. (c) $NbSe_2$ (red) on pre-patterned contacts capped with h-BN (black). (d) $NbSe_2$ (red) exfoliated on SiO_2/Si and capped with h-BN (black). (e) Side contacts realized on (d) after patterning of the heterostructure. Scale bars for (a-b) are 5μm, while for (c-e) are 10μm.

In order to integrate $NbSe_2$ into optoelectronic devices I prepared samples adopting several methods. Fig.9.3 depicts four different techniques I used to prepare $NbSe_2$ devices. The least complicated method is the one shown in Fig.9.3(a). Here $NbSe_2$ is exfoliated either directly on SiO_2/Si or on PDMS and then stamped on SiO_2/Si substrates as discussed in Sect.5.2. A layer of PMMA is then immediately spin-coated on top to protect the sample from exposure to the environment. Metal contacts are then realized with e-beam lithography, evaporation of titanium(Ti)/Au 5/50nm and lift-off. Ti is preferred to Cr as the magnetic property of the latter can perturb the behaviour of the superconductor[316]. The sample exposure to the environment is kept <1-2 hours.

To further minimize the exposure time I realized pre-patterned contacts on SiO_2/Si and then stamped the $NbSe_2$ on top. However I often experienced tearing of the flake as shown in Fig.9.3(b), typically lowering the yield of successful devices and/or the number of contacts available for measuring. An alternative approach to prevent exposure of $NbSe_2$ to the environment is that of capping or encapsulation with h-BN. Fig.9.3(c) shows a flake of $NbSe_2$ stamped on pre-patterned contacts on SiO_2/Si and capped with an h-BN flake (red dashed line). The h-BN layer was transferred on top of $NbSe_2$ by means of dry transfer: h-BN was first exfoliated on SiO_2/Si and picked up at room temperature with a PC/PDMS stack, then the h-BN/PC/PDMS structure was brought in contact with $NbSe_2$ under a microscope and temperature was raised to ∼150°C to release h-BN/PC on $NbSe_2$. PC was finally removed in chloroform leaving h-BN on $NbSe_2$. Finally I also tried realizing side-contacts[107] on h-BN capped $NbSe_2$ flakes as shown in Fig.9.3(d-e). h-BN/$NbSe_2$ structure were indeed etched with RIE, using a plasma formed from a mix of CF_4 and O_2 (ratio 4:1) under a forward power of 30W. However the $NbSe_2$ proved much harder to etch with this gas mixture with respect to h-BN. Prolonged exposures to the plasma often caused cross-linking of the PMMA as shown in (e), which complicated the fabrication of metal contacts, often resulting in unsuccessful measurements, *i.e.* the $NbSe_2$ was not conducting. The latter method was thus discarded and a range of devices where fabricated with methods (a),(b) and (c).

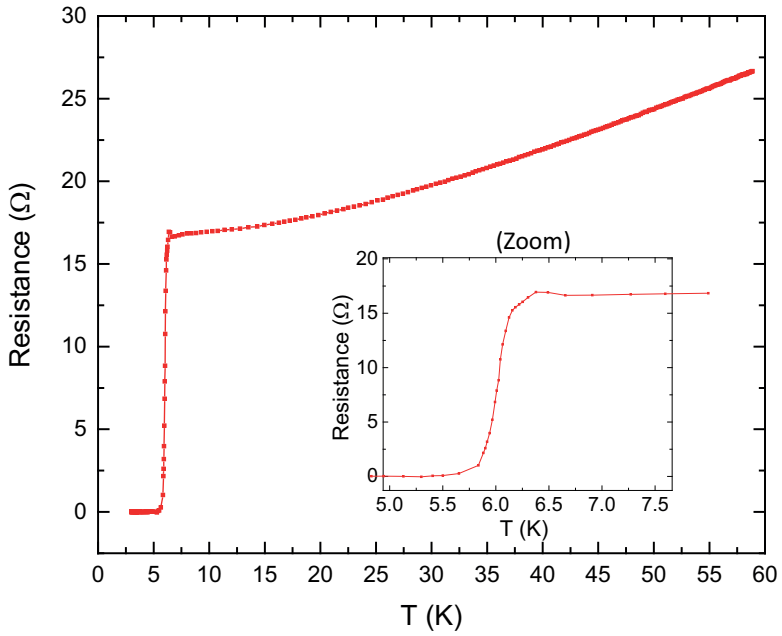

Figure 9.4: Representative R vs T curve of a 5L-$NbSe_2$ device. The inset shows a close-up to the superconducting transition.

Fig.9.4 shows a representative resistance (R) versus temperature (T) curve of a 5L-$NbSe_2$. This was realized by loading the sample in a cryo-cooler with base temperature of ∼1.8K and biasing with a current I_{DS} while monitoring the voltage in a 4-wire configuration. The samples becomes superconducting at ∼6K, in line with the results in Refs.[40, 41]. The transition takes place in less than <1K, which is promising for sensitive applications.

As $NbSe_2$ devices were destined to superconducting photodetectors and given their high-sensitivity, standard electrical measurements were often to be by-passed in order to reduce the stress to the sample and minimize the exposure time.

9.4 Superconducting transport in highly doped MoS_2

In recent years, EDL gating has proved to add an extra degree of control on the electrical properties of TMDs[41, 317–319], by allowing us to efficiently tune the Fermi level in ultrathin flakes and explore transport at high carrier concentrations (up to $n \sim 10^{14}\text{cm}^{-2}$)[41, 317–319]. In particular, interface superconductivity was induced at the surface of liquid-gated MoS_2[317], which has already been presented in this disseration as a semiconductor in standard conditions. Moreover, the gate-induced SC state has been shown to survive down to the single-layer limit[320] as for $NbSe_2$[40, 41].

In the 2H-MoS_2 crystal structure, the hexagonal 2d Brillouin zone features the high-symmetry points Γ, M and K (Fig.9.5). The point mid-way between K and Γ is known as Q. Most of the results of superconductivity in liquid-gated MoS_2 have been interpreted in terms of the population of the conduction band minima at the K and K' points of the First Brillouin Zone (FBZ). K and K' points were indeed found to be the global minima in both single-layer[32] and few-layer[317, 321, 322] MoS_2[323]. Thus, for relatively small doping values $n < 10^{13}\text{cm}^{-2}$ only the valley at K is populated by electrons. For sufficiently large doping values, instead, the Fermi level should eventually cross the bands at Q and both valleys become populated[323].

Here I provide evidence for multi-valley transport at the surface of liquid-gated few-layer MoS_2 via low-temperature transport measurements. I exploit the capabilities of the dual-gate geometry to finely tune the doping level across a wide range of carrier densities in order to probe the crossing of high-energy sub-bands by detecting characteristic "kinks" in the transconductance of the measured samples[324].

I prepared few-layer MoS_2 flakes by micro-mechanical cleavage of 2H-MoS_2 bulk crystals on low resistivity (<0.005Ω·cm) Si coated with a 90nm or 285nm SiO_2 layer. The electrodes are defined by patterning the contacts area by means of e-beam lithography,

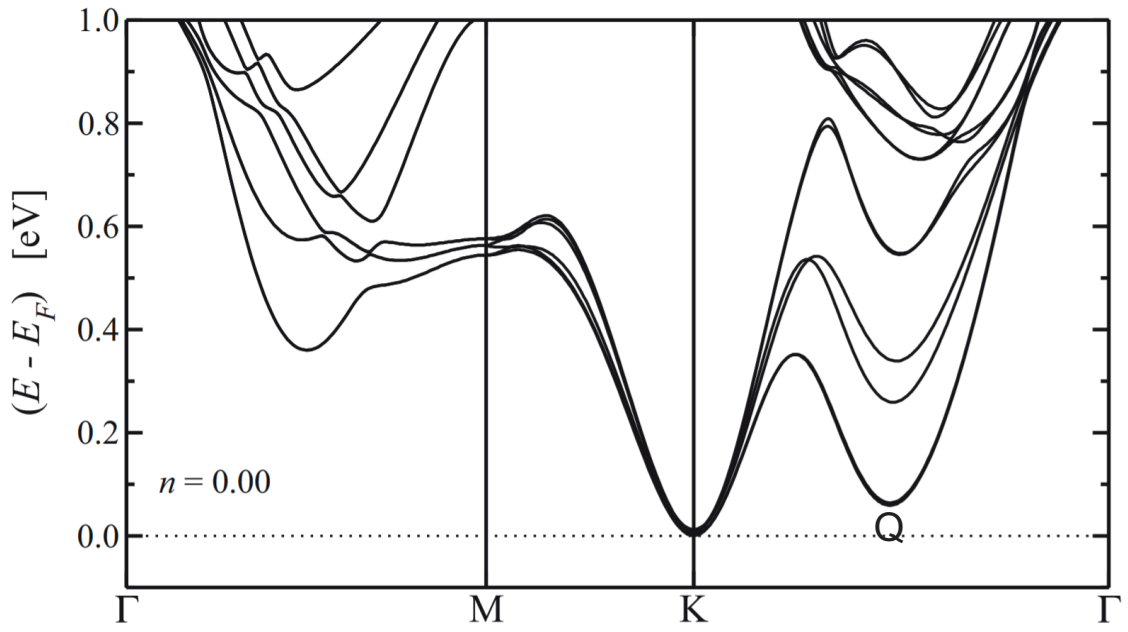

Figure 9.5: Plot of the conduction band structure in the FBZ of undoped trilayer MoS_2. Adapted from Ref.[323]

followed by Ti:10nm/Au:50nm evaporation and lift-off, as shown in Fig.9.6(a) and Fig.9.6(b). Flakes with irregular shapes were further patterned in the shape of Hall bars by using PMMA as a mask and removing the unprotected MoS_2 with reactive ion etching (RIE) in a 150mTorr atmosphere of CF_4 and O_2 gases, with ratio CF_4:O_2=5:1 and 20W power. A droplet of 1-Butyl-1-methylpiperidinium bis(trifluoromethylsulfonyl)imide (BMPPD-TFSI) was used to cover the surface of the few layer MoS_2 and part of the top electrode for liquid gate (LG) (see Fig.9.6(a)). Raman characterization and atomic force microscopy (AFM) are used to investigate the exact thickness of the few layer flakes and the effects of the application of the liquid gate on MoS_2.

Raman spectroscopy is performed at 514nm excitation wavelength. The power was kept below 200μW to avoid any damage on the samples. A representative Raman spectrum of an as-exfoliated MoS_2 sample is shown in Fig.9.7(a) (blue curve). In the high frequency region above $\sim$200cm^{-1} lie some of the Raman fingerprints of MoS_2. The E^1_{2g} peak at $\sim$385cm^{-1} and the A_{1g} peak at $\sim$409cm^{-1} correspond respectively to in-plane and out-of plane relative vibrations of molybdenum and sulfur atoms as explained in Sect.2.4.4[81, 82]. Their frequency difference is typically used to monitor the number of layers when the thickness of MoS_2 is expected to be up to three layers[83]. Indeed, when the MoS_2 thickness increases to N layers (where N>3), the E^1_{2g}-A_{1g} frequency

difference-change from N layers to N+1 starts approaching the accuracy of the instrument ($\sim$1cm^{-1}) and this method cannot be used any longer[79, 83].

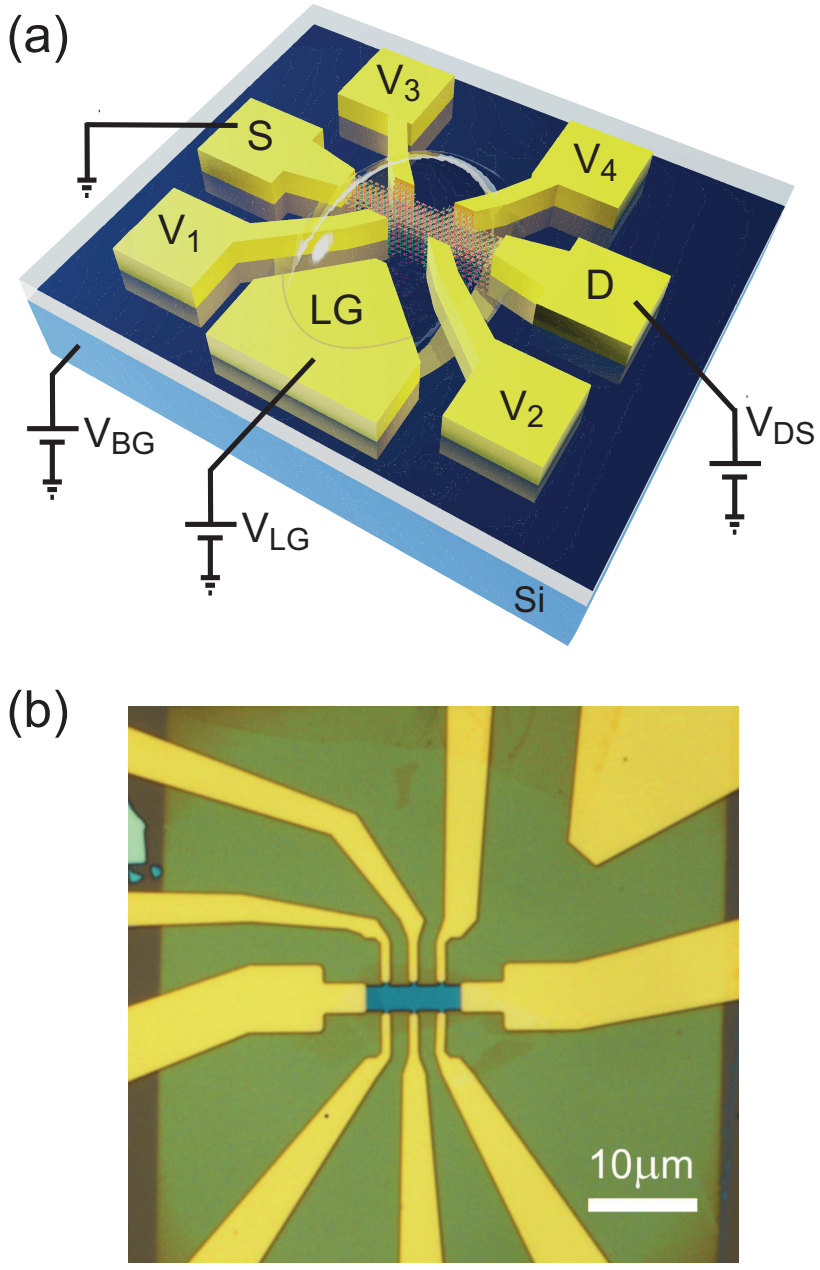

Figure 9.6: (a) Schematics of Hall bar fabricated for a few layer MoS_2 flake with voltage probes (V_i), source (S), drain (D) and liquid-gate (LG) elctrodes. A droplet of ionic liquid covers the flake and part of the LG electrode. The sample is biased with voltage V_{DS} and dual gate control is enabled by a voltage applied on the liquid gate (V_{LG}) and one on the back gate (V_{BG}). (b) Optical image of a patterned Hall bar with six voltage probes. The LG electrode is on the upper-right corner.

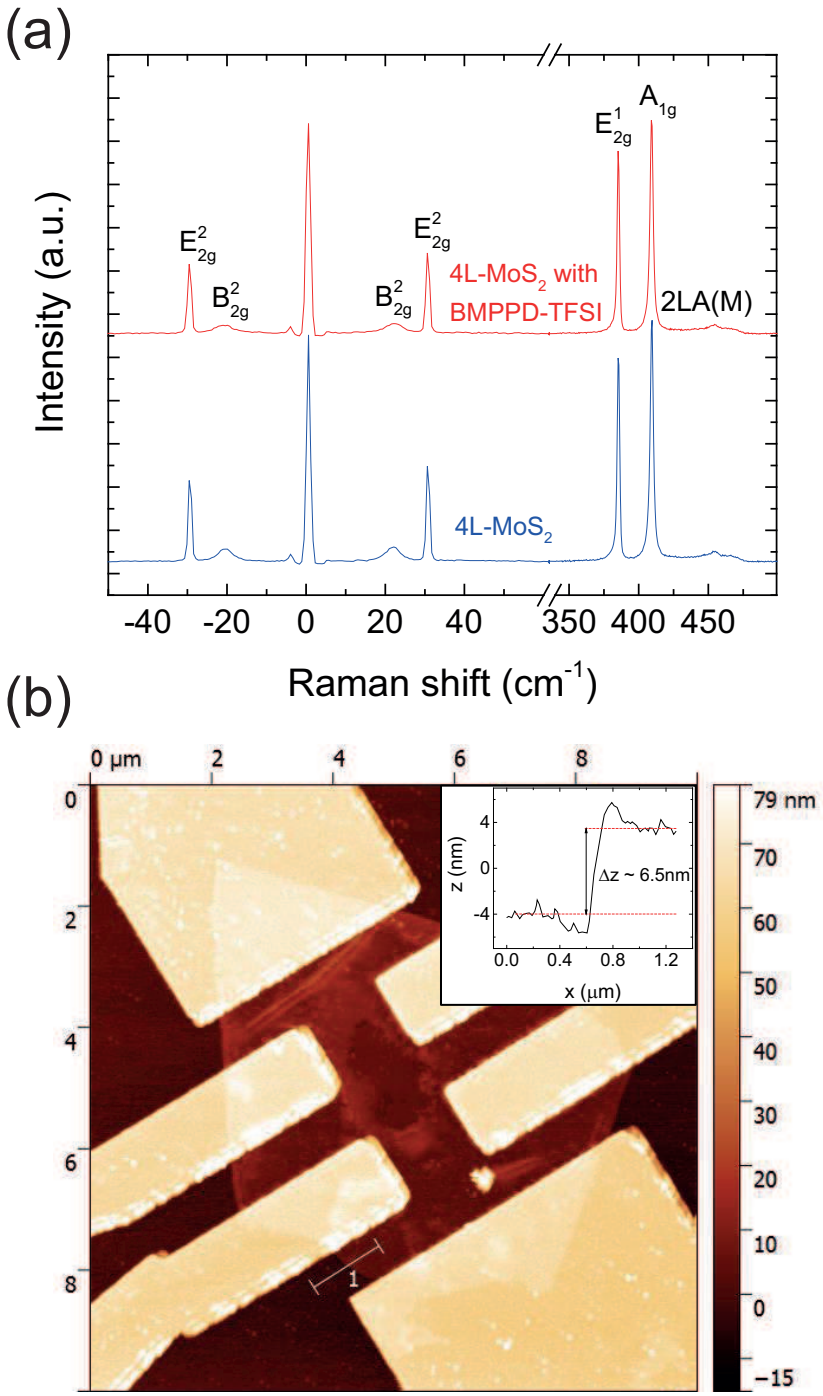

Figure 9.7: (a) Representative Raman spectra at 514nm of a 4L-MoS_2 flake before (blue curve) and after (red curve) the fabrication/deposition of the ionic liquid droplet. (b) AFM scan of the Hall bar for checking sample thickness

The last band in the high frequency region is the 2LA(M) band at ∼455cm^{-1} and it is due to second order longitudinal acoustic mode at the M point of the Brillouin zone[325].

For few layer flakes utilized in this study ultra-low frequency modes (<100cm^{-1}) were used to monitor the number of layers[79].

At these wavelengths, it is possible to observe shear (C) and layer breathing modes (LBM), which are due to relative motions of the atomic planes, either perpendicular or parallel to their normal[79]. The E^2_{2g} C mode at ∼30cm^{-1} and the B^2_{2g} LBM peaked at ∼22cm^{-1} indicate the fingerprint of a 4L-MoS_2[79]. For the sample in Fig.9.7(a) the Raman features remain practically unchanged after fabrication (red curve) and deposition of the BMPPD-TFSI ionic liquid, suggesting that MoS_2 has not been substantially doped or damaged.

First the T dependence of the resistivity ρ_{xx} under the effect of the liquid top gate is investigated. EDL gating with ionic liquid is a similar concept with that explained for the PE. However here the gate is liquid at RT. The liquid gate voltage V_{LG} is applied at $T = 240$K, immediately above the glass transition temperature of the electrolyte, under high vacuum conditions (pressure< 10^{-5}mbar) to minimize unwanted electrochemical interactions with the samples and extend the electrochemical stability window of the ionic liquid[326]. After V_{LG} is applied, the ion dynamics are allowed to settle for ∼10 minutes, then the sample is cooled down to the base temperature of the cryogenic system (2.7K).

Fig.9.8 shows the T-dependence of ρ_{xx}, measured in a standard four-probe configuration, for different values of the applied gate voltage V_{LG} and induced carrier density n. These devices display a behaviour in line with the previous reports[317], undergoing first an insulator-to-metal transition at low carrier densities ($n < 1 \cdot 10^{13}$cm^{-2}), followed by a metal-to-superconductor transition at high carrier densities ($n > 6 \cdot 10^{13}$cm^{-2}). The associated values of the carrier density are estimated by low-T Hall effect measurements. Specifically, we have explained in this dissertation how Hall measurements allow us to directly probe the carrier density n. n can then be correlated with V_{LG} by the linear relation in Eq.9.1, *i.e* by using a slightly modified version of Eq.4.25. This allows us to extrapolate the liquid gate capacitance C_{LG}, as for Fig.9.9(a). Here V_{th} is the threshold voltage needed to trigger a finite conductivity in the sample, replacing the V_{CNP} in graphene. In general, the gate capacitance is the combination of C_{LG} and the quantum capacitance C_Q. However, in MoS_2, C_Q is ∼120μF/cm^2[323, 324], two orders of magnitude bigger than C_{LG}. In a series of capacitances, the smaller dominates.

$$n = \frac{C_{LG}(V_{LG} - V_{th})}{q} \tag{9.1}$$

To visualize the predicted σ fluctuations at the crossing of the Q band, a curve of σ_{xx} vs n has to be plotted. This can be done by using points at a fixed temperature from

Fig.9.8. Alternatively, the use of a back gate, after having polarized the sample with a certain top-gate voltage can allow a fine tuning of the charge n, around the one induced by V_{LG}. Hence, the sample is polarized in the low-density range of the metallic state by applying $V_{LG} = 0.9$V and the system is cooled down to 2.7K.

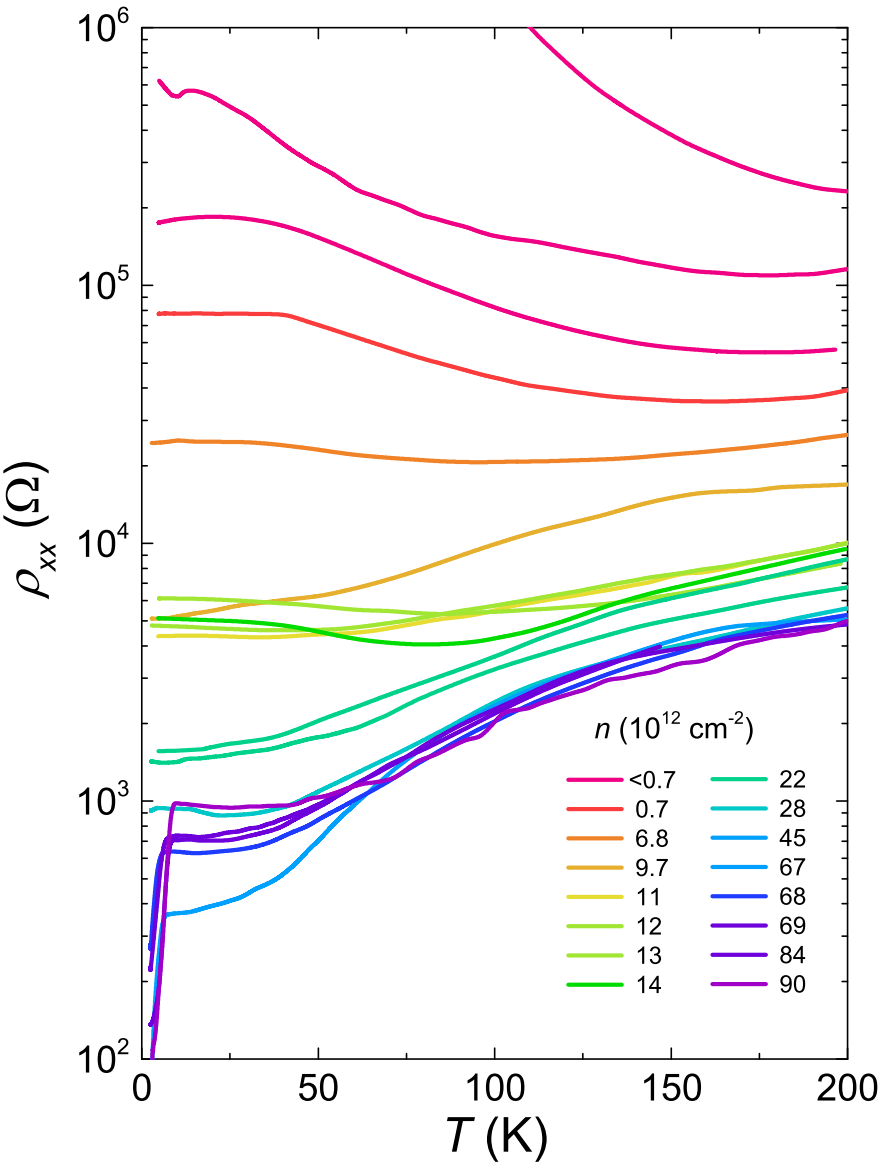

Figure 9.8: ρ_{xx} vs. T for different values of n in dual-gated MoS_2.

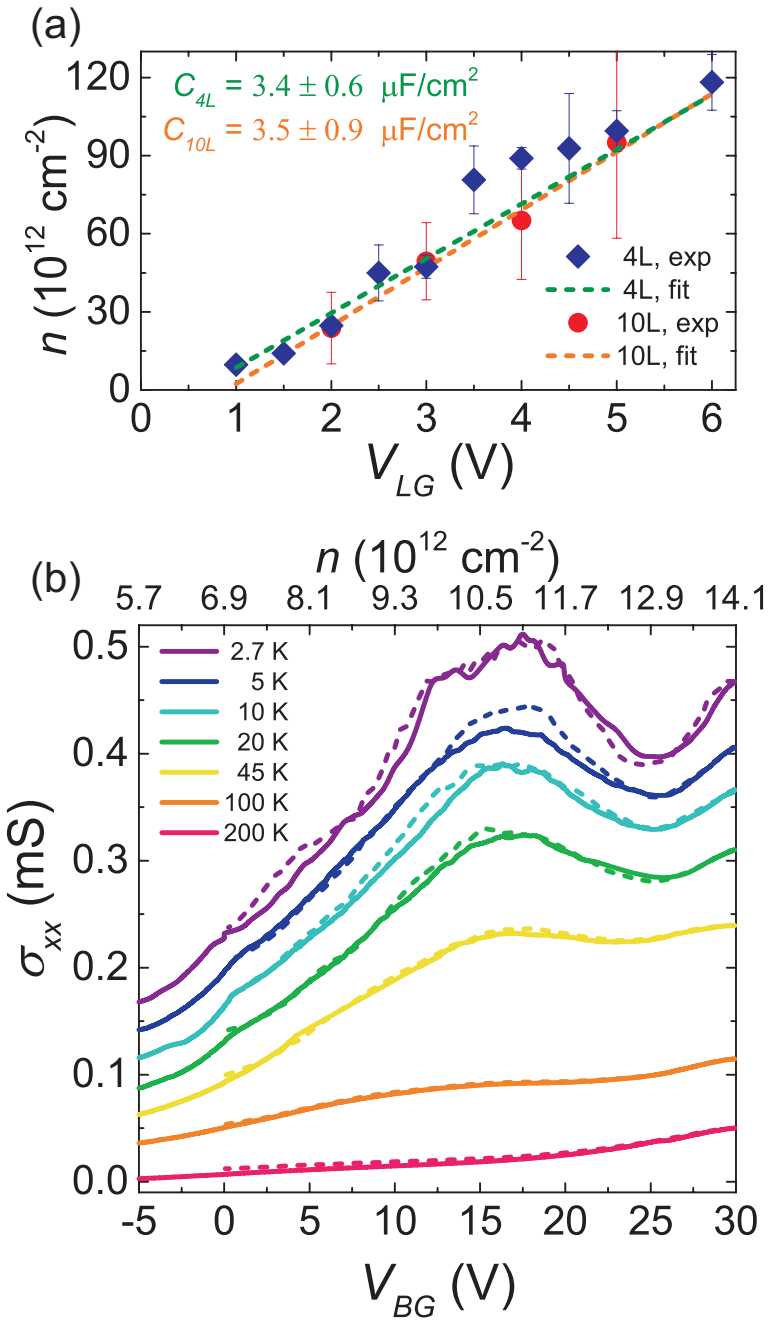

Figure 9.9: (a) n vs. V_{LG} as determined via Hall effect measurements, for a 4- and a 10-layer device. The liquid gate capacitances are obtained by a linear fit of the experimental data. (b) σ_{xx} vs. V_{BG} at $V_{LG} = 0.9$V, for different operating T.

The back gate is then swept revealing the kink in Fig.9.9(b). The leakage current is always monitored to avoid dielectric breakdown during the measurements. The solid back gate endows us with an independent tool to estimate the induced carrier density in the system:

$$n = \frac{C_{ox}(V_{BG} - V_{th})}{q} \tag{9.2}$$

This allows us to obtain the carrier density scale shown in the top axis of Fig.9.9(b). The signal hysteresis between increasing and decreasing V_{BG} ramps is rather minimal. Furthermore, the intensity of the kink is suppressed by increasing the sample temperature. This first kink however appears before the metal-to-superconducting transition. A point-to-point plot of ρ_{xx} in Fig.9.8 as a function of n yields the plot in Fig.9.10.

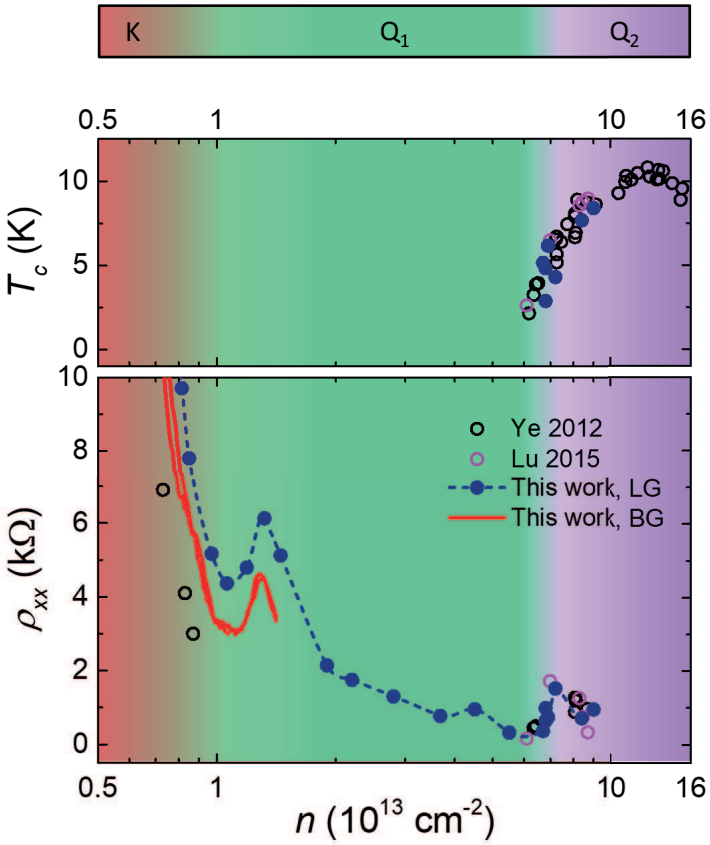

Figure 9.10: Superconducting dome of liquid-gated MoS_2 as a function of n (top). T_C is determined at 90% of the total transition. (bottom) ρ_{xx} as a function of n, both upon increasing V_{LG} (blue filled circles) and V_{BG} (solid red line).

An additional kink is visible at $n > 6 \cdot 10^{13}\text{cm}^{-2}$, where the metal-to-superconducting transitions occurs. These results can be interpreted as follows: when n <1·10^{13}cm^{-2}, only the spin-orbit split sub-bands at K are populated (Fig.9.11). Around n ~1.5-2·10^{13}cm^{-2}, the Fermi level crosses the bottom of a first sub-band at Q, which we can call Q_1. Once Q_1 is populated and the doping is large enough (n ~6.7·10^{13}cm^{-2}), the system

sharply becomes superconducting, while the Fermi level crosses the bottom of the second sub-band at Q, *i.e.* Q_2.

Interestingly, the experimentally observed kinks emerge at different n values with respect to the theoretically predicted ones[324]. This is probably due to differences in the strain values in experimentally-measured devices, compared to the values used theoretically. It is also possible to note that the maximum T_C ~11K is reached at n ~$12{\cdot}10^{14}$cm^{-2} after the closing of the second kink. This suggests that the full population of both Q_1 and Q_2 sub-bands might be a relevant factor for full SC transport in MoS_2, thus pointing to multi-valley transport in the superconducting state.

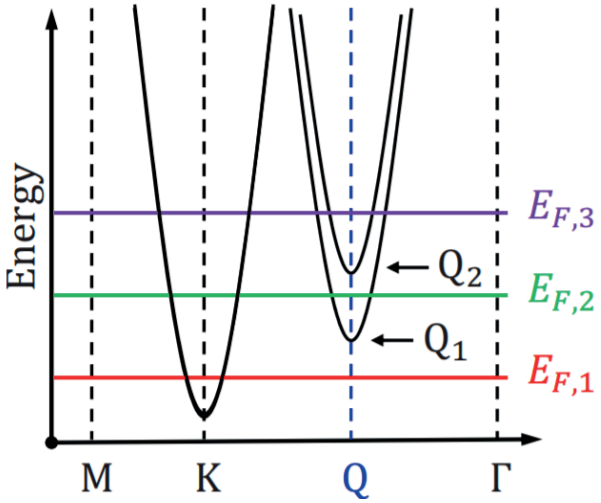

Figure 9.11: Sketch of the band structure for few-layer gated MoS_2, and the Fermi level E_F for three different doping values. The color code matches that of Fig.9.10.

9.5 Conclusions

In this chapter I probed the potential of superconducting transport in the layered materials SLG, $NbSe_2$ and MoS_2. Unconventional superconductivity can be induced in SLG by proximity with the high temperature cuprate superconductor PCCO. A mixture of V-shaped gaps, strong ZBCPs and split ZBCPs are observed, depending on the position of the STM tip in STS measurements.

I also prepared superconducting devices of ultrathin $NbSe_2$ flakes. Different approaches are utilized for the device fabrication in order to ensure minimization of the sample exposure to the environment. T_C measured in superconducting $NbSe_2$ devices match those of previous reports.

The large carrier density modulation provided by ionic gating has allowed me to explore sub-band population phenomena and multivalley transport in MoS_2 ultrathin flakes. Measurements show evidence for two pronounced kinks in the device conductivity, associated to the doping-induced crossing of the two sub-bands at the Q valley. Superconductivity emerges in gated MoS_2 only after the Q_1 and Q_2 valleys are populated.

Chapter 10

Superconducting Photodetectors with $NbSe_2$

10.1 Introduction

As anticipated in previous chapters, $NbSe_2$ is an interesting layered superconductor due to exotic properties such as the coexistence of SC and CDW order[41, 42] and the persistance of SC even upon application of high magnetic fields (Ising SC)[327]. However research on the optical properties of $NbSe_2$ is still lacking.

Current state-of-the-art superconducting single photon detectors (SSPDs) mainly rely on niobium nitride (NbN), whose thin (∼5-10nm thick) films can be grown by reactive sputtering with good reliability and offer a T_C ∼10K, slightly lower with respect to that of the bulk[139, 146]. Single photon detection was achieved with patterned nanowires of NbN of ∼100nm width and μm length designed in a meander configuration to maximize the fill factor of the area impinged by photons[139, 146]. This configuration allowed them to achieve high performance in terms of DE (∼60%) and count rate (∼1GHz).

The search for materials able to overcome the properties of NbN films and broaden the spectrum of single-photon detection wavelengths is always active and has led to the exploration of alternatives such as tungsten silicide[143], niobium silicide[328] and tantalum nitride[329] films. In this chapter I report on the investigation of superconducting PDs with few-layer $NbSe_2$ flakes, which represents the first attempt of superconducting detection with layered materials.

10.2 Results

$NbSe_2$ devices are prepared as discussed in Sect.5.2 and 9.3, while the characterization of ultra-thin flakes, including how to determine the number of layers has been presented in Sect.5.2. For measurement of the optical response only two metal leads are needed.

The measurement setup is shown in Fig.10.1. This was built by Prof. Robert Hadfield, Gavin Orchin and co-workers at the University of Glasgow. A laser generates light at λ=1550nm. A waveform generator converts the laser output in a train of pulses at a frequency of 1MHz, so that there are 10^6 pulses of laser light every second. The signal can then be attenuated by two attenuators in series down to the power needed to have maximum one photon per pulse. An optical fibre delivers light to the sample loaded in a cryo-cooler able to achieve temperatures down to 300mK.

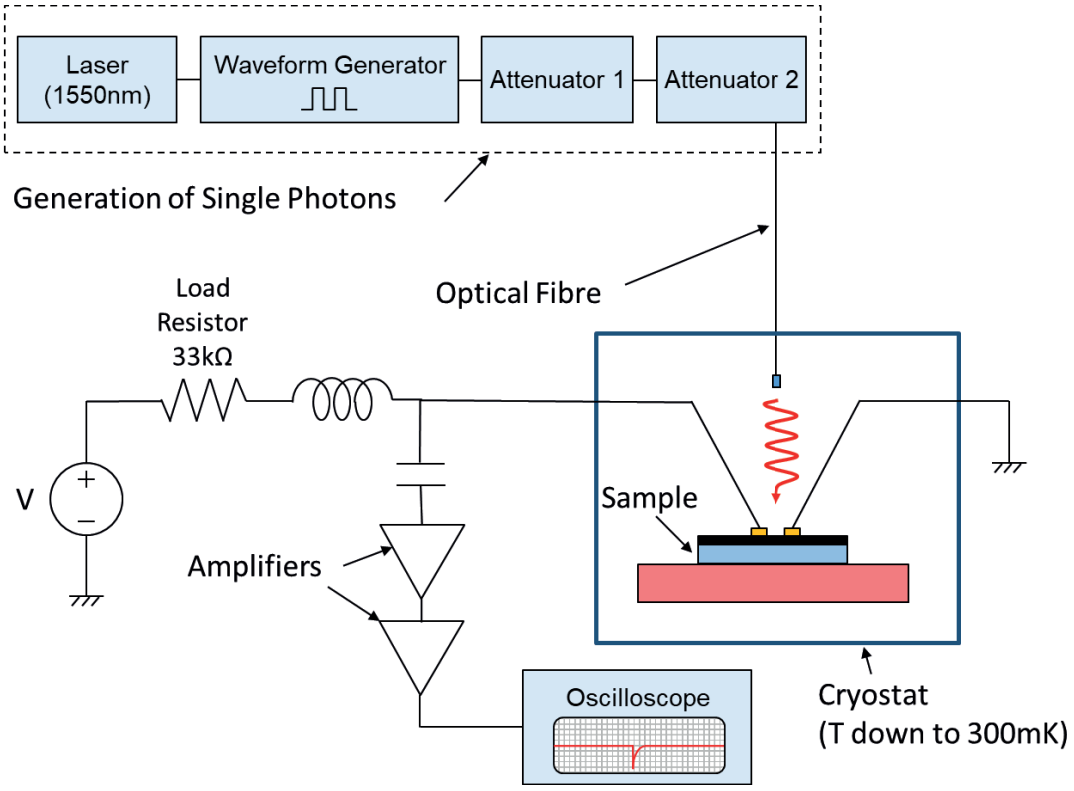

Figure 10.1: Measurements setup for superconducting photon detectors at 1550nm

The sample is biased in current, by having a voltage generation in series with a variable load resistor. Whenever the sample is in a steady SC state (in dark) a constant current flows in it and no current flows in the side branch connected to the oscilloscope. This is because a capacitor filters out the direct current (DC) component. Whenever a photon is detected, the samples becomes resistive for a short time interval and a current

flows in the side branch, producing a voltage drop signal. The latter is amplified and read by an oscilloscope. Alternatively, the side branch can be connected to a counter. The counter can detect the number of times a set voltage threshold is overcome during a certain intergration time. By setting an integration time of 1 second and a threshold (in mV or V), the counter will count the events which overcome this threshold, *i.e.* the photo-detection events per laser pulse.

The sample is cooled to the cryostat base temperature, *i.e.* either 300mK or 5K, thus brought into the SC state. Then, a reflection map is collected by shining light on the sample and detecting reflections with a IR camera mounted on a piezo-stage. This allows us to understand at which point light pulses need to be delivered. The significance of the critical current density J_C in SSPDs has been discussed in Sect.4.2.4: J_C defines the bias operation point. I-V curves are therefore taken for each sample as shown in Fig.10.2. The slope of the I-V curve represents the device resistance, as R=V/I. Superconductors are expected to have a negligible resistance R, therefore I-V slope $\rightarrow \infty$. However the measurements is performed with two-probes, therefore the measured R includes contributions such as the lead resistance and the contact resistance R_C, which yield a finite slope. The slope change highlighted by the red line, is the result of a change in the sample resistance, which is induced by the transition to the resistive state and disappearance of SC. The value of current corresponding to this transition is called the critical current I_C, related to J_C ($J_C = I_C/A$, with A being the flake cross section).

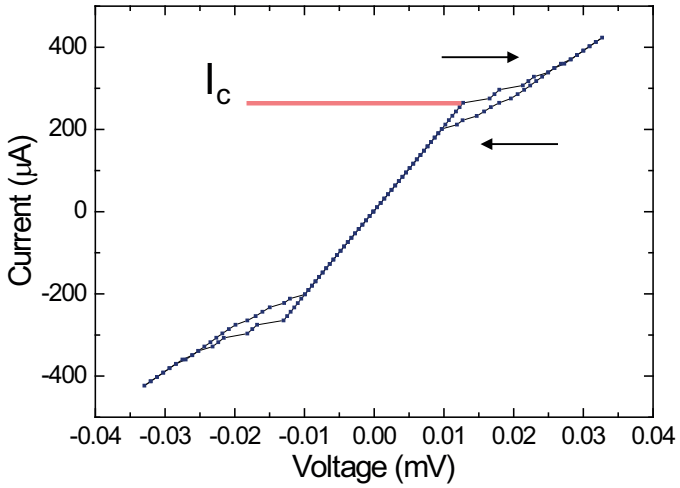

Figure 10.2: Representative I-V curve of a 5L-$NbSe_2$ device with I_C highlighted. A negligible hysteresis is registered between the negative-to-positive and positive-to-negative voltage sweeps.

The next step involves the opto-electronic characterization. The sample is biased with current close to I_C. The power of the laser is attenuated, while the number of detection events is read by the counter. This allows us to produce the count map in Fig.10.3. The smallest signal the sample can detect corresponds to the maximum attenuation (∼32dB). The second spike around I ∼165μA indicates non-homogeneous SC across the flake.

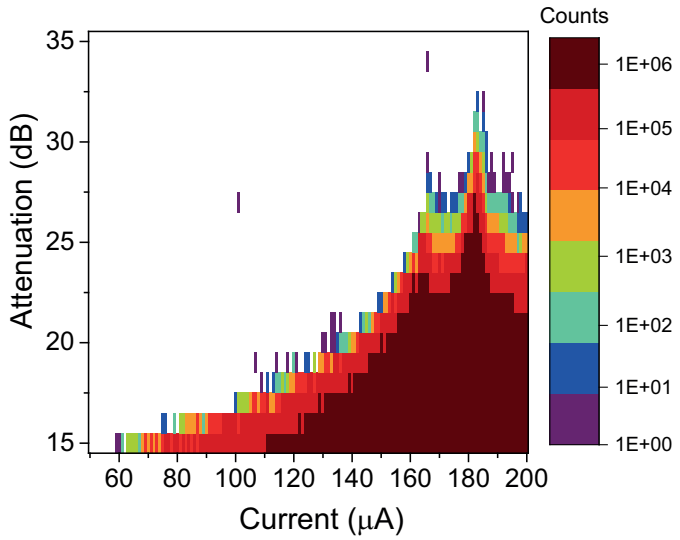

Figure 10.3: Count map of the device in Fig.10.2

The conversion from attenuation to photons is performed as follows. The energy E_p of one photon at λ=1550nm is $E \simeq$0.8eV=1.28·10^{-19}J. The power of the laser with no attenuation is $P_o \simeq 1.04\mu$W which corresponds to 1.04μJ/second. The laser power is monitored each time before starting the measurements. The attenuation, measured in dB is the ratio between attenuated power P_{att} and P_o, therefore:

$$P_{att} = P_o \cdot 10^{\text{-Attenuation[dB]}/10} \tag{10.1}$$

The number of photons N_{ph} per unit time is then:

$$N_{ph}/t = \frac{P_{att}}{E_p} \tag{10.2}$$

Finally as there are 10^6 pulses/second (1MHz), the number of photons per pulse is:

$$N_{ph}/\text{pulse} = \frac{N_{ph}/t}{10^6} \tag{10.3}$$

A single photon detector has to be able to show 1 count/second at attenuated laser powers such that N_{ph}/pulse ≤1. Unfortunately, none of the measured devices was able to

resolve single photons. As shown in Fig.10.4, the minimum number of photons triggering a detection event was found to be of few thousands. Interestingly a 2L-$NbSe_2$ capped with h-BN showed no significant performance degradation with respect to the 5L device.

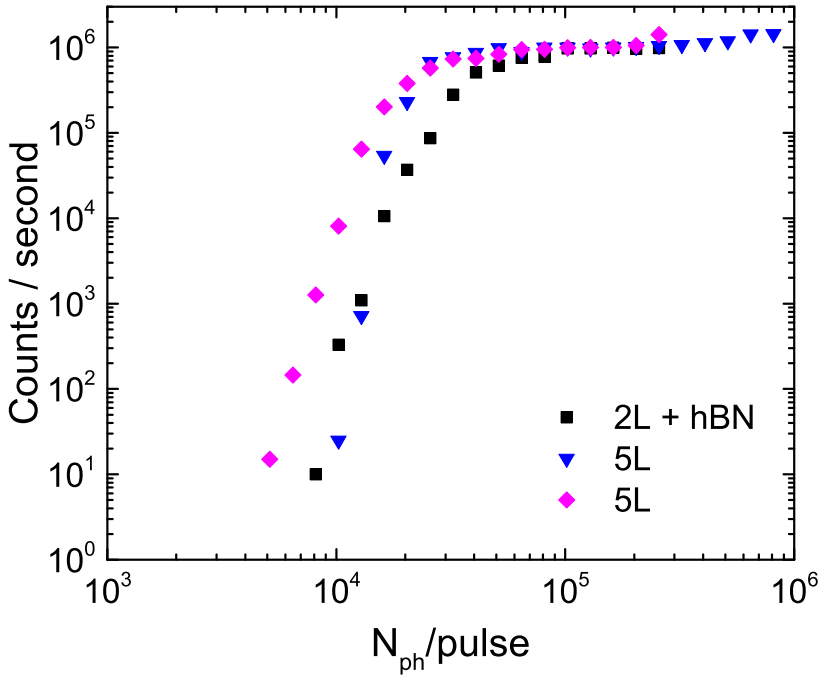

Figure 10.4: Count/second vs number of resolved photons/pulse in three $NbSe_2$ devices.

Subsequently, the counter was replaced by an oscilloscope to visualize the pulse shape of a 5L-$NbSe_2$ device as shown in Fig.10.5. The dashed line (Fig.10.5(a)) represents the threshold set during the measurements with the counter (∼10mV). The response is in the order of tens of ns. The pulse height increases with optical power and goes sub-threshold for power attenuations >26dB. A close-up to the pulse shape at higher attenuations (Fig.10.5(b)) shows that a response is still present, however this is almost comparable to the noise. The modulation of the pulse height points toward a more bolometric-type response rather than a response which can be described by the hotspot model, as the sample seems to be becoming more resistive, but not going to the full superconducting-to-metal transition. In contrast, in SSPDs the pulse height does not typically depend on P_{att}.

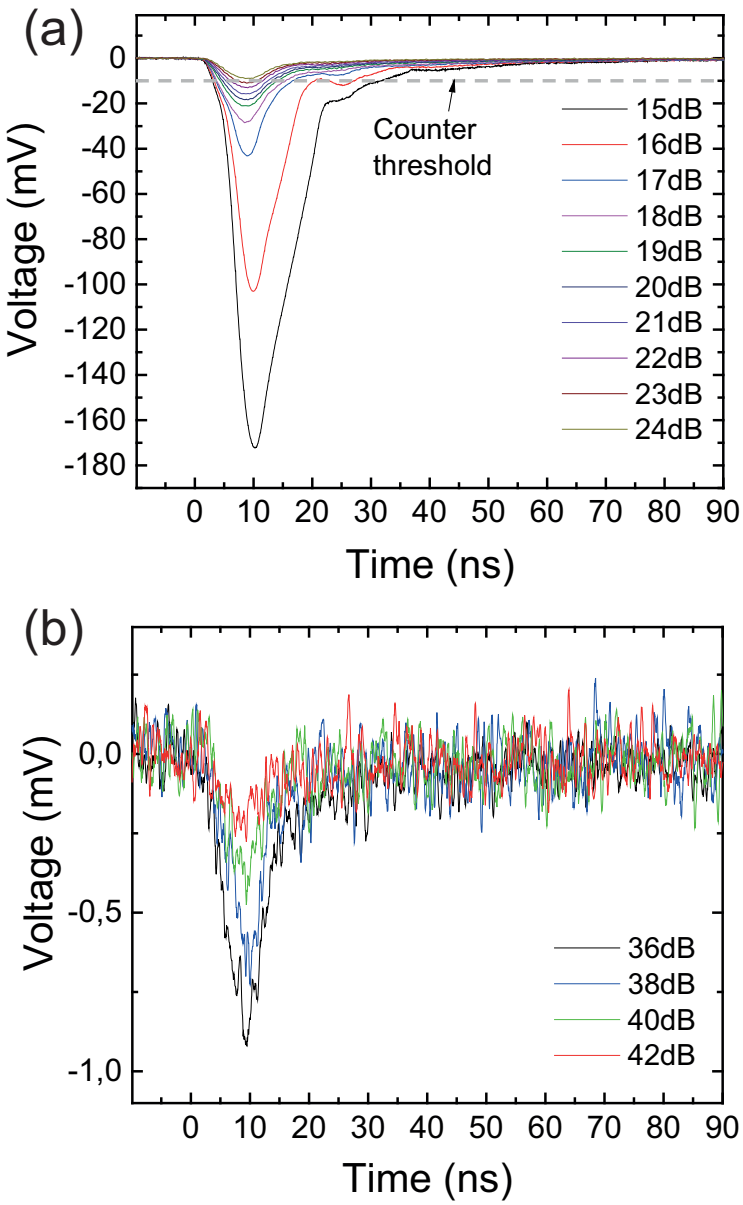

Figure 10.5: (a) Pulse shape of a 5L-$NbSe_2$ detector for several power attenuations. The counter threshold is highlighted by a dashed line. (b) Sub-threshold signals at higher powers attenuations (36dB to 42dB)

As most of the SSPD-figures of merit could not be assessed, I therefore measured the device responsivity (Fig.10.6), considering the pulse threshold as the input signal . The responsivity R_{ext} increases exponentially with decreasing laser power and approaches a $R_{ext} \sim 2{\cdot}10^4$V/W, before the signal becomes undetectable. This is one order of magnitude lower than a cooled graphene bolometer $R_{ext}{\cdot} \sim 10^5$V/W and in the range of commercial silicon bolometers $R_{ext}{\cdot} \sim 10^5$-10^7V/W[330].

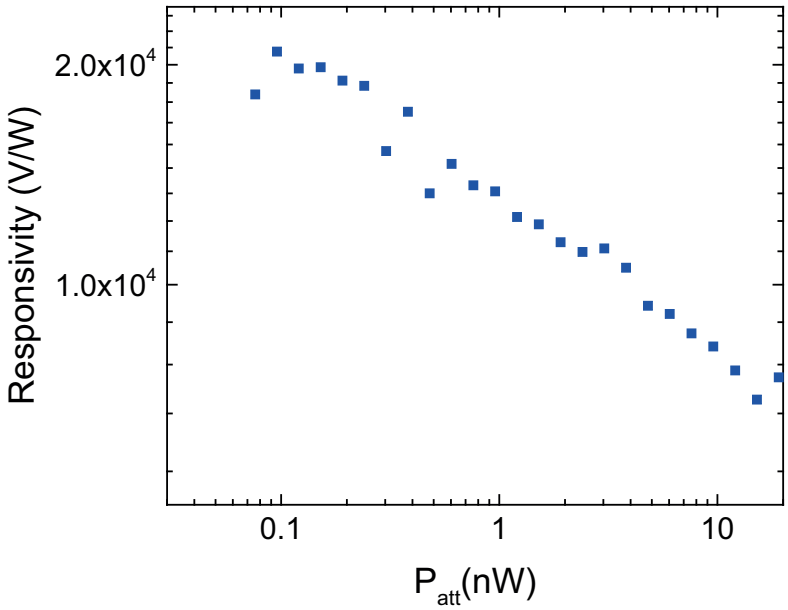

Figure 10.6: Responsivity R_{ext} as a function of attenuated power P_{att} for a 5L-$NbSe_2$ device.

10.3 Conclusions

I demonstrated superconducting photodetection with $NbSe_2$ ultrathin flakes down to the 2L. To the best of my knowledge this represents the demonstration of a superconducting PD exploiting the thinnest material thus far. Photodetection is observed both at 300mK and 5K. The best achieved sensitivity is to $\sim 10^3$ photons, far from single photon resolution. The response of the sample shows bolometric features and takes place in a timescale of tens of ns. The responsivity is $R_{ext} \sim 2{\cdot}10^4$V/W, in line with commercial bolometers. These results are encouraging and suggest that further improvements could perhaps make photodetection with $NbSe_2$ competitive with existing technologies.

Chapter 11

Conclusions and Future Work

11.1 Conclusions

In this dissertation I tackled technological issues in modern optoelectronic technologies and specifically in photodetectors. I showed high-performance photodetectors able to target the visible, near and mid-infrared wavelength range.

From the fabrication point of view I reported on high mobility wet-transferred graphene encapsulated in h-BN layers, which could serve as a robust platform for high-speed integrated photodetectors. The mobility μ is up to $\sim 70\,000\,\mathrm{cm^2V^{-1}s^{-1}}$ at room temperature, of similar magnitude with respect to all-dry transferred graphene procedures[109], which however require the oxidation of the grown substrate to be performed.

I then directed my attention toward a wavelength of paramount importance for telecom applications, *i.e.* the telecom wavelength λ ∼1550nm in the near-infrared, where losses in waveguides are lowest[2]. I developed three photodetectors, working in the telecom spectral band: two upon vertical illumination and one for on-chip applications. All of the built photodetectors exploited the concept of Schottky junctions. The first photodetector for vertical illumination exploits a Fabry-Perot cavity to force the recirculation of light in the structure and enhance absorption at the silicon/graphene interface. The devices are spectrally(λ)-selective. Taking advantage of multiple light reflections at resonance, a spectrally-selective photoresponse with maximum responsivity R_{ext} ∼20mA/W was obtained. The second approach was that of exploiting avalanche multiplication in a graphene/silicon Schottky junction. The device was driven at a reverse bias ∼-3V to trigger impact ionisation in the silicon depletion region and lead to carrier multiplication. This gain mechanism pushed the responsivity from the mA/W regime to $R_{ext} \sim$ 1A/W. In parallel, I demonstrated a compact, waveguide-integrated gold/graphene/silicon Schottky

photodetector. The detection mechanism relied on transfer of photo-generated charges from gold/graphene to silicon. The presence of graphene at the Schottky interface improved the PD responsivity to 85mA/W, one order of magnitude higher with respect to reference devices without graphene. The responsivity was pushed to 0.37A/W with a drive voltage of ∼-3V which triggered avalanche multiplication. This class of graphene-based Schottky photodetectors challenges the current technology, relying on costly manufacturing of germanium/silicon interfaces[191–194] or III-V semiconductors[201, 202].

I then targeted the mid-infrared spectral range, where the radiation from objects at room temperature has a peak (λ ∼10μm)[131]. I showed a graphene-based pyroelectric bolometer with TCR up to ∼900%/K and a device footprint of ∼300×300μm^2. This is two orders of magnitude higher than state-of-the-art mid-infrared photodetectors with similar footprint[131, 229, 331]. The working principle is based on a dual-gated graphene sheet transferred on pyroelectric lithium niobate. A floating metallic structure concentrates the charge generated by the pyroelectric substrate over an integrated graphene field effect transistor. The bolometer was able to resolve temperature variations down to 15mK at 1 Hz. Due to its responsivity, speed and NEP this technology is competitive with current highly sensitive detector in the mid-infrared.

The visible range is widely covered by silicon photodetectors for applications on chip[2]. However the flexible platform still offers considerable room for improvement. Here I reported on a flexible photodetector working at λ=642nm with responsivity up to ∼45.5A/W and operation voltage voltage $<$ 1V, which preserves an overall optical transparency of $>$ 82%. The responsivity was at least two orders of magnitude higher than in semiconductor flexible membranes[238, 250]. The device was based on heterostructures of graphene and 1L-MoS_2. MoS_2 acts as an absorber while graphene works as a channel for current flow. The structure was then covered by a polymer electrolyte to allow gate-tunability and bent without performance loss for radii of curvature down to ∼1.4cm. Graphene/MoS_2 flexible photodetectors are therefore attractive for wearable, low-power opto-electronic applications[246, 247, 251].

In order to target ultra-sensitive photodetectors I studied superconducting transport in layered materials. I found signs of unconventional superconductivity in graphene. I fabricated $NbSe_2$ superconducting devices with a variety of methods. The electrical properties of MoS_2 were continuously tuned from semiconducting to metallic and superconducting by gating with an ionic liquid. Non-monotonicity was found in the sheet conductivity of MoS_2 few layers as a function of doping, which clarified the nature of

superconducting transport in MoS_2 as originating from Fermi level crossing of sub-bands at the Q point in the Brillouin zone.

$NbSe_2$ devices were utilized for ultra-sensitive superconducting photodetectors at λ=1550nm. These were not able to resolve single photons and a significant response was triggered only with thousands of photons impinging on the device. The time response is in the ns regime, while the nature of the response appeared to be bolometric. The responsivity is R_{ext} $\sim 2 \cdot 10^4$V/W in the range of commercial silicon bolometers[330].

All the described results strengthen the role of layered materials in optoelectronics and photodetectors. In particular the integration of graphene with silicon photonics is widely powered, challenging the main competitors: germanium and III-V semiconductors. Graphene and related materials technologies have proved also their huge potential for visible and mid-infrared sensing, both on rigid and flexible platforms. Superconductivity is also a path with great potential, however much improvement is needed to target state-of-the-art applications.

11.2 Future work

A considerable effort should be devoted to improving the quality of the starting materials for photodetectors. Specifically, the significance of the mobility of graphene and its importance in PDs has been discussed across this dissertation. However the mobility of poly-crystalline CVD graphene used for the applications shown in this work is $\sim$ 3 000 $cm^2V^{-1}s^{-1}$ at room temperature, over one order of magnitude lower with respect to the encapsulated CVD graphene achieved with the wet transfer method explained in Sect.5.5. The lateral size of graphene crystals grown by CVD is in constant increase and soon high-quality wafer-size single crystals will be available, already allowing an improvement of mobility of a factor of two on a large scale without the need for encapsulation. Thus far, the real bottleneck for achieving large area high-mobility encapsulated graphene has been the size of h-BN flakes. A tough challenge to be engaged in the future will consist in growing high-quality CVD h-BN to abruptly increase the graphene mobility and therefore the responsivity and speed of photodetectors.

The role of thickness in CVD h-BN films should be investigated: it is still unclear what is the minimum thickness of h-BN necessary to have a significant improvement in mobility, while screening the substrate roughness and charged impurity effects. As for single layer graphene, growing large area CVD 1L-h-BN single crystals thus far has overall proved to be a more feasible task with respect to growing flat multilayer h-BN. Research should be performed in the direction of checking whether one or few high-quality 1L-h-BN

transferred one on top of the other could provide the same mobility enhancement effect of exfoliated h-BN multilayers.

An additional issue is the transfer method. Many transfer procedures are now fully established and mastered. It is however clear that wet etching or oxidation of the substrates used for growth is not a sustainable practise from an industrial point of view. However, in some cases, these have proved to be the only available paths for detaching graphene or h-BN from the grown substrate, while preserving the quality of the films. A long-term plan would be that of investigating possible dry transfer methods of graphene or h-BN grown films, which do not require oxidation of the substrate. This could then be up-scaled in a roll-to-roll process, making of graphene encapsulation a fully-acceptable industrial process. Another ideal path would be also that of direct growth of LM on semiconducting or insulating Si-technology-compatible substrates such as on germanium, which would avoid the necessity of transferring the grown films.

Indeed, the focus on possible substrates or capping layers for graphene should not be limited to h-BN only. Other materials compatible with Si- technologies, and already available on a large scale, such as planarized silicon nitride could also be tested to try and push the graphene mobility over $\sim 10\,000\ \mathrm{cm^2V^{-1}s^{-1}}$ in the short term. All the shown PDs would indeed widely benefit from an improvement of the mobility of the graphene layer.

Schottky PDs in vertical illumination could also be improved by employing higher finesse cavities to enhance the graphene absorption. The integration of antennas could instead help toward the achievements of wavelength-selectivity. As an alternative to the Schottky photodetection mechanism also PTE-based PDs should be investigated.

The large heat capacity of bulk lithium niobate in pyroelectric detectors can degrade the device TCR as well as the speed. The direction to be taken in the case of mid-IR detectors is that of substituting bulk lithium niobate with thin (nm-thick) pyroelectric membranes, ideally suspended, to minimize the heat capacity. In fact, the direct effect from the pyroelectric substrate has been proved to be almost negligible. Therefore the graphene layer could be located away from the pyroelectric pixel. This design would allow for instance encapsulation of graphene with h-BN to further boost the device performance. The h-BN would have the dual role of acting as a top gate and providing for a mobility enhancement. Wavelength selectivity could again be achieved by using spectrally-selective antennas.

However, not all applications require wavelength-selectivity. Some applications instead require broadband sensitivity. Schottky and pyroelectric graphene-based PDs could be combined to realize a broadband super-sensor, spectrally active from visible to the mid-IR.

For example a graphene/silicon Schottky junction, active in the visible and near-IR could be realized, while a pyroelectric pixel could be fabricated on the side to provide senitivity in the mid-IR. Ideally, the whole process should be designed to be compatible with silicon technologies, but with a successful realization the super-sensor would have no competitors or alternatives on the market.

The main limit of the presented graphene/MoS_2 flexible photodetector is the use of a photoconducting mode with a semi-metallic channel. This means that a rather large current flows in graphene even in the OFF state, with consequent energy loss and background noise. Moreover, the gating technique relies on droplets of polymer electrolyte drop-casted on the heterostructure, which is hard to imagine in the context of industrial scalability. Additionally the drop-casting results in a μm thick polymer electrolyte layer, which limits the gate speed due to the slow movement of ions in the electrolyte. On the one hand, a possibility to improve the flexible photodetector design would be to sacrifice a portion of the photoconductive gain by using a semiconducting channel (*e.g.* by using a TMD). The absorption in the TMD could potentially be enhanced with the use of quantum dots, which would also make the detector spectrally-selective. On the other hand, the drop-casted deposition of polymer electrolyte could be substituted by controlled spin-coating of thin layers. Alternatively, the polymer electrolyte could also be replaced by thin low-temperature-deposited dielectrics such as aluminium oxide or hafnium oxide, although the resistance to bending of such materials should be tested.

Finally the route for optimizing superconducting detectors is much more complicated. Results have demonstrated a bolometric-type response of $NbSe_2$ devices. The sample does not undergo the full transition when only a few photons are impinging on the device. In order to confine the heat and the flowing current to force the transition from the superconducting state to the resistive state, the material should be patterned in a nanowire shape, as for current SSPDs. Lithography and etching steps need therefore to be optimized. Besides, in order to minimize the sample exposure to the environment, the device assembly could be performed entirely in an inert atmosphere. In parallel, highly doped semiconductors can be turned into superconductors as shown in Chapter 9. The performance of these as superconducting detectors could also be assessed and compared with existing technologies. Alternatively, the library and knowledge of layered materials is in constant expansion and could soon lead to the discovery of superconductors with higher critical temperature and better properties compared to $NbSe_2$.

Bibliography

[1] S. M. Sze and K. K. Ng, *Physics of semiconductor devices*, John Wiley & Sons (2006)

[2] B. E. Saleh and M. C. Teich, *Fundamentals of photonics*, Wiley New York (1991)

[3] S. Sze, *VLSI Technology (2nd Edition)*, McGraw-Hill (2003)

[4] P. R. Wallace, "*The band theory of graphite*", Physical Review **71**, 622 (1947)

[5] N. Mounet, M. Gibertini, P. Schwaller, A. Merkys, I. E. Castelli, A. Cepellotti, G. Pizzi, and N. Marzari, "*Novel two-dimensional materials from high-throughput computational exfoliation of experimentally known compounds*", arXiv:161105234 (2016)

[6] R. F. Frindt and A. D. Yoffe, "*Physical properties of layer structures: optical properties and photoconductivity of thin crystals of molybdenum disulphide*", Proceedings of the Royal Society of London **273**, 69 (1963)

[7] R. F. Frindt, "*Single crystals of MoS_2 several molecular layers thick*", Journal of Applied Physics **37**, 1928 (1966)

[8] R. F. Frindt, "*Superconductivity in ultrathin $NbSe_2$ layers*", Physical Review Letters **28**, 299 (1972)

[9] R. Peierls, "*Quelques proprietes typiques des corps solides*", Annales de l'Institut Henri Poincare **5**, 177 (1935)

[10] L. D. Landau, "*Zur theorie der phasenumwandlungen II*", Physikalische Zeitschrift der Sowjetunion **11**, 26 (1937)

[11] N. D. Mermin, "*Crystalline order in two dimensions*", Physical Review **176**, 250 (1968)

[12] A. K. Geim and K. S. Novoselov, "*The rise of graphene*", Nature Materials **6**, 183 (2007)

[13] K. S. Novoselov, A. K. Geim, S. V. Morozov, D. Jiang, Y. Zhang, S. V. Dubonos, I. V. Grigorieva, and A. A. Firsov, "*Electric field effect in atomically thin carbon films*", Science **306**, 666 (2004)

[14] A. K. Geim and A. H. MacDonald, "*Graphene: exploring carbon flatland*", Physics Today **60**, 35 (2007)

[15] A. H. Castro Neto, F. Guinea, N. M. R. Peres, K. S. Novoselov, and A. K. Geim, "*The electronic properties of graphene*", Reviews of Modern Physics **81**, 109 (2009)

[16] J. C. Charlier, P. C. Eklund, J. Zhu, and A. C. Ferrari, "*Electron and phonon properties of graphene: their relationship with carbon nanotubes*", Carbon Nanotubes **111**, 673 (2008)

[17] J. C. Slonczewski and P. R. Weiss, "*Band structure of graphite*", Physical Review **109**, 272 (1958)

[18] K. S. Novoselov, A. K. Geim, S. V. Morozov, D. Jiang, M. I. Katsnelson, I. V. Grigorieva, S. V. Dubonos, and A. A. Firsov, "*Two-dimensional gas of massless Dirac fermions in graphene*", Nature **438**, 197 (2005)

[19] Y. B. Zhang, Y. W. Tan, H. L. Stormer, and P. Kim, "*Experimental observation of the quantum Hall effect and Berry's phase in graphene*", Nature **438**, 201 (2005)

[20] P. Blake, E. W. Hill, A. H. C. Neto, K. S. Novoselov, D. Jiang, R. Yang, T. J. Booth, and A. K. Geim, "*Making graphene visible*", Applied Physics Letters **91**, 063124 (2007)

[21] C. Casiraghi, A. Hartschuh, E. Lidorikis, H. Qian, H. Harutyunyan, T. Gokus, K. S. Novoselov, and A. C. Ferrari, "*Rayleigh imaging of graphene and graphene layers*", Nano Letters **7**, 2711 (2007)

[22] A. B. Kuzmenko, van E. Heumen, F. Carbone, and van der D. Marel, "*Universal optical conductance of graphite*", Physical Review Letters **100**, 117401 (2008)

[23] R. R. Nair, P. Blake, A. N. Grigorenko, K. S. Novoselov, T. J. Booth, T. Stauber, N. M. R. Peres, and A. K. Geim, "*Fine structure constant defines visual transparency of graphene*", Science **320**, 1308 (2008)

[24] V. G. Kravets, A. N. Grigorenko, R. R. Nair, P. Blake, S. Anissimova, K. S. Novoselov, and A. K. Geim, "*Spectroscopic ellipsometry of graphene and an exciton-shifted van Hove peak in absorption*", Physical Review B **81**, 155413 (2010)

[25] F. Bonaccorso, Z. Sun, T. Hasan, and A. C. Ferrari, "*Graphene photonics and optoelectronics*", Nature Photonics **4**, 611 (2010)

[26] F. Bonaccorso, A. Lombardo, T. Hasan, Z. P. Sun, L. Colombo, and A. C. Ferrari, "*Production and processing of graphene and 2d crystals*", Materials Today **15**, 564 (2012)

[27] R. S. Pease, "*Crystal structure of boron nitride*", Nature **165**, 722 (1950)

[28] C. R. Dean, A. F. Young, I. Meric, C. Lee, L. Wang, S. Sorgenfrei, K. Watanabe, T. Taniguchi, P. Kim, K. L. Shepard, and J. Hone, "*Boron nitride substrates for high-quality graphene electronics*", Nature Nanotechnology **5**, 722 (2010)

[29] K. Watanabe, T. Taniguchi, and H. Kanda, "*Direct-bandgap properties and evidence for ultraviolet lasing of hexagonal boron nitride single crystal*", Nature Materials **3**, 404 (2004)

[30] G. Giovannetti, P. A. Khomyakov, G. Brocks, P. J. Kelly, and van den J. Brink, "*Substrate-induced band gap in graphene on hexagonal boron nitride: ab initio density functional calculations*", Physical Review B **76**, 073103 (2007)

[31] M. Chhowalla, H. S. Shin, G. Eda, L. J. Li, K. P. Loh, and H. Zhang, "*The chemistry of two-dimensional layered transition metal dichalcogenide nanosheets*", Nature Chemistry **5**, 263 (2013)

[32] K. F. Mak, C. Lee, J. Hone, J. Shan, and T. F. Heinz, "*Atomically thin MoS_2: a new direct-gap semiconductor*", Physical Review Letters **105**, 136805 (2010)

[33] R. Suzuki, M. Sakano, Y. J. Zhang, R. Akashi, D. Morikawa, A. Harasawa, K. Yaji, K. Kuroda, K. Miyamoto, T. Okuda, K. Ishizaka, R. Arita, and Y. Iwasa, "*Valley-dependent spin polarization in bulk MoS_2 with broken inversion symmetry*", Nature Nanotechnology **9**, 611 (2014)

[34] A. Splendiani, L. Sun, Y. B. Zhang, T. S. Li, J. Kim, C. Y. Chim, G. Galli, and F. Wang, "*Emerging photoluminescence in monolayer MoS_2*", Nano Letters **10**, 1271 (2010)

[35] T. Cao, G. Wang, W. Han, H. Ye, C. Zhu, J. Shi, Q. Niu, P. Tan, E. Wang, B. Liu, and J. Feng, "*Valley-selective circular dichroism of monolayer molybdenum disulphide*", Nature Communications **3**, 887 (2012)

[36] D. Xiao, G. B. Liu, W. X. Feng, X. D. Xu, and W. Yao, "*Coupled spin and valley physics in monolayers of MoS_2 and other group-VI dichalcogenides*", Physical Review Letters **108**, 196802 (2012)

[37] B. Radisavljevic, A. Radenovic, J. Brivio, V. Giacometti, and A. Kis, "*Single-layer MoS_2 transistors*", Nature Nanotechnology **6**, 147 (2011)

[38] Q. H. Wang, K. Kalantar-Zadeh, A. Kis, J. N. Coleman, and M. S. Strano, "*Electronics and optoelectronics of two-dimensional transition metal dichalcogenides*", Nature Nanotechnology **7**, 699 (2012)

[39] K. F. Mak and J. Shan, "*Photonics and optoelectronics of 2D semiconductor transition metal dichalcogenides*", Nature Photonics **10**, 216 (2016)

[40] Y. Cao, A. Mishchenko, G. L. Yu, E. Khestanova, A. P. Rooney, E. Prestat, A. V. Kretinin, P. Blake, M. B. Shalom, C. Woods, J. Chapman, G. Balakrishnan, I. V. Grigorieva, K. S. Novoselov, B. A. Piot, M. Potemski, K. Watanabe, T. Taniguchi, S. J. Haigh, A. K. Geim, and R. V. Gorbachev, "*Quality hterostructures from two-dimensional crystals unstable in air by their assembly in inert atmosphere*", Nano Letters **15**, 4914 (2015)

[41] X. Xi, L. Zhao, Z. Wang, H. Berger, L. Forró, J. Shan, and K. F. Mak, "*Strongly enhanced charge-density-wave order in monolayer $NbSe_2$*", Nature Nanotechnology **10**, 765 (2015)

[42] M. M. Ugeda, A. J. Bradley, Y. Zhang, S. Onishi, Y. Chen, W. Ruan, C. Ojeda-Aristizabal, H. Ryu, M. T. Edmonds, H.-Z. Tsai, A. Riss, S.-K. Mo, D. Lee, A. Zettl, Z. Hussain, Z.-X. Shen, and M. F. Crommie, "*Characterization of collective ground states in single-layer $NbSe_2$*", Nature Physics **12**, 92 (2016)

[43] K. S. Novoselov, D. Jiang, F. Schedin, T. J. Booth, V. V. Khotkevich, S. V. Morozov, and A. K. Geim, "*Two-dimensional atomic crystals*", Proceedings of the National Academy of Sciences of the United States of America **102**, 10451 (2005)

[44] A. K. Geim, "*Graphene: status and prospects*", Science **324**, 1530 (2009)

[45] T. Taniguchi and K. Watanabe, "*Synthesis of high-purity boron nitride single crystals under high pressure by using Ba-BN solvent*", Journal of Crystal Growth **303**, 525 (2007)

[46] A. Ubaldini, J. Jacimovic, N. Ubrig, and E. Giannini, "*Chloride-driven chemical vapor transport method for crystal growth of transition metal dichalcogenides*", Crystal Growth & Design **13**, 4453 (2013)

[47] C. Mattevi, H. Kim, and M. Chhowalla, "*A review of chemical vapour deposition of graphene on copper*", Journal of Materials Chemistry **21**, 3324 (2011)

[48] A. Reina, X. T. Jia, J. Ho, D. Nezich, H. B. Son, V. Bulovic, M. S. Dresselhaus, and J. Kong, "*Large area, few-layer graphene films on arbitrary substrates by chemical vapor deposition*", Nano Letters **9**, 30 (2009)

[49] X. S. Li, W. W. Cai, J. H. An, S. Kim, J. Nah, D. X. Yang, R. Piner, A. Velamakanni, I. Jung, E. Tutuc, S. K. Banerjee, L. Colombo, and R. S. Ruoff, "*Large-area synthesis of high-quality and uniform graphene films on copper foils*", Science **324**, 1312 (2009)

[50] S. Bae, H. Kim, Y. Lee, X. F. Xu, J. S. Park, Y. Zheng, J. Balakrishnan, T. Lei, H. R. Kim, Y. I. Song, Y. J. Kim, K. S. Kim, B. Ozyilmaz, J. H. Ahn, B. H. Hong, and S. Iijima, "*Roll-to-roll production of 30-inch graphene films for transparent electrodes*", Nature Nanotechnology **5**, 574 (2010)

[51] X. S. Li, C. W. Magnuson, A. Venugopal, R. M. Tromp, J. B. Hannon, E. M. Vogel, L. Colombo, and R. S. Ruoff, "*Large-area graphene single crystals grown by low-pressure chemical vapor deposition of methane on copper*", Journal of the American Chemical Society **133**, 2816 (2011)

[52] H. L. Zhou, W. J. Yu, L. X. Liu, R. Cheng, Y. Chen, X. Q. Huang, Y. Liu, Y. Wang, Y. Huang, and X. F. Duan, "*Chemical vapour deposition growth of large single crystals of monolayer and bilayer graphene*", Nature Communications **4** (2013)

[53] X. Xu, Z. Zhang, L. Qiu, J. Zhuang, L. Zhang, H. Wang, C. Liao, H. Song, R. Qiao, P. Gao, Z. Hu, L. Liao, Z. Liao, D. Yu, E. Wang, F. Ding, H. Peng, and K. Liu, "*Ultrafast growth of single-crystal graphene assisted by a continuous oxygen supply*", Nature Nanotechnology **11**, 930 (2016)

[54] I. Vlassiouk, M. Regmi, P. Fulvio, S. Dai, P. Datskos, G. Eres, and S. Smirnov, "*Role of hydrogen in chemical vapor deposition growth of large single-crystal graphene*", ACS Nano **5**, 6069 (2011)

[55] A. C. Ferrari, F. Bonaccorso, V. Fal'ko, K. S. Novoselov, S. Roche, P. Boggild, S. Borini, F. H. L. Koppens, V. Palermo, N. Pugno, J. A. Garrido, R. Sordan, A. Bianco, L. Ballerini, M. Prato, E. Lidorikis, J. Kivioja, C. Marinelli, T. Ryhanen, A. Morpurgo, J. N. Coleman, V. Nicolosi, L. Colombo, A. Fert, M. Garcia-Hernandez, A. Bachtold, G. F. Schneider, F. Guinea, C. Dekker, M. Barbone, Z. Sun, C. Galiotis, A. N. Grigorenko, G. Konstantatos, A. Kis, M. Katsnelson, L. Vandersypen, A. Loiseau, V. Morandi, D. Neumaier, E. Treossi, V. Pellegrini, M. Polini, A. Tredicucci, G. M. Williams, B. Hee Hong, J.-H. Ahn, J. Min Kim, H. Zirath, van B. J. Wees, van der H. Zant, L. Occhipinti, A. Di Matteo, I. A. Kinloch, T. Seyller, E. Quesnel, X. Feng, K. Teo, N. Rupesinghe, P. Hakonen, S. R. T. Neil, Q. Tannock, T. Lofwander, and J. Kinaret, "*Science and technology roadmap for graphene, related two-dimensional crystals, and hybrid systems*", Nanoscale **7**, 4598 (2015)

[56] A. R. Jang, S. Hong, C. Hyun, S. I. Yoon, G. Kim, H. Y. Jeong, T. J. Shin, S. O. Park, K. Wong, S. K. Kwak, N. Park, K. Yu, E. Choi, A. Mishchenko, F. Withers, K. S. Novoselov, H. Lim, and H. S. Shin, "*Wafer-scale and wrinkle-free epitaxial growth of single-orientated multilayer hexagonal boron nitride on sapphire*", Nano Letters **16**, 3360 (2016)

[57] L. Song, L. Ci, H. Lu, P. B. Sorokin, C. Jin, J. Ni, A. G. Kvashnin, D. G. Kvashnin, J. Lou, B. I. Yakobson, and P. M. Ajayan, "*Large scale growth and characterization of atomic hexagonal boron nitride layers*", Nano Letters **10**, 3209 (2010)

[58] Y. M. Shi, C. Hamsen, X. T. Jia, K. K. Kim, A. Reina, M. Hofmann, A. L. Hsu, K. Zhang, H. N. Li, Z. Y. Juang, M. S. Dresselhaus, L. J. Li, and J. Kong, "*Synthesis of few-layer hexagonal boron nitride thin film by chemical vapor deposition*", Nano Letters **10**, 4134 (2010)

[59] Y. H. Lee, X. Q. Zhang, W. J. Zhang, M. T. Chang, C. T. Lin, K. D. Chang, Y. C. Yu, J. T. W. Wang, C. S. Chang, L. J. Li, and T. W. Lin, "*Synthesis of large-area MoS_2 atomic layers with chemical vapor deposition*", Advanced Materials **24**, 2320 (2012)

[60] van der A. M. Zande, P. Y. Huang, D. A. Chenet, T. C. Berkelbach, Y. You, G.-H. Lee, T. F. Heinz, D. R. Reichman, D. A. Muller, and J. C. Hone, "*Grains and*

grain boundaries in highly crystalline monolayer molybdenum disulphide", Nature Materials **12**, 554 (2013)

[61] Y. Yu, C. Li, Y. Liu, L. Su, Y. Zhang, and L. Cao, "*Controlled scalable synthesis of uniform, high-quality monolayer and few-layer MoS_2 Films*", Scientific Reports **3**, 1866 (2013)

[62] J.-K. Huang, J. Pu, C.-L. Hsu, M.-H. Chiu, Z.-Y. Juang, Y.-H. Chang, W.-H. Chang, Y. Iwasa, T. Takenobu, and L.-J. Li, "*Large-area synthesis of highly crystalline WSe_2 monolayers and device applications*", ACS Nano **8**, 923 (2013)

[63] K. Kang, S. E. Xie, L. J. Huang, Y. M. Han, P. Y. Huang, K. F. Mak, C. J. Kim, D. Muller, and J. Park, "*High-mobility three-atom-thick semiconducting films with wafer-scale homogeneity*", Nature **520**, 656 (2015)

[64] C. Casiraghi, A. Hartschuh, H. Qian, S. Piscanec, C. Georgi, A. Fasoli, K. S. Novoselov, D. M. Basko, and A. C. Ferrari, "*Raman spectroscopy of graphene edges*", Nano Letters **9**, 1433 (2009)

[65] M. M. Benameur, B. Radisavljevic, J. S. Heron, S. Sahoo, H. Berger, and A. Kis, "*Visibility of dichalcogenide nanolayers*", Nanotechnology **22** (2011)

[66] R. V. Gorbachev, I. Riaz, R. R. Nair, R. Jalil, L. Britnell, B. D. Belle, E. W. Hill, K. S. Novoselov, K. Watanabe, T. Taniguchi, A. K. Geim, and P. Blake, "*Hunting for monolayer boron nitride: optical and Raman signatures*", Small **7**, 465 (2011)

[67] J. C. Meyer, A. K. Geim, M. I. Katsnelson, K. S. Novoselov, T. J. Booth, and S. Roth, "*The structure of suspended graphene sheets*", Nature **446**, 60 (2007)

[68] J. C. Meyer, A. K. Geim, M. I. Katsnelson, K. S. Novoselov, D. Obergfell, S. Roth, C. Girit, and A. Zettl, "*On the roughness of single- and bi-layer graphene membranes*", Solid State Communications **143**, 101 (2007)

[69] P. Y. Huang, C. S. Ruiz-Vargas, van der A. M. Zande, W. S. Whitney, M. P. Levendorf, J. W. Kevek, S. Garg, J. S. Alden, C. J. Hustedt, Y. Zhu, J. Park, P. L. McEuen, and D. A. Muller, "*Grains and grain boundaries in single-layer graphene atomic patchwork quilts*", Nature **469**, 389 (2011)

[70] A. C. Ferrari and D. M. Basko, "*Raman spectroscopy as a versatile tool for studying the properties of graphene*", Nature Nanotechnology **8**, 235 (2013)

[71] C. V. Raman and K. S. Krishnan, "*A new type of secondary radiation*", Nature **121**, 501 (1928)

[72] A. C. Ferrari, J. C. Meyer, V. Scardaci, C. Casiraghi, M. Lazzeri, F. Mauri, S. Piscanec, D. Jiang, K. S. Novoselov, S. Roth, and A. K. Geim, "*Raman spectrum of graphene and graphene layers*", Physical Review Letters **97**, 187401 (2006)

[73] D. M. Basko, S. Piscanec, and A. C. Ferrari, "*Electron-electron interactions and doping dependence of the two-phonon Raman intensity in graphene*", Physical Review B **80**, 165413 (2009)

[74] C. Thomsen and S. Reich, "*Double resonant Raman scattering in graphite*", Physical Review Letters **85**, 5214 (2000)

[75] A. C. Ferrari, "*Raman spectroscopy of graphene and graphite: disorder, electron-phonon coupling, doping and nonadiabatic effects*", Solid State Communications **143**, 47 (2007)

[76] A. Das, S. Pisana, B. Chakraborty, S. Piscanec, S. K. Saha, U. V. Waghmare, K. S. Novoselov, H. R. Krishnamurthy, A. K. Geim, A. C. Ferrari, and A. K. Sood, "*Monitoring dopants by Raman scattering in an electrochemically top-gated graphene transistor*", Nature Nanotechnology **3**, 210 (2008)

[77] L. G. Cancado, A. Jorio, E. H. Ferreira, F. Stavale, C. A. Achete, R. B. Capaz, M. V. Moutinho, A. Lombardo, T. S. Kulmala, and A. C. Ferrari, "*Quantifying defects in graphene via Raman spectroscopy at different excitation energies*", Nano Letters **11**, 3190 (2011)

[78] P. H. Tan, W. P. Han, W. J. Zhao, Z. H. Wu, K. Chang, H. Wang, Y. F. Wang, N. Bonini, N. Marzari, N. Pugno, G. Savini, A. Lombardo, and A. C. Ferrari, "*The shear mode of multilayer graphene*", Nature Materials **11**, 294 (2012)

[79] X. Zhang, W. P. Han, J. B. Wu, S. Milana, Y. Lu, Q. Q. Li, A. C. Ferrari, and P. H. Tan, "*Raman spectroscopy of shear and layer breathing modes in multilayer MoS_2*", Physical Review B **87**, 115413 (2013)

[80] R. Geick, C. H. Perry, and Rupprech.G, "*Normal modes in hexagonal boron nitride*", Physical Review **146**, 543 (1966)

[81] J. L. Verble and T. J. Wieting, "*Lattice mode degeneracy in MoS_2 and other layer compounds*", Physical Review Letters **25**, 362 (1970)

[82] T. J. Wieting and J. L. Verble, "*Infrared and Raman studies of long-wavelength optical phonons in hexagonal MoS_2*", Physical Review B **3**, 4286 (1971)

[83] C. Lee, H. G. Yan, L. E. Brus, T. F. Heinz, J. Hone, and S. Ryu, "*Anomalous lattice vibrations of single- and few-layer MoS_2*", ACS Nano **4**, 2695 (2010)

[84] S. El-Bana, Mohammed, D. Wolverson, S. Russo, G. Balakrishnan, D. M. Paul, and J. Bending, Simon, "*Superconductivity in two-dimensional $NbSe_2$ field effect transistors*", Superconductor Science and Technology **26**, 125020 (2013)

[85] A. Ramasubramaniam, "*Large excitonic effects in monolayers of molybdenum and tungsten dichalcogenides*", Physical Review B **86**, 115409 (2012)

[86] A. Chernikov, T. C. Berkelbach, H. M. Hill, A. Rigosi, Y. Li, O. B. Aslan, D. R. Reichman, M. S. Hybertsen, and T. F. Heinz, "*Exciton binding energy and nonhydrogenic Rydberg series in monolayer WS_2*", Physical Review Letters **113**, 076802 (2014)

[87] K. F. Mak, L. Ju, F. Wang, and T. F. Heinz, "*Optical spectroscopy of graphene: from the far infrared to the ultraviolet*", Solid State Communications **152**, 1341 (2012)

[88] R. S. Sundaram, M. Engel, A. Lombardo, R. Krupke, A. C. Ferrari, P. Avouris, and M. Steiner, "*Electroluminescence in single layer MoS_2*", Nano Letters **13**, 1416 (2013)

[89] G. Soavi, F. Scotognella, G. Lanzani, and G. Cerullo, "*Ultrafast photophysics of single-walled carbon nanotubes*", Advanced Optical Materials **4**, 1670 (2016)

[90] D. Brida, A. Tomadin, C. Manzoni, Y. J. Kim, A. Lombardo, S. Milana, R. R. Nair, K. S. Novoselov, A. C. Ferrari, G. Cerullo, and M. Polini, "*Ultrafast collinear scattering and carrier multiplication in graphene*", Nature Communications **4** (2013)

[91] R. Wang, B. A. Ruzicka, N. Kumar, M. Z. Bellus, H.-Y. Chiu, and H. Zhao, "*Ultrafast and spatially resolved studies of charge carriers in atomically thin molybdenum disulfide*", Physical Review B **86**, 045406 (2012)

[92] L. Britnell, R. V. Gorbachev, R. Jalil, B. D. Belle, F. Schedin, A. Mishchenko, T. Georgiou, M. I. Katsnelson, L. Eaves, S. V. Morozov, N. M. R. Peres, J. Leist, A. K.

Geim, K. S. Novoselov, and L. A. Ponomarenko, "*Field-effect tunneling transistor based on vertical graphene heterostructures*", Science **335**, 947 (2012)

[93] A. Mishchenko, J. S. Tu, Y. Cao, R. V. Gorbachev, J. R. Wallbank, M. T. Greenaway, V. E. Morozov, S. V. Morozov, M. J. Zhu, S. L. Wong, WithersF, C. R. Woods, Y. J. Kim, K. Watanabe, T. Taniguchi, E. E. Vdovin, O. Makarovsky, T. M. Fromhold, V. I. Fal'ko, A. K. Geim, L. Eaves, and K. S. Novoselov, "*Twist-controlled resonant tunnelling in graphene/boron nitride/graphene heterostructures*", Nature Nanotechnology **9**, 808 (2014)

[94] C.-H. Lee, G.-H. Lee, van der A. M. Zande, W. Chen, Y. Li, M. Han, X. Cui, G. Arefe, C. Nuckolls, T. F. Heinz, J. Guo, J. Hone, and P. Kim, "*Atomically thin p–n junctions with van der Waals heterointerfaces*", Nature Nanotechnology **9**, 676 (2014)

[95] F. Withers, O. Del Pozo-Zamudio, A. Mishchenko, A. P. Rooney, A. Gholinia, K. Watanabe, T. Taniguchi, S. J. Haigh, A. K. Geim, A. I. Tartakovskii, and K. S. Novoselov, "*Light-emitting diodes by band-structure engineering in van der Waals heterostructures*", Nature Materials **14**, 301 (2015)

[96] A. K. Geim and I. V. Grigorieva, "*Van der Waals heterostructures*", Nature **499**, 419 (2013)

[97] Z. Liu, L. Song, S. Zhao, J. Huang, L. Ma, J. Zhang, J. Lou, and P. M. Ajayan, "*Direct growth of graphene/hexagonal boron nitride stacked layers*", Nano Letters **11**, 2032 (2011)

[98] Y. Shi, W. Zhou, A.-Y. Lu, W. Fang, Y.-H. Lee, A. L. Hsu, S. M. Kim, K. K. Kim, H. Y. Yang, L.-J. Li, J.-C. Idrobo, and J. Kong, "*Van der Waals epitaxy of MoS_2 layers using graphene as growth templates*", Nano Letters **12**, 2784 (2012)

[99] Y. Gong, J. Lin, X. Wang, G. Shi, S. Lei, Z. Lin, X. Zou, G. Ye, R. Vajtai, B. I. Yakobson, H. Terrones, M. Terrones, B. K. Tay, J. Lou, S. T. Pantelides, Z. Liu, W. Zhou, and P. M. Ajayan, "*Vertical and in-plane heterostructures from WS_2/MoS_2 monolayers*", Nature Materials **13**, 1135 (2014)

[100] Y.-C. Lin, R. K. Ghosh, R. Addou, N. Lu, S. M. Eichfeld, H. Zhu, M.-Y. Li, X. Peng, M. J. Kim, L.-J. Li, R. M. Wallace, S. Datta, and J. A. Robinson, "*Atomically thin resonant tunnel diodes built from synthetic van der Waals heterostructures*", Nature Communications **6**, 7311 (2015)

[101] Q. Wu, S. K. Jang, S. Park, S. J. Jung, H. Suh, Y. H. Lee, S. Lee, and Y. J. Song, "*In situ synthesis of a large area boron nitride/graphene monolayer/boron nitride film by chemical vapor deposition*", Nanoscale **7**, 7574 (2015)

[102] A. Reina, H. Son, L. Jiao, B. Fan, M. S. Dresselhaus, Z. Liu, and J. Kong, "*Transferring and identification of single- and few-layer graphene on arbitrary substrates*", The Journal of Physical Chemistry C **112**, 17741 (2008)

[103] D. Dumcenco, D. Ovchinnikov, K. Marinov, P. Lazić, M. Gibertini, N. Marzari, O. L. Sanchez, Y.-C. Kung, D. Krasnozhon, M.-W. Chen, S. Bertolazzi, P. Gillet, Fontcuberta i A. Morral, A. Radenovic, and A. Kis, "*Large-area epitaxial monolayer MoS_2*", ACS Nano **9**, 4611 (2015)

[104] Y. Wang, Y. Zheng, X. F. Xu, E. Dubuisson, Q. L. Bao, J. Lu, and K. P. Loh, "*Electrochemical delamination of CVD-grown graphene film: toward the recyclable use of copper catalyst*", ACS Nano **5**, 9927 (2011)

[105] A. Castellanos-Gomez, M. Buscema, R. Molenaar, V. Singh, L. Janssen, van der H. S. J. . Zant, and G. A. Steele, "*Deterministic transfer of two-dimensional materials by all-dry viscoelastic stamping*", 2D Materials **1**, 011002 (2014)

[106] M. A. Meitl, Z.-T. Zhu, V. Kumar, K. J. Lee, X. Feng, Y. Y. Huang, I. Adesida, R. G. Nuzzo, and J. A. Rogers, "*Transfer printing by kinetic control of adhesion to an elastomeric stamp*", Nature Materials **5**, 33 (2006)

[107] L. Wang, I. Meric, P. Y. Huang, Q. Gao, Y. Gao, H. Tran, T. Taniguchi, K. Watanabe, L. M. Campos, D. A. Muller, J. Guo, P. Kim, J. Hone, K. L. Shepard, and C. R. Dean, "*One-dimensional electrical contact to a two-dimensional material*", Science **342**, 614 (2013)

[108] P. J. Zomer, M. H. D. Guimarães, J. C. Brant, N. Tombros, and van B. J. Wees, "*Fast pick up technique for high quality heterostructures of bilayer graphene and hexagonal boron nitride*", Applied Physics Letters **105**, 013101 (2014)

[109] L. Banszerus, M. Schmitz, S. Engels, J. Dauber, M. Oellers, F. Haupt, K. Watanabe, T. Taniguchi, B. Beschoten, and C. Stampfer, "*Ultrahigh-mobility graphene devices from chemical vapor deposition on reusable copper*", Science Advances **1**, e1500222 (2015)

[110] A. V. Kretinin, Y. Cao, J. S. Tu, G. L. Yu, R. Jalil, K. S. Novoselov, S. J. Haigh, A. Gholinia, A. Mishchenko, M. Lozada, T. Georgiou, C. R. Woods, F. Withers, P.

Blake, G. Eda, A. Wirsig, C. Hucho, K. Watanabe, T. Taniguchi, A. K. Geim, and R. V. Gorbachev, "*Electronic properties of graphene encapsulated with different two-dimensional atomic crystals*", Nano Letters **14**, 3270 (2014)

[111] F. Pizzocchero, L. Gammelgaard, B. S. Jessen, J. M. Caridad, L. Wang, J. Hone, P. Boggild, and T. J. Booth, "*The hot pick-up technique for batch assembly of van der Waals heterostructures*", Nature Communications **7**, 11894 (2016)

[112] C. H. Lui, Z. P. Ye, C. Ji, K. C. Chiu, C. T. Chou, T. I. Andersen, C. Means-Shively, H. Anderson, J. M. Wu, T. Kidd, Y. H. Lee, and R. He, "*Observation of interlayer phonon modes in van der Waals heterostructures*", Physical Review B **91**, 165403 (2015)

[113] F. Ceballos, M. Z. Bellus, H. Y. Chiu, and H. Zhao, "*Ultrafast charge separation and indirect exciton formation in a MoS_2-$MoSe_2$ van der Waals heterostructure*", ACS Nano **8**, 12717 (2014)

[114] P. Rivera, J. R. Schaibley, A. M. Jones, J. S. Ross, S. Wu, G. Aivazian, P. Klement, K. Seyler, G. Clark, N. J. Ghimire, J. Yan, D. G. Mandrus, W. Yao, and X. Xu, "*Observation of long-lived interlayer excitons in monolayer $MoSe_2$–WSe_2 heterostructures*", Nature Communications **6**, 6242 (2015)

[115] F. H. L. Koppens, T. Mueller, P. Avouris, A. C. Ferrari, M. S. Vitiello, and M. Polini, "*Photodetectors based on graphene, other two-dimensional materials and hybrid systems*", Nature Nanotechnology **9**, 780 (2014)

[116] X. T. Gan, R. J. Shiue, Y. D. Gao, I. Meric, T. F. Heinz, K. Shepard, J. Hone, S. Assefa, and D. Englund, "*Chip-integrated ultrafast graphene photodetector with high responsivity*", Nature Photonics **7**, 883 (2013)

[117] A. Pospischil, M. Humer, M. M. Furchi, D. Bachmann, R. Guider, T. Fromherz, and T. Mueller, "*CMOS-compatible graphene photodetector covering all optical communication bands*", Nature Photonics **7**, 892 (2013)

[118] X. M. Wang, Z. Z. Cheng, K. Xu, H. K. Tsang, and J. B. Xu, "*High-responsivity graphene/silicon-heterostructure waveguide photodetectors*", Nature Photonics **7**, 888 (2013)

[119] G. Konstantatos, M. Badioli, L. Gaudreau, J. Osmond, M. Bernechea, de F. P. G. Arquer, F. Gatti, and F. H. L. Koppens, "*Hybrid graphene-quantum dot phototransistors with ultrahigh gain*", Nature Nanotechnology **7**, 363 (2012)

[120] K. Roy, M. Padmanabhan, S. Goswami, T. P. Sai, G. Ramalingam, S. Raghavan, and A. Ghosh, "*Graphene-MoS_2 hybrid structures for multifunctional photoresponsive memory devices*", Nature Nanotechnology **8**, 826 (2013)

[121] W. J. Zhang, C. P. Chuu, J. K. Huang, C. H. Chen, M. L. Tsai, Y. H. Chang, C. T. Liang, Y. Z. Chen, Y. L. Chueh, J. H. He, M. Y. Chou, and L. J. Li, "*Ultrahigh-gain photodetectors based on atomically thin graphene-MoS_2 heterostructures*", Scientific Reports **4**, 3826 (2014)

[122] O. Lopez-Sanchez, D. Lembke, M. Kayci, A. Radenovic, and A. Kis, "*Ultrasensitive photodetectors based on monolayer MoS_2*", Nature Nanotechnology **8**, 497 (2013)

[123] P. A. Hu, L. F. Wang, M. Yoon, J. Zhang, W. Feng, X. N. Wang, Z. Z. Wen, J. C. Idrobo, Y. Miyamoto, D. B. Geohegan, and K. Xiao, "*Highly responsive ultrathin GaS nanosheet photodetectors on rigid and flexible substrates*", Nano Letters **13**, 1649 (2013)

[124] D. B. Farmer, R. Golizadeh-Mojarad, V. Perebeinos, Y.-M. Lin, G. S. Tulevski, J. C. Tsang, and P. Avouris, "*Chemical doping and electron-hole conduction asymmetry in graphene devices*", Nano Letters **9**, 388 (2009)

[125] M. C. Lemme, F. H. L. Koppens, A. L. Falk, M. S. Rudner, H. Park, L. S. Levitov, and C. M. Marcus, "*Gate-activated photoresponse in a graphene p-n junction*", Nano Letters **11**, 4134 (2011)

[126] G. Giovannetti, P. A. Khomyakov, G. Brocks, V. M. Karpan, van den J. Brink, and P. J. Kelly, "*Doping graphene with metal contacts*", Physical Review Letters **101**, 026803 (2008)

[127] F. N. Xia, T. Mueller, Y. M. Lin, A. Valdes-Garcia, and P. Avouris, "*Ultrafast graphene photodetector*", Nature Nanotechnology **4**, 839 (2009)

[128] T. Mueller, F. N. A. Xia, and P. Avouris, "*Graphene photodetectors for high-speed optical communications*", Nature Photonics **4**, 297 (2010)

[129] A. Pospischil, M. M. Furchi, and T. Mueller, "*Solar-energy conversion and light emission in an atomic monolayer p-n diode*", Nature Nanotechnology **9**, 257 (2014)

[130] B. W. H. Baugher, H. O. H. Churchill, Y. Yang, and P. Jarillo-Herrero, "*Optoelectronic devices based on electrically tunable p-n diodes in a monolayer dichalcogenide*", Nature Nanotechnology **9**, 262 (2014)

[131] P. W. Kruse, *Uncooled thermal imaging: arrays, systems, and applications*, SPIE press (2001)

[132] R. A. Wood, C. J. Han, and P. W. Kruse, *Technical Digest IEEE Solid-State Sensor and Actuator Workshop*, "*Integrated uncooled infrared detector imaging arrays*", 132–135 (1992)

[133] A. Rogalski, "*Infrared detectors: status and trends*", Progress in Quantum Electronics **27**, 59 (2003)

[134] M. Moreno, A. Kosarev, A. Torres, and R. Ambrosio, "*Fabrication and performance comparison of planar and sandwich structures of micro-bolometers with Ge thermosensing layer*", Thin Solid Films **515**, 7607 (2007)

[135] S. B. Lang, "*Pyroelectricity: from ancient curiosity to modern imaging tool*", Physics Today **58**, 31 (2005)

[136] R. W. Whatmore, "*Pyroelectric devices and materials*", Reports on Progress in Physics **49**, 1335 (1986)

[137] Y.-W. Tan, Y. Zhang, H. L. Stormer, and P. Kim, "*Temperature dependent electron transport in graphene*", The European Physical Journal Special Topics **148**, 15 (2007)

[138] M. Freitag, T. Low, W. Zhu, H. Yan, F. Xia, and P. Avouris, "*Photocurrent in graphene harnessed by tunable intrinsic plasmons*", Nature Communications **4**, 1951 (2013)

[139] R. H. Hadfield, "*Single-photon detectors for optical quantum information applications*", Nature Photonics **3**, 696 (2009)

[140] K. Irwin and G. Hilton, *Transition-edge sensors*, 63–150, Springer Berlin Heidelberg, Berlin, Heidelberg (2005)

[141] M. Tinkham, *Introduction to superconductivity*, Courier Corporation (1996)

[142] A. D. Semenov, G. N. Gol'tsman, and A. A. Korneev, "*Quantum detection by current carrying superconducting film*", Physica C **351**, 349 (2001)

[143] C. Natarajan, M. G. Tanner, and R. H. Hadfield, "*Superconducting nanowire single-photon detectors: physics and applications*", Superconductor Science & Technology **25**, 063001 (2012)

[144] G. N. Gol'tsman, O. Okunev, G. Chulkova, A. Lipatov, A. Semenov, K. Smirnov, B. Voronov, A. Dzardanov, C. Williams, and R. Sobolewski, "*Picosecond superconducting single-photon optical detector*", Applied Physics Letters **79**, 705 (2001)

[145] A. E. Lita, A. J. Miller, and S. W. Nam, "*Counting near-infrared single-photons with 95% efficiency*", Optics Express **16**, 3032 (2008)

[146] K. M. Rosfjord, J. K. W. Yang, E. A. Dauler, A. J. Kerman, V. Anant, B. M. Voronov, G. N. Gol'tsman, and K. K. Berggren, "*Nanowire single-photon detector with an integrated optical cavity and anti-reflection coating*", Optics Express **14**, 527 (2006)

[147] N. M. Gabor, J. C. W. Song, Q. Ma, N. L. Nair, T. Taychatanapat, K. Watanabe, T. Taniguchi, L. S. Levitov, and P. Jarillo-Herrero, "*Hot carrier-assisted intrinsic photoresponse in graphene*", Science **334**, 648 (2011)

[148] M. Dyakonov and M. Shur, "*Shallow-water analogy for a ballistic field-effect transistor*", Physical Review Letters **71**, 2465 (1993)

[149] M. Dyakonov and M. Shur, "*Detection, mixing, and frequency multiplication of terahertz radiation by two-dimensional electronic fluid*", IEEE Transactions on Electron Devices **43**, 380 (1996)

[150] L. Vicarelli, M. S. Vitiello, D. Coquillat, A. Lombardo, A. C. Ferrari, W. Knap, M. Polini, V. Pellegrini, and A. Tredicucci, "*Graphene field-effect transistors as room-temperature terahertz detectors*", Nature Materials **11**, 865 (2012)

[151] M. Fox, *Optical properties of solids*, Oxford University Press, New York (2001)

[152] R. Soref and B. Bennett, "*Electro-optical effects in silicon*", IEEE Journal of Quantum Electronics **23**, 123 (1987)

[153] S. O. Kasap, *Optoelectronics & photonics: principles & practices*, Pearson Higher Ed. (2013)

[154] G. T. Reed, G. Mashanovich, F. Y. Gardes, and D. J. Thomson, "*Silicon optical modulators*", Nature Photonics **4**, 518 (2010)

[155] R. S. Weis and T. K. Gaylord, "*Lithium niobate: summary of physical properties and crystal structure*", Applied Physics A **37**, 191 (1985)

[156] M. Liu, X. B. Yin, E. Ulin-Avila, B. S. Geng, T. Zentgraf, L. Ju, F. Wang, and X. Zhang, "*A graphene-based broadband optical modulator*", Nature **474**, 64 (2011)

[157] C. T. Phare, Y.-H. Daniel Lee, J. Cardenas, and M. Lipson, "*Graphene electro-optic modulator with 30 GHz bandwidth*", Nature Photonics **9**, 511 (2015)

[158] S. H. Lee, M. Choi, T. T. Kim, S. Lee, M. Liu, X. Yin, H. K. Choi, S. S. Lee, C. G. Choi, S. Y. Choi, X. Zhang, and B. Min, "*Switching terahertz waves with gate-controlled active graphene metamaterials*", Nature Materials **11**, 936 (2012)

[159] Z. Sun, A. Martinez, and F. Wang, "*Optical modulators with 2D layered materials*", Nature Photonics **10**, 227 (2016)

[160] E. F. Schubert, T. Gessmann, and J. K. Kim, *Light emitting diodes*, Wiley Online Library (2005)

[161] T. Ando, "*Screening effect and impurity scattering in monolayer graphene*", Journal of the Physical Society of Japan **75**, 074716 (2006)

[162] A. S. Mayorov, R. V. Gorbachev, S. V. Morozov, L. Britnell, R. Jalil, L. A. Ponomarenko, P. Blake, K. S. Novoselov, K. Watanabe, T. Taniguchi, and A. K. Geim, "*Micrometer-scale ballistic transport in encapsulated graphene at room temperature*", Nano Letters **11**, 2396 (2011)

[163] E. H. Hwang and S. Das Sarma, "*Acoustic phonon scattering limited carrier mobility in two-dimensional extrinsic graphene*", Physical Review B **77**, 115449 (2008)

[164] J. H. Chen, C. Jang, S. D. Xiao, M. Ishigami, and M. S. Fuhrer, "*Intrinsic and extrinsic performance limits of graphene devices on SiO_2*", Nature Nanotechnology **3**, 206 (2008)

[165] A. Das, B. Chakraborty, S. Piscanec, S. Pisana, A. K. Sood, and A. C. Ferrari, "*Phonon renormalization in doped bilayer graphene*", Physical Review B **79**, 155417 (2009)

[166] M. Bruna, A. K. Ott, M. Ijas, D. Yoon, U. Sassi, and A. C. Ferrari, "*Doping dependence of the Raman spectrum of defected graphene*", ACS Nano **8**, 7432 (2014)

[167] Q. Yu, L. A. Jauregui, W. Wu, R. Colby, J. Tian, Z. Su, H. Cao, Z. Liu, D. Pandey, D. Wei, T. F. Chung, P. Peng, N. P. Guisinger, E. A. Stach, J. Bao, S.-S. Pei, and Y. P. Chen, "*Control and characterization of individual grains and grain boundaries in graphene grown by chemical vapour deposition*", Nature Materials **10**, 443 (2011)

[168] A. W. Tsen, L. Brown, M. P. Levendorf, F. Ghahari, P. Y. Huang, R. W. Havener, C. S. Ruiz-Vargas, D. A. Muller, P. Kim, and J. Park, "*Tailoring electrical transport across grain boundaries in polycrystalline graphene*", Science **336**, 1143 (2012)

[169] P. Braeuninger-Weimer, B. Brennan, A. J. Pollard, and S. Hofmann, "*Understanding and controlling Cu-catalyzed graphene nucleation: the role of impurities, roughness, and oxygen scavenging*", Chemistry of Materials **28**, 8905 (2016)

[170] W. Gannett, W. Regan, K. Watanabe, T. Taniguchi, M. F. Crommie, and A. Zettl, "*Boron nitride substrates for high mobility chemical vapor deposited graphene*", Applied Physics Letters **98**, 242105 (2011)

[171] N. Petrone, C. R. Dean, I. Meric, van der A. M. Zande, P. Y. Huang, L. Wang, D. Muller, K. L. Shepard, and J. Hone, "*Chemical vapor deposition-derived graphene with electrical performance of exfoliated graphene*", Nano Letters **12**, 2751 (2012)

[172] V. E. Calado, S. E. Zhu, S. Goswami, Q. Xu, K. Watanabe, T. Taniguchi, G. C. A. M. Janssen, and L. M. K. Vandersypen, "*Ballistic transport in graphene grown by chemical vapor deposition*", Applied Physics Letters **104**, 023103 (2014)

[173] A. A. Lagatsky, Z. Sun, T. S. Kulmala, R. S. Sundaram, S. Milana, F. Torrisi, O. L. Antipov, Y. Lee, J. H. Ahn, C. T. A. Brown, W. Sibbett, and A. C. Ferrari, "*2μm solid-state laser mode-locked by single-layer graphene*", Applied Physics Letters **102**, 013113 (2013)

[174] N. J. G. Couto, D. Costanzo, S. Engels, D. K. Ki, K. Watanabe, T. Taniguchi, C. Stampfer, F. Guinea, and A. F. Morpurgo, "*Random strain fluctuations as dominant disorder source for high-quality on-substrate graphene devices*", Physical Review X **4**, 041019 (2014)

[175] L. Banszerus, M. Schmitz, S. Engels, M. Goldsche, K. Watanabe, T. Taniguchi, B. Beschoten, and C. Stampfer, "*Ballistic transport exceeding 28μm in CVD grown graphene*", Nano Letters **16**, 1387 (2016)

[176] P. Blake, R. Yang, S. V. Morozov, F. Schedin, L. A. Ponomarenko, A. A. Zhukov, R. R. Nair, I. V. Grigorieva, K. S. Novoselov, and A. K. Geim, "*Influence of metal contacts and charge inhomogeneity on transport properties of graphene near the neutrality point*", Solid State Communications **149**, 1068 (2009)

[177] D. De Fazio, I. Goykhman, D. Yoon, M. Bruna, A. Eiden, S. Milana, U. Sassi, M. Barbone, D. Dumcenco, K. Marinov, A. Kis, and A. C. Ferrari, "*High responsivity, large-area graphene/MoS_2 flexible photodetectors*", ACS Nano **10**, 8252 (2016)

[178] H. Li, Q. Zhang, C. C. R. Yap, B. K. Tay, T. H. T. Edwin, A. Olivier, and D. Baillargeat, "*From bulk to monolayer MoS_2: evolution of Raman scattering*", Advanced Functional Materials **22**, 1385 (2012)

[179] S. P. S. Porto and R. S. Krishnan, "*Raman effect of corundum*", The Journal of Chemical Physics **47**, 1009 (1967)

[180] F. J. Boerio, S. K. Bahl, and G. E. McGraw, "*Vibrational analysis of polyethylene terephthalate and its deuterated derivatives*", Journal of Polymer Science **14**, 1029 (1976)

[181] D. Y. Qiu, da F. H. Jornada, and S. G. Louie, "*Optical spectrum of MoS_2: many-body effects and diversity of exciton states*", Physical Review Letters **111**, 216805 (2013)

[182] G. P. Agrawal, *Fiber-optic communication systems, 4th Edition*, John Wiley & Sons, New York (2010)

[183] E. Leitgeb, M. Gebhart, and U. Birnbacher, "*Optical networks, last mile access and applications*", Journal of Optical and Fiber Communications Reports **2**, 56 (2005)

[184] H. Kaushal and G. Kaddoum, "*Optical communication in space: challenges and mitigation techniques*", IEEE Communications Surveys & Tutorials **99**, 1 (2016)

[185] M. Ijaz, Z. Ghassemlooy, S. Rajbhandari, H. Le Minh, J. Perez, and A. Gholami, *8th International Symposium on Communication Systems, Networks & Digital Signal Processing*, "*Comparison of 830 nm and 1550 nm based free space optical communications link under controlled fog conditions*", IEEE (2012)

[186] S. Ishida and N. Nishizawa, "*Quantitative comparison of contrast and imaging depth of ultrahigh-resolution optical coherence tomography images in 800-1700 nm wavelength region*", Biomedical Optics Express **3**, 282 (2012)

[187] M. Flood, "*Laser altimetry: from science to commercial lidar mapping*", Photogrammetric Engineering and Remote Sensing **67**, 1209 (2001)

[188] R. Parrish, C.; Osiri, *AGU Fall Meeting Abstracts 2011*, "*Lidar wavelength considerations and radiometric performance*" (2011)

[189] P. C. Eng, S. Song, and B. Ping, "*State-of-the-art photodetectors for optoelectronic integration at telecommunication wavelength*", Nanophotonics **4**, 277 (2015)

[190] M. Casalino, L. Sirleto, L. Moretti, F. D. Corte, and I. Rendina, "*Design of a silicon resonant cavity enhanced photodetector based on the internal photoemission effect at 1.55μm*", Journal of Optics A **8**, 909 (2006)

[191] Y. M. Kang, H. D. Liu, M. Morse, M. J. Paniccia, M. Zadka, S. Litski, G. Sarid, A. Pauchard, Y. H. Kuo, H. W. Chen, W. S. Zaoui, J. E. Bowers, A. Beling, D. C. McIntosh, X. G. Zheng, and J. C. Campbell, "*Monolithic germanium/silicon avalanche photodiodes with 340 GHz gain-bandwidth product*", Nature Photonics **3**, 59 (2009)

[192] G. Masini, V. Cencelli, L. Colace, F. De Notaristefani, and G. Assanto, "*Monolithic integration of near-infrared Ge photodetectors with Si complementary metal-oxide-semiconductor readout electronics*", Applied Physics Letters **80**, 3268 (2002)

[193] S. J. Koester, J. D. Schaub, G. Dehlinger, and J. O. Chu, "*Germanium-on-SOI infrared detectors for integrated photonic applications*", IEEE Journal of Selected Topics in Quantum Electronics **12**, 1489 (2006)

[194] J. Michel, J. F. Liu, and L. C. Kimerling, "*High-performance Ge-on-Si photodetectors*", Nature Photonics **4**, 527 (2010)

[195] S. Assefa, F. Xia, and Y. A. Vlasov, "*Reinventing germanium avalanche photodetector for nanophotonic on-chip optical interconnects*", Nature **464**, 80 (2010)

[196] S. Y. Zhu, M. B. Yu, G. Q. Lo, and D. L. Kwong, "*Near-infrared waveguide-based nickel silicide Schottky-barrier photodetector for optical communications*", Applied Physics Letters **92**, 081103 (2008)

[197] I. Goykhman, B. Desiatov, J. Khurgin, J. Shappir, and U. Levy, "*Locally oxidized silicon surface-plasmon Schottky detector for telecom regime*", Nano Letters **11**, 2219 (2011)

[198] I. Goykhman, B. Desiatov, J. Khurgin, J. Shappir, and U. Levy, "*Waveguide based compact silicon Schottky photodetector with enhanced responsivity in the telecom spectral band*", Optics Express **20**, 28594 (2012)

[199] M. Casalino, M. Iodice, L. Sirleto, S. Rao, I. Rendina, and G. Coppola, "*Low dark current silicon-on-insulator waveguide metal-semiconductor-metal-photodetector*

based on internal photoemissions at 1550 nm", Journal of Applied Physics **114**, 153103 (2013)

[200] A. Akbari, R. N. Tait, and P. Berini, "*Surface plasmon waveguide Schottky detector*", Optics Express **18**, 8505 (2010)

[201] R. H. Walden, *GaAs IC Symposium IEEE Gallium Arsenide Integrated Circuit Symposium. 18th Annual Technical Digest 1996*, "*A review of recent progress in InP-based optoelectronic integrated circuit receiver front-ends*", 255–257 (1996)

[202] Y. Kang, P. Mages, A. R. Clawson, P. K. L. Yu, M. Bitter, Z. Pan, A. Pauchard, S. Hummel, and Y. H. Lo, "*Fused InGaAs-Si avalanche photodiodes with low-noise performances*", IEEE Photonics Technology Letters **14**, 1593 (2002)

[203] D. L. Harame, S. J. Koester, G. Freeman, P. Cottrel, K. Rim, G. Dehlinger, D. Ahlgren, J. S. Dunn, D. Greenberg, A. Joseph, F. Anderson, J. S. Rieh, S. A. S. T. Onge, D. Coolbaugh, V. Ramachandran, J. D. Cressler, and S. Subbanna, "*The revolution in SiGe: impact on device electronics*", Applied Surface Science **224**, 9 (2004)

[204] J. A. Wang and S. Lee, "*Ge-photodetectors for Si-based optoelectronic integration*", Sensors **11**, 696 (2011)

[205] D. W. Peters, "*An infrared detector utilizing internal photoemission*", Proceedings of the Institute of Electrical and Electronics Engineers **55**, 704 (1967)

[206] M. L. Brongersma, N. J. Halas, and P. Nordlander, "*Plasmon-induced hot carrier science and technology*", Nature Nanotechnology **10**, 25 (2015)

[207] M. Casalino, "*Internal photoemission theory: comments and theoretical limitations on the performance of near-infrared silicon Schottky photodetectors*", IEEE Journal of Quantum Electronics **52**, 1 (2016)

[208] I. Goykhman, B. Desiatov, J. Shappir, J. B. Khurgin, and U. Levy, "*Model for quantum efficiency of guided mode plasmonic enhanced silicon Schottky detectors*", arXiv:14012624 (2014)

[209] M. Casalino, G. Coppola, R. M. De La Rue, and D. F. Logan, "*State-of-the-art all-silicon sub-bandgap photodetectors at telecom and datacom wavelengths*", Laser & Photonics Reviews **10**, 895 (2016)

[210] B. Desiatov, I. Goykhman, N. Mazurski, J. Shappir, J. B. Khurgin, and U. Levy, "*Plasmonic enhanced silicon pyramids for internal photoemission Schottky detectors in the near-infrared regime*", Optica **2**, 335 (2015)

[211] M. Amirmazlaghani, F. Raissi, O. Habibpour, J. Vukusic, and J. Stake, "*Graphene-Si Schottky IR detector*", IEEE Journal of Quantum Electronics **49**, 589 (2013)

[212] X. H. An, F. Z. Liu, Y. J. Jung, and S. Kar, "*Tunable graphene-silicon heterojunctions for ultrasensitive photodetection*", Nano Letters **13**, 909 (2013)

[213] I. Goykhman, U. Sassi, B. Desiatov, N. Mazurski, S. Milana, D. De Fazio, A. Eiden, J. Khurgin, J. Shappir, U. Levy, and A. C. Ferrari, "*On-chip integrated, silicon–graphene plasmonic Schottky photodetector with high responsivity and avalanche photogain*", Nano Letters **16**, 3005 (2016)

[214] M. Casalino, U. Sassi, I. Goykhman, A. Eiden, E. Lidorikis, S. Milana, D. De Fazio, F. Tomarchio, M. Iodice, and G. Coppola, "*Vertically-illuminated, resonant-cavity-enhanced, graphene-silicon Schottky photodetectors*", ACS Nano **10**, 10955 (2017)

[215] S. Tongay, M. Lemaitre, X. Miao, B. Gila, B. R. Appleton, and A. F. Hebard, "*Rectification at graphene-semiconductor interfaces: zero-gap semiconductor-based diodes*", Physical Review X **2**, 011002 (2012)

[216] A. Di Bartolomeo, "*Graphene Schottky diodes: an experimental review of the rectifying graphene/semiconductor heterojunction*", Physics Reports **606**, 1 (2016)

[217] C. C. Chen, M. Aykol, C. C. Chang, A. F. J. Levi, and S. B. Cronin, "*Graphene-silicon Schottky diodes*", Nano Letters **11**, 1863 (2011)

[218] H. H. Li, "*Refractive index of silicon and germanium and its wavelength and temperature derivatives*", Journal of Physical and Chemical Reference Data **9**, 561 (1980)

[219] M. Nada, H. Yokoyama, Y. Muramoto, T. Ishibashi, and H. Matsuzaki, "*50-Gbit/s vertical illumination avalanche photodiode for 400-Gbit/s ethernet systems*", Optics Express **22**, 14681 (2014)

[220] A. V. Zayats, I. I. Smolyaninov, and A. A. Maradudin, "*Nano-optics of surface plasmon polaritons*", Physics Reports **408**, 131 (2005)

[221] Comsol-Multiphysics, "*https://www.comsol.com/*"

[222] B. Desiatov, I. Goykhman, and U. Levy, "*Demonstration of submicron square-like silicon waveguide using optimized LOCOS process*", Optics Express **18**, 18592 (2010)

[223] P. L. Richards and C. R. McCreight, "*Infrared detectors for astrophysics*", Physics Today **58**, 41 (2005)

[224] B. F. Jones, "*A reappraisal of the use of infrared thermal image analysis in medicine*", IEEE Transactions on Medical Imaging **17**, 1019 (1998)

[225] A. Koh, S. R. Gutbrod, J. D. Meyers, C. F. Lu, R. C. Webb, G. C. Shin, Y. H. Li, S. K. Kang, Y. G. Huang, I. R. Efimov, and J. A. Rogers, "*Ultrathin injectable sensors of temperature, thermal conductivity, and heat capacity for cardiac ablation monitoring*", Advanced Healthcare Materials **5**, 373 (2016)

[226] P. Rudol and P. Doherty, *Aerospace Conference, 2008 IEEE*, "*Human body detection and geolocalization for UAV search and rescue missions using color and thermal imagery*", 1–8, IEEE (2008), ISBN 1424414873

[227] R. Gade and T. B. Moeslund, "*Thermal cameras and applications: a survey*", Machine Vision and Applications **25**, 245 (2014)

[228] J. Yun and S. S. Lee, "*Human movement detection and identification using pyroelectric infrared sensors*", Sensors **14**, 8057 (2014)

[229] A. Rogalski, *Infrared detectors*, CRC press (2011)

[230] U. Sassi, R. Parret, S. Nanot, M. Bruna, S. Borini, D. De Fazio, Z. Zhao, E. Lidorikis, F. H. L. Koppens, A. C. Ferrari, and A. Colli, "*Graphene-based mid-infrared room-temperature pyroelectric bolometers with ultrahigh temperature coefficient of resistance*", Nature Communications **8**, 14311 (2017)

[231] C.-Y. Hsieh, Y.-T. Chen, W.-J. Tan, Y.-F. Chen, W. Y. Shih, and W.-H. Shih, "*Graphene-lead zirconate titanate optothermal field effect transistors*", Applied Physics Letters **100**, 113507 (2012)

[232] M. S. Choi, S. H. Lee, and W. J. Yoo, "*Plasma treatments to improve metal contacts in graphene field effect transistor*", Journal of Applied Physics **110**, 073305 (2011)

[233] S. Kim, J. Nah, I. Jo, D. Shahrjerdi, L. Colombo, Z. Yao, E. Tutuc, and S. K. Banerjee, "*Realization of a high mobility dual-gated graphene field-effect transistor with Al_2O_3 dielectric*", Applied Physics Letters **94**, 062107 (2009)

[234] A. A. Balandin, "*Low-frequency 1/f noise in graphene devices*", Nature Nanotechnology **8**, 549 (2013)

[235] E. S. Kulkarni, S. P. Heussler, A. V. Stier, I. Martin-Fernandez, H. Andersen, C. T. Toh, and B. Ozyilmaz, "*Exploiting the IR transparency of graphene for fast pyroelectric infrared detection*", Advanced Optical Materials **3**, 34 (2015)

[236] D. Akinwande, N. Petrone, and J. Hone, "*Two-dimensional flexible nanoelectronics*", Nature Communications **5**, 5678 (2014)

[237] T. T. Ryhänen, *Nanotechnologies for future mobile devices*, Cambridge University Press (2010)

[238] H.-C. Yuan, J. Shin, G. Qin, L. Sun, P. Bhattacharya, M. G. Lagally, G. K. Celler, and Z. Ma, "*Flexible photodetectors on plastic substrates by use of printing transferred single-crystal germanium membranes*", Applied Physics Letters **94**, 13102 (2009)

[239] Z. Liu, G. Chen, B. Liang, G. Yu, H. Huang, D. Chen, and G. Shen, "*Fabrication of high-quality ZnTe nanowires toward high-performance rigid/flexible visible-light photodetectors*", Optics Express **21**, 7799 (2013)

[240] S.-I. Park, Y. Xiong, R.-H. Kim, P. Elvikis, M. Meitl, D.-H. Kim, J. Wu, J. Yoon, C.-J. Yu, Z. Liu, Y. Huang, K.-C. Hwang, P. Ferreira, X. Li, K. Choquette, and J. A. Rogers, "*Printed assemblies of inorganic light-emitting diodes for deformable and semitransparent displays*", Science **325**, 977 (2009)

[241] Z. Qiang, H. Yang, L. Chen, H. Pang, Z. Ma, and W. Zhou, "*Fano filters based on transferred silicon nanomembranes on plastic substrates*", Applied Physics Letters **93**, 061106 (2008)

[242] Z. Chen, W. Ren, L. Gao, B. Liu, S. Pei, and H.-M. Cheng, "*Three-dimensional flexible and conductive interconnected graphene networks grown by chemical vapour deposition*", Nature Materials **10**, 424 (2011)

[243] E. Bosman, G. Van Steenberge, B. Van Hoe, J. Missinne, J. Vanfleteren, and P. Van Daele, "*Highly reliable flexible active optical links*", Photonics Technology Letters, IEEE **22**, 287 (2010)

[244] S. Shahi, "*Photovoltaics: flexible optoelectronics*", Nature Photonics **4**, 506 (2010)

[245] J. Yoon, L. Li, A. V. Semichaevsky, J. H. Ryu, H. T. Johnson, R. G. Nuzzo, and J. A. Rogers, "*Flexible concentrator photovoltaics based on microscale silicon solar cells embedded in luminescent waveguides*", Nature Communications **2**, 343 (2011)

[246] H. C. Ko, M. P. Stoykovich, J. Song, V. Malyarchuk, W. M. Choi, C.-J. Yu, J. B. Geddes III, J. Xiao, S. Wang, Y. Huang, and J. A. Rogers, "*A hemispherical electronic eye camera based on compressible silicon optoelectronics*", Nature **454**, 748 (2008)

[247] D.-H. Kim, N. Lu, R. Ma, Y.-S. Kim, R.-H. Kim, S. Wang, J. Wu, S. M. Won, H. Tao, A. Islam, K. J. Yu, T.-i. Kim, R. Chowdhury, M. Ying, L. Xu, M. Li, H.-J. Chung, H. Keum, M. McCormick, P. Liu, Y.-W. Zhang, F. G. Omenetto, Y. Huang, T. Coleman, and J. A. Rogers, "*Epidermal electronics*", Science **333**, 838 (2011)

[248] N. H. MacMillan, "*The theoretical strength of solids*", Journal of Materials Science **7**, 239 (1972)

[249] J. S. Blakemore, "*Semiconducting and other major properties of gallium-arsenide*", Journal of Applied Physics **53**, 123 (1982)

[250] W. Yang, H. Yang, G. Qin, Z. Ma, J. Berggren, M. Hammar, R. Soref, and Z. Weidong, "*Large-area InP-based crystalline nanomembrane flexible photodetectors*", Applied Physics Letters **96**, 121107 (2010)

[251] S. Lee, S. W. Jung, S. Park, J. Ahn, S. J. Hong, H. J. Yoo, M. H. Lee, and D. I. Cho, *MEMS IEEE 25th International Conference*, "*Ultra-high responsivity, silicon nanowire photodetectors for retinal prosthesis*", 1364–1367 (2012), ISBN 1084-6999

[252] G. Chen, B. Liang, Z. Liu, G. Yu, X. Xie, T. Luo, Z. Xie, D. Chen, M.-Q. Zhu, and G. Shen, "*High performance rigid and flexible visible-light photodetectors based on aligned X(In, Ga)P nanowire arrays*", Journal of Materials Chemistry C **2**, 1270 (2014)

[253] G. Yu, Z. Liu, X. Xie, X. Ouyang, and G. Shen, "*Flexible photodetectors with single-crystalline GaTe nanowires*", Journal of Materials Chemistry C **2**, 6104 (2014)

[254] Z. P. Sun, T. Hasan, F. Torrisi, D. Popa, G. Privitera, F. Q. Wang, F. Bonaccorso, D. M. Basko, and A. C. Ferrari, "*Graphene mode-locked ultrafast laser*", ACS Nano **4**, 803 (2010)

[255] K. S. Kim, Y. Zhao, H. Jang, S. Y. Lee, J. M. Kim, K. S. Kim, J.-H. Ahn, P. Kim, J.-Y. Choi, and B. H. Hong, "*Large-scale pattern growth of graphene films for stretchable transparent electrodes*", Nature **457**, 706 (2009)

[256] J. Chen, M. Badioli, P. Alonso-Gonzalez, S. Thongrattanasiri, F. Huth, J. Osmond, M. Spasenovic, A. Centeno, A. Pesquera, P. Godignon, A. Zurutuza Elorza, N. Camara, de F. J. G. Abajo, R. Hillenbrand, and F. H. L. Koppens, "*Optical nano-imaging of gate-tunable graphene plasmons*", Nature **487**, 77 (2012)

[257] Z. Fei, A. S. Rodin, G. O. Andreev, W. Bao, A. S. McLeod, M. Wagner, L. M. Zhang, Z. Zhao, M. Thiemens, G. Dominguez, M. M. Fogler, A. H. C. Neto, C. N. Lau, F. Keilmann, and D. N. Basov, "*Gate-tuning of graphene plasmons revealed by infrared nano-imaging*", Nature **487**, 82 (2012)

[258] L. Ju, B. Geng, J. Horng, C. Girit, M. Martin, Z. Hao, H. A. Bechtel, X. Liang, A. Zettl, Y. R. Shen, and F. Wang, "*Graphene plasmonics for tunable terahertz metamaterials*", Nature Nanotechnology **6**, 630 (2011)

[259] H. G. Yan, X. S. Li, B. Chandra, G. Tulevski, Y. Q. Wu, M. Freitag, W. J. Zhu, P. Avouris, and F. N. Xia, "*Tunable infrared plasmonic devices using graphene/insulator stacks*", Nature Nanotechnology **7**, 330 (2012)

[260] T. J. Echtermeyer, L. Britnell, P. K. Jasnos, A. Lombardo, R. V. Gorbachev, A. N. Grigorenko, A. K. Geim, A. C. Ferrari, and K. S. Novoselov, "*Strong plasmonic enhancement of photovoltage in graphene*", Nature Communications **2**, 458 (2011)

[261] M. M. Furchi, A. Pospischil, F. Libisch, J. Burgdörfer, and T. Mueller, "*Photovoltaic effect in an electrically tunable van der Waals heterojunction*", Nano Letters **14**, 4785 (2014)

[262] Y.-J. Hsiao, T.-H. Fang, L.-W. Ji, and B.-Y. Yang, "*Red-shift effect and sensitive responsivity of MoS_2/ZnO flexible photodetectors*", Nanoscale Research Letters **10**, 1 (2015)

[263] L. Britnell, R. M. Ribeiro, A. Eckmann, R. Jalil, B. D. Belle, A. Mishchenko, Y. J. Kim, R. V. Gorbachev, T. Georgiou, S. V. Morozov, A. N. Grigorenko, A. K. Geim, C. Casiraghi, A. H. Castro Neto, and K. S. Novoselov, "*Strong light-matter interactions in heterostructures of atomically thin films*", Science **340**, 1311 (2013)

[264] S. R. Tamalampudi, Y. Y. Lu, U. R. Kumar, R. Sankar, C. D. Liao, B. K. Moorthy, C. H. Cheng, F. C. Chou, and Y. T. Chen, "*High performance and bendable few-layered InSe photodetectors with broad spectral response*", Nano Letters **14**, 2800 (2014)

[265] M. Amani, A. Burke, Robert, M. Proie, Robert, and M. Dubey, "*Flexible integrated circuits and multifunctional electronics based on single atomic layers of MoS_2 and graphene*", Nanotechnology **26**, 115202 (2015)

[266] Y. Xue, Y. Zhang, Y. Liu, H. Liu, J. Song, J. Sophia, J. Liu, Z. Xu, Q. Xu, Z. Wang, J. Zheng, Y. Liu, S. Li, and Q. Bao, "*Scalable production of a few-layer MoS_2/WS_2 vertical heterojunction array and its application for photodetectors*", ACS Nano **10**, 573 (2016)

[267] F. Withers, H. Yang, L. Britnell, A. P. Rooney, E. Lewis, A. Felten, C. R. Woods, V. S. Romaguera, T. Georgiou, A. Eckmann, Y. J. Kim, S. G. Yeates, S. J. Haigh, A. K. Geim, K. S. Novoselov, and C. Casiraghi, "*Heterostructures produced from nanosheet-based inks*", Nano Letters **14**, 3987 (2014)

[268] D. J. Finn, M. Lotya, G. Cunningham, R. J. Smith, D. McCloskey, J. F. Donegan, and J. N. Coleman, "*Inkjet deposition of liquid-exfoliated graphene and MoS_2 nanosheets for printed device applications*", Journal of Materials Chemistry C **2**, 925 (2014)

[269] C. H. Liu, Y. C. Chang, T. B. Norris, and Z. H. Zhong, "*Graphene photodetectors with ultra-broadband and high responsivity at room temperature*", Nature Nanotechnology **9**, 273 (2014)

[270] D. B. Velusamy, R. H. Kim, S. Cha, J. Huh, R. Khazaeinezhad, S. H. Kassani, G. Song, S. M. Cho, S. H. Cho, I. Hwang, J. Lee, K. Oh, H. Choi, and C. Park, "*Flexible transition metal dichalcogenide nanosheets for band-selective photodetection*", Nature Communications **6**, 8063 (2015)

[271] M. G. Faraj, K. Ibrahim, and M. K. M. Ali, "*PET as a plastic substrate for the flexible optoelectronic applications*", Optoelectronics and Advanced Materials **5**, 879 (2011)

[272] L. G. P. Martins, Y. Song, T. Y. Zeng, M. S. Dresselhaus, J. Kong, and P. T. Araujo, "*Direct transfer of graphene onto flexible substrates*", Proceedings of the National Academy of Sciences of the United States of America **110**, 17762 (2013)

[273] R. Thiele, C.; Das, *Carbon nanotubes and graphene for electronics applications 2010-2020*, IDTechEx (2009)

[274] M. C. Lemme, T. J. Echtermeyer, M. Baus, and H. Kurz, "*A graphene field-effect device*", Electron Device Letters, IEEE **28**, 282 (2007)

[275] T. O. Wehling, K. S. Novoselov, S. V. Morozov, E. E. Vdovin, M. I. Katsnelson, A. K. Geim, and A. I. Lichtenstein, "*Molecular doping of graphene*", Nano Letters **8**, 173 (2008)

[276] J. T. Ye, M. F. Craciun, M. Koshino, S. Russo, S. Inoue, H. T. Yuan, H. Shimotani, A. F. Morpurgo, and Y. Iwasa, "*Accessing the tansport properties of graphene and its multilayers at high carrier density*", Proceedings of the National Academy of Sciences of the United States of America **108**, 13002 (2011)

[277] H. Sirringhaus, T. Kawase, R. H. Friend, T. Shimoda, M. Inbasekaran, W. Wu, and E. P. Woo, "*High-resolution inkjet printing of all-polymer transistor circuits*", Science **290**, 2123 (2000)

[278] H. Du, X. Lin, Z. Xu, and D. Chu, "*Electric double-layer transistors: a review of recent progress*", Journal of Materials Science **50**, 5641 (2015)

[279] P. Azaïs, L. Duclaux, P. Florian, D. Massiot, M.-A. Lillo-Rodenas, A. Linares-Solano, J.-P. Peres, C. Jehoulet, and F. Béguin, "*Causes of supercapacitors ageing in organic electrolyte*", Journal of Power Sources **171**, 1046 (2007)

[280] D. K. Efetov and P. Kim, "*Controlling electron-phonon interactions in graphene at ultrahigh carrier densities*", Physical Review Letters **105**, 256805 (2010)

[281] M. Sup Choi, G.-H. Lee, Y.-J. Yu, D.-Y. Lee, S. Hwan Lee, P. Kim, J. Hone, and W. Jong Yoo, "*Controlled charge trapping by molybdenum disulphide and graphene in ultrathin heterostructured memory devices*", Nature Communications **4**, 1624 (2013)

[282] S. Das, H.-Y. Chen, A. V. Penumatcha, and J. Appenzeller, "*High performance multilayer MoS_2 transistors with scandium contacts*", Nano Letters **13**, 100 (2013)

[283] Y.-J. Yu, Y. Zhao, S. Ryu, L. E. Brus, K. S. Kim, and P. Kim, "*Tuning the graphene work function by electric field effect*", Nano Letters **9**, 3430 (2009)

[284] B. Shan and K. Cho, "*First principles study of work functions of single wall carbon nanotubes*", Physical Review Letters **94**, 236602 (2005)

[285] B. J. Kim, H. Jang, S.-K. Lee, B. H. Hong, J.-H. Ahn, and J. H. Cho, "*High-performance flexible graphene field effect transistors with ion gel gate dielectrics*", Nano Letters **10**, 3464 (2010)

[286] S. K. Lee, H. Y. Jang, S. Jang, E. Choi, B. H. Hong, J. Lee, S. Park, and J. H. Ahn, "*All graphene-based thin film transistors on flexible plastic substrates*", Nano Letters **12**, 3472 (2012)

[287] I. Meric, M. Y. Han, A. F. Young, B. Ozyilmaz, P. Kim, and K. L. Shepard, "*Current saturation in zero-bandgap, top-gated graphene field-effect transistors*", Nature Nanotechnology **3**, 654 (2008)

[288] J. A. Robinson, M. LaBella, M. Zhu, M. Hollander, R. Kasarda, Z. Hughes, K. Trumbull, R. Cavalero, and D. Snyder, "*Contacting graphene*", Applied Physics Letters **98**, 053103 (2011)

[289] T. Fang, A. Konar, H. Xing, and D. Jena, "*Carrier statistics and quantum capacitance of graphene sheets and ribbons*", Applied Physics Letters **91**, 092109 (2007)

[290] J. Xia, F. Chen, J. Li, and N. Tao, "*Measurement of the quantum capacitance of graphene*", Nature Nanotechnology **4**, 505 (2009)

[291] C. Lu, Q. Fu, S. Huang, and J. Liu, "*Polymer electrolyte-gated carbon nanotube field-effect transistor*", Nano Letters **4**, 623 (2004)

[292] T. Ozel, A. Gaur, J. A. Rogers, and M. Shim, "*Polymer electrolyte gating of carbon nanotube network transistors*", Nano Letters **5**, 905 (2005)

[293] W. B. Russel, D. A. Saville, and W. R. Schowalter, *Colloidal dispersions*, Cambridge University Press (1989)

[294] M. Salomon, M. Xu, E. M. Eyring, and S. Petrucci, "*Molecular structure and dynamics of $LiClO_4$-polyethylene oxide-400 (dimethyl ether and diglycol systems) at 25°C*", The Journal of Physical Chemistry **98**, 8234 (1994)

[295] R. H. Boyd, "*The dielectric constant of lamellar semicrystalline polymers*", Journal of Polymer Science **21**, 505 (1983)

[296] H. Shi, R. Yan, S. Bertolazzi, J. Brivio, B. Gao, A. Kis, D. Jena, H. G. Xing, and L. Huang, "*Exciton dynamics in suspended monolayer and few-layer MoS_2 2D crystals*", ACS Nano **7**, 1072 (2013)

[297] A. P. Drozdov, M. I. Eremets, I. A. Troyan, V. Ksenofontov, and S. I. Shylin, "*Conventional superconductivity at 203 kelvin at high pressures in the sulfur hydride system*", Nature **525**, 73 (2015)

[298] J. M. Blatt and C. J. Thompson, "*Shape resonances in superconducting thin films*", Physical Review Letters **10**, 332 (1963)

[299] T.-C. Chiang, "*Superconductivity in thin films*", Science **306**, 1900 (2004)

[300] S. Y. Qin, J. Kim, Q. Niu, and C. K. Shih, "*Superconductivity at the two-dimensional limit*", Science **324**, 1314 (2009)

[301] M. Strongin, R. S. Thompson, O. F. Kammerer, and J. E. Crow, "*Destruction of superconductivity in disordered near-monolayer films*", Physical Review B **1**, 1078 (1970)

[302] A. M. Goldman and N. Markovic, "*Superconductor-insulator transitions in the two-dimensional limit*", Physics Today **51**, 39 (1998)

[303] Y. Guo, Y. F. Zhang, X. Y. Bao, T. Z. Han, Z. Tang, L. X. Zhang, W. G. Zhu, E. G. Wang, Q. Niu, Z. Q. Qiu, J. F. Jia, Z. X. Zhao, and Q. K. Xue, "*Superconductivity modulated by quantum size effects*", Science **306**, 1915 (2004)

[304] Y. Ivry, C.-S. Kim, A. E. Dane, D. De Fazio, A. N. McCaughan, K. A. Sunter, Q. Zhao, and K. K. Berggren, "*Universal scaling of the critical temperature for thin films near the superconducting-to-insulating transition*", Physical Review B **90**, 214515 (2014)

[305] J.-F. Ge, Z.-L. Liu, C. Liu, C.-L. Gao, D. Qian, Q.-K. Xue, Y. Liu, and J.-F. Jia, "*Superconductivity above 100 K in single-layer FeSe films on doped $SrTiO_3$*", Nature Materials **14**, 285 (2015)

[306] V. N. Kotov, B. Uchoa, V. M. Pereira, F. Guinea, and A. H. Castro Neto, "*Electron-electron interactions in graphene: current status and perspectives*", Reviews of Modern Physics **84**, 1067 (2012)

[307] B. M. Ludbrook, G. Levy, P. Nigge, M. Zonno, M. Schneider, D. J. Dvorak, C. N. Veenstra, S. Zhdanovich, D. Wong, P. Dosanjh, C. Straßer, A. Stöhr, S. Forti, C. R. Ast, U. Starke, and A. Damascelli, "*Evidence for superconductivity in Li-decorated monolayer graphene*", Proceedings of the National Academy of Sciences **112**, 11795 (2015)

[308] J. Chapman, Y. Su, C. A. Howard, D. Kundys, A. N. Grigorenko, F. Guinea, A. K. Geim, I. V. Grigorieva, and R. R. Nair, "*Superconductivity in Ca-doped graphene laminates*", Scientific Reports **6**, 23254 (2016)

[309] C. Tonnoir, A. Kimouche, J. Coraux, L. Magaud, B. Delsol, B. Gilles, and C. Chapelier, "*Induced superconductivity in graphene grown on rhenium*", Physical Review Letters **111**, 246805 (2013)

[310] A. Di Bernardo, O. Millo, M. Barbone, H. Alpern, Y. Kalcheim, U. Sassi, A. K. Ott, D. De Fazio, D. Yoon, M. Amado, A. C. Ferrari, J. Linder, and J. W. A. Robinson, "*p-wave triggered superconductivity in single-layer graphene on an electron-doped oxide superconductor*", Nature Communications **8**, 14024 (2017)

[311] O. Fischer, M. Kugler, I. Maggio-Aprile, C. Berthod, and C. Renner, "*Scanning tunneling spectroscopy of high-temperature superconductors*", Reviews of Modern Physics **79**, 353 (2007)

[312] Y. Tanaka and S. Kashiwaya, "*Theory of tunneling spectroscopy of d-wave superconductors*", Physical Review Letters **74**, 3451 (1995)

[313] S. Kashiwaya and Y. Tanaka, "*Tunnelling effects on surface bound states in unconventional superconductors*", Reports on Progress in Physics **63**, 1641 (2000)

[314] E. Revolinsky, G. A. Spiering, and D. J. Beerntsen, "*Superconductivity in the niobium-selenium system*", Journal of Physics and Chemistry of Solids **26**, 1029 (1965)

[315] N. E. Staley, J. Wu, P. Eklund, Y. Liu, L. Li, and Z. Xu, "*Electric field effect on superconductivity in atomically thin flakes of $NbSe_2$*", Physical Review B **80**, 184505 (2009)

[316] L. F. Bates and A. Baqi, "*The magnetic properties of chromium*", Proceedings of the Physical Society **48**, 781 (1936)

[317] J. T. Ye, Y. J. Zhang, R. Akashi, M. S. Bahramy, R. Arita, and Y. Iwasa, "*Superconducting dome in a gate-tuned band insulator*", Science **338**, 1193 (2012)

[318] D. Braga, I. Gutiérrez Lezama, H. Berger, and A. F. Morpurgo, "*Quantitative determination of the band gap of WS_2 with ambipolar ionic liquid-gated transistors*", Nano Letters **12**, 5218 (2012)

[319] Y. Yu, F. Yang, X. F. Lu, Y. J. Yan, H. ChoYong, L. Ma, X. Niu, S. Kim, Y.-W. Son, D. Feng, S. Li, S.-W. Cheong, X. H. Chen, and Y. Zhang, "*Gate-tunable phase transitions in thin flakes of 1T-TaS_2*", Nature Nanotechnology **10**, 270 (2015)

[320] D. Costanzo, S. Jo, H. Berger, and A. F. Morpurgo, "*Gate-induced superconductivity in atomically thin MoS_2 crystals*", Nature Nanotechnology **11**, 339 (2016)

[321] J. M. Lu, O. Zheliuk, I. Leermakers, N. F. Q. Yuan, U. Zeitler, K. T. Law, and J. T. Ye, "*Evidence for two-dimensional Ising superconductivity in gated MoS_2*", Science **350**, 1353 (2015)

[322] Y. Saito, Y. Nakamura, M. S. Bahramy, Y. Kohama, J. Ye, Y. Kasahara, Y. Nakagawa, M. Onga, M. Tokunaga, T. Nojima, Y. Yanase, and Y. Iwasa, "*Superconductivity protected by spin-valley locking in ion-gated MoS_2*", Nature Physics **12**, 144 (2016)

[323] T. Brumme, M. Calandra, and F. Mauri, "*First-principles theory of field-effect doping in transition-metal dichalcogenides: structural properties, electronic structure, Hall coefficient, and electrical conductivity*", Physical Review B **91**, 155436 (2015)

[324] T. Brumme, M. Calandra, and F. Mauri, "*Determination of scattering time and of valley occupation in transition-metal dichalcogenides doped by field effect*", Physical Review B **93**, 081407 (2016)

[325] A. M. Stacy and D. T. Hodul, "*Raman spectra of IVB and VIB transition metal disulfides using laser energies near the absorption edges*", Journal of Physics and Chemistry of Solids **46**, 405 (1985)

[326] K. Ueno, H. Shimotani, H. T. Yuan, J. T. Ye, M. Kawasaki, and Y. Iwasa, "*Field-induced superconductivity in electric double layer transistors*", Journal of the Physical Society of Japan **83**, 032001 (2014)

[327] X. Xi, Z. Wang, W. Zhao, J.-H. Park, K. T. Law, H. Berger, L. Forro, J. Shan, and K. F. Mak, "*Ising pairing in superconducting $NbSe_2$ atomic layers*", Nature Physics **12**, 139 (2016)

[328] S. N. Dorenbos, P. Forn-Díaz, T. Fuse, A. H. Verbruggen, T. Zijlstra, T. M. Klapwijk, and V. Zwiller, "*Low gap superconducting single photon detectors for infrared sensitivity*", Applied Physics Letters **98**, 251102 (2011)

[329] A. Engel, A. Aeschbacher, K. Inderbitzin, A. Schilling, K. Il'in, M. Hofherr, M. Siegel, A. Semenov, and H. W. Hübers, "*Tantalum nitride superconducting single-photon detectors with low cut-off energy*", Applied Physics Letters **100**, 062601 (2012)

[330] J. Yan, M. H. Kim, J. A. Elle, A. B. Sushkov, G. S. Jenkins, H. M. Milchberg, M. S. Fuhrer, and H. D. Drew, "*Dual-gated bilayer graphene hot-electron bolometer*", Nature Nanotechnology **7**, 472 (2012)

[331] J. J. Bae, J. H. Yoon, S. Jeong, B. H. Moon, J. T. Han, H. J. Jeong, G.-W. Lee, H. R. Hwang, Y. H. Lee, S. Y. Jeong, and S. C. Lim, "*Sensitive photo-thermal response of graphene oxide for mid-infrared detection*", Nanoscale **7**, 15695 (2015)